On the structure and dynamics of the Asian monsoon anticyclone

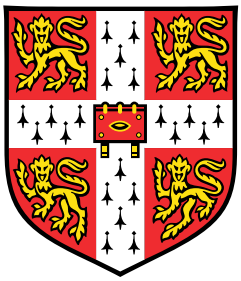

Philip Rupp

Supervisor:
Prof. Peter Haynes

Department of Applied Mathematics and Theoretical Physics
University of Cambridge

A dissertation submitted for the degree of
Doctor of Philosophy

Queens' College

September 2018

Abstract

The Asian summer monsoon circulation has been the subject of continuous research for several decades. Much emphasis has been given to the lower level cyclone, but while various models and mechanisms have been proposed to explain certain features of the upper level anticyclone, like the zonal scale or time dependence, a comprehensive theory combining these characteristics is still lacking.

We re-visited the steady and linear 2D monsoon model proposed by Gill and Matsuno, which potentially captures the time-mean response of the flow, but fails to account for any kind of temporal evolution and requires a strong mechanical friction throughout the atmosphere, which is a questionable assumption for the upper troposphere/lower stratosphere region. We then re-modelled the monsoon flow as a response to a localised heat source using a numerical model that is able to capture the time dependence, non-linearity and three-dimensional nature of the system, which we see as necessary to successfully model the monsoon anticyclone.

In addition to the explicit heating driving the monsoon we included a simple representation of mid-latitude dynamics into the model by imposing a relaxation towards a baroclinically unstable state. The simulated flow therefore includes mid-latitude westerly jets and baroclinic eddies. We then explored the parameter space by varying for example the forcing magnitude or the meridional temperature gradient of the basic state and investigated changes of the response. This way it was possible to identify various parameter combinations for which the response shows similar structures and behaviours to what has been observed in re-analysis data in relation to the monsoon anticyclone. This includes a finite zonal length scale of the response, as well as temporal evolution in the form of east- and westward shedding of eddies.

Many characteristics of the behaviour of the upper level monsoon anticyclone can potentially be investigated by considering the dynamical evolution of a single fluid layer forced by a steady mass source. Such a single-layer model can be used to perform more in-depth studies than are possible in a 3D model. Using this approach we explained a variety of phenomena related to westward eddy shedding from the monsoon anticyclone as a consequence of an absolute instability of the flow field. By performing a comprehensive spatial stability analysis of an idealised representation of the system we were able to develop a theory for the transition between different shedding states.

Adapting a simple analytic theory based on a centre-of-mass approach further allowed us to explain the near-steady propagation of the eddies shed from the monsoon. We also showed that the eddy propagation in our system is not modified by the fact that eddies are not well-separated and shed as a series of vortices, in contrast to findings of previous authors. By extending the theory and including a zonal background wind we were further able to explain some aspects of the changes due to thermal damping and the interaction of the flow with a zonal mean background wind like the mid-latitude jet.

The presented study covers various observed features and behaviours of the Asian monsoon anticyclone and shows how they arise in simple dynamical models for certain ranges of values of external parameters.

Acknowledgements

Firstly, I would like to thank my supervisor Prof. Peter Haynes for all the support and guidance during my PhD studies. He made an invaluable contribution to this dissertation with his deep understanding of physical systems and mathematical methods, as well as his expertise in scientific research and academic writing. His continued motivation and encouragement to follow my scientific curiosity allowed me to grow as a researcher.

Secondly, I am grateful to my family, friends and colleagues for the support, feedback and collaboration throughout the years. In particular, I want to thank my office-mate Jacob Smith for many stimulating discussions, the assistance in countless bug-hunts and all those highly enjoyable coffee breaks. Many thanks also to my dear friend Nora Laraki, without whom I would have not even started this PhD.

I gratefully acknowledge the various funding sources received towards my studies from the European project StratoClim (7th Framework Programme, project no. 603557) and the ACCI project of the European Research Council (project no. 267760). I am further thankful for financial support from the Cambridge Philosophical Society and the Queens' College Cambridge.

Declaration

I hereby declare that except where specific reference is made to the work of others, the contents of this dissertation are original and have not been submitted in whole or in part for consideration for any other degree or qualification in this, or any other university. This dissertation is my own work and contains nothing which is the outcome of work done in collaboration with others, except as specified in the text and in the acknowledgements.

Philip Rupp
September 2018

Table of contents

Chapter 1

The Asian monsoon as part of the climate system

The Earth's climate system has a huge impact on all living organisms. Harvesting times, architectural needs, travel planning and the arrangement of our every day lives strongly depend on e.g. the current season or climatological zone we live in. In general what we refer to as the climate system is actually a collection of sub-systems, such as the oceans, the atmosphere or the biosphere. All of these systems can be regarded as separate and isolated to some extent but in reality form a complex network of complicated interactions and dependencies.

Even though the climate is influenced and controlled by numerous sub-systems the atmosphere has probably the most direct and one of the most significant impacts on humanity. Being able to understand, and eventually to predict, the circulation patterns and details of the atmosphere is crucial to e.g. minimise the impact of natural disasters and maximise our living standards. In this chapter we will at first outline some of the main characteristics of the atmosphere's general circulation and the Asian monsoon flow in particular (sections 1.1 and 1.2). Section 1.3 will then give an overview of the structure of this thesis.

1.1 The atmosphere and its general circulation

For many purposes the atmosphere can be described as a thin layer of fluid surrounding a rotating sphere. Within this layer a variety of coupled and complex dynamical, chemical, radiative and other processes are active. These processes determine, individually or in combination, the overall structure of the atmosphere and drive various flow patterns on many length and time scales. Within this dissertation we will focus on the range of daily to monthly time scales and synoptic ($\sim 10^3$-10^4km) length scales. The dynamic state of the atmosphere on these scales is commonly referred to as the general circulation. We will now outline some aspects of the atmospheric general circulation that are important to understand the analyses

and results presented in the following chapters. A comprehensive description of the general state of the atmosphere and many of the processes explained in this chapter is given by Andrews [2000].

In principle the atmosphere can behave dynamically quite differently depending on the latitudinal range of interest. One of the main reasons is that the vertical component of the Earth's angular velocity vector changes with latitude and thus the Coriolis force on a (horizontally) moving air parcel can play a different role at different latitudes. This means the use of certain approximations might depend on the studied region, as explained later in more detail. This thesis will mostly focus on the tropical belt, which extents from roughly 20° S to 20° N Latitude and the sub-tropics which extents about an additional 10° further polewards from there. Alongside with the tropics one commonly speaks about the mid-latitudes (or extratropics) between $30-65°$ on both hemispheres and the polar regions form everything beyond 65°.

In the vertical the atmosphere forms a number of layers that can be defined via the vertical temperature profile of the atmosphere. The different layers and their relation to the temperature structure is shown in figure 1.1. As can be seen, the vertical temperature gradient (the lapse rate) changes sign for neighbouring layers (which is commonly used as their definition). The exact profile differs between tropics and poles but the overall structure stays the same. In general the extratropical tropopause tends to be lower than it is in the tropics, and is located more at around 10km. Similarly the with height exponentially decreasing pressure (see axes in figure 1.1) is a common feature of tropical and extra-tropical regions, although the vertical decay rate varies.

The vertical temperature profile of the atmosphere gets basically set by two factors: the incoming thermal radiation from the sun and the vertically varying absorption properties of the atmosphere. Near the surface temperatures are relatively high because a lot of the incoming short-wave radiation is absorbed by the ground. It then gets re-emitted as long-wave radiation which can be absorbed by the lower troposphere. With increasing height the radiative heat-flux from the surface decreases and the temperature drops until the tropopause is reached. Here temperatures increase again due to the increasing concentration of ozone in the stratosphere and its ability to absorb short-wave radiation. The high ozone concentration in the stratosphere can mainly be explained by certain coupled chemical and physical processes [Dobson 1956] and their dependency on low temperatures and ultra-violet radiation, respectively. Far above the mesosphere, in the thermosphere, the temperatures increase to even higher values since here the highly energetic cosmic radiation starts to be absorbed.

The layers of the atmosphere can differ substantially in their dynamic, chemical and physical properties. The lowest layer, the troposphere, is where our weather is 'happening'. This layer is vertically well mixed in terms of its static stability (more details later). Horizontally the troposphere is characterised by strong zonal anomalies in most of the dynamic fields, partly caused by the asymmetric distribution of land-masses. At a height of about $16km$ (in the tropics) the vertical temperature gradient changes it sign. This height is called (cold-point) tropopause and it is where the stratosphere starts. In the stratosphere the atmosphere is generally very dry and calm. The influence of the bottom topography

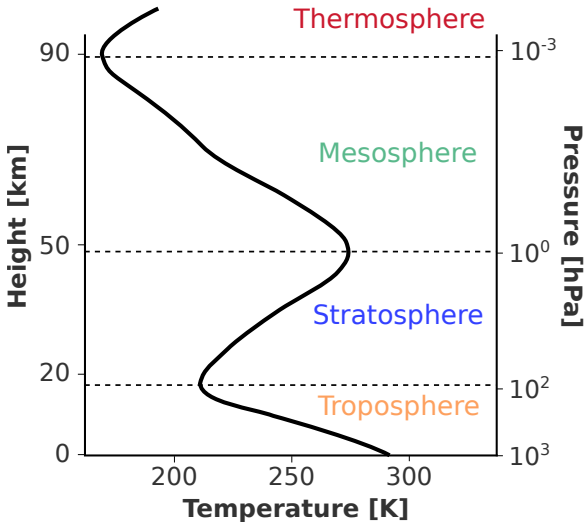

Fig. 1.1 Atmospheric layers within the tropics defined by the vertical extrema of the mean temperature profile (black contour). After Andrews [2000].

and other surface-related processes overall weakens for the higher atmospheric layers and can often (though not always) be neglected for stratospheric dynamics. The stratosphere shows a high degree of zonal symmetry [Fueglistaler et al. 2009a] and is, in particular in the tropics, statically more stable than the troposphere. The dryness of the stratosphere can mostly be explained by freeze-drying of vertically transported air through the low-temperature regions of the cold-point tropopause [Brewer 1949].

As we go higher the atmospheric layers have generally less and less dynamical impact on the troposphere and hence the weather system. However, over the past decades the importance of the stratosphere and its coupling to the state of the troposphere became evident [Boville 1984; Kodera et al. 1990] and research on its properties and the coupling mechanisms was emphasised in order to improve climate and weather forecasts (e.g. Baldwin et al. [2003]). This thesis will be focussing on dynamical processes in the broad region of the upper troposphere and lower stratosphere (UTLS or middle atmosphere) and aspects of the corresponding coupling between these two layers. As explained, the transition is usually given in terms of the cold-point tropopause (especially in the tropics). In recent years the idea was established that the boundary between the troposphere and stratosphere in the tropics is better described by a transition-region with finite vertical extent, the tropical tropopause layer (TTL). This special region combines characteristics of troposphere and stratosphere and forms an important gateway between the two [Fueglistaler et al. 2009a]. Figure 1.2 illustrates the general temperature structure of TTL.

A useful quantity to describe the (vertical) structure of the atmosphere is the potential temperature (Θ), which gives the theoretical temperature of an air parcel if its pressure were adiabatically changed to a reference value (e.g. surface pressure). It is therefore conserved by dry adiabatic processes, which is why surfaces of constant potential temperature are sometimes referred to as isentropic surfaces. The potential temperature of an ideal gas is defined by

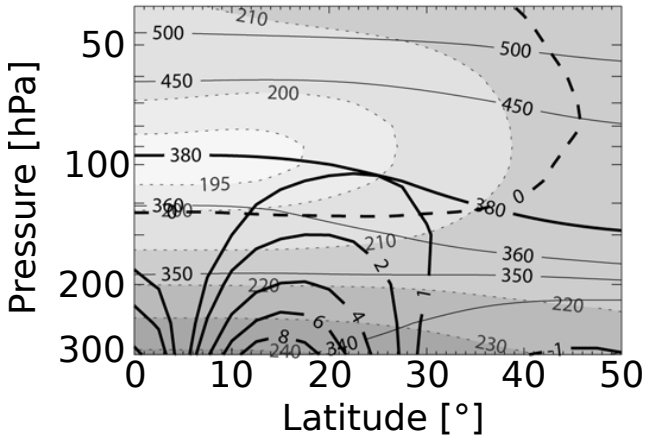

Fig. 1.2 Various temporally and zonally averaged fields within the TTL, taken from ERA-I re-analysis date (see chapter 2). Shading shows temperature (in K), solid lines show potential temperature (in K) and bold lines show streamfunction. From Fueglistaler et al. [2009a], see corresponding article for more detailed description.

$$\Theta = T\sigma^{-\frac{R}{c_p}}, \tag{1.1}$$

where T is temperature, sigma the ratio of pressure and surface pressure $\sigma = p/p_0$, R the specific gas constant of the system and c_p the heat capacity of the gas at constant pressure. Details on the properties of potential temperature can be found in Andrews [2000].

The potential temperature Θ can provide direct information on the stability of the system. A positive vertical Θ gradient describes a statically stable system. If the vertical Θ gradient is negative, a parcel could reduce its potential energy be rising to a higher level and hence the system would re-organise to minimise its total potential energy. Correspondingly a finite positive vertical gradient will suppress vertical motion as it requires an energy input to be sustained. The potential temperature structure of the TTL is illustrated in figure 1.2. The tropopause in the tropics is roughly given by the 380K isentropic surface. Besides that we can make two additional observations: first, the vertical Θ gradient seems to be large above the tropopause compared to below and, second, the (potential) temperature field seems to have finite meridional gradients (with opposite sign) above and below the 350K isentrope (about 10km).

Since Θ generally increases monotonically with height it can be used as vertical coordinate. One advantage of such an isentropic coordinate system is when representing potential vorticity (PV) fields. PV is a dynamical quantity that combines information about the circulation of an air parcel (its vorticity) and the stratification of the system in terms of the vertical potential temperature gradient. A quantitative definition of PV will be given later in equation 3.1. PV is conserved on isentropic surfaces under adiabatic and frictionless processes and is therefore useful quantity when describing and analysing the

dynamics of the mid-latitude atmosphere [Hoskins 1991; Hoskins et al. 1985]. It behaves like a passive tracer on potential temperature surfaces with sinks and sources given by diabatically active regions. Any adiabatic flow thus tends to follow contours of constant PV and air within a closed PV contour is usually well isolated from surrounding air.

The general circulation in subtropical and mid-latitude regions of the middle atmosphere is mostly characterised by strong zonal winds in the form of the mid-latitude (or subtropical) jet. Figure 1.3 shows the temporally and zonally averaged zonal wind field. Clear jets can be identified, centred at about 10km height and $\pm 40^\circ$ latitude. The jets are related to the pressure gradient arising from the strong meridional gradient in (potential) temperature at mid-latitudes (see figure 1.2). The corresponding meridional winds get deflected eastwards due to the acceleration by the Coriolis force until a geostrophic balance is reached, where the Coriolis force balances the pressure gradient force and the flow is purely zonal.

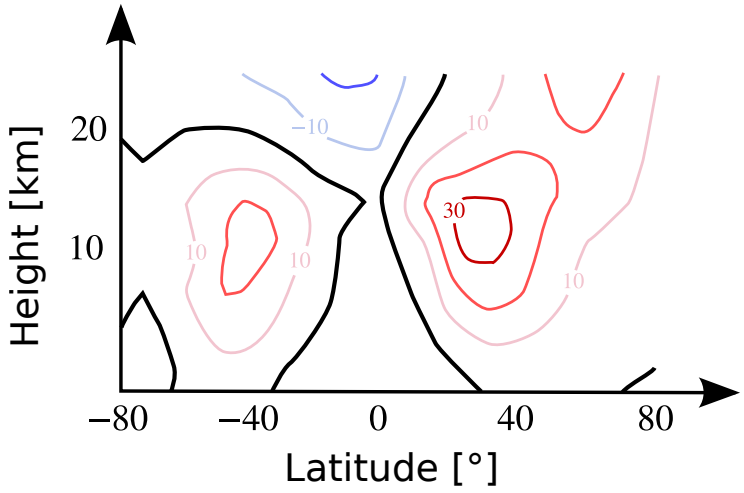

Fig. 1.3 Schematic mean zonal wind profile of the lower and middle atmosphere in January (after Andrews [2000]). Values are given in m/s and zero contour is plotted in thick black.

However, this state of a meridional thermal contrast balanced by a zonal wind is not entirely stable. Eady [1949] and Charney [1947] independently developed simple models to show that corresponding wind and temperature gradients of the steady jet-system are unstable to certain modes. The corresponding instability is referred to as baroclinic instability and the correspondingly induced perturbations are called baroclinic eddies. The mid-latitude region of the lower and middle atmosphere is therefore not only characterised by a strong mean westerly wind, but also by a high variability and transient perturbations. It is important to realise that jet and eddies form a coupled system (due to eddy-mean-interactions) and thus often react as such to external perturbations.

As can be seen in figure 1.3 the mean zonal wind shows clear hemispheric asymmetries. These differences are induced by the seasonal cycle of solar radiation and thus in temperature. The meridional temperature gradient of the winter hemisphere is generally larger and hence the system develops a

stronger mid-latitude jet and baroclinic eddies. In return, the summer-hemisphere jet and eddies are weaker than in the annual mean state, which, since the monsoon is active during boreal summer, will be the most relevant situation for the studies of this dissertation.

This section described a range of characteristics of the zonally symmetric general state of the atmosphere and in particular of the middle atmosphere in the tropics and mid-latitudes. One of the most pronounced zonally asymmetric features of the atmosphere is the Asian monsoon circulation, which is our primary subject of interest. The next section will describe and explain certain properties of the monsoon and its main drivers. In some situations in chapters 5 to 6 we will think of the monsoon circulation as being a zonally asymmetric (or azonal) perturbation of a zonally symmetric basic state, where the basic state will usually be defined to have similar characteristics to the once described earlier.

1.2 Properties of the Asian monsoon anticyclone

The Asian monsoon is a large-scale tropical circulation and one of the most important dynamic features in the global atmospheric system. It is active during the boreal summer months (June-August), roughly spans south Asia and affects more than 60% of the world's population [Wu et al. 2012]. In this section we will point out and describe some of the key aspects of the monsoon anticyclone. A comprehensive overview of known characteristics, drivers and interactions related to the monsoon was given by Chang [2004].

Dynamically the monsoon is caused by the thermal contrast of the warm landmasses of the Asian continent and the colder waters of the Indian Ocean during summer. The warm air above the land rises and causes an influx of cooler, moist air from the sea, which subsequently also heats up and rises. As it rises, the air cools due to adiabatic expansion and the contained water vapour condenses. The large scale condensation of the water vapour in the middle troposphere leads to heavy rain fall at the surface. In some regions of India and south Asia up to 85% of the annual precipitation is observed during the monsoon season (May-September, see Wang [2002]).

The condensation process further leads to a release of latent heat and thus diabatic heating, which further accelerates the ascent. Although the initial thermal land-sea contrast near the surface triggers the circulation, it is the latent heat release in the middle troposphere that drives the flow. The general structure of the monsoon and its main features are illustrated in figure 1.4.

When reaching the upper troposphere the air parcels have lost the majority of their original water content and the ascent of air parcels, and the thus latent heat release, comes to a stop[1]. The continuous vertical influx of air, however, leads to a horizontal divergence within the upper section of the monsoon and, due to the influence of the Coriolis force, to an anticyclonic circulation. Correspondingly the

[1] The extent of the heating is potentially further influenced by the changes in vertical temperature profile within the TTL.

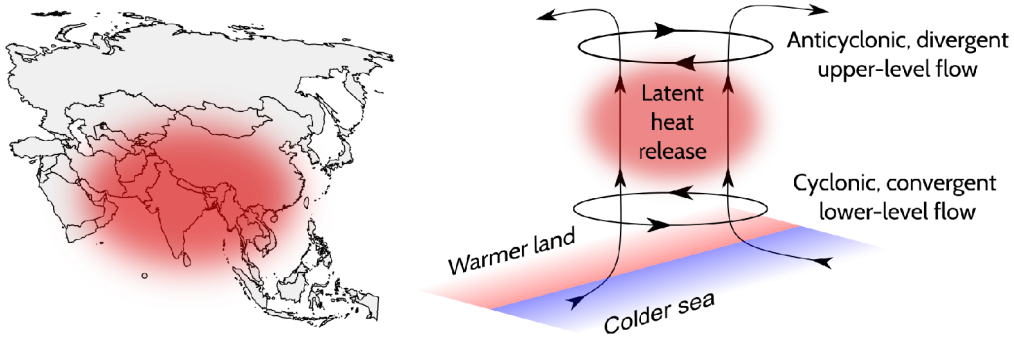

Fig. 1.4 Schematic illustration of the horizontal position (left) and structure and drivers (right) of the monsoon flow.

convergence within the lower section creates a cyclonic flow. This thesis will mainly focus on the properties, characteristics and behaviours of the upper level anticyclone.

The high mountains of the Tibetan plateau in south Asia provide an additional driving force for the monsoon circulation in two ways. On one hand can the steep slopes of the orography lead to ascent of horizontally moving (moist) air. On the other hand the elevated land mass of the plateau can diabatically heat the otherwise cool surrounding air. Both mechanisms can potentially help triggering the monsoon flow via latent heat release of ascending, moist air, as explained earlier.

However, various authors have investigated the role of orography in driving the monsoon circulation, although the exact influence of mountains on the monsoon flow remains unclear and debated. Hahn and Manabe [1975] performed a series of numerical experiments in a comprehensive three-dimensional model with and without mountains. They concluded orography to have a strong impact on the low-level circulation, while orography mainly results in a northward shift of the upper-level anticyclone (but with relatively small changes in magnitude and extent). Liu et al. [2007] imposed different individual distributions and combinations of thermal and orographic forcing profiles in a numerical model. They found the time-mean structure of the monsoon anticyclone (e.g. given by the 200hPa streamfunction) to be mainly set by thermal forcing and the orographic influence to be weak.

Boos and Kuang [2010] observed a south-west shift of the upper-level temperature anomaly associated with the monsoon anticyclone when removing all orography from their simulations, similar to the results of Hahn and Manabe [1975]. They further showed that the sensible heating of the Tibetan plateau does strongly affect the monsoon rainfall, but not the (low-level) circulation. In contrast to that, Wu et al. [2012] concluded from observational data and numerical experiments that the increased thermal forcing due to elevated sensible heating by the Tibetan plateau influences the monsoon circulation much more strongly than the corresponding mechanical forcing. Within this dissertation we will completely neglect the influence of orography on the monsoon flow and solely investigate the characteristics of the circulation forced by an imposed mid-tropospheric heating. This heating in general could represent a combination of monsoon latent heating and Tibetan plateau sensible heating.

Schneider and Bordoni [2008] and Bordoni and Schneider [2008] performed a series of idealised experiments with a dry general circulation model that included a representation of the seasonal cycle in radiative heating of the atmosphere. Following a change in large-scale eddy momentum fluxes they found a transition in the resulting zonal mean flow of the Hadley cell that has resemblance to the onset and end of the monsoon. They proposed a corresponding mechanism, i.e. a change of the zonal mean flow due to a change in latitudinal position of the maximum radiative forcing, to explain the onset of the monsoon circulation[1]. The aim of our research, however, is less to investigate the initial drivers of the monsoon flow and the processes that determine the structure and strength of e.g. the latent heating distribution in the monsoon region, but rather to investigate the response of the atmosphere to said heating distribution once it has formed. Correspondingly we will later model the monsoon circulation as response to an imposed heating distribution and study the dependence of the resulting flow and e.g. the strength and structure of the this heating.

Similarly all our numerical experiments will be performed with a steady forcing, although the monsoon itself is clearly a seasonal feature and the studies mentioned above suggest that seasonality might be important for the onset of the monsoon. However, we will assume that the monsoon response does build up on a time scale much shorter than its lifespan and thus the anticyclone is in a general steady state. Some of the results presented in chapter 3, e.g. figure 3.9, indicate that the monsoon is indeed in a statistical steady state and hence support the justify of a steady heating. Further, we aim to investigate to what extent the temporal variability of the circulation can be explained by the internal dynamics, rather than simply being set by the time dependence of the underlying heating distribution. The assumption of a steady forcing is therefore a necessary part of our model design.

As described earlier, the upper branch of the monsoon latent heating is associated with anticyclonic, divergent outflow (see figure 1.4) and hence manifests as a localised PV minimum. The sharp horizontal PV gradients of the monsoon anticyclone can act as a transport barrier for chemical trace gases, water vapour and aerosols [Ploeger et al. 2015]. This isolation of contained air provides, in combination with the steady ascent of the monsoon circulation, an effective vertical pathway from the troposphere to the stratosphere [Park et al. 2008].

However, in recent years various authors have proposed another potentially important pathway for troposphere/stratosphere exchange based on horizontal transport across the mid-latitude tropopause. The isolated air can leave the confinement of the PV minimum of the monsoon anticyclone through eddy-shedding phenomena [Ploeger et al. 2013; Vogel et al. 2014], where smaller anticyclones get detached from the main PV low and either propagate westward or get transported eastward by the mid-latitude jet. In that sense the monsoon anticyclone can be regarded as a source region for trace gases and chemical constituents from the lower atmosphere [Fadnavis et al. 2013; Randel et al. 2010; Park et al. 2007; Gettelman et al. 2004a]. Horizontal transport across the mid-latitude tropopause can additionally provide a potential mechanism for moist tropospheric air to bypass the very cold temperatures of the

[1] In such a setting the zonal confinement of the monsoon circulation could be explained due to the inhomogeneous distribution of landmasses which breaks the symmetry of the zonally symmetric flow found in their studies.

TTL and the monsoon anticyclone might thus form an important source region for stratospheric water vapour [Bannister et al. 2004; Gettelman et al. 2004b].

It is still a matter of current research what roles the processes of vertical and horizontal transport play and if one of them is dominant. In order to answer these questions it is crucial to have a good understanding of the fundamental dynamics of the monsoon anticyclone. For example, the vertical structure and extent of the monsoon flow will have a huge influence on the effectiveness of the vertical transport pathway, whereas the details of the horizontal structure of the anticyclone and its temporal behaviour (like the frequency of the eddy shedding phenomena) will strongly determine the effectiveness of the horizontal transport. Besides affecting transport the horizontal structure of the monsoon circulation (in the form of the response to a localised heating) is linked to meteorological and climatological phenomena, as will be explained in detail later.

Although the Asian monsoon is an annual feature of the atmosphere with a lifetime of several months it is also associated with large temporal variability on daily and inter-annual time scales. Its onset, strength, extent and withdrawal vary strongly from year to year and are still very hard to predict. Nevertheless, even small anomalies in e.g. the Monsoon precipitation can significantly affect the agricultural yields or cause disastrous flooding in India and south China [Chang and Krishnamurti 1987]. A realistic and accurate representation of the monsoon system in climate models is therefore crucial. This makes it necessary to understand the drivers and properties of the monsoon and how the flow interacts with the general circulation of the atmosphere. Although the discussed behaviours, scales and variabilities will potentially have meteorological implications (e.g. for rainfall predictions), we will focus on a more climatological and climate-based description of the monsoon.

The potential importance of the anticyclone motivates a re-investigation of the underlying dynamics, in particular in terms of the vertical and horizontal structure as well as the temporal behaviour of the circulation. In this dissertation we will study some of the general dynamical aspects of the monsoon anticyclone and aim to make scientific advances in three areas. On one hand we aim to (simply) investigate the behaviour of different numerical models depending on the physical processes included in the model representation. Such idealised sensitivity studies are important to correctly interpret comprehensive weather- and climate prediction models as well as to understand the basic physical and dynamical interactions of the system. Second we want to develop a comprehensive model setting that is able to reproduce a range of behaviours and characteristics that are associated with the monsoon (anticyclone). As we will discuss in chapter 3, most current theories and models are only able to capture certain particular aspects of the monsoon.

A more comprehensive model of the circulation and its features would make it possible to conduct more comprehensive studies, e.g. on the relative importance of different transport pathways or the interaction of different monsoon phenomena. Third, we aim to obtain concrete insights into some specific processes related to the monsoon circulation. This includes in particular the dependence of monsoon flow characteristics (e.g. the zonal structure of the response or the eddy shedding frequency)

on the details of the latent heating distribution and the background state. The last point will involve a range of more general fluid-dynamical experiments and studies.

1.3 Outline of this dissertation

The beginning of chapter 1 gave an overview on some of the fundamental basics of atmospheric fluid dynamics and aspects of the general circulation and the Asian monsoon were discussed. This section will explain the structure of the remainder of this thesis and outline the research questions that will be addressed.

In chapter 2 we are going to introduce some of the models and data sources for our experiments and surveys. We will discuss in particular the re-analysis dataset ERA-Interim, a three-dimensional primitive equation model and are a quasi-geostrophic single-layer model. Important aspects of the theoretical basis and the numerical implementation of these models will be described to allow a comprehensive understanding and authentic reproduction of our findings.

Chapter 3 forms the first of four results chapters. We will present a re-analysis study on various characteristics of the monsoon circulation and in particular on the monsoon anticyclone. This includes a discussion of the horizontal scales, the vertical structure and extent in relation to the tropopause and the vertical structure of the heating, and two types of temporal dependency of the flow in the form of east- and westward eddy shedding. In addition we will present and discuss different idealised attempts to model the monsoon flow or reproduce related characteristic behaviour, including a set of numerical experiments with a simple three-dimensional model. Particular focus will be given on the various difficulties that arise when trying to model certain aspects of the monsoon anticyclone.

In chapter 4 we will then expand our numerical studies by including a simple representation of mid-latitude dynamics (mid-latitude jets and baroclinic eddies) to the system. This will lead to various changes in the flow behaviour and give insights into the dependencies of the model and the physical system of the monsoon circulation. We will show that the discussed model setting exhibits a range of interesting behaviours and is able to reproduce a variety of phenomena and characteristics that can be associated with the Asian monsoon.

The following two chapters will focus on studies using a single-layer system in order to isolate certain phenomena and behaviours observed in the three-dimensional model. Chapter 5 will entirely focus on the temporal behaviour of the monsoon response. We will present a theory for westward eddy shedding as a result of an absolute instability of the flow. Following a comprehensive spatio-temporal stability analysis we are going to discuss under which circumstances and model-parameter combinations the instability occurs and eddy shedding can be observed.

In chapter 6 we then study how the monsoon anticyclone response is modified by various background physical processes. This involves the development of a theory for the propagation of discrete vortices

shed from the anticyclone and how their evolution is affected by e.g. thermal damping or a background flow.

Chapter 7 will summarise and briefly discuss the main findings of this dissertation and and suggest potential ways to continue and extent the research.

Chapter 2

Model set-ups and data sources

A part of the analyses performed in this dissertation will be based on numerical model simulations and the processing and use of atmospheric data sets. This chapter will explain in detail the characteristics and specifications of the models and data sources used.

2.1 ERA-Interim

Like every scientific discipline climate research is strongly reliant on observations, either to validate theories, deduce future evolution or infer physical and dynamical principles. Due to the complex interactions over a huge range of scales within the climate system it is, however, practically challenging to obtain comprehensive observations of the full state of the atmosphere.

One attempt to overcome this problem is formed by the so-called re-analysis projects. These datasets are constructed from a range of observational data archives via state-of-the-art data assimilation methods. The result is a temporally and spatially continuous and overall consistent representation of the atmospheric state. In section 3.1 we will be showing results based on the ERA-Interim (ERA-I) re-analysis dataset of the European Centre for Medium-Range Weather Forecasts (ECMWF). The used data are given on a $1^\circ \times 1^\circ$-grid with 32 pressure levels between 10-1000hPa or 15 isentropic levels between 265-850K, respectively. Seasonal means are calculated from monthly averaged fields for the years 2000-2009, while snapshots are showing fields at 12:00noon UTC.

For simplified comparison of results from other sections we will represent vertical positions in terms of a quasi-height[1] scale defined by the log-pressure coordinate

$$z = -7km \times \ln \frac{p}{p_0}, \tag{2.1}$$

[1] Describing the height-pressure relation of an isothermal, hydrostatic atmosphere with a scale height of 7km.

where we will choose p_0 to be surface pressure for GCM experiments (see section 2.2) or a scale pressure of $10^5 hPa$ when using ERA-I data.

Re-analyses combine advantages of globally and comprehensively accessible data of a model with the representativeness and accuracy of observations. Even though re-analysis datasets are not actual observations and the use of model-equations and data-processing tools will introduce further uncertainties and discrepancies those datasets are usually very close to observations. For the purposes of this study we will therefore regard them as 'real world'. We will show results based on ERA-I in section

Simmons [2006] summarised the main aspects of the ERA-I projects and the corresponding difference to the previous ECMWF re-analysis dataset ERA-40. A more comprehensive description of the configuration and reproduction skill of ERA-I was given by Dee et al. [2011]. Bao and Zhang [2013] compared the output various of dynamic quantities from several re-analysis datasets (including ERA-I) during boreal summer 1998 and over the region of the Tibetan plateau with independent observations and found overall good agreement.

2.2 General circulation model

In chapters 3 and 4 we perform a series of numerical experiments using a simple, dry, three-dimensional general circulation model (GCM). These experiments are conducted with a modified version of the intermediate general circulation model IGCM1 developed at the University of Reading and the corresponding diagnostics package IGFLUX. The model is based on the set of fully-non-linear, baroclinic primitive-equations described by Hoskins and Simmons [1975].

Horizontal dimensions are represented via a spherical harmonics series, using a triangular truncation at wave number 42 (corresponding to a grid resolution of about 2.8° at the equator). The vertical dimension is discretised using a centred-differences scheme with 40 σ-levels (ratio of pressure and surface pressure). As for the ERA-I fields, we will be present the results obtained from GCM experiments on a vertical log-pressure scale defined via equation 2.1, where p_0 describes the surface pressure. The vertical levels in our GCM experiments are then equally distributed in z with constant spacing of 0.7km.

The performed GCM studies use three types of direct physical forcing:

- An explicit heating with magnitude Q_0 and structure Q, as part of our experimental design,
- a Newtonian relaxation of temperatures towards a restoration profile T_r on a time scale ε^{-1},
- and a Rayleigh mechanical damping acting on wind field with a time scale δ^{-1}, which consists of a low-level drag layer and a bulk-atmospheric friction which is not always applied.

The structure of the imposed heating distribution Q is described in subsection 3.2.2. Newtonian cooling and Rayleigh friction are simple linear parametrisations of radiative and dissipative sub-grid-scale

processes, which are the only non-dynamical processes represented by the model. The Rayleigh friction does include a bottom-drag-layer with a time scale of 1 day linearly decreasing between $\sigma = 1$ and $\sigma = 0.7$ active in all experiments.

In addition we will use two different basic state configurations, both based on the state proposed by Held and Suarez [1994] and mainly characterised by the structure of the corresponding zonally symmetric temperature restoration profile for the Newtonian cooling. One basic state is given by the full Held and Suarez (HS) state, which follows the general definition in Held and Suarez [1994] for various sets of parameters. In addition we will define a horizontally uniform Held and Suarez state (UHS), which is given by only using the profile of the HS state at the equator and neglecting all latitudinal dependence. Figure 2.1 displays the restoration profiles of the HS and UHS states. The two basic states are described in more detail in subsections 3.2.2 and 4.1.1, respectively. In principle the temperature relaxation towards the HS restoration profile leads to the development of zonal mid-latitude jets and baroclinic eddies due to baroclinic instability, while the UHS state is baroclinically stable and resembles an atmosphere at rest. The HS state therefore includes a simple representation of mid-latitude dynamics and can be used to study corresponding effects on the monsoon flow forced by an additional imposed heating.

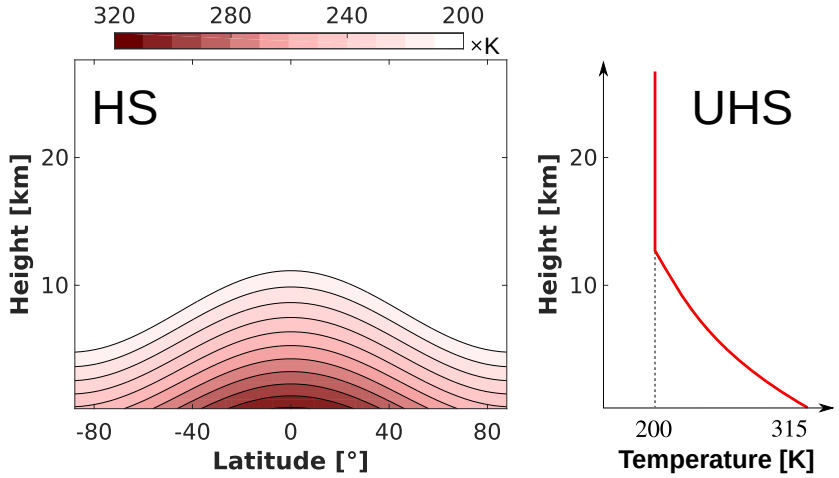

Fig. 2.1 Temperature restoration profiles for the Newtonian relaxation used in the HS and UHS basic states. The horizontally uniform UHS profile is defined by the vertical structure of the HS profile at the equator.

To ensure numerical stability the model uses an 8^{th}-order hyper-diffusion with a fixed time scale of 0.1 days for the smallest represented scales and acting on the temperature, vorticity and divergence field.

All experiments are initiated from an atmosphere at rest. Experiments using the HS configuration are initiated with a small-amplitude random white noise perturbation of the surface pressure field to trigger baroclinic instabilities. The UHS basic state is in balance and does not develop any flow, while the HS basic state exhibits the formation of a background circulation, reaching a sufficiently steady state after

1000 days. The imposed heating in perturbation-experiments was switched on at day 1 for UHS runs and day 3000 for HS experiments. Time means were calculated over time periods of at least 2000 days, starting at least 1000 days after the switch on of the heating to ensure a steady state was reached. The presented results were not sensitive to changes in the hyper-diffusion time scale and the length of spin-up or averaging periods. Further, the response of the model in the upper troposphere/lower stratosphere region was not sensitive to small changes in the details of the used bottom drag layer.

In subsection 4.1.1 we will discuss the non-trivial state proposed by Held and Suarez [1994] as a model comparison for dry dynamical cores and defined by a set of specific temperature restoration and damping rate profiles. The good agreement between the resulting flow and temperature fields of our model experiments and the corresponding plots presented in Held and Suarez [1994] (not shown here) gives confidence in the correct and intended set-up and usage of the model.

2.3 Single-layer models

A part of this thesis will make use of two idealised single-layer (SL) models in order to perform a more in-depth investigation of some of the processes involved in creating the Asian summer monsoon anticyclone. These models assume no vertical dependency of any of the quantities involved and are therefore usually used to study the behaviour of shallow horizontal layers in the atmosphere or the ocean.

As we will explain in more detail in section 3.1, the monsoon anticyclone is associated with horizontal scales of the order of the Rossby radius of deformation, which can be estimated via $R_D \approx \frac{NH}{f}$. Here H is the vertical scale, N the static stability and f the Coriolis parameter. In the (sub-)tropics the ratio of typical horizontal and vertical scales is usually small, with $\frac{H}{R_D} \approx \frac{f}{N} \ll 1$. Hence vertical variations are relatively small in this region and vertical communication of neighbouring layers can be assumed as weak, justifying the use of a single layer model. The layer itself can be thought of as being defined by, for example, two given isentropic surfaces in which case any mass flux into or out of the layer can be associated with diabatic processes, e.g. through the monsoon latent heating or radiative dissipation.

All though the use of an idealised (single-layer) model reduces the direct applicability of results to (three-dimensional) real-world-problems, it allows us to investigate the system in a simpler setting and isolate some of the main dynamical processes. This way it becomes possible to obtain a more complete understanding of the physics that set the corresponding time and length scales of the system. A commonly used version of single layer model is described by the non-dimensional shallow water (SW) equations:

$$\begin{aligned}\partial_t u &= -(\boldsymbol{u}\cdot\nabla)u - fv - \partial_x h \\ \partial_t v &= -(\boldsymbol{u}\cdot\nabla)v + fu - \partial_y h + f\hat{U} \\ \partial_t h &= -\nabla\cdot[\boldsymbol{u}(1+h-b)] + F - \varepsilon h,\end{aligned} \tag{2.2}$$

where x and y represent zonal and meridional directions, u and v are the zonal and meridional components of 2D wind vector $\boldsymbol{u}$, h and b describe the surface displacement and bottom topography of the layer, f is the Coriolis parameter and $\nabla \equiv (\partial_x, \partial_y)$ is the two-dimensional gradient operator. The imposed mass source has spatio-temporal structure $F(x,y,t)$ (with magnitude F_0) and ε describes the thermal dissipation rate. The numeric parameter $\hat{U}$ is used to impose a non-vanishing meridional mean background zonal wind in the system and is a result of equal meridional net-slopes in h and b leading to a zonal wind in the system without producing unrealistic changes in the background PV gradient. The idea is based on a concept used by Kraucunas and Hartmann [2007] and will be visualised in figure 2.2.

This model (with $\varepsilon, \hat{U}, b \equiv 0$) was used by Davey and Killworth [1989] to investigate the time dependency of the response to a steady mass source (further discussed in chapter 5). We will make use of the SW model presented in equation 2.2 in an analytic calculation presented in part of section 6.1.

Table 2.1 indicates the physical meaning of the used quantities and their corresponding normalisation constants, as well as the parameters of the model and their fixed values. Note that we will use the unit of "days" to specify points in time, rather than the unit of inverse Coriolis parameter, in order to simplify the interpretation and comparison of various plots and time scales[1]. All equations, however, will assume the normalisation shown in table 2.1.

For simplification we will mostly use a β-plane approximation giving the Coriolis parameter as $f = 1 + \beta y$, where the non-dimensional parameter $\beta = 0.51$ describes the meridional gradient of the basic state and corresponds to the dimensional meridional derivative of the Coriolis parameter at 20° latitude. This definition of f also defines the meridional origin of the model domain to have $y = 0$ where $f = 1$. The value for the mean layer depth H is given through the choice of gravitational acceleration $g = R_D^2 f_0^2 / H = 9.8 m/s^2$ and the corresponding values for Coriolis frequency and Rossby radius.

For most of our analysis we will apply an additional approximation to the single-layer model in equation 2.2 and restrict ourselves to quasi-geostrophic (QG) theory. The QG approximation assumes the Rossby number[2] of the system to be finite, but small. A main characteristic of QG models is that they do not support fast gravity waves, which we assume to have a negligible impact on the large length and long time scales we are interested in. Similar QG models were previously used to e.g. investigate the propagation of isolated eddies [Cushman-Roisin et al. 1990; Lam and Dritschel 2001; Early et al. 2011],

[1] Similarly numeric values for frequencies will be given in $rad/days$.

[2] The Rossby number $R_0 = U/(Lf)$ is given as ratio of inertial and Coriolis force, with U and L being typical horizontal velocity and length scales.

Table 2.1 Physical quantities and their normalisation used in the single-layer model.

Symbol	Physical meaning	Normalisation
t	Time	f_0^{-1}
x,y	Zonal and meridional position	R_D
$\boldsymbol{u}(x,y) \equiv (u,v)$	Wind (Zonal, Meridional)	$R_D f_0$
$h(x,y)$	Height anomaly	H
$b(x,y)$	Bottom topography	H
$q(x,y)$	(QG) Potential Vorticity	f_0
$F(x,y)$	Forcing with magnitude F_0	$H f_0$
$f(y) = 1+\beta y$	Coriolis parameter	f_0
β	Background PV gradient	$f_0 R_D^{-1}$
$\hat{U}$	Meridional mean zonal wind	$R_D f_0$
ε	Thermal damping rate	f_0

Symbol	Physical meaning	Value
H	Unperturbed Layer Depth	$400m$
f_0	Coriolis Frequency (at 20°)	$5 \times 10^{-5} s^{-1}$
R_D	Rossby radius of deformation	$1250km$

analogous to our research in chapter 6. One of the main restrictions of the QG approximation is that it is not able to account for equatorial Kelvin waves. These, however, can be expected to have only little influence on the Rossby wave dominated flow if the imposed forcing is located in the sub-tropics and sufficiently far away from the equator.

The QG approximation leads to a simplified set of two equations for the height anomaly h and potential vorticity q:

$$\begin{aligned} \partial_t q &= -(\boldsymbol{u}\cdot\nabla)q - F + \varepsilon h \\ q &= \nabla^2 h - h + b + \beta y. \end{aligned} \tag{2.3}$$

As can be seen, the mass source F directly translates to a PV forcing of opposite sign. Further note, that the meridional mean zonal wind parameter $\hat{U}$ does enter the equations via the definitions of the geostrophic winds $u = -\partial_y h + \hat{U}$ and $v = \partial_x h$.

We implemented the presented QG model exclusively for the purpose of this dissertation. The non-dimensional model equations 2.3 were discretised on a uniform grid spanning a domain of length $L_x = 320$ and width $L_y = 40$ with grid spacings $\Delta x = \delta y = 0.1562$, corresponding to 2048 and 256 grid

points, respectively. The implementation uses a 2^{nd} order Runge-Kutta discretisation in time, a spectral Fourier representation in the zonal direction and a 2^{nd} order meridional central difference scheme. Correspondingly we choose the boundary conditions as no slip in y (i.e. h and all its derivatives vanish) and periodic in x.

Figure 2.2 illustrates the meridional structure of the model set-up and some of the relevant quantities. As mentioned earlier, the model dynamics are acting on a "tilted layer", where height anomaly and bottom topography are defined with respect to a meridional net-increase with slope $\hat{U}$, illustrated by the dashed lines. This will allow us to include an arbitrary zonal background wind for some of the experiments without changing mean layer depth and hence the PV gradient [Bao and Hartmann 2014]. The model is fully periodic in the zonal direction.

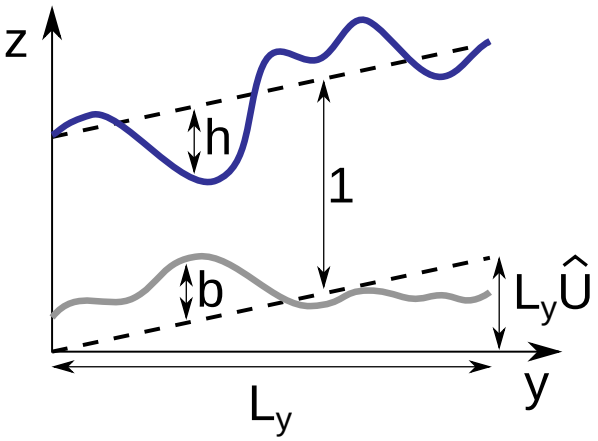

Fig. 2.2 Conceptual illustration of the meridional structure of the model. Blue and grey solid curves indicate the height anomaly (h) and bottom topography (b), respectively, and show their definition with respect to a meridional net-increase of slope $\hat{U}$. Note that h vanishes at the meridional boundaries. Zonally the model is fully periodic (not shown).

Table 2.2 lists the numerical parameters used in our experiments and their corresponding dimensional units.

Table 2.2 Numerical parameters used and their typical non-dimensional values.

Quantity	**Physical meaning**	**Value**	**Unit**
L_x,L_y	Channel length and width	320,40	R_D
Δx,Δy	Zonal and meridional grid spacing	0.1562,0.1562	R_D
Δt	Time step	0.005	*days*
ε_s	Sponge region damping rate	2	f_0
ε_h	Hyper-diffusion parameter	10^{-4}	$R_D^4 f_0$

We further implemented a sponge region for some of the experiments and a 4^{th} order hyper-diffusion in the form of additional terms $-\varepsilon_s S(x,y)(q-q_0)$ and $-\varepsilon_h \nabla^4 (q-q_0)$, respectively, to the right side of the evolution equation 2.3. Here q_0 describes a specified background PV profile, which might e.g. be

associated with an imposed background flow, and ensures that neither sponge region nor hyper-diffusion modifies the basic state. The sponge region has spatial structure $S(x,y)$, which is zero everywhere except in a zonally confined and meridionally symmetric region to the far west of the forcing. It has a magnitude of $\varepsilon_s = 2$ and hence strongly dampens the azonal part of the PV anomaly with the purpose of simulating an infinitely long channel.

The hyper-diffusion uses strength parameter ε_h and is implemented via an implicit scheme. It acts directly on the PV field and is applied separately after every time step. Without such a diffusion numerical instabilities, in the form of grid-scale oscillations, tend to occur in regions of strong PV anomalies and gradients. The hyper-diffusion, in combination with sufficiently small grid spacing, is aiming to suppress these instabilities without affecting the large-scale behaviour of the flow. Figure 2.3 shows a typical example of the PV response to a local forcing (see equation 2.4) of three experiments only differing in their strength of the hyper-diffusion. As can be seen a carefully chosen value of ε_h can successfully suppress the numerical instabilities without significantly disturbing the large scale flow.

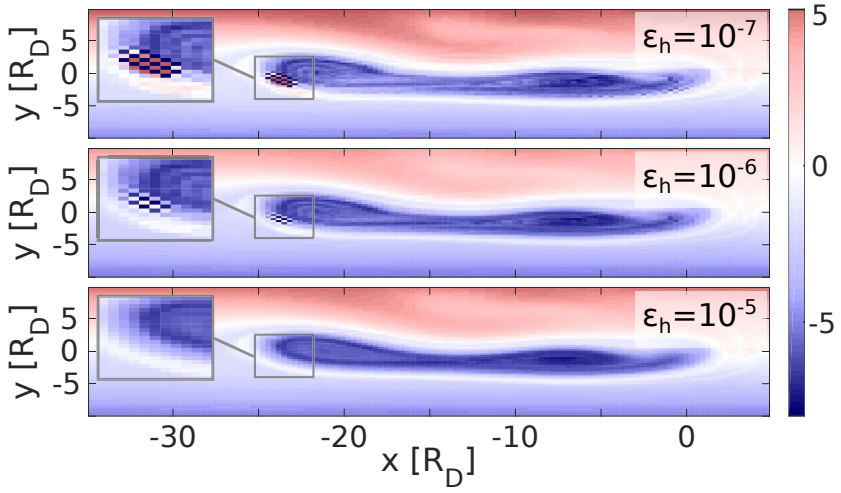

Fig. 2.3 PV snapshot comparison of the three experiments only differing in their value for the hyper-diffusion strength ε_h and corresponding indication of small scale oscillations for weak diffusion.

Since the QG approximation simplifies the SW model the two will allow for different dynamical behaviours. We want to ensure that the model-set up is still appropriate to investigate the response to a local mass source. Figure 2.4 illustrates the response of the QG model presented in equation 2.3 to a steady, confined forcing compared to the results of Davey and Killworth [1989], who used the full SW model shown in equation 2.2. Shown is the response at day 600 for two different sets of forcing characteristics (top/bottom panel) for the two models (left/right panel), with otherwise the same parameters used in all cases and both models. The response of the two models to the localised steady forcing is in good agreement with each other, which gives confidence in our choice of model to investigate the the corresponding systems.

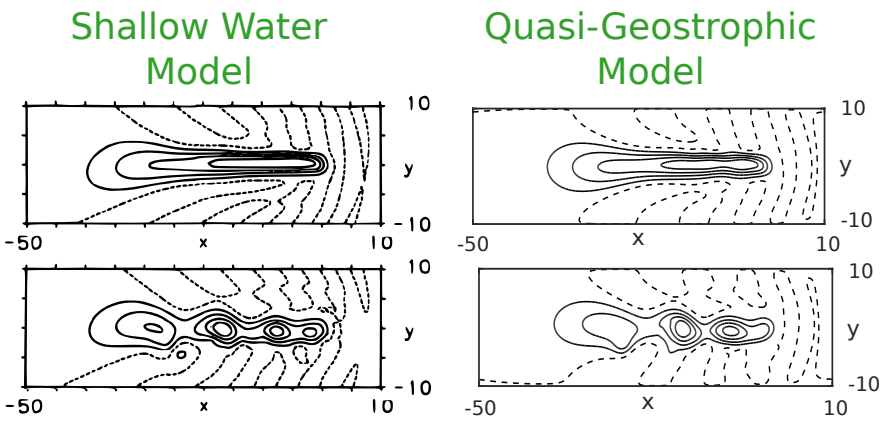

Fig. 2.4 Comparison of the response to different forcing characteristics (top/bottom) in the SW model used by Davey and Killworth [1989] and the QG model used in this chapter. Negative contours are dashed and contour intervals are the same for the top and bottom panels, respectively.

2.3.1 Response to a steady and local mass source

In the following we will present some general aspects of the response of the numerical QG-PV model described in section 2.3 to a local, steady mass source. Unless stated otherwise, all experiments will be forced using a localised mass source with spatial structure of length scale r_0:

$$F(x,y) = \begin{cases} F_0 \cos^2\left(\frac{\pi x}{2r_0}\right) \cos^2\left(\frac{\pi y}{2r_0}\right) & \text{if } |x|, |y| \leq r_0 \\ 0 & \text{otherwise} \end{cases}. \tag{2.4}$$

The results shown in this thesis are not sensitive to the precise structure of the forcing. Additional experiments (not shown) have lead to the conclusion that a circular source, vanishing radially according to a $\cos^2$ profile, will lead to (qualitatively) almost identical behaviour with only minor quantitative differences. The forcing is spun up following a sin^2 profile to reduce switch-on perturbations of the system. It reaches its maximum value F_0 at day 10 and it kept steady for the remainder of each model run. In the following subsection we will analyse the response of the model during the spin up period.

2.3.2 The spin-up period of the model

In order to obtain as complete an understanding as possible of the response to a localised mass source we will start by explaining the behaviour of the system during the finite switch-on period of the forcing. This will have the additional advantage of comparing the model response to certain predictions of established theories and thus gain confidence in the correct implementation and usage of the model. Since the spin-up is smooth we can expect any initially generated waves and perturbations to be weak and hence being well described by linear Rossby wave theory. The group velocities c_g of linear Rossby waves in

the zonal and meridional direction can be represented in terms of the respective wave numbers k and l:

$$c_{g,x} = \frac{\beta(k^2 - l^2 - 1)}{(k^2 + l^2 + 1)^2}, \qquad c_{g,y} = \frac{2\beta kl}{(k^2 + l^2 + 1)^2}. \tag{2.5}$$

Figure 2.5 shows the PV response to a forcing at different times during the spin-up period together with some auxiliary lines. The vertical brown lines indicate the meridional extent of the -0.05 PV (solid black line), which can be roughly interpreted as the most westward extent of the forced anomaly. The vertical yellow lines represent the meridional length scale of the response at a given position in x and the magenta lines have a slope of 45°.

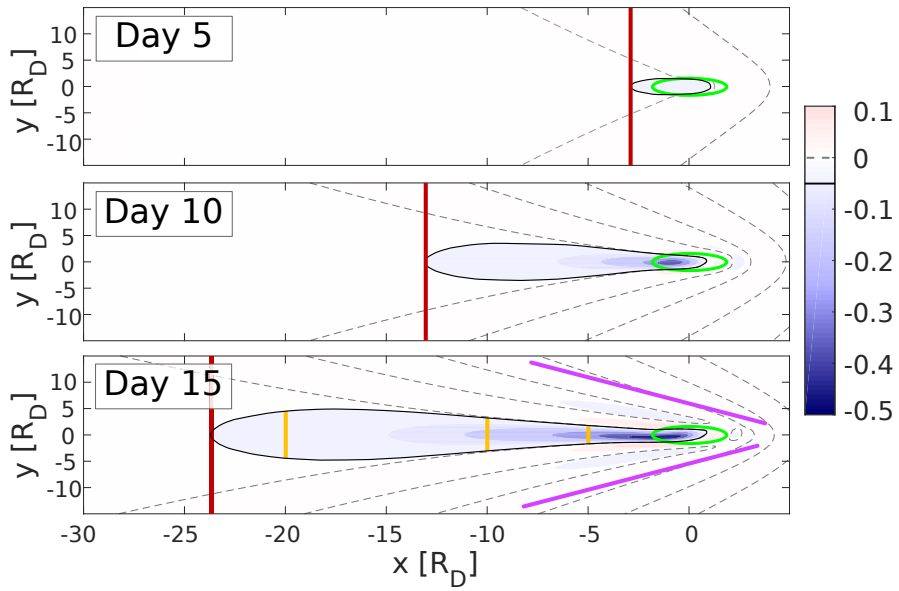

Fig. 2.5 PV anomaly response for $r_0 = 2$ and $F_0 = 0.05$ at different times during the switch-on period with dashed lines along the zero contours. The green ellipse indicates the forcing region, the brown vertical lines show the most eastward point of the -0.05 PV contour, the vertical yellow lines visualise the meridional extent of the -0.05 PV contour and magenta lines represent coordinate lines sloping in $\pm 45°$ angles to the zonal direction.

We can now use linear wave theory to explain certain features of the flow.

- The maximum extent (brown lines) is determined by the fastest travelling waves in the system, which according to equation 2.5 correspond to $k, l = 0$. These waves do only have a zonal group velocity component of magnitude $c_{g,x} = -\beta = -0.51$, meaning β can be directly interpreted as the long Rossby wave speed of the system. Figure 2.5 suggests a westward expansion of the -0.05

PV contour of about 20 Rossby radii from Days 5 to Day 15, which is in very good agreement with the prediction of linear wave theory for fast waves.

- The wave number of waves that can reach a given point west of the forcing at a fixed time is simply a function of their corresponding group velocities. As we just have stated waves with $k, l = 0$ are fastest and hence travel the farthest in a given period. At a given time finite mode waves will be confined to regions closer to the forcing. The meridional length scale of the response (yellow lines) should therefore increase with westward distance.
- Equations 2.5 suggest that waves moving primarily westward have to have $k \approx 0$, since they otherwise obtain a strong meridional velocity component or will travel eastwards. We therefore expect the spin-up flow to have small zonal variations along the negative x-axis.
- Waves with $k \approx l$ will have a very small zonal group velocity component. Hence, north and south of the forcing region we can observe wave crests which are tilted at about 45° (parallel to the magenta lines).
- East of the forcing region we find waves with large values of k, which lead to the rapid sign changes in PV anomaly when moving east. However, the projection of the forced anomaly profile on higher wave numbers strongly depends on the length scale of the forcing since the width power spectrum is generally inversely proportional to the width of the forced anomaly. Hence a forcing spanning several Rossby radii in the zonal direction will have almost no frequency components with large k and hence the eastward response will be very weak.

To test the last hypothesis we performed a counter experiment with an elliptic forcing of a scale of $1/20$ in the zonal and 1 in the meridional direction. Such a forcing should excite more modes with large k and small l and hence have a finite eastward response. Figure 2.6 shows a clear wave pattern excited east of the forcing. However, we still find the main part of the flow consisting of westward propagating anomaly.

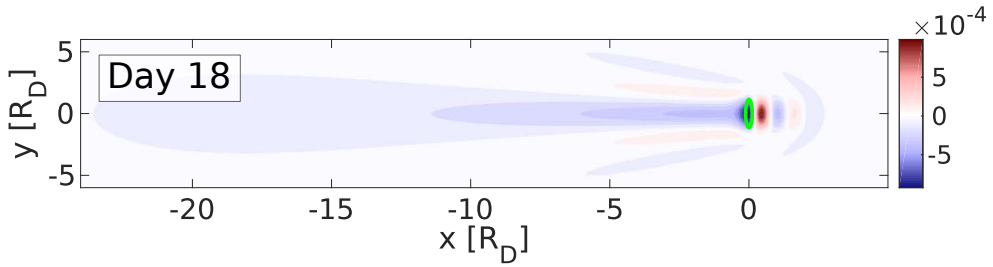

Fig. 2.6 PV anomaly response for a forcing with zonal length scale $r_{0,x} = 1/20$ and meridional scale $r_{0,y} = 1$ producing pronounced eastwards propagating waves. The green circle indicates the forcing region

For the following analyses and experiments we want to make sure the system has reached a sufficiently steady state. In order to check the steadiness of the response we plotted in figure 2.7 the time series of

surface displacement averaged over the line $x = -10$, $-5 < y < 5$ for different combinations of typical forcing parameters. Two features of the line become apparent. First, the system seems to undergo an adjustment period of about 100 days or less in all shown cases. The response becomes statistically steady afterwards. As mentioned, a typical velocity scale for disturbances is the long Rossby wave speed $\beta = 0.51$. All following experiments and analyses will be performed for time periods starting at least 300 days after the switch on. Since we are mostly interested in the finite region within about $150R_D$ west of the forcing we can assume the system to have achieved a completely steady state within this period.

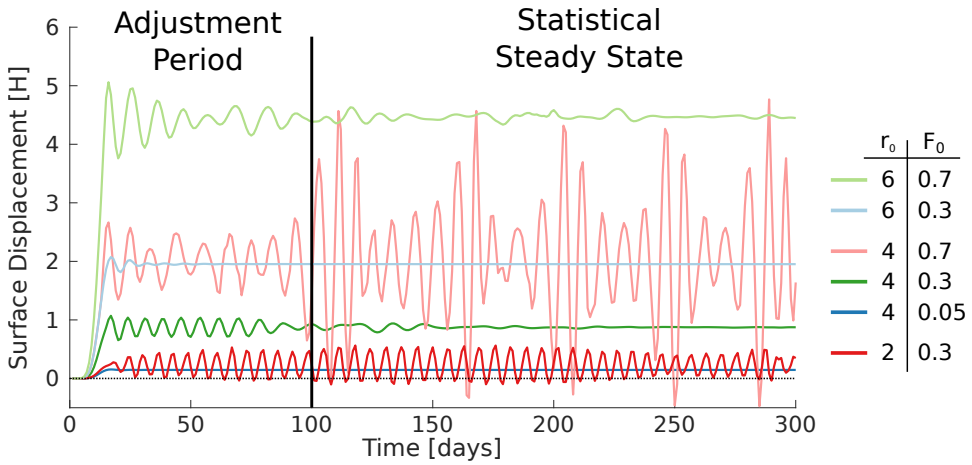

Fig. 2.7 Time series of surface displacement at $x = -10$ and averaged over $-5 < y < 5$ for different forcing parameters.

Second, all cases seem to show a pronounced oscillatory behaviour just after the forcing is switched on. In some cases this temporal oscillation persists, while in others it dies out quickly. The likely cause of these initial oscillations is the generation of waves during the finite switch on period. In the cases with persisting oscillations other processes seem to be generating or amplifying wave patterns.

Chapter 3

The monsoon anticyclone in re-analyses and simple models

In the second half of the 20^{th} century the importance of tropical circulations in the dynamics of the global atmosphere became more and more prominent. One of the most pronounced of such features is the Asian summer monsoon, a seasonal, synoptic-scale circulation consisting of a cyclonic flow pattern near the ground and anticyclonic flow in the upper troposphere and lower stratosphere (UTLS), as illustrated in figure 3.1. Generally there are various monsoon systems in the atmosphere (e.g. an Australian and an African monsoon), with the Asian monsoon being the most pronounced one. Therefore this study will focus on the Asian monsoon (e.g. the re-analysis observations in section 3.1), although many of the results and dynamical explanations might as well hold for other monsoon systems.

In principle the monsoon circulation can be thought of as being triggered by thermal land-sea contrast, although its strong winds are effectively driven by latent heat release due to rising moist air. It is therefore possible to model a monsoon-like flow by directly imposing a localised heat source in the middle troposphere, representing the monsoon latent heating. This thesis will focus on the dynamics of the monsoon anticyclone and aim to give insights into which flow characteristics and physical processes determine its structure and evolution.

In section 3.1 we will give a rough overview of features and behaviours that can be observed in re-analysis data (see section 2.1) in relation with the monsoon anticyclone. We will then, in section 3.2, discuss the simple theory developed by Matsuno [1966] and Gill [1980], which is widely used to explain the time-mean structure of the monsoon. However, as we will discuss, a Gill-Matsuno-like model does not capture the observed time dependence of the monsoon flow. In addition the model requires a strong large scale friction in the whole atmosphere to produce a zonally localised response.

Since it is questionable if any physical process can provide such a frictional damping in the UTLS region [Sardeshmukh and Hoskins 1985; Hsu and Plumb 2000; Lin et al. 2008], section 4.1 will aim to develop a more comprehensive model setting, by including a representation of mid-latitude dynamics. This way we were able to reproduce a monsoon anticyclone featuring a realistic temporal dependency and a

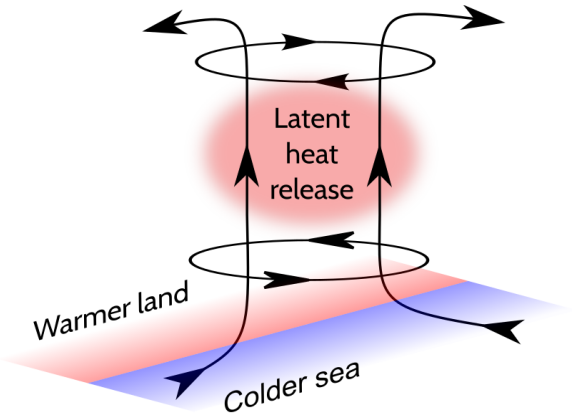

Fig. 3.1 Schematic structure of the Asian monsoon circulation showing a lower level cyclone and an upper level anticyclone.

zonally localised time mean flow. Finally, section 4.2 will investigate how the response depends on the vertical structure of the forcing and hence give insights into the vertical extent of the monsoon.

3.1 The monsoon anticyclone in re-analysis data

The monsoon anticyclone acts as a source region for trace gases and water vapour in the UTLS due to the role of the monsoon as major pathway from the troposphere into the stratosphere [Bannister et al. 2004; Park et al. 2007; Randel et al. 2010; Garny and Randel 2013]. Over the past decades, numerous studies have therefore attempted to explore the physical and dynamical processes that drive and control the structure and evolution of the monsoon anticyclone [Hahn and Manabe 1975; Gill 1980; Hsu and Plumb 2000; Boos and Kuang 2010]. Despite the potential importance of the monsoon anticyclone in determining the state of the stratosphere many questions about its structure (e.g. horizontal scale or vertical extent) and evolution (e.g. intra-seasonal time dependence) and the corresponding impact on transport and weather-phenomena still seem to be unanswered and a matter of ongoing research [Garny and Randel 2016; Fadnavis et al. 2018; Luo et al. 2017; Ren et al. 2015]. In the following subsection we will therefore give an overview of certain characteristics and behaviours of the monsoon in re-analysis data (see section 2.1).

3.1.1 Horizontal structure and scale

The monsoon circulation is mainly driven by latent heat released due to condensation processes over south east Asia. Figure 3.2 shows the distribution of latent heat release averaged over June, July and August (JJA), computed from ERA-I output. Since the summer monsoon peaks during boreal summer, averages over the JJA period are commonly used when studying the monsoon (e.g. Hoskins and Rodwell

[1995]). For simplified comparison with results from other sections in this chapter, the vertical scales are given as log-pressure coordinate, as explained in section 2.1.

The heating rates are calculated as difference of the assimilation increments of the total diabatic heating and the radiative heating. This gives us an estimate for the heating associated with temperature changes caused by latent heat release and mixing processes (see Fueglistaler et al. [2009b]). Since the latter is likely to be small on large scales we will use the calculated fields as estimates for the latent heating. The vertical profile of the mean heating distribution in figure 3.2 vanishes near the tropopause at a height of about 15km. This will be of importance to the vertical extent of the circulation, as discussed in subsection 3.1.2 and section 4.2.In the numerical models discussed in this report, e.g. in section 3.2, we will model the monsoon circulation as direct response to a heating, representing the latent heat release of the monsoon region.

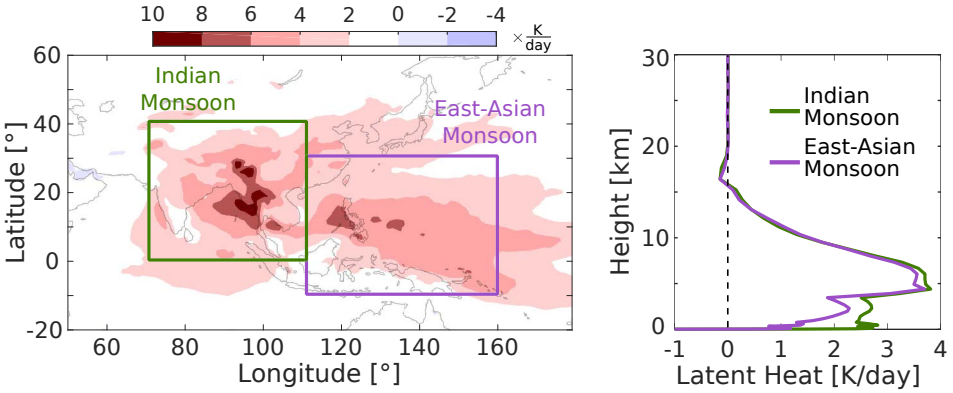

Fig. 3.2 Years 2000-2005 JJA-averaged ERA-I latent heating field at $z = 6.5km$ (left) and vertical profiles averaged over the indicated horizontal regions (right).

Some studies distinguish in their research between the Indian and the east-Asian monsoon [Yihui and Chan 2005], referring to two distinct flow and rainfall patterns caused by two maxima in the heating field (as indicated in figure 3.2). Wang [2002] analysed various rainfall characteristics and diagnostic measured and suggested the existence of three distinct, but correlated, Asian monsoon systems. Wang et al. [2001] argued that the differences in internal variability of the various (sub-)monsoon-circulations can have a large influence on the rainfall in these regions. The horizontal (small scale) structure of the heating distribution shown in figure 3.2 indeed seems to strongly correlate with the structure of the JJA mean rainfall shown in figure 1 of Wang et al. [2001] (not shown here). However, these studies are all based on analyses of precipitation data and the monsoon rainfall is mostly linked to the lower-level cyclone.

The upper level anticyclone, on the other hand, does not seem to inherit the same correlation with the horizontal latent heat field. This can be seen in figure 3.3, showing the horizontal potential vorticity (PV) structure of the Asian monsoon anticyclone. Since this study is focussing on the monsoon anticyclone,

will not make any further distinctions between different monsoon circulations and will simply refer to "the Asian monsoon" as a single, coherent feature of the atmosphere.

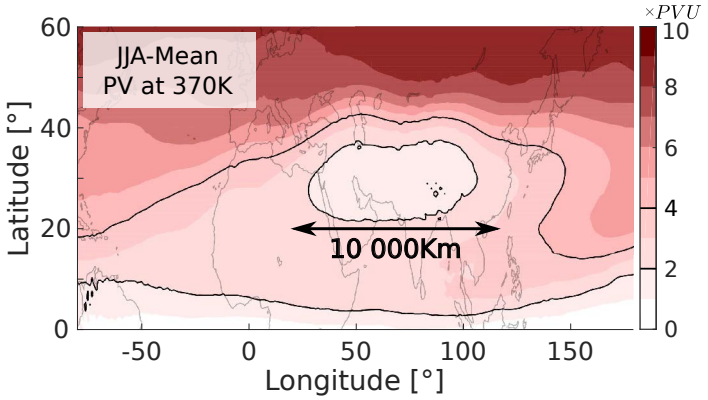

Fig. 3.3 Years 2000-20009 JJA-average of ERA-I potential vorticity on the 370K isentropic surface. The 2 and 4 PVU contours are emphasised and a length of 10 000km at 20° latitude is indicated.

The upper branch of the monsoon heating acts as a negative PV forcing, due to the negative vertical gradient of the heating and the abrupt increase in background static stability at the tropopause (further discussed in section 4.2). Correspondingly, the monsoon anticyclone is linked to a pronounced PV minimum. Figure 3.3 shows the horizontal time mean structure of this PV minimum on the 370K potential temperature isentropic surface. Although being a large-scale feature of the atmosphere, the time mean PV anomaly is zonally confined with a horizontal scale of the order of about 10 000 kilometres. The localisation and zonal scale of the monsoon flow will be further discussed in sections 3.2.2 and 4.1.2.

The Rossby radius of deformation R_D can be used as a measure for the importance of rotational effects within a fluid system. In a quasi-geostrophic (QG) sense, for example, the vorticity component of PV features with horizontal length scales above R_D will tend to outweigh the vertical stretching term. Following approximations for vertically slowly varying layers in a three-dimensional QG system, one can approximate the Rossby radius as $R_D \approx HN/f$. Here H is the depth of the coherent layer, i.e. the vertical scale of the monsoon anticyclone, f is the Coriolis parameter and N is a static stability measure of defined by $N^2 = R\left[RT/(Hc_p) + \partial_z T\right]/H$ (see section 4.2 for further details).

From calculations based on satellite data presented by Grise et al. [2010] one can estimate a value of around $N^2 = 2 \times 10^{-4} s{-}1$ at $20°N$ and near the tropopause at around 15km during JJA, with tropical values ranging from about $1 \times 10^{-4} s{-}1$ in the troposphere to about $7 \times 10^{-4} s{-}1$ in the stratosphere. From the vertical structure of the PV anomaly in figure 3.6 we can further estimate the vertical scale of the monsoon anticyclone to be about $H = 10km$. The Coriolis parameter at 30° is given by $f \approx 7.3 \times 10^{-5} rad/s$. This leads to a Rossby radius of roughly $R_D \approx 1900km$. Comparing this value to the horizontal scale of the PV low (figure 3.3) suggests the monsoon anticyclone to be several Rossby radii in size, although one should be cautious regarding precise comparisons with our very rough order-of

magnitude estimate of R_D. This will affect the dynamics of the flow and is an important estimate that has to be considered in chapters 6 and 5.

3.1.2 Vertical profile and extent

Next we will summarise and point out certain features of the vertical structure of the monsoon anticyclone, including its vertical extent in relation to the tropopause. One commonly used quantity to identify and characterise the anticyclone is potential vorticity, usually in the form shown in equation 3.1 as proposed by Ertel [1942],

$$PV = (\zeta + f)\,\frac{\partial_z \Theta}{\rho}, \tag{3.1}$$

where ζ is the relative vorticity of the flow, f the Coriolis parameter, Θ the potential temperature gradient of the system and ρ its density distribution. Equation 3.1 consists of two factors which, in simple terms, describe the rotation $(\zeta + f)$ of an air parcel and the (inverse) vertical extent $(\partial_z \Theta/\rho)$ of an infinitesimal parcel with a fixed potential temperature. One of the main advantages of PV is its material conservation on isentropic surfaces in the absence of diabatic processes and friction, giving it a unique potential for the use of describing and analysing the dynamics of circulations.

Ertel's PV generally increases rapidly with height, making it difficult to quantitatively interpret vertical PV structures or compare horizontal fields at different vertical levels. To weaken the vertical dependence we will adapt an approach proposed by Dunkerton and Delisi [1986] and use a rescaled version of potential vorticity. The rescaling approach we will use is given in equation 3.2.

$$\widehat{PV} = (\zeta + f)\,\frac{\overline{\rho}\,\partial_z \Theta}{\rho\,\overline{\partial_z \Theta}} = PV\,\frac{\overline{\rho}}{\overline{\partial_z \Theta}} = PV\ \chi(\Theta), \tag{3.2}$$

where $\overline{\partial_z \Theta}$ is the vertical gradient of potential temperature of the zonal mean state averaged over the monsoon region 0-40° latitude (see subsection 3.1.1) and we use a simplified hydrostatic density given by $\overline{\rho} = e^{-z/H}$ with $H = 7km$. Since we constructed the rescaling factor $\chi(\Theta)$ to be a function of potential vorticity only its value is constant on a given isentropic surface and the rescaling will preserve the conservation properties of Ertel's PV.

Other practical issues might arise when representing vertical PV structures in height or pressure-based coordinates. Since PV naturally varies with latitude (due to the change in f) and height (if not rescaled), spatial averages can lead to significantly different results depending on the underlying coordinate system. To ensure a variation of the vertical profile of PV is indeed due to diabatic processes or isentropic

reorganisation of PV, and is not due to a contribution from a change in potential temperature at a given height, it is crucial to perform averages and calculate anomalies on isentropic surfaces before converting the field onto a different vertical scale.

The right plot in figure 3.4 shows a comparison of ERA-I time mean vertical profiles of the anomaly from the zonal mean (the azonal part) of Ertel's PV, averaged over a horizontal region on isentropic or height surfaces. Clear differences are visible in magnitude, zero crossings and general shape between the profiles averaged on different surfaces. The orange curve in the right plot shows the corresponding PV profile averaged on isentropic surfaces and rescaled according to equation 3.2. As expected, we find rescaling to emphasise the lower level structures of the profile and de-emphasise the upper levels[1]. Correspondingly the stratospheric cyclonic feature (positive PV maximum at about 20km) is drastically reduced in magnitude during the rescaling process. The conventional definition of PV might suggest a major role for the stratospheric part of the circulation, while the rescaled PV indicates only a weak cyclonic flow above the tropopause.

In addition the height of the anticyclonic extremum in figure 3.4 shifts from about 15km to about 10km and the general vertical scale of the anticyclone increases for the rescaled PV compared to the conventional PV. For comparison the relative isentropic vorticity, i.e. the vorticity of winds following isentropic surfaces, is shown in the loft plot. Although having different magnitudes, the profiles follow each other closely and show an anticyclone of similar depth, supporting the idea that the rescaled PV anomaly is a good measure of the circulation.

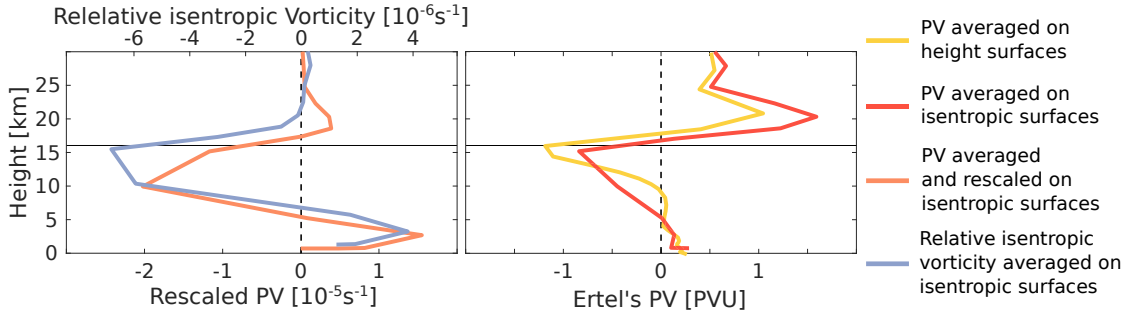

Fig. 3.4 Azonal part of potential vorticity obtained from ERA-I data and averaged over the JJA period of the years 2000-2009, as well as the area 0-40° latitude and 70-110° longitude, with averages being performed on either isentropic or height surfaces. The far left plot shows rescaled PV calculated with equation 3.2 and the relative vorticity of isentropic winds.

We can now investigate the characteristics of the vertical structure of the monsoon anticyclone. However, we should first specify a horizontal region that we associate with the monsoon and that the following vertical profiles correspond to. This is potentially important since a careful comparison of figures 3.2 and 3.3 suggests a north-west ward shift of the monsoon PV response with respect to the forcing region.

[1] When comparing the magnitude of rescaled and Ertel's PV keep in mind that the latter is given in $PVU = 10^{-6} m^2 K/(sKg)$.

Figure 3.5 illustrates the sensitivity of the vertical PV profiles on the exact choice of monsoon region that is used for horizontal averages. Shown are profiles for three different regions:

- **Region of latent heating**: between 0-40° latitude and 70-110° longitude, corresponding to the region of latent heating of the "Indian Monsoon" as shown in figure 3.2.
- **Region of low PV**: between 20-40° latitude and 0-100° longitude, roughly corresponding to the PV low shown in figure 3.5.
- **Garny&Randel**: between 0-30° latitude and 20-120° longitude, the region used by Garny and Randel [2016] to compute vertical profiles of isentropic divergence to investigate the vertical extent of the monsoon

As can be seen in figure 3.5, the profiles averaged over the respective regions clearly differ in both, magnitude and height of the PV minimum. Slight differences in the vertical extent of the anticyclone can be seen, although this might partially be due to low resolution of the data. The overall shape of the circulation seems to be the same in all three cases, showing a lower tropospheric cyclone, an anticyclone in the UTLS region, and a weak positive PV feature in the lower stratosphere.

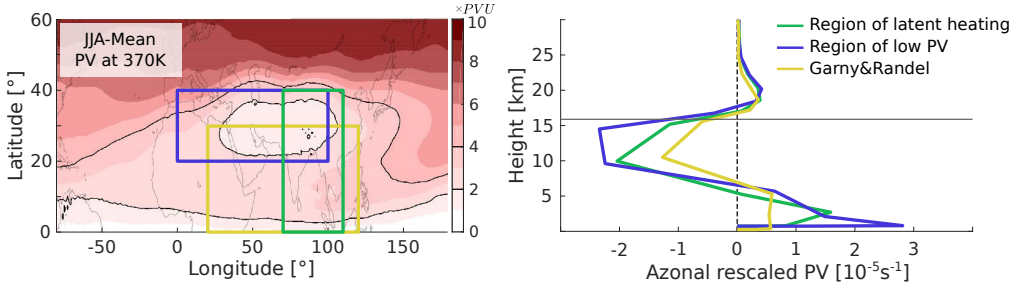

Fig. 3.5 Left: same as figure 3.3, with three different horizontal regions indicated. Right: years 2000-2009 JJA mean vertical profiles of rescaled PV averaged over the horizontal regions shown in the left plot.

Since the general vertical structure and the vertical extent of the circulation do not seem to be very sensitive to the precise choice of horizontal location, and to make comparisons with the model experiments explained in the following sections more consistent, we will restrict ourselves to the monsoon region defined by the region of latent heating and perform all analyses of vertical profiles in this section with respect to the corresponding area. However, it should be noted that the region of latent heating figure 3.5 extends substantially further south than the corresponding region of low PV. Although we find a northward extent of the anticyclone beyond the heating region in some of our numerical experiments (e.g. figure 4.4), the response does usually cover the entire forcing region.

Figure 3.6 shows vertical profiles of four different fields averaged over the JJA period and the region of latent heating shown in figure 3.5. The bottom left plot shows the temperature profile of the region. The pronounced minimum and the abrupt reversal of vertical temperature gradient at about 16*km* mark

the location of the cold-point tropopause. The distribution of latent heating is well confined within the troposphere, i.e. it vanishes at the tropopause height.

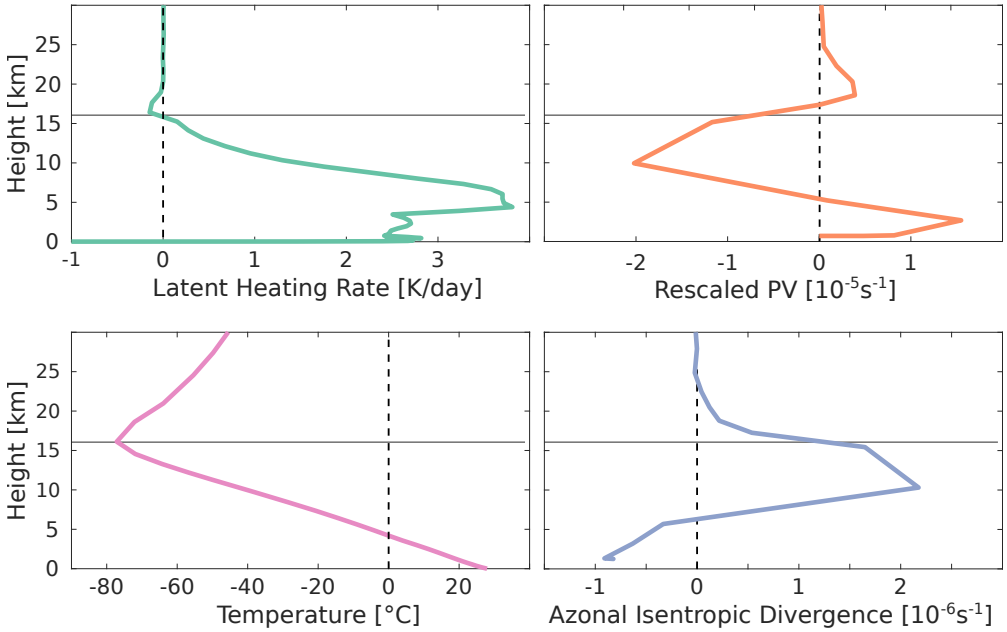

Fig. 3.6 Various vertical profiles of ERA-I fields averaged in the monsoon region over $0-40°$ latitude and $70-110°$ longitude. Heating rates are averages over the JJA-period of years $2000-2005$, all other fields use $2000-2009$. The solid horizontal line indicates height of the cold point tropopause at about 16km.

Rescaled PV is a quantity that represents flow characteristics of the circulation. A clear anticyclonic structure, i.e. negative PV, can be seen within the range of 5-17km, with the upper limit roughly corresponding to the height of the tropopause (grey horizontal line). The vertical profile seems to extend slightly above the tropopause (about 1-2km), although the low resolution of the underlying available ERA-I dataset makes a definitive conclusion regarding the vertical extent of monsoon based on the shown profiles difficult.

Due to the conservation of mass the vertical net-flow of the monsoon leads to a divergence in the wind field at the upper level. The Coriolis force acting on the out-flowing air then drives the anticyclonic circulation of the upper level branch of the monsoon. The divergence of isentropic winds can be seen in the bottom right plot of figure 3.6. The profile also suggests a vertical extension of the monsoon anticyclone above the tropopause. Garny and Randel [2016] present similar vertical profiles of isentropic divergence with finite positive values in the lower stratosphere and conclude that the circulation penetrates the tropopause.

To potentially obtain more robust conclusions on the vertical extent of the monsoon anticyclone we want to study the horizontal PV distribution on various vertical levels. However, due to the natural latitudinal dependence of potential vorticity, horizontal structures are best investigated on isentropic

surfaces, rather than height surfaces. Figure 3.7 illustrates the relation of potential temperature and (hydrostatic) height in the monsoon region, as well as the vertical profile of the azonal rescaled PV distribution of the monsoon circulation. As indicated, the tropopause height of about 16km roughly corresponds to the 380K isentrope.

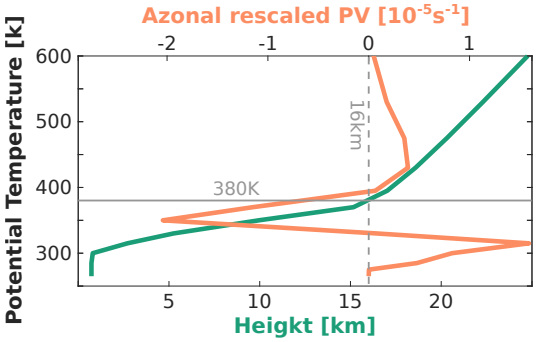

Fig. 3.7 Deviation from the zonal mean of PV rescaled according to equation 3.2 (orange) and hydrostatic height calculated via equation 2.1. Vertical profiles are extracted from the year 2000-2009 JJA mean of the ERA-I re-analysis dataset, averaged over the region 0-40° latitude and 70-110° longitude. The grey lines indicate the 380K isentropic surface (solid) and the tropopause height of about 16km (dashed).

Figure 3.8 displays the mean rescaled PV field on various potential temperature surfaces. The top panel shows the deviation from the zonal mean and a pronounced anticyclone can be seen on the 350K and 370K isentropes. Above the tropopause the rescaled PV field becomes much more zonally symmetric. We further find a stronger latitudinal dependence of the zonal mean part, which is potentially explained by the strong westerlies of the jet stream and the corresponding meridional gradient in relative vorticity. On 395K we can still find a coherent negative azonal PV structure, although the magnitude is much weaker compared to lower levels and the zonal mean background distribution. The location and horizontal extent of the feature is similar to the structure seen on the lower levels and we can therefore identify the feature as being part of a coherent monsoon anticyclone. This supports the conclusions drawn from figure 3.6, that the monsoon penetrates the tropopause and extends into the stratosphere.

We do not find evidence of any monsoon feature on the 430K surface, although figure 3.7 suggests a positive PV anomaly at these heights and figure 3.8 does show a distribution of positive PV anomaly within the monsoon region. The positive PV structure, however, is centred at about 20° latitude, while the negative structure on 395K has a pronounced maximum at about 40° latitude. This large southward displacement makes it unlikely that the two features belong to the same coherent structure and we conclude that the anticyclonic circulation of the monsoon does not reach the 430K surface.

Fueglistaler et al. [2009a] find a coherent monsoon anticyclone feature in the temperature and wind fields, as well as in certain trace gas concentration, extending vertically up to 70hPa (roughly corresponding to the 425K isentrope). In general the extent of a localised circulation feature can be different depending on the studies field. In, for example, a quasi-geostrophic PV inversion problem the streamfunction (SF)

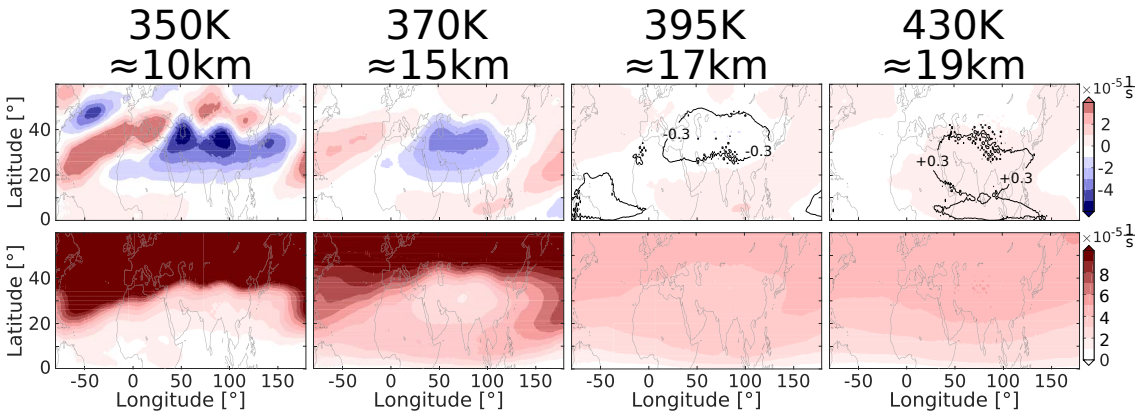

Fig. 3.8 Year 2000-20009 JJA mean rescaled potential vorticity on various isentropic surfaces. Top panel shows the deviation from the zonal mean, bottom panel shows the full field. The contours, respectively, are highlighted in two of the plots. The given heights of the isentropic levels are estimated via figure 3.7.

and PV are related in a non-local way and it is possible to sustain a SF anomaly beyond the bounds of a PV feature. The most pronounced azonal feature potentially corresponding to the monsoon anticyclone at 70hPa presented in figure 5 (not shown here) of Fueglistaler et al. [2009a] is a negative temperature anomaly and their findings only hint towards a weakly (if any at all) azonal circulation pattern in that region.

We will discuss the circulation and temperature response due to a vertically localised heating in more detail in section 4.2. This will include further discussion of the relation of a forced anticyclone in terms of a PV low and the vertical structure of the forcing and background temperature field, as well as the development of a negative temperature anomaly above the circulation produced by a vertically localised heating.

3.1.3 Time dependence and evolution

Besides the characteristics of its time mean structure we also want to investigate the temporal evolution of the monsoon anticyclone. Various authors have observed and described west- [Hsu and Plumb 2000; Popovic and Plumb 2001] and eastward [Dethof et al. 1999] shedding of vortices from the monsoon anticyclone. These vortices (or eddies) are defined via localised, coherent PV or geopotential height structures and can transport trace gases or water vapour out of the monsoon region [Garny and Randel 2016; Vogel et al. 2014].

Figure 3.9 shows examples of the mentioned shedding events as presented by Popovic and Plumb [2001]. Clear westward moving PV minima can be seen, as well as indication for some eastward shedding. Note that the propagation of both, the west- and eastward shed vortices, seem to be fairly steady with a velocity of the order of $7m/s$, close to the value of $8m/s$ observed later in the numerical simulations

presented in figure 4.16 of subsection 4.1.3. This gives confidence in the corresponding theories and model experiments and their explanations regarding the physics and dynamics describing the shedding events. Note that the PV minimum in figure 3.9 is confined to a longitudinal range of about 40-100°. Further the plot does not indicate any systematic change of the flow structure and behaviour over the course of the main monsoon period, supporting the assumption of a steady forcing in the numerical experiments presented later.

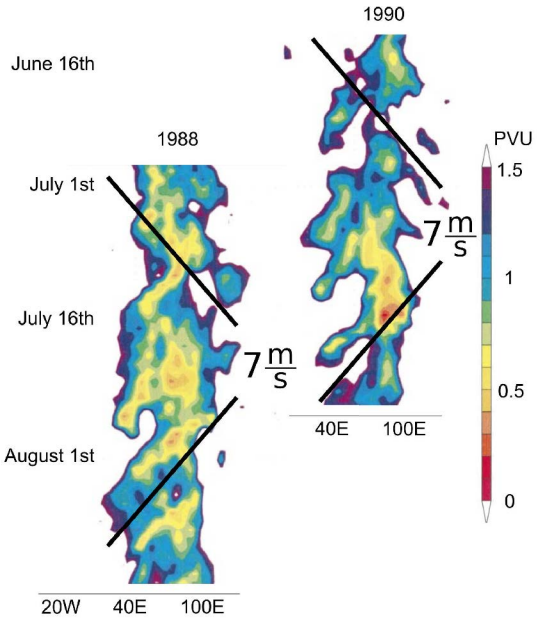

Fig. 3.9 Time evolution of daily ERA-I mean PV at 370K averaged over the latitudinal band $25-35°$ (from Popovic and Plumb [2001], modified). Solid lines indicate an east- and westward velocity of $7m/s$.

The mechanisms for the two types of time dependency are potentially very different. Hsu and Plumb [2000] showed that the response of a single-layer model to a local steady forcing can become unstable for certain parameter ranges and hence experience westward eddy shedding behaviour. We will discuss in section 3.2.3 and (in detail) in chapter 5 how westward eddy shedding can be interpreted as result of a dynamic instability of the horizontal PV low associated with the anticyclone and a subsequent westward movement of "broken-off" PV-patches. Analysing Fourier spectra of ERA-I PV data Fadnavis et al. [2018] concluded that the periodic shedding events happen with a frequency on synoptic time scales (10 days). Although their findings and conclusions do not seem to be very precise the estimated shedding frequency seems to be in rough agreement with the findings of Popovic and Plumb [2001] and our model experiments from section 4.1 (e.g. figure 4.16).

According to the mechanism proposed by Dethof et al. [1999] eastward shedding, on the other hand, is caused by the interaction of the monsoon PV low with the mid-latitude background flow. Baroclinic perturbations pull low-PV filaments out of the bulk anticyclone, which then get advected to the east by

the mid-latitude jet. We were able to reproduce similar behaviour in a numerical model and will further discuss the phenomenon and its dependency on certain model parameters in subsection 4.1.3.

Although the occurrence of these shedding events seems to be well known among monsoon-researchers, certain problems regarding the precise mechanisms and scales involved still seem to be unsolved. It is also not clear if these shedding events are related to a potential bi-modality of the monsoon anticyclone [Zhang et al. 2002]) or phenomena like the Bonin high with strong meteorological implications for surface temperatures and rainfall [Enomoto et al. 2003].

In that sense some of the features and behaviours described by other authors in relation with the monsoon can potentially be interpreted as signatures of eddy shedding. Hoskins and Rodwell [1995] analyse the short-term response to three-dimensional semi-realistic heating distribution and obtain good agreement between the instantaneous model streamfunction field and climatological JJA averaged obtained from re-analysis data. However, they point out a "major defect" of their model response in the form of a "split into three separate centres, with additional maxima near east Africa and Japan" that is not clearly visible in the JJA averaged re-analysis fields. These structures can potentially be explained by east- and westward shedding events.

In accordance with these findings Enomoto et al. [2003] describe and analyse the atmospheric feature of the Bonin high, a subtropical anticyclone observed near Japan in boreal summer. Presenting evidence that the feature can be observed in both, instantaneous and monthly mean geopotential height fields, they conclude that the feature composes of a temporally fluctuating and a quasi-stationary component. Enomoto et al. [2003] further show that the Bonin high is caused by (stationary) Rossby wave patterns propagating on the strong westerlies at the northern edge of the monsoon anticyclone. Enomoto [2004] confirmed these results in a subsequent study and further concluded that the geopotential height structure over Japan is caused by an additional wave source to the north-east of the monsoon anticyclone and a corresponding zonal wave activity flux along the mid-latitude jet. As we will show in subsection 4.1.2 we can reproduce a similar anticyclonic feature to the north-east of the main monsoon without any extra local wave source.

Ren et al. [2015] used a composite analysis and PV budget calculations to investigate mechanisms corresponding to an eastward extension-phases of the monsoon anticyclone. They further find a strong correlation between the eastward extension and anomalous heat and rainfall patterns over east Asia. Similarly, Luo et al. [2017] describe and analyse an east-west oscillation event of the monsoon anticyclone during 2016. These oscillation events can include a split of the monsoon anticyclone and a zonal shift of its geopotential height maximum. Luo et al. [2017] further show that this shift can lead to a substantial zonal mass flux and thus might have important implications for horizontal transport. They link the oscillatory behaviour to a bi-modality of the monsoon, as it was described by Zhang et al. [2002]. These zonal extensions and oscillations can potentially be explained as signatures of east- and westward shedding events.

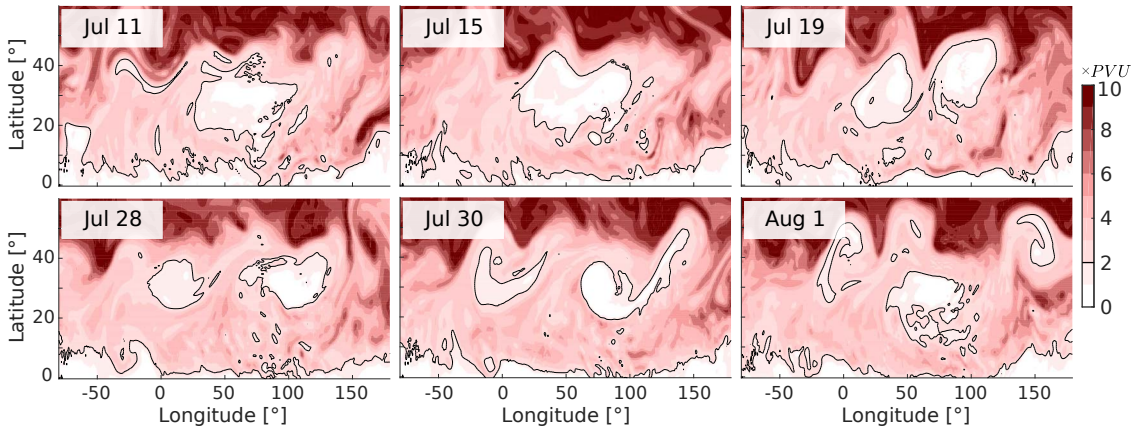

Fig. 3.10 ERA-I potential vorticity on the 370K isentropic surface for various days of the year 2000. The 2PVU contour is emphasised. Note the unequal time step between the plots.

Various authors have discussed in detail examples of the evolution of the horizontal monsoon anticyclone PV structure during specific east- or westwards shedding events [Hsu and Plumb 2000; Garny and Randel 2013; Vogel et al. 2014]. Figure 3.10 illustrates again several shedding events observed in re-analysis data during the year 2000. The top panel shows a localised anticyclone in form of a PV minimum centred at about 70° longitude and 30° latitude on 11th of July. Over the following days the edge of anticyclone becomes distorted and the elongated patch of low PV eventually breaks into two almost equally sized anticyclones. In this case the broken-off anticyclone does not propagate westwards very far, but stays rather in place. The reason might potentially be the interaction with the mid-latitude jet and a pronounced baroclinic eddy, which can be seen at about -30° latitude on 19th of July. The meridional wind associated with the eddy further seems to disintegrate the shed vortex over the period around August 1st.

A few days after the westward shedding event, on 30th of July, we can observe an example of an eastward shedding event. A filament of low PV gets pulled out of the main anticyclone due to meridional advection of a passing by baroclinic eddy and then breaks off, rolls-up and subsequently gets advected eastwards by the mid-latitude jet, in accordance with the mechanism described by Dethof et al. [1999].

In the next section we want to review some existing theories on the dynamics and driving mechanisms related to the Asian monsoon anticyclone. We will then perform a series of numerical experiments with the aim to understand some of the structures, features and evolutions observed in re-analysis data and discussed in this section.

3.2 Explaining the structure and evolution of the monsoon

The significant role of the monsoon anticyclone in determining the composition of the stratosphere makes it necessary for us to understand its dynamics and the physical processes involved in driving it. An early

model for the time mean structure of the monsoon was developed by Gill [1980]. The model was linear and two-dimensional, but captures essential scales and elements of the circulation. Since then many other authors have proposed mechanisms and processes to explain certain characteristics and features. Dethof et al. [1999] proposed a mechanism leading to eastward eddy shedding by the anticyclone, while Hsu and Plumb [2000] reproduced westward shedding from a steadily forced anticyclone in a shallow water system.

Our aim is to develop a numerical model that gives a comprehensive representation of the monsoon anticyclone, reproducing realistic scales and showing a range of behaviours similar to observations. We will start by re-visiting the Gill-Matsuno model in subsection 3.2.1, forming the starting point for our studies. In subsection 3.2.2, we will then re-model the system in a fully three-dimensional, non-linear model and explore the response as we change certain input parameters, such as the heating magnitude or the UTLS friction.

3.2.1 The Gill-Matsuno model

A simple linear theory for steady heat-induced circulations was developed by Gill [1980] as an extension of the Matsuno [1966] model. Gill decoupled the vertical and horizontal dependencies of wind and pressure response to a zonally localised, equatorial heating in a stably stratified, resting atmosphere. Since it can be argued major contributions only arise from the one vertical baroclinic mode with half-wave length comparable to the vertical heating length scale of approximately $L = 10km$ (comparable to the vertical heating scale seen in figure 3.2), the problem becomes separable and one can solve the vertical dependence independently. Winds and pressure are then found to follow a half-cosine profile in the vertical. This approach made it possible for Gill to define effectively two antisymmetric shallow layers, as illustrated schematically in Figure 3.11.

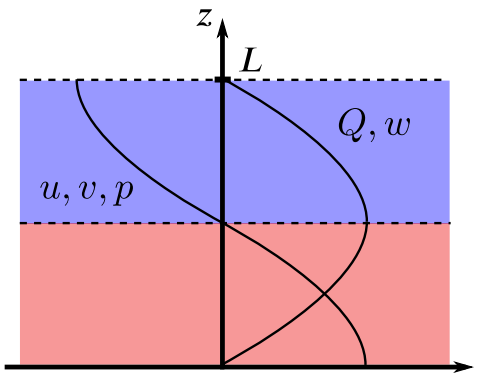

Fig. 3.11 Relation between horizontal winds u,v, pressure p and the leading order vertical mode of the heating Q in the Gill-Matsuno model. Two layers with (anti-)symmetric behaviour can be defined.

The equations determining the corresponding, simplified horizontal field dependencies are based on a shallow water model (similar to the one described in section 2.3) and read for an equatorial beta-plane

$$\begin{aligned} \varepsilon u - \frac{1}{2} y v &= -\partial_x p, \\ \frac{1}{2} y u &= -\partial_y p, \\ \varepsilon p + \partial_x u + \partial_y v &= -Q. \end{aligned} \tag{3.3}$$

All variables are rescaled using $\sqrt{c/(2\beta)}$, $\sqrt{1/(2\beta c)}$ and $10^5 hPa$ as length, time and pressure scale, respectively. Here β is the gradient of the background potential vorticity field and $c = \sqrt{gH}$ is the long gravity wave speed for a vertical rigid lid atmosphere of height H (Gill also chose a value of $H = 400m$, see table 2.1). Note that this value is similar to the gravity wave speed chosen in the single-layer model described in section 2.3 and used in chapters 5 and 6.

The Q in equation 3.3 is a thermal forcing term intended to model the latent heating distribution of the monsoon an ε represents a linear damping parameter. The damping is acting equally on the pressure and wind fields and hence models mechanical friction, as well as radiative damping processes. Those dissipation parametrisations are commonly referred to as Rayleigh friction and Newtonian damping, acting on a time scale ε^{-1}. Choosing the same time scale for both processes allows for an analytical solution of the problem. In the numerical model experiments described later we will choose different time scales for thermal and frictional dissipation in order to obtain a more realistic representation of the atmosphere.

For a specific (localised) heating distributions (parabolic cylinder functions) the simultaneous equations 3.3 can be solved analytically. The resulting horizontal low level response for an equatorial heating confined to $|x| < 2$ is shown in figure 3.12, with the equatorial heating being localised around the origin. The response can be interpreted in terms of three main features. Equatorially trapped Kelvin waves travel eastwards, while Rossby waves are propagating to the west. Both waves produce a strong zonal inflow into the heating area (and corresponding outflow at the upper level). Since the long Rossby wave speed is one third of the Kelvin wave speed in this model, those waves do not travel as far before being damped out and the eastern (Kelvin-wave) inflow region is three times zonally extended as the western (Rossby-wave) branch.

The third feature corresponds to meridional outflow near the centre of the heating. This was explained by Gill as consequence of the vertical motion in the heating region, which leads to vortex stretching and a corresponding change in relative vorticity. In order to conserve the absolute vorticity, air parcels have to move polewards leading to two cyclones north- and south-west of the forcing region. Recall that the

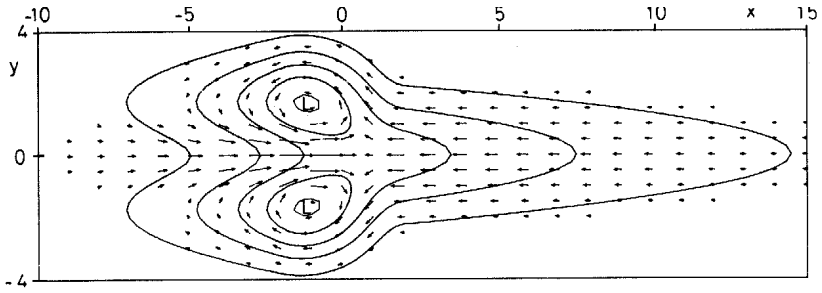

Fig. 3.12 Horizontal low level response of the Gill-Matsuno model to a heating centred at the Equator and extending about 2 rescaled units in both directions [Gill 1980]. Contours show pressure and arrows represent horizontal winds.

upper level wind and pressure (anomaly) fields are exactly antisymmetric to those at the lower level. Hence the top layer is characterized by anticyclones and zonal outflow.

Gill's theory was used to explain the zonal asymmetry of the equatorial Walker circulation, a zonally overturning flow in the tropical belt caused by localised thermal forcing. However, it also can be used to model an off-equatorial Monsoon flow by adding up the responses of a symmetric heating and a profile which is antisymmetric about the equator. The latter leads to a northern cyclone at the ground level and a southern anticyclone, which cancels the southern cyclone of the symmetric response, illustrated in figure 3.13. A pronounced northward-shifted convergent low level cyclone occurs, corresponding to a divergent upper level anticyclone.

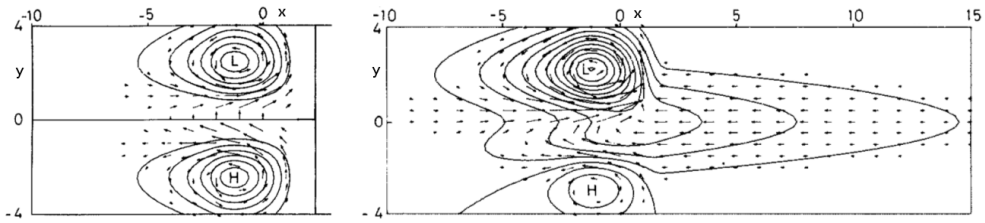

Fig. 3.13 Low level response to a hemispherically antisymmetric heating (left) and formation of a pronounced cyclone as sum of symmetric and antisymmetric response (right). Contours show pressure and arrows represent horizontal winds [Gill 1980].

Many authors have tried to extend the Gill-Matsuno model by including a higher vertical resolution and more vertical modes, non-linearities or forms of temporal evolution. Heckley and Gill [1984] investigated the geostrophic adjustment of an atmosphere at rest when a tropical heating is switched on. Gill and Phlips [1986] extended the model by adding non-linear effects and investigated the steady model response in the limit of vanishing friction.

In the context of a south American circulation pattern, DeMaria [1985] investigated the sensitivity of the (steady and transient) model to an increased number of included vertical modes (corresponding to an increased vertical resolution). They found the horizontal response to be quite similar to the single-mode case. In contrast, Wu et al. [2000a] used a dry primitive equation model with an equatorial heating to

study the response sensitivity in an isothermal atmosphere to changes in the vertical forcing profile and found significant differences in the horizontal propagation speed of the response away from the source region for different vertical profiles.

The Gill-Matsuno model (including UTLS friction) is a widely used concept, forms the basis of various studies on the monsoon and tropical circulations and still plays a fundamental role when it comes to understanding the structure of the monsoon flow [Yang et al. 2007; Lee et al. 2009; Chen et al. 2001]. This is mainly because the response to a confined off-equatorial heat source is a good representation of the time-mean structure of the monsoon. In particular, the model leads to a zonally confined anticyclone (see figure 3.3).

However, there are various problems and limitations associated with the model. For once, the inclusion of a strong momentum damping is a questionable assumption for the upper troposphere. Further, the steadiness of the Gill-Matsuno model does not provide the chance to reproduce the time dependence observed in relation with the monsoon anticyclone (see figure 3.9). We will address these issues in subsection 3.2.2, where we will re-model a Gill-Matsuno-like response with a simple three-dimensional model and investigate its sensitivity to parameter changes.

3.2.2 Modelling the monsoon with a simple GCM

In the following we will describe numerical experiments performed with a dry general circulation model (GCM) based on the primitive equations presented by Hoskins and Simmons [1975]. This model is a simple GCM and has a very simple representation of physical processes. It is a fully non-linear, dry model and is only intended to reproduce the large-scale dynamics of the response. A more detailed description of the model is given in section 2.2.

Held and Suarez [1994] proposed a model-setting for quantitative comparisons of dry dynamical cores in terms of a Newtonian relaxation towards a given temperature restoration profile T_r and a bottom drag layer. Since the configuration leads to a simple, but relatively accurate, representation of mid-latitude dynamics[1], the full Held and Suarez (HS) configuration was subsequently used as a common basic state for idealised atmospheric studies. We will discuss the imposed profiles of the HS configuration in subsection 4.1 and now specify the (horizontally) uniform Held and Suarez (UHS) background configuration, introduced earlier and defined by the corresponding equatorial profiles.

The corresponding vertical structure of the resulting profiles of restoration temperature T_r and thermal and frictional damping rated ε and δ of the UHS state are illustrated in figure 3.14. The scales and profiles are chosen similar to the corresponding values and structures proposed by Held and Suarez [1994]. Note that we defined a 'stratospheric friction parameter' δ_0 which can be varied, while keeping a significant surface drag up to about 2.5km representing boundary effects. For the case of re-modelling the Gill-Matsuno response we chose $\delta_0 = 0.4$ to correspond to the global damping time scale as specified

[1] In a perpetual equinox state.

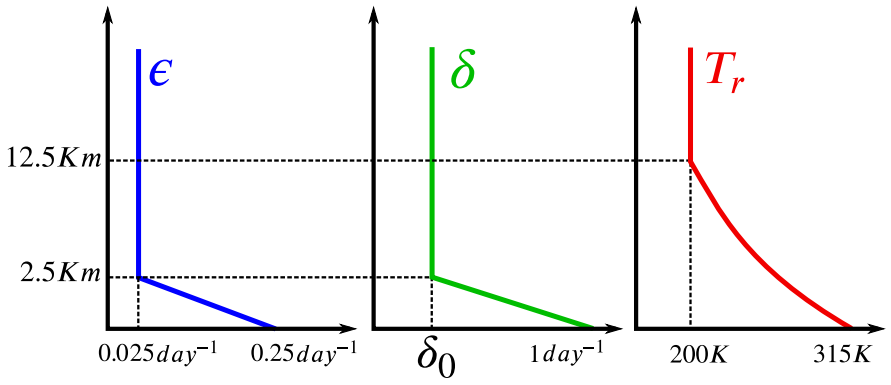

Fig. 3.14 Vertical structure of the UHS background state, i.e. height dependency of the temperature (left) and momentum (middle) damping time scales as well as the corresponding temperature restoration profile (right).

in Gill's original formulation of the problem. We will, however, choose the stratospheric thermal damping to be $\varepsilon = 0.025 days^{-1}$ for all experiments presented in this chapter. This value is a commonly used stratospheric thermal damping rate[1] and is significantly smaller than the value of 0.4 used by Gill [1980]. It is important to remember that momentum and thermal damping act in different ways in the tropical atmosphere, as pointed out by Wu et al. [2000b], and thermal damping usually has a much weaker effect on PV anomalies dominated by the contribution of relative vorticity.

A tropical monsoon flow is then forced by imposing a confined heating with structure $Q(\phi,\lambda,z)$ (of magnitude Q_0) on top of this basic state. The corresponding forcing has the specific form

$$Q(\phi,\lambda,z) = \begin{cases} Q_0 V(z) \cos^2\left(\pi \frac{\phi-\phi_0}{2r_0}\right) \cos^2\left(\pi \frac{\lambda-\lambda_0}{2r_0}\right) & \text{if } |\phi-\phi_0| < r_0 \text{ and } |\lambda-\lambda_0| < r_0 \\ 0 & \text{otherwise ,} \end{cases} \tag{3.4}$$

where ϕ and λ represent latitude and longitude[2], respectively, and the vertical structure is given by

$$V(z) = \begin{cases} \sin\left(\frac{\pi}{2}\frac{z}{z_{max}}\right) & \text{if } z < z_{max} \\ \sin^2\left(\frac{\pi}{2}\frac{z_{top}-z}{z_{top}-z_{max}}\right) & \text{if } z_{max} \le z < z_{top} \\ 0 & \text{otherwise.} \end{cases} \tag{3.5}$$

The vertical and horizontal structure of the forcing is displayed in figure 3.15. The heating profile roughly resembles and has similar scales to the heating distributions shown in section 3.1 and used in other monsoon studies (e.g. the semi-realistic heating shown in Rodwell and Hoskins [1995]).

[1] Newman and Rosenfield [1997] estimated an observationally based global and annual mean thermal damping time at $100hPa$ of about $28days$.

[2] With ranges of $\phi \in [-90°, 90°[$ and $\lambda \in [0°, 360°[$.

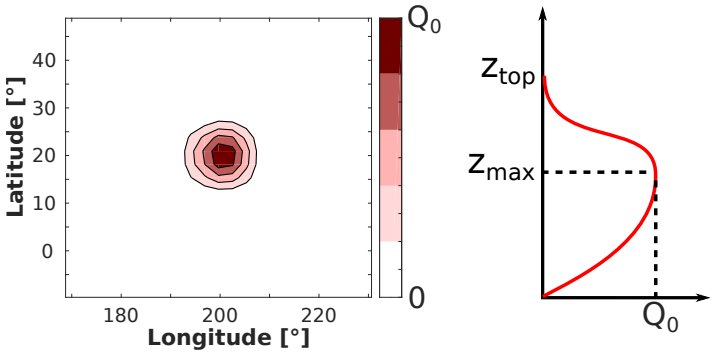

Fig. 3.15 Visualisation of horizontal (left) and vertical (right) profiles of the explicitly imposed heating with magnitude Q_0. The profile has a maximum at height z_{max} and vanishes above z_{top}.

The heating therefore confined to a height below z_{top} and is maximum at z_{max}. Table 3.1 gives an overview of the parameters values used in this report. The basic state is zonally symmetric and hence the exact longitudinal location of the monsoon forcing is irrelevant. We will make the arbitrary choice of $\phi_0 = 200°$ for all experiments. Further, we will chose $z_{max} = 10km$ and $z_{top} = 15km$ for all experiments except those presented in section 4.2. The forcing is switched on smoothly over 25 days following a sin^2 profile. The system enters a steady state after about 200 days. Temporal mean states are obtained by averaging the corresponding field for at least 1000 days starting 1000 days after the switch on of the forcing[1].

Table 3.1 Physical parameters used in the GCM.

Symbol	Physical meaning	Value Range
Q_0	Forcing magnitude	0.5-10K/day
z_{max}	Height of maximum heating	5-13km
z_{top}	Maximum height of heating	10-18km
r_0	Radius of the forcing	10°
ϕ_0	Latitudinal forcing centre	20°
λ_0	Longitudinal forcing centre	200°

Note that the parameters of the forcing (magnitude,position,extent) are roughly comparable with the corresponding characteristics of the latent heat distribution of the monsoon region, shown in figure 3.2. We can therefore interpret the forcing profile as idealisation of the forcing driving the Asian monsoon. All field anomalies are calculated by subtracting the corresponding time averaged background state field from the response of the perturbed atmosphere.

Forcing the model with the described tropical heating distribution then indeed produces a Gill-Matsuno-like time mean response, when choosing a stratospheric friction parameter of $\delta_0 = 0.4day^{-1}$, equal to Gill [1980]. The system does then form two layers with similar antisymmetric structure to that illustrated

[1]Figure 3.21 suggests that the response is indeed statistically steady at day 1400.

in schematic 3.11. Figure 3.16 shows the mean streamfunction (SF) response of the system. Clear maxima of cyclonic (negative) and anticyclonic (positive) SF can be seen at heights of about 2.5km and 13km. The main driver of differences between the upper and lower level response is the bottom drag layer, imposing an additional friction (see figure 3.14).

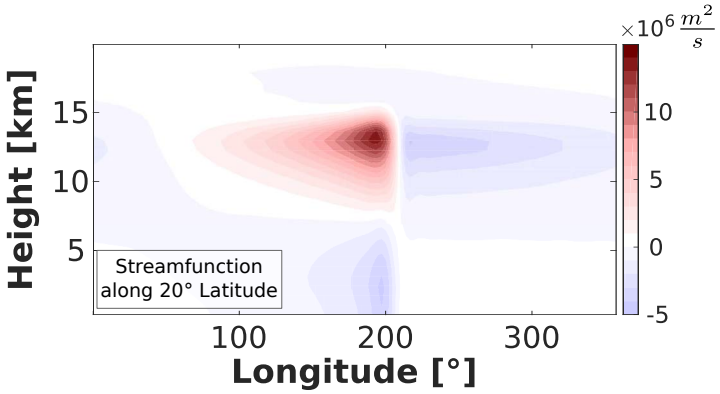

Fig. 3.16 Streamfunction along 20° latitude for a Gill-Matsuno-like system in a UHS basic state. The forcing has magnitude $Q_0 = 5K/day$, is maximum at $z_{max} = 10km$ and vanishes at $z_{top} = 15km$. The stratospheric friction is $\delta_0 = 0.4day^{-1}$.

The horizontal SF response of the two layers is shown in figure 3.17. The corresponding streamfunction fields match the qualitative shape predicted by the Gill theory. For the upper level response this includes in particular the formation of a pronounced localised anticyclone, a significant cross-equatorial flow and a (weak) countering cyclone on the other side of the equator.

As was shown before in theoretical studies by Gill and Phlips [1986] and Wu et al. [2000a] neither non-linearity nor a more sophisticated vertical forcing structure alters the qualitative Gill-like tropical time-mean response too much if the forcing mainly projects on the first vertical mode of the system. Except from minor differences we can reproduce the Gill-Matsuno flow by a localised heating and therefore take this model representation of the monsoon as starting point for further research.

For the rest of this chapter (and thesis) we will solely focus on the upper level anticyclone of the response. The flow in the corresponding numerical simulations will usually have less qualitative vertical symmetry as in figure 3.17 and we will not try to model a realistic response of the lower level flow.

3.2.3 Zonal scale and time dependence of the flow

A common critique at the Gill theory arises from the inclusion of strong linear friction in the Upper troposphere/lower stratosphere (UTLS) region [Battisti et al. 1999]. While there is clearly a boundary drag acting on the low level flow it is still an open question if any atmospheric mechanism can provide a significant large scale momentum damping in the middle atmosphere.

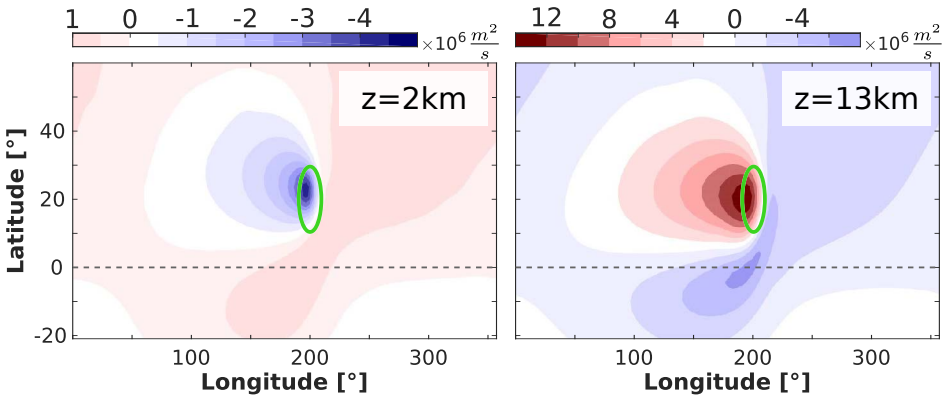

Fig. 3.17 streamfunction responses to a localised heating at effective (antisymmetric) lower and upper levels. The structure follows the typical Gill-response (see figure 3.13) with cross-equatorial in-/out-flow and cyclonic/anticyclonic motion west of the heating region.

As explained, the Gill-Matsuno flow is mostly characterised by westward Rossby (and Kelvin) wave propagation. If those waves are not sufficiently damped they can travel westward for long distances and eventually wrap around the globe and start to interact with each other. The corresponding large zonal length scale of the response is in disagreement with the observed localisation of the monsoon circulation (see figures 3.3 and 3.9). However, the reduction of the mechanical friction in the model also leads to other major changes in the qualitative flow patterns, the PV structure and the temporal behaviour. This subsection will look at some aspects of those changes.

Figure 3.18 shows the days 1000-3000 mean streamfunction (SF) anomaly at 13km for various stratospheric friction parameters δ_0, as defined for the UHS profile in figure 3.14. It can be seen how the zonal length scale of the anticyclone increases as the damping is reduced. From the solution presented by Gill [1980] it is apparent that the zonal scale of the response is proportional to the inverse friction parameter. For vanishing δ_0 the response wraps around the spherical domain and superimposes itself, strongly increasing the response magnitude. Only the weak thermal damping with a rate of $1/40 days$ ensures the system to obtain a balanced and statistically steady state. However, the thermal damping is not sufficient to localise the response.

In any case we first have to explore the possibility of a physical or dynamical process can lead to a strong enough friction in the UTLS region to localise the monsoon anticyclone. One idea to take account of the vertical transport of horizontal momentum in cumulus clouds, which might provide a sort of large-scale 'cumulus friction'.

Zhang and McFarlane [1995] showed that the inclusion of cumulus friction can lead to substantial changes in the overall response of a general circulation model, including effects in the monsoon region. Lin et al. [2008] investigated if the friction used by Gill [1980] can be interpreted as cumulus friction in the UTLS and conclude that it can indeed account for a significant damping, although they point out the high spatial variability of the resulting cumulus friction damping rate. Romps [2014] use a simple

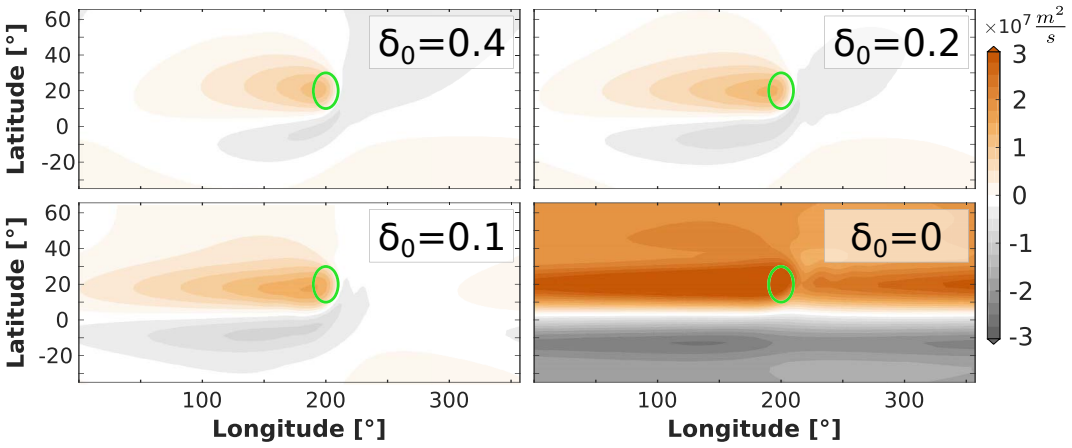

Fig. 3.18 Mean streamfunction anomaly on the 13km surface for a forcing with magnitude $Q_0 = 5K/day$ and the UHS background with different values of Stratospheric friction parameter δ_0 (in $days^{-1}$), as defined in figure 3.14.

model for the vertical convective momentum flux and and conclude that cumulus friction can provide middle atmospheric friction time scales of the order of 1-10days for features with vertical wavelength between 2-10km.

However, the use of cumulus friction as damping mechanism for the monsoon anticyclone is questionable since it is not fully understood yet to what extent cumulus momentum transport, based on localised vertical cloud movements, can act as a large scale friction. Sardeshmukh and Held [1984] and Sardeshmukh and Hoskins [1985] analysed the vorticity balance in the upper troposphere in a general circulation model and with re-analysis data, respectively. Both conclude that the dynamics in the tropical UTLS is essentially non-linear and nearly inviscid. Both studies suggest major contributions from horizontal advection and concluded that convective cumulus transport is of lesser importance. Sardeshmukh and Held [1984] further confirmed results obtained by Holton and Colton [1972], who stated the requirement of a strong external damping when linearising the model about a zonal mean flow. Though important, those findings are purely investigative and cannot explain what processes and mechanisms balance the negative forcing of potential vorticity above the monsoon heating or what controls the zonal structure of the anticyclone.

Other studies used a less radical approach to damp the response in numerical simulations of the tropical middle atmosphere and the monsoon circulation [Liu et al. 2007; Hoskins and Rodwell 1995]. The general idea of various studies is to relax the mean zonal wind component towards climatological or idealised profiles, while keeping the wave-part freely evolving, and obtained reasonably localised tropical responses. Damping the zonal mean can affect the azonal flow components (i.e. the deviation from the zonal mean) through small-scale turbulence and diffusive processes. However, it is not clear in what way fixing the mean zonal wind suppresses the wave structures and therefore acts as a damping in this direction. Certainly the inclusion of climatologically representative fields contains numerous

implicit correlations and might indirectly provide the mechanism to localise the circulation without the need for a deeply fundamental understanding. It is hard to link such a complex numerical feature to a physical process and hence such studies are not useful to investigate the actual mechanisms controlling the Monsoon circulation. It is also not clear what might couple the damping of zonal fields to the azonal components of the flow.

Hoskins and Jin [1991] performed initial value experiments for tropical circulations. Among other cases they perturbed a resting atmosphere and a climatological zonal mean wind profile with a Gill-like streamfunction to find the second system significantly suppressing the equatorial flow and causing a polewards propagation of Rossby waves. This study, however, can only give limited insights into a potential (steady) zonal confinement of the response since the model is not constantly forced and the initial flow becomes strongly modified due to baroclinically after about 14 days.

Various authors further model the upper level monsoon response to thermal forcing in a semi-realistic setting, but suppress the development of baroclinic instabilities or avoid their occurrence by restricting experiments to early times (usually to about day 20).

Hoskins and Rodwell [1995] modelled the monsoon in a fully three-dimensional, non-linear model as response to a thermal and orographic forcing and investigated the importance of non-linear effects and mountains. They found the general structure of the monsoon anticyclone to be well reproduced by a linear, thermally forced model. As mentioned, Hoskins and Rodwell [1995] restrict their experiments to early times in order to avoid baroclinic instabilities developing in their system. Such short integration lengths might simply bypass the problem of unrealistic zonal extension (shown in figure 3.18) without the system actually reaching a steady state. We will show in section 4.1 that a baroclinically unstable basic state can, in fact, have a localising effect on the monsoon flow. Jin and Hoskins [1995] used a very similar approach and an equatorial heating to model tropical flows, but also limited the survey to early times.

Ting and Yu [1998] investigated the steady response of a baroclinic three-dimensional model with climatological basic state to a localised equatorial heating, but mostly suppressed the occurrence of baroclinic instability by adding a 15-day mechanical and thermal damping to the system. Such a friction does directly affect the explicitly forced flow and hence explains the localised response they found. Hendon [1986] performed Gill-like tropical heating experiments in a 2-layer model with baroclinically unstable background to study the relative position of the upper level anticyclones without restricting their experiments to early times or suppress the instability of the basic state. However, they did not address the problem of zonal localisation.

The Gill-Matsuno model describes the steady response of the system to a steady heat source, while the GCM response in our experiments can actually exhibit strong, non-trivial and spontaneously emerging time dependency in cases with vanishing stratospheric friction, despite the use of a steady forcing. The temporal variability, however, does only occur for sufficiently strong forcing magnitudes. The response to a weak heating is steady and qualitatively close to the prediction of the linear Gill-Matsuno model for

weak damping. The model response extends to the west in form of a steady beta-plume with zonal scale limited by the weak thermal damping operating in the stratosphere (see subsection 3.2.2).

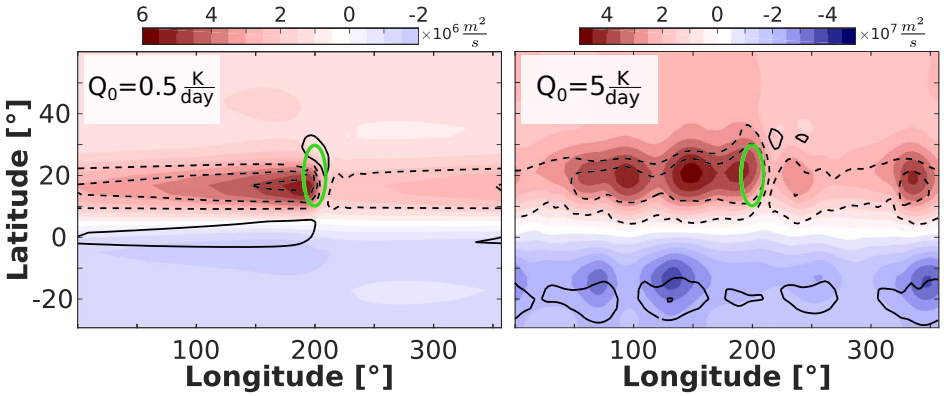

Fig. 3.19 Day 1525 streamfunction anomaly response at 13km using the UHS basic state without stratospheric friction ($\delta_0 = 0$) for two different forcing magnitudes. Contour lines show the day 1525 PV anomaly on the 340K isentropic surface, with dashed contours representing negative values, the zero contour is not shown and the contour interval being $0.2PVU$ and $1PVU$, respectively. The green ellipses indicate the forcing region.

The horizontal structure of the typical response to two different forcing magnitudes is displayed in figure 3.19, showing SF and PV snapshots for systems with two different forcing magnitudes. The response decays monotonically west of the forcing in the case with $Q_0 = 0.5K/day$ due to the weak thermal damping. In the other case, i.e. when $Q_0 = 5K/day$, a clear eddy-chain structure can be seen.

In the case with a strong heating the system does exhibit a periodic creation and westward shedding of vortices from the (steady) heating region and the response forms a zonal chain of (weakly connected) vortices. However, if we time-average the response to a strong forcing the meridional velocities and the zonal SF/PV variations of the discrete eddies averages out and all that remains is a single elongated feature dominated by zonal winds, as shown in the middle plot of figure 3.20.

You can further see that the time mean response of a system in the shedding regime ($Q_0 = 5K/day$) is mostly linear. The top row of figure 3.20 shows the SF response to a forcing with three different magnitudes Q_0, where the shown field was multiplied by a certain factor in each case. We will regard the response to the (relatively) weak forcing with $Q_0 = 0.05K/day$ as almost linear. The difference between the various plots and the linear case then indicates non-linearities of the response (bottom row in figure 3.20).

The non-linearities in the case of the response in the steady regime (bottom left plot in figure 3.20) is zonally localised to the vicinity of the forcing region and meridionally confined to the latitudes of the forcing. It seems to correspond to a southward shift of the response near the forcing region, potentially induced due to advection by the strong meridional winds in that area. In general non-linearities seem to be small compared to the full SF response.

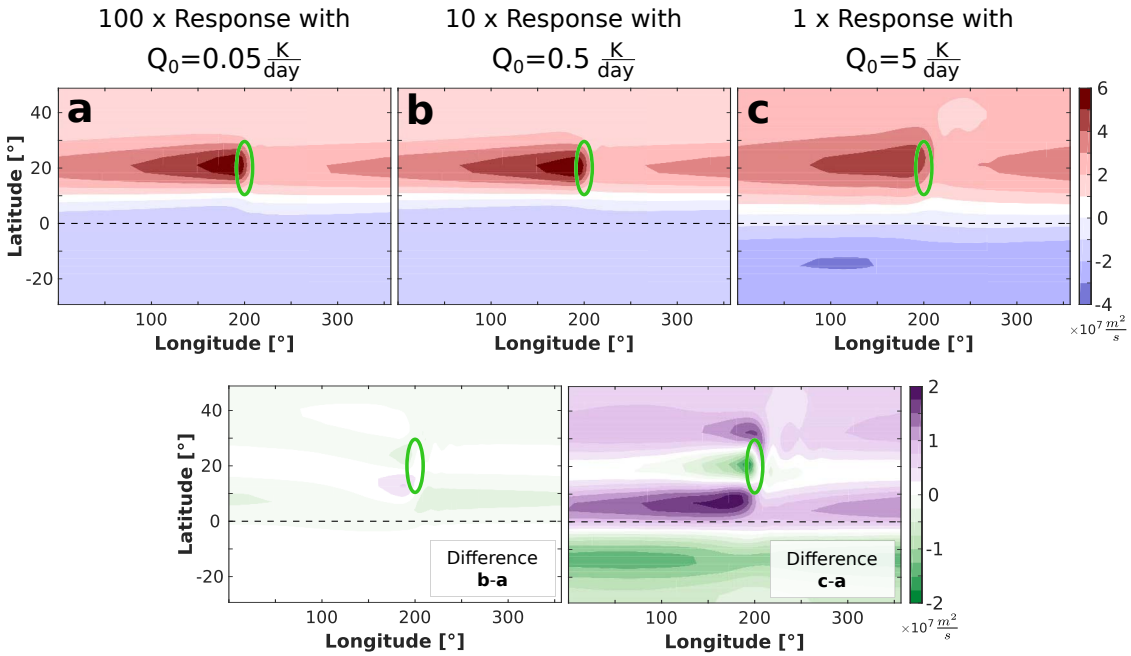

Fig. 3.20 Time mean SF response at 13km of the UHS basic state without stratospheric friction to a forcing with different magnitudes Q_0 (top row) and differences between certain fields (bottom row). The response shown in the top plot was multiplied with a certain factor, to make the fields easier to compare and highlight linear and non-linear effects. The green ellipse indicates the forcing region and the dashed line shows the equator.

In the case of the response in the shedding regime (bottom right plot in figure 3.20) non-linearity seems to have mostly two effects on the mean SF: it seems to shift the zonally extended response southward beyond the meridional extent of the forcing and induces a localised positive SF feature to the north of the heating region. In section 5.1 we will show that the transition into the shedding regime can lead to a southward displacement of the response to a steady forcing in a single-layer model. The reason is an intrinsic meridional drift of isolated eddies on a beta plane. The strength of the meridional drift depends on e.g. the magnitude and size of the eddy. The southern non-linearity signature of the response in the shedding regime shown in figure 3.20 can potentially be explained by the described mechanism of meridionally displaced vortices. The strong zonal and meridional confinement of the non-linearities in the steady response case compared to the shedding case might further indicate a qualitative different type of response that potentially relies on the discrete eddy nature of the flow.

In accordance with the discussed eddy shedding threshold behaviour we do not find any time variations of the azonal SF response along the centre-latitude of the forcing in the weak-forcing case, as shown figure 3.21. The right plot with $Q_0 = 5K/day$, on the other hand, displays an almost periodic creation and shedding of vortices in the forcing region, corresponding to the almost equidistant and parallel lines of equal field strength. The eddies propagate westward at a roughly constant speed of about $12m/s$, indicated by the constant slope of the diagonal lines. Due to the potential importance and applications it might have for the overall flow, we will investigate the zonal propagation of discrete vortices in more detail in chapter 6 in the framework of a single-layer model.

Note that figure 3.21 suggests a time period of about 10 days per shedding event, which is in good agreement with the roughly bi-weekly observed shedding of the monsoon anticyclone (see e.g. Ortega et al. [2017]). We will propose a theory for the shedding process in chapter 5 and with it a constructive way to estimate the shedding frequency.

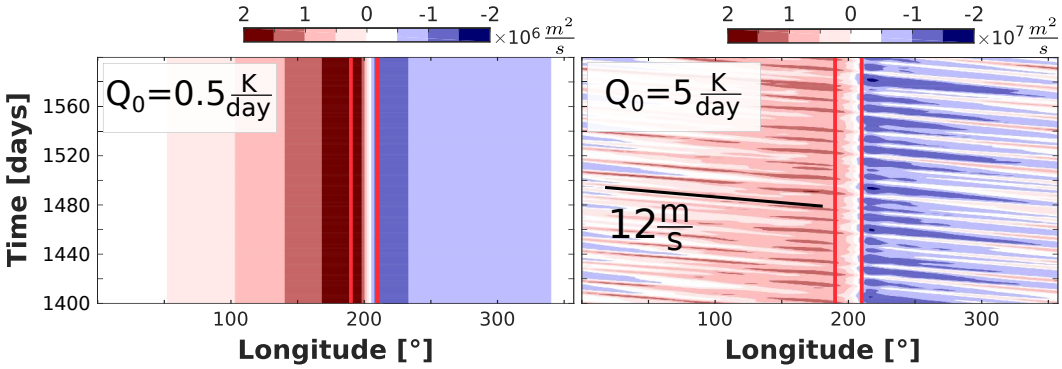

Fig. 3.21 Evolution of azonal streamfunction along the $13km/20°$ latitude line for the UHS basic state without stratospheric friction and different forcing magnitudes. Red vertical lines indicate the extent of the forcing region, the slope of the diagonal black line corresponds to a velocity of $12m/s$.

Various groups have previously investigated the idea of eddy shedding and mechanisms and phenomena

related to it, to some extent in relation to the monsoon anticyclone. Plumb [2007] showed theoretically that, in general, an eddy shedding process is necessary to obtain a steady flow when working in an inviscid background. Since for such a system one cannot have divergent outflow over constant-PV lines, this mechanism helps to locally reduce the persistent PV forcing in the heating region. Hsu and Plumb [2000] performed several single-layer numerical experiments aiming to simulate a steady monsoon forcing on a beta plane and encountered shedding behaviours if the background asymmetry becomes strong enough. Their studies, however, included a finite large scale damping. Popovic and Plumb [2001] showed using re-analysis data that similar westward shed PV features can be seen in the monsoon anticyclone region (see figure 3.9). Liu et al. [2007] studied the response of a three-dimensional model to idealised and semi-realistic monsoon thermal forcing distributions and also observed a periodic shedding of eddies from the monsoon anticyclone for sufficiently strong heating magnitudes.

Davey and Killworth [1989] analysed the response to a steady mass source in a single layer beta-plane model intending to describe and explain oceanographic phenomena. They observed a threshold transition from a steady to a eddy-shedding state as the strength of the mass source increases, similar to the transition shown in figures 3.19 and 3.21.

We will investigate the phenomenon of eddy shedding from a steady source in more detail in chapter 5 using a single-layer model. As we will show, the formation of discrete vortices can be regarded as a result of an absolute instability breaking up the zonally extending zonally (almost) symmetric plume of anomaly, predicted by steady, linear theory.

It is worthwhile to mention that we do not find eddy shedding processes when imposing a substantial stratospheric friction. For this case we find a steady, but zonally quickly decaying, response without internal time variability which is qualitatively close to the steady, linear Gill-Matsuno response (as shown in figure 3.18). A possible explanation might be changes in the stability properties of the flow or a direct suppression of absolute instability due to the imposed friction. These findings are in agreement with our results in chapter 6, section 6.2.3, where we show a change in time behaviour and spatial structure of the response to a steady forcing in a single-layer model when introducing a strong thermal damping. Generally, however, we will not assume any strong damping in the stratosphere, besides from the weak 40day thermal relaxation.

The lack of strong dissipation in our experiments leads to an extreme westward elongation of the response and an eventual re-emergence of air parcels in the forcing region due to the spherical geometry of the domain. This can lead to two different phenomena. At first, the wrapping around of the forced beta-plume will lead to a continuous increase in the strength of the response. Figure 3.22 shows how the SF anomaly in the forcing region increases over the course of several hundred days. It also can lead to a delayed entering of the shedding state. In the case of $Q_0 = 1.1K/day$ shown in figure 3.22 the initial response does not produce clear and distinct vortices. Only after the anomaly wrapped around the periodic domain that the response becomes unstable and enters the shedding state. Due to this

self-amplification of the response long spin up times of the system of at least 1000 days are required to achieve statistical steady states.

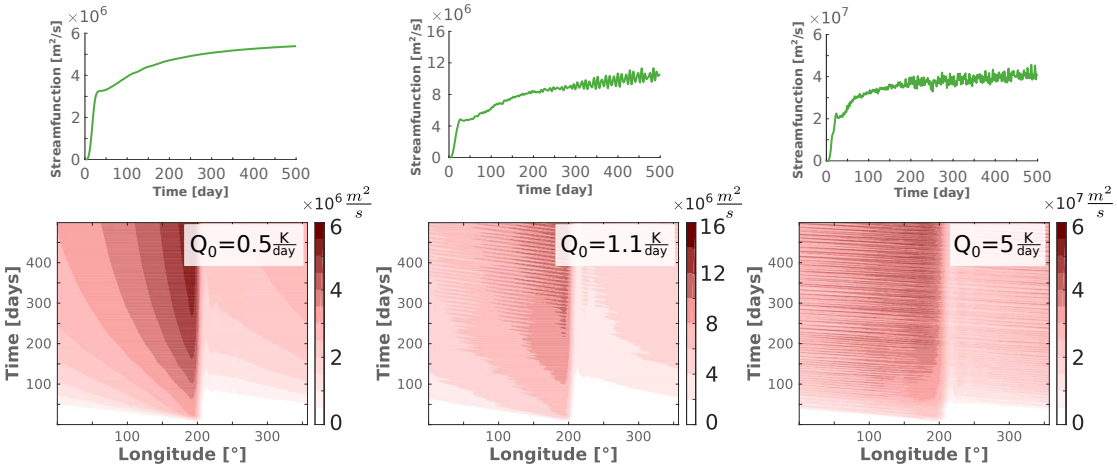

Fig. 3.22 Streamfunction response to a heating with three different magnitudes Q_0. Top panel shows the time evolution in the centre of the forcing at 13km, bottom panel shows the evolution along the 13km/20° latitude line. Note the different scaling factors for the three graphs.

In the case of strong forcing magnitudes and corresponding eddy shedding of the system, we face another phenomenon caused by the periodic domain. Once a vortex travelled around the globe it will interact with the forcing region and is likely to trigger another shedding event. This process eventually leads to a phase-locking of incoming and outgoing vortices. Figure 3.23 shows the correlation of SF at the centre of the forcing with the SF along the 20° latitude line. It can be seen how incoming vortices simply travel "through" the forcing region, without any evidence of actual new eddies being created.

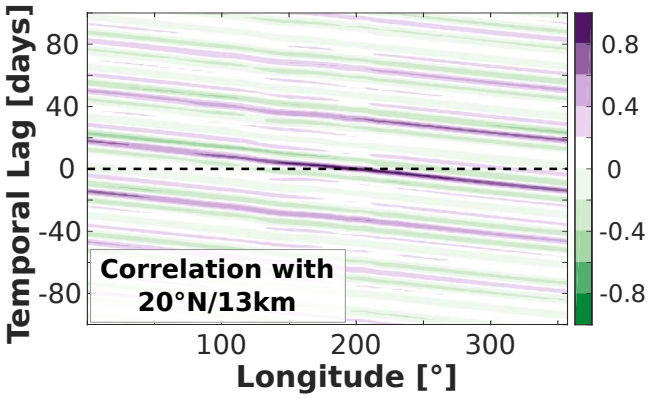

Fig. 3.23 Two point correlation of streamfunction at the centre of the forcing at 13km with points on the 13km/20° latitude line for an experiment with $Q_0 = 5K/day$ and various correlation time lags.

Such a phase-locking mechanism can potentially influence flow characteristics like the shedding frequency or the size of shed vortices. Other authors have previously investigated eddy shedding in a

periodic domain, but either restricted their experiments to early time behaviour [Davey and Killworth 1989] or did not mention corresponding phenomena [Hsu and Plumb 2000]. For all following experiments in this chapter, we will be focussing on strongly forced experiments in the shedding regime.

3.3 Summary and research questions

In this chapter we have analysed ERA-I data and identified a range of behaviours and characteristics of the monsoon anticyclone, including a zonal localisation of the response, a non-trivial temporal dependence in the form of eddy shedding and a potential vertical extension of the flow into the stratosphere. We have further discussed various simple numerical and analytic models and conceptual theories to describe and explain certain properties of the monsoon flow. However, the different approaches presented here were only able to explain or reproduce isolated specific features of the response and did not lead to a comprehensive model that can describe the full range of phenomena associated with the monsoon.

Subsection 3.2.1 discussed a range of approaches used in existing literature to model the anticyclone and gain insights into the physical processes driving it. Special focus was given to the model presented by Matsuno [1966] and Gill [1980], which potentially captures the time-mean response of the monsoon flow, but does not include any time dependence and additionally relies on an unrealistically strong mechanical friction throughout the atmosphere. Using a similar setting as starting point, we showed how the response to a steady localised heating in a simple GCM is modified when we remove the mechanical friction in the upper troposphere and lower stratosphere. As shown, the physical interactions represented in the model are not able to confine the response to the vicinity of the forcing region without a sufficiently strong dissipative process. This behaviour is in contrast to observations, which show a zonally localised anticyclone in the form of a confined PV low. The corresponding experimental results suggest the need for additional physical processes to be included in order to model a realistic monsoon anticyclone.

On the other hand we showed that for vanishing friction and sufficiently strong magnitudes of the imposed steady heating the monsoon anticyclone starts to exhibit spontaneously emerging time dependence in the form of westward eddy shedding. This phenomenon is a potential explanation for the westward eddy shedding observed in relation with the monsoon anticyclone. It is particularly interesting that the shedding process induces a temporal variability to the response without the need for a time-varying heating.

The process of eddy shedding and the question of zonal confinement of the response can potentially have a strong impact on e.g. the horizontal transport behaviour of the monsoon. The modelling of the anticyclone in a three-dimensional model (compared to a single-layer-model) has the additional advantage that we can obtain insights into the vertical structure, which can potentially influence the vertical transport pathways of the monsoon. Although transport is not directly the topic of this thesis,

we want to further investigate the dynamical properties of the circulation in order to improve our fundamental understanding of the system.

We think that many processes and phenomena discussed here have not been sufficiently studied in the existing literature and it is not clear which interactions determine the various scales involved. Following the presented results and their discussion we can now formulate a set of specific questions and problems that we aim to address in the remainder of this dissertation:

- Which mechanisms can lead to a zonal localisation of the time mean response?
- Which physical processes set the threshold heating magnitude above which the response exhibits westward eddy shedding?
- How does the frequency of the westward shedding process depend on the forcing parameters?
- What is the propagation speed of shed vortices and how does it depend on the size and strength of the eddies?
- In what way is the eddy propagation modified by the inclusion of a background flow or the fact that shed eddies form a zonal chain of (weakly connected) vortices?
- How sensitive is the response to the inclusion of thermal damping or a steady zonal background flow?
- What sets the vertical extent and position of the monsoon anticyclone and what is their dependency on the vertical structure of the heating or the background state?
- What influence does the interaction with mid-latitude dynamics have on the forced monsoon anticyclone and can we use it to model the phenomenon of eastward eddy shedding?

In the next chapter we will perform a set of GCM experiments in a more realistic basic state that includes a simple representation of some large-scale mid-latitude dynamical features, like sub-tropical jet streams and baroclinic eddies. As we will see, the interaction with the background flow can lead to a zonal localisation and does influence the temporal behaviour of the flow. Section 4.2 will then discuss the vertical profile of the response. We will show that the corresponding model set-up does indeed correspond to a comprehensive description of the monsoon and is able to reproduce a range of different behaviours and properties that have been observed, thus giving insights into the processes and mechanisms involved.

Chapter 4

A comprehensive model for the monsoon anticyclone

We now want to extend the numerical studies introduced in chapter 3 and use the described GCM to obtain a minimal model for the monsoon anticyclone that is able to reproduce the range of behaviours and characteristics identified earlier.

4.1 Interactions with mid-latitude dynamics

In subsection 3.2.1 we reviewed the linear steady Gill-Matsuno theory as a model for the monsoon anticyclone forced by a localised, steady heat source. We used a similar approach to remodel the anticyclone in an idealised GCM (described in section 2.2) and investigated the emergence of non-linearity and time dependence when reducing the mechanical friction of the UTLS region. Many features of the modelled anticyclone can be seen in re-analysis data. However, the removal of stratospheric friction led to an unrealistic zonal stretching of the response, as can be seen in figure 3.18. We now want to perform a similar set of GCM experiments, but this time force the anticyclone in a more realistic representation of the Earth's atmosphere instead of a resting fluid.

4.1.1 The Held-Suarez background configuration

Held and Suarez [1994] proposed a standard test-case for dry dynamical cores, which quickly became a much used basic state for idealised experiments (e.g. by Butler et al. [2010] or Kidston et al. [2011]) since it provided an easy and reliable way to produce a simple representation of the large scale circulation of the mid-latitude atmosphere. The mid-latitude dynamics is forced by a relaxation of temperatures towards a restoration profile that is a function of latitude and height, inducing a zonal mean wind with strong temporal and spatial variability due to baroclinic instability of the forced circulation. We will refer

to the resulting flow as full Held and Suarez (HS) state or configuration, in contrast to the (horizontally) uniform Held and Suarez state (UHS) which was introduced in subsection 3.2.2.

Polvani and Kushner [2002] added a term $\tau_{asym} \sin\phi$ to the HS restoration profile, allowing them to introduce hemispherical asymmetry and hence a even better representation of the seasonal variability in mid-latitude dynamics. The internal variability of the modified state was further studied by McGraw and Barnes [2016] and used by Chen and Plumb [2014] to investigate eddy transport in the lower atmosphere, both using a asymmetry parameter of $\tau_{asym} = 20K$. We will use both, an hemispherically symmetric HS state with $\tau_{asym} = 0K$ and an asymmetric HS case with $\tau_{asym} = 20K$ to obtain a more realistic representation of the northern hemisphere jet during the monsoon season in boreal summer.

The modified HS restoration temperature and the corresponding damping rate ε are defined by

$$T_r = \max\left[T_{strat}, \left(T_{surf} - \Delta T \sin^2\phi - \tau_{asym}\sin\phi - \Delta\Theta \ln\sigma \cos^2\phi\right)\sigma^{\frac{2}{7}}\right], \tag{4.1}$$
$$\varepsilon = \varepsilon_{atmos} + (\varepsilon_{surf} - \varepsilon_{atmos}) \max\left[0, \frac{\sigma - \sigma_b}{1 - \sigma_b}\right] \cos^4\phi,$$

where ϕ is the latitude and $\sigma = p/p_0$ is the ratio of pressure and surface pressure. Recall that we will use a height-like log-pressure scale for the vertical dimension, given by equation 2.1.

Table 4.1 describes the parameters appearing in equation 4.1 and displays the ranges of values used for our simulations. Note that the UTLS thermal damping rate of $\varepsilon_{atmos} = 1/40 days$ is a realistic value for the middle atmosphere and corresponds to a relatively weak damping (Newman and Rosenfield [1997] used an observation based radiative transfer model to estimate a global and annual mean thermal damping time at $100hPa$ of about $28days$). The value of

Table 4.1 Physical parameters used to define the Held-Suarez profile defined in equation 4.1.

Symbol	Physical meaning	Values used
T_{strat}	Homogeneous temperature of the stratosphere	$200K$
T_{surf}	Surface temperature at the equator	$315K$
ΔT	Meridional temperature gradient measure	$0-60K$
$\Delta\Theta$	Vertical temperature gradient measure	$10K$
ε_{atmos}	Homogeneous damping rate of the bulk atmosphere	$0.025 day^{-1}K$
ε_{surf}	Surface damping rate at the equator	$0.25 day^{-1}K$
σ_b	Boundary layer height	0.7
τ_{asym}	Asymmetry parameter	$0K$ and $20K$

Relaxing the temperature of a resting atmosphere towards this basic state leads to a baroclinic instability of the system, since the corresponding state in theoretical thermal wind balance is unstable. The thermal

wind balance relates the meridional gradient of the zonal mean temperature to the vertical gradient of the zonal mean zonal wind. Hence, the HS system will tend to produce strong time mean zonal jets in the mid-latitude UTLS atmosphere, where the temperature restoration profile has strong meridional gradients. The instability of this time mean state will then produce strong temporal and spatial variability in the form of mid-latitude baroclinic eddies. A detailed description of the basic state is given by Held and Suarez [1994].

We will still keep the boundary layer friction active (illustrated in figure 3.14) with a surface damping rate of $\delta_0 = 1 day^{-1}$. Within this chapter we will refer to the basic state as HS state, background or configuration, meaning the flow and temperature fields produced by relaxing the system to the corresponding specified profiles shown in figure 4.1.

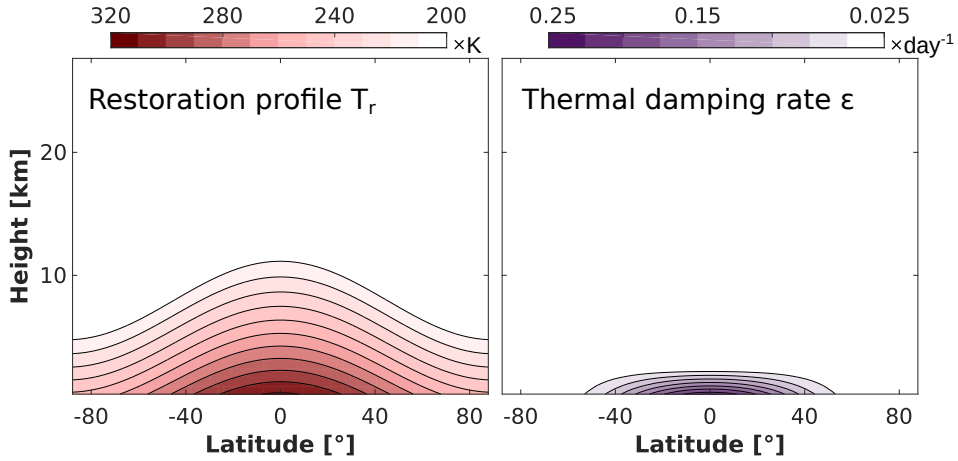

Fig. 4.1 Held-Suarez (HS) temperature restoration profile and corresponding thermal damping rate according to equation 4.1 and $\Delta T = 60K$.

Figure 4.2 shows characteristics of the generated basic state. In the left plot one can see two zonal jets centred at about $\pm 40^\circ$ latitude and 10km height. The plot is in very good agreement with the mean zonal wind field shown in Held and Suarez [1994], giving confidence about the correct implementation of the system. The mean magnitude of the jets is about $35 m/s$. The middle plot shows a snapshot of the azonal streamfunction at 10km, indicating several baroclinic eddies forming a zonal band at about $\pm 40^\circ$. On the very right, one can see the time evolution of the zonal wind at a point close to the centre of the northern hemisphere jet.

A large variability of the jet due to baroclinic eddies can be seen in the right plot of figure 4.2. Despite the strong temporal variations the flow reaches a statistically steady state and the time mean response converges onto the displayed mean jets within about 200 days. In all cases using the baroclinically unstable HS configuration we let the system evolve unperturbed (no explicit local heating) for at least 1000 days to ensure a steady state is reached. The imposed forcing is then switched on smoothly over the next 25 days, as explained in subsection 3.2.2.

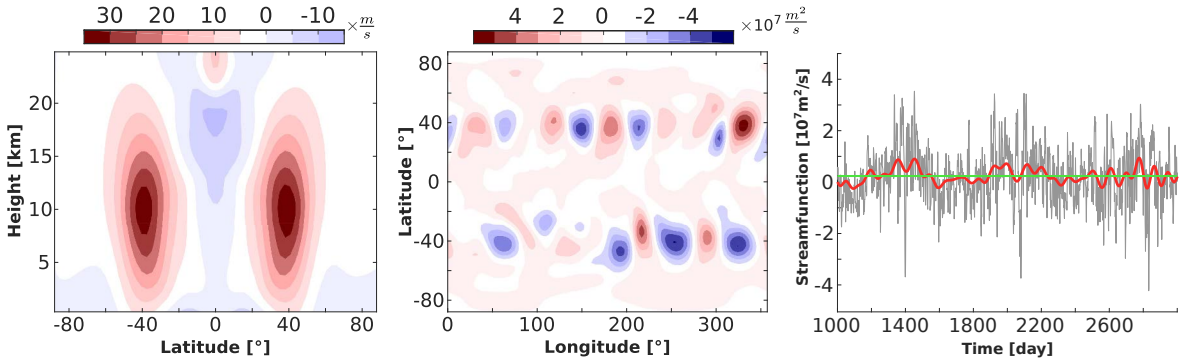

Fig. 4.2 Left: temporal and zonal mean zonal wind profile, Middle: azonal streamfunction on the 10km surface at day 1500, Right: time evolution of streamfunction at 20° latitude, 0° longitude and 10km height. Red line is high-pass filtered and green line indicates the mean.

The two main dynamical features of the HS state are the westerly mean jets and the baroclinic eddies that are associated with waves propagating on the corresponding sharp PV gradients of the jets. The eddies and the corresponding jets are strongly correlated features and form a coherent structure of the system. That means in particular, that a change in the HS parameters, e.g. ΔT or τ_{asym}, will affect eddies and jets alike and it is not possible to vary the corresponding features separately.

Turbulent mixing by the mid-latitude baroclinic eddies affects the temperature structure of the basic state. Figure 4.3 shows the zonal and time mean temperature and potential temperature profiles for an hemispherically symmetric HS state with $\Delta T = 60$ and the mean vertical profiles at the centre of the explicit forcing at 20° latitude. The equilibrium field shows a change in the structure of the cold-point tropopause. The vertical temperature minimum in the forcing region is about $4km$ higher and more than $5°C$ colder than in the non-baroclinic UHS state. The change in lapse rate at the tropopause is also far less abrupt due to a smoothing by the turbulent background.

Haqq-Misra et al. [2011] investigated the mechanism via which baroclinic eddies in equivalent simple GCM settings can generate a realistic tropopause profile and found an elevation of the tropical tropopause caused by eddy interactions. Kim and Son [2015] conducted a similar study specificity for the HS state and also found an increase in height and decrease in temperature of the tropical tropopause (compared to the restoration profile) due to wave-driven upwelling. The modified vertical tropopause structure will have effects for the PV forcing arising from the imposed heating, as explained later in section 4.2.

Note, that the changed temperature profile at 20° latitude will have an effect on the vertical potential temperature profile. For a heating profile defined in height or sigma coordinates this will subsequently lead to a change of the isentropic level at which the PV maximum occurs. We will hence show PV fields in following plots on various isentropic levels, corresponding to the vertical maximum of the anomaly. The changed temperature structure of the basic state will also affect the PV forcing arising from to the imposed heating, which will be further discussed in section 4.2.

We will now investigate how the system responses to a steady, local heating, defined in section 3.2.2.

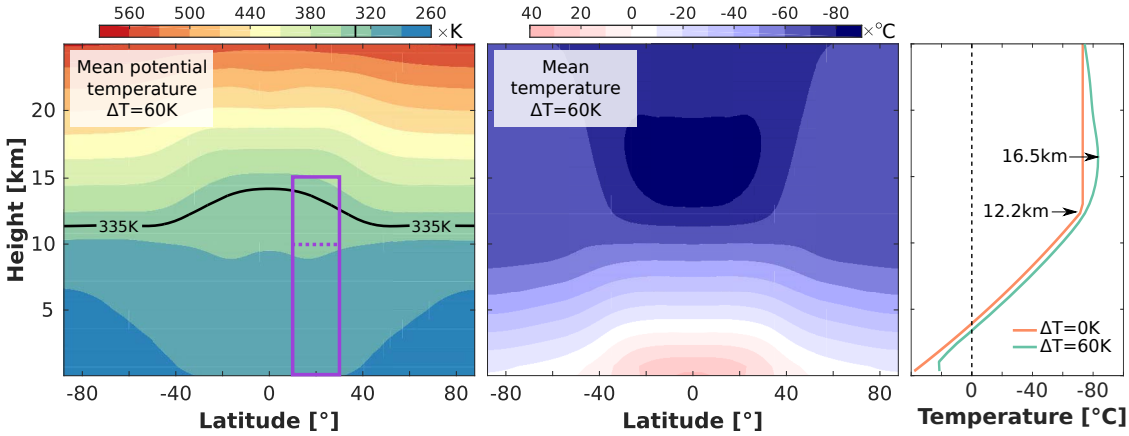

Fig. 4.3 Zonally and temporally averaged potential temperature (left) and temperature (middle and right) of the symmetric HS background state with $\tau_{asym} = 0K$ and $\Delta T = 60K$. The 335K isentrope is highlighted, the purple rectangle shows the extent of the imposed heating ($z_{max} = 10km$,$z_{top} = 15km$) with the dashed line indicating the height of the maximum. The profiles on the right show the vertical temperature structure at 20° latitude and 200° longitude for the UHS and HS profiles. Arrows indicate the height of the cold-point tropopause.

The forcing is centred at 20° latitude and 200° longitude, with a 10° radius, and kept unchanged during this entire study. However, as explained earlier, the longitudinal position of the forcing is completely arbitrary and has no influence on the results, since the model does not include topography or any other zonally asymmetric features other than the explicit heating.

4.1.2 A localised monsoon anticyclone

This section will give insights on how the interaction of a steady localised forcing with mid-latitude dynamics can lead to a zonally localised monsoon anticyclone response. As explained in subsection 3.2.3, it is not clear what physical or dynamical processes can cause a zonal localisation in an nearly inviscid atmosphere. The problem was recently investigated by Amemiya and Sato [2018], who found that the meridionally varying depth of a single-layer model can have a localising effect on the response to a confined mass source. Such a meridional depth gradient does introduce a zonal mean wind (a westerly jet in their case) and does therefore correspond to a simple representation of certain dynamic mid-latitude characteristics.

As described in section 3.1 (and reviewed later in section 4.2) a vertically varying heat-source can act as a PV forcing. The so created change in PV will be associated with a temperature anomaly and, more importantly, a circulation anomaly. If the corresponding time scales are sufficiently long and the system has time to adjust, the flow will be close to (quasi-) geostrophic balance and the horizontal winds almost divergence-free, enabling us to represent the circulation field in terms of a streamfunction. Figure 4.4 shows the horizontal structure of the anomalous mean streamfunction (SF) and potential vorticity (PV) response.

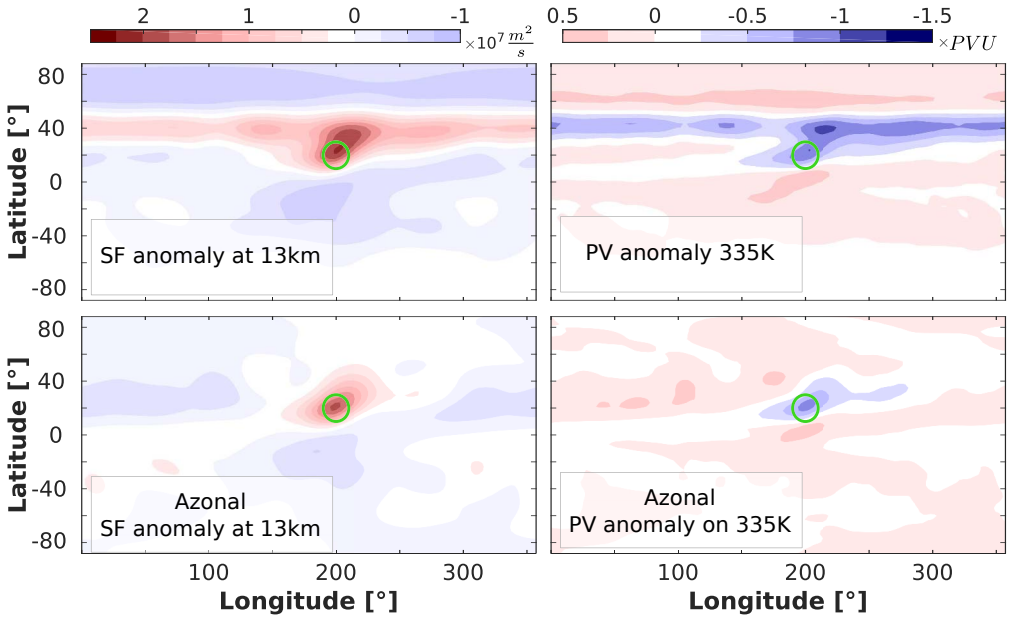

Fig. 4.4 Time mean streamfunction anomaly on the 13km surface (left) and potential vorticity anomaly on the 335K isentrope (right) for an experiment with baroclinically unstable background, i.e. the symmetric HS state with $\Delta T = 60K$. The forcing magnitude is $Q_0 = 5K/day$. Bottom panel shows plots with zonal mean removed. Green circles indicate position and extent of the forcing region.

The top panel shows the full anomaly response and two main features can be seen:

- A zonally confined patch around the forcing region (green circle) and
- An elongated zonal band of anomaly north to the forcing.

In the bottom panel of figure 4.4 we only plotted the azonal component of the SF and PV response, i.e. with zonal mean subtracted, we find that the anticyclone in form of a confined anomaly patch remains mostly unchanged as we remove the zonal mean of the response, while the northern, elongated feature disappears almost entirely. It is important to understand, that such a zonally symmetric structure is often only visible when plotting the change in PV/SF with respect to an unperturbed basic state (in this case the HS state without explicit heating). In a physical system like the Earth's atmosphere it is quite non-trivial to define such a basic state (and a corresponding anomaly from it), and hence we might not necessarily observe such a feature even if present.

The middle plot in figure 4.5 shows the response of the system to a forcing without a zonal mean component (the zonal mean of the original heating was subtracted along the entire latitude band). As can be seen, the zonally symmetric band-structure is not present in this case and the PV anomaly response looks almost identical to the case with full heating (including zonal mean), when subtracting the zonal mean of the response (right plot). This indicates that the zonal mean part and the azonal part of the

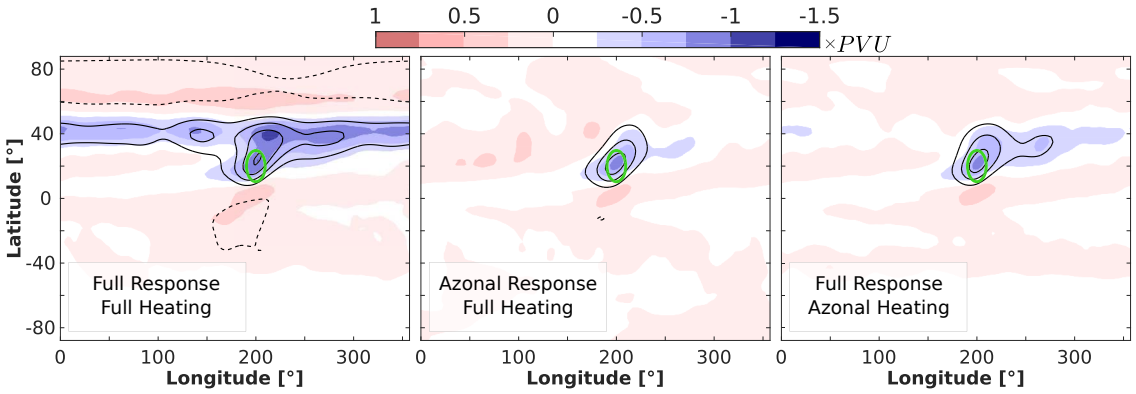

Fig. 4.5 Mean PV anomaly at $335K$ (shading) and mean SF anomaly at $13km$ (contours) for the symmetric HS basic state with $\Delta T = 60K$. Contour interval is $5 \cdot 10^6 m^2/s$. Left plot shows full anomaly for full heating. Middle and right plots show response without zonal mean and for a heating without zonal mean, respectively.

heating act almost independently on the basic state and the zonally extended feature is not caused by the "local contribution" of the forcing but only by its zonal mean.

This further suggests the zonally extended band represents an annular-mode-like response of the system. Annular modes are hemispheric scale patterns of climate variability and the leading mode of mid-latitudinal variability in terms of empirical orthogonal functions (EOFs) (see e.g. Thompson and Wallace [2000] for a detailed description on annular modes and examples for the observed variability of the atmosphere). A perturbation of the global temperature structure and flow fields by an imposed forcing can cause a response similar to such an annular mode. Effectively, the structure and/or position of the resulting baroclinic jet and eddy features can change. This might lead to a meridional shift of the time mean jet and can thus manifest as a zonally symmetric PV or SF structure.

Various studies, e.g. Butler et al. [2010] or Ring and Plumb [2007], have shown that simple dry GCMs with basic states similar to the HS configuration can indeed exhibit annular-mode-like responses when perturbed by a zonally symmetric forcing. As we have shown, the response to the zonally symmetric part of the heating can, however, be separated from the confined monsoon anticyclone response to the localised heating.

A characteristic of annular-mode-like responses, in contrast to a simple advection of low (monsoon) PV by the mean flow, is that the coupled system of mean winds and the baroclinic eddies responds as a whole. Figure 4.6 illustrates the similarity of the zonal mean response of our system and an annular mode structure. The left plot shows the time and zonal mean zonal wind profile of the HS basic state (contours) and the time and zonal mean of the meridional eddy advection of zonal wind $u'v'$ (shading). The latter is a measure for the strength of the baroclinic eddies and indicates their role in driving the mean flow of the system. The middle plot shows the corresponding modification of the zonal wind and eddy flux when the system is forced by a local heating with $Q_0 = 5K/day$. A polewards shift of the jet

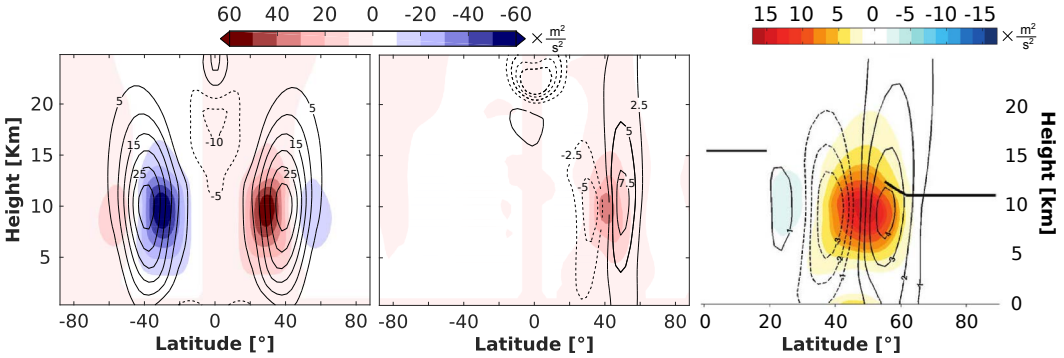

Fig. 4.6 Left: contours show time and zonal mean zonal wind field of the HS basic state with $\Delta T = 60K$, the shading shows the time and zonal mean eddy momentum flux $\overline{u'v'}$ (primes indicating deviations from the zonal mean). Middle: as left, but anomalies from the basic state caused by a forcing with magnitude $Q_0 = 5K/day$. Right: contours show the first EOF of the zonal mean zonal wind, shading gives $\overline{u'v'}$ regressed on the principle component time series of the EOF [from Butler et al. 2010]. Right-hand plot only shows the northern hemisphere and vertical scale was transformed into log-pressure coordinates according to equation 2.1.

can be seen, driven by a change in $u'v'$. Note that the mean flow and the eddies seem to respond as a coupled system.

One of course has to be careful since the shown anomalies include the localised anticyclone structure in the forcing region that can be seen in the middle plot of figure 4.6. However, since the change in mean zonal wind is centred at about 40° latitude, and hence north of the forcing, it seems to indeed mostly capture the annular-mode-like feature. The right plot of figure 4.6 shows the first EOF of the zonal wind field in the HS state (contours) as computed by Butler et al. [2010]. The striking similarity of the shown EOF and the zonal wind anomaly in our system gives confidence that the structure is indeed an annular-mode-like excitation of an internal mode of variability, and does not correspond to an extension of the monsoon anticyclone.

The presented results indicate the (relative) unimportance of the elongated feature of the time mean response shown in figure 4.4. Since it is caused by the zonal mean contribution of the forcing and seems correspond to an annular-mode-like response of the basic state supports the idea that the mid-latitude dynamics forced by a baroclinically unstable basic state can indeed have a localising effect on the response to a confined heating.

We now want to investigate in more detail how the response changes as we again introduce the baroclinic HS basic state, but this time by gradually increasing the meridional temperature gradient parameter ΔT. This will lead to a change in zonal jet centre position, strength and shape, as well as corresponding changes in the baroclinic eddies. Figure 4.7 shows the meridional profiles of the mean zonal wind at $13km$. It can be seen how the jets generally shift polewards and become stronger as ΔT is increased. Note that the strength and shear of the zonal wind within the forcing region $(10-30°)$ is almost the same in all three cases.

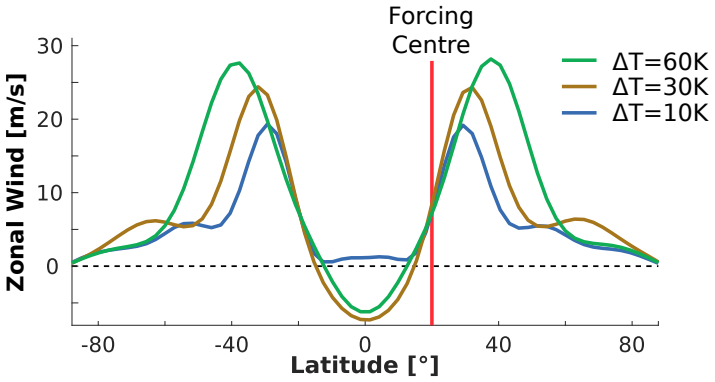

Fig. 4.7 Time and zonal mean profiles of zonal wind at $13km$ for the symmetric HS background using $\tau_{asym} = 0K$ and different values of the meridional temperature gradient parameter ΔT. Red vertical line indicates the centre of the forcing region at 20° latitude.

Various studies investigated the effect of parameter changes HS-like states, e.g. Zurita-Gotor [2008] who found a similar tendency for poleward-shift, strengthening and broadening of the jets when changing the meridional temperature gradient over a range of $60 \leq \Delta T \leq 180$ (although they kept the mean surface temperature gradient of the restoration profile fixed, opposed to the temperature gradient at the equator like in the original HS setting).

The altered background state does affect the time mean response of the flow, as can be seen in figure 4.8. As we increase the meridional temperature gradient ΔT we see how the two features mentioned at the beginning of this subsection start to become more apparent. First, the response gradually becomes zonally localised at the latitudes of the heating, forming a coherent anticyclone in the forcing region. Second, the zonal mean component of the anomaly response seems to shift northward. This is likely to be the formation and change of the annular-mode-like band structure discussed earlier. As can be seen in figure 4.7 the jet maximum tends to move polewards as ΔT increases and a similar polewards shift of the corresponding EOF would not be surprising.

In the following we want to investigate the sensitivity of the response to a different change in basic state and introduce a hemispherical asymmetry to the basic state, as discussed for figure 1.3 in section 1.1. The asymmetry itself is not necessarily likely to have a huge effect on the response, since the southern hemisphere jet and eddy track is considerably far away from the forcing region, but the intention is to obtain a general state that is a potentially more realistic representation of the atmosphere during northern hemispherical summer time, rather than an annual mean state. To generate such a seasonal basic state Polvani and Kushner [2002] introduced an additional term into the equation for the HS restoration profile proportional to the asymmetry parameter τ_{asym}. (see equation 4.1)

Figure 4.9 shows the mean jet profile of the asymmetric HS state for an asymmetry parameter $\tau_{asym} = 20K$. Note in particular the zonal wind of the asymmetric jets are close to zero in the centre of the forcing region at 20° latitude. The chosen value of τ_{asym} is twice as large as the one used originally in Polvani and Kushner [2002], but follows the choice used by other authors to generate more realistic

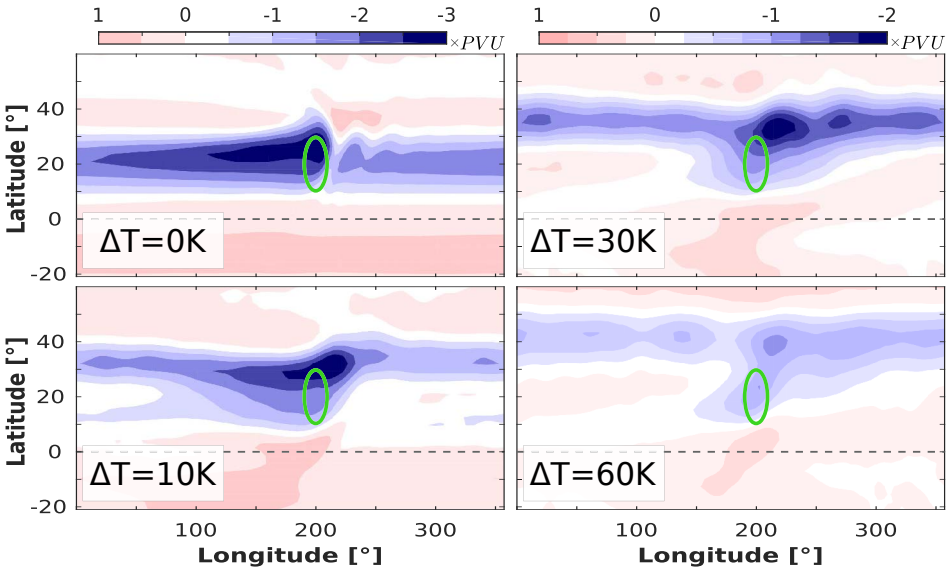

Fig. 4.8 Time mean PV anomaly response at $340K$ (left panel) and $335K$ (right panel) for a forcing with magnitude $Q_0 = 5K/day$ and baroclinic HS basic states with $\tau_{asym} = 0K$ and different values of meridional temperature gradient parameter ΔT. Green ellipses indicate the forcing region.

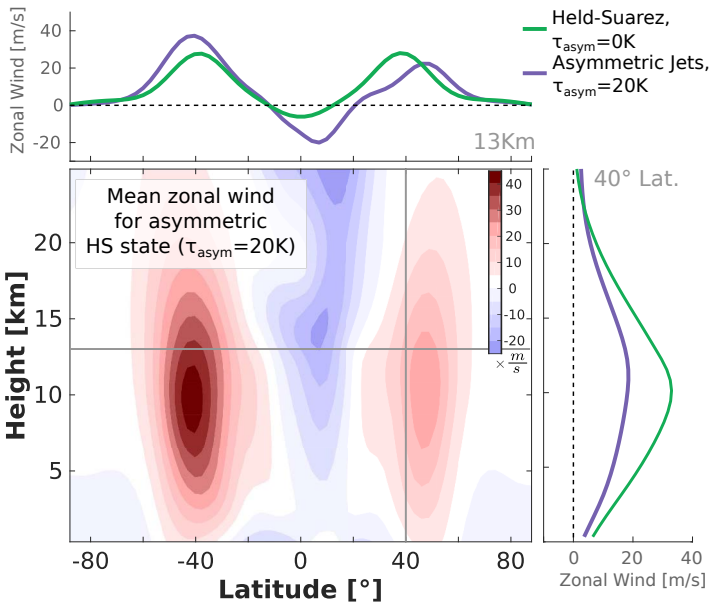

Fig. 4.9 Zonal and time mean zonal wind profiles for the asymmetric HS basic state, using $\tau_{asym} = 20K$ and $\Delta T = 60K$. The line plots show the profiles at $13km$ and $40°$ latitude, respectively, indicated by grey straight lines.

summer/winter jets, e.g. by Chen and Plumb [2014] who studied the effective diffusion of tracers in a dry primitive equation model with an asymmetric HS background state.

McGraw and Barnes [2016] investigated the seasonal jet variability by imposing a time-dependent asymmetry to the HS with a varying asymmetry parameter of magnitude $\tau_{asym} = 20K$. Besides finding a similar northward shift and weakening of the summer jet to what is shown in figure 4.9 compared to the original HS setting, they find an additional northward displacement of the jet when adding a zonally symmetric tropical heating to the system. These findings are in very good agreement with our conclusions from figure 4.6 about the excitation of an annular mode.

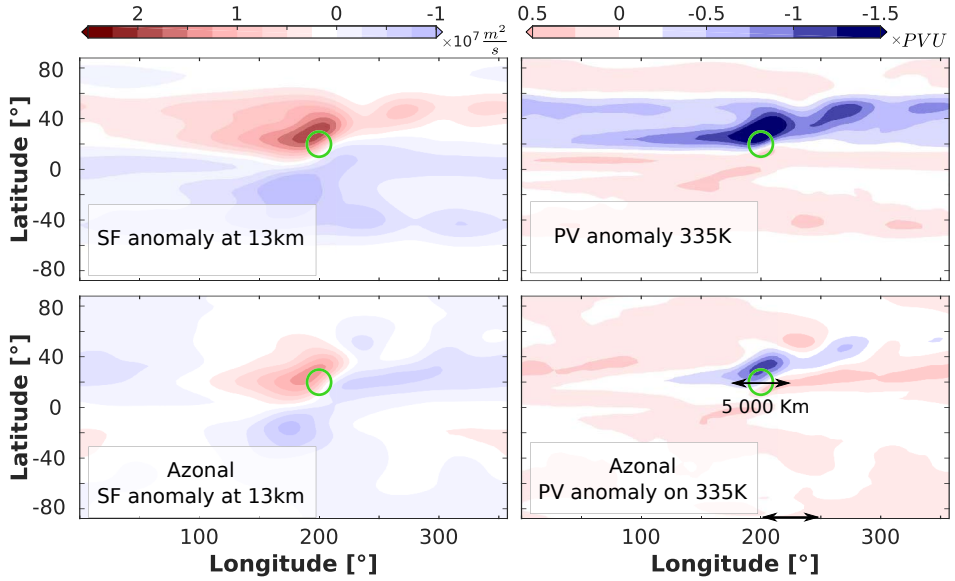

Fig. 4.10 Mean streamfunction (left) and potential vorticity (right) anomaly response to a forcing with $Q_0 = 5K/day$ perturbing the asymmetric HS basic state with $\tau_{asym} = 20K$ and $\Delta T = 60K$. Bottom panel shows the zonally asymmetric part of the response. Circles indicate the forcing region and the black arrow has a length of 5 000km at 20° latitude.

The upper level SF and PV response of the asymmetric HS state to a localised tropical forcing are shown in figure 4.10. As for the symmetric case (figure 4.4), we find an annular-mode response in the form of a zonally symmetric band and a pronounced localised anticyclone in the forcing region. The annular-mode-part of the response seems to be broader and span a larger latitudinal range than that observed in the symmetric case. The structure of the localised anticyclone, however, seems to be qualitatively similar. Note that the anticyclone in form of the azonal PV response seems to be located to the north of the forcing region. Correspondingly the heating extends significantly further south than the PV response. This characteristic of the forced flow is similar to what can be seen in ERA-I data for the time mean PV response and the region of latent heating (see figure 3.5).

The azonal mean response seems to show zonal extensions, with the response stretching eastward to the north and westward to the south of the main response, giving the response a "tilted" appearance

with respect to latitude lines. Similar extensions can be seen in the symmetric HS case (figure 4.4) although they do not seem to extend as far out of the forcing region and are less pronounced. These zonal extensions are potentially a result of east- and westward eddy shedding. As we will explain in subsection 4.1.3 eastward shedding is based on the advection of the mid-latitude jet and hence happens preferably closer to the jet-centre north of the forcing, while westward shedding can only occur in the absence of strong eastward winds, i.e. further to the south (where the zonal winds are even westwards). In the next section we further investigate the time dependency of the monsoon response in a baroclinic background, with special interest in the mentioned east- and westward shedding.

4.1.3 Transient response in a baroclinic background

Besides the time-mean structure of the response the model shows a range of interesting transient behaviours. As mentioned in subsection 4.1.1 the HS basic state[1] has a large degree of variability due to the turbulent stirring by the forced baroclinic eddies. Hence the PV and streamfunction fields generally show a range of quickly evolving spatial structures which can correspond to anomalies of fairly large magnitude compared to the time mean field (see figure 4.2). The response magnitude of the explicitly forced anticyclone strongly depends on the forcing strength. Figure 4.11 shows instantaneous snapshots of the PV response to heating distributions with various magnitudes. For the case with $Q_0 = 10K/day$ a clear patch of low PV can be seen in the vicinity of the forcing region, relating to a clearly visible anticyclone.

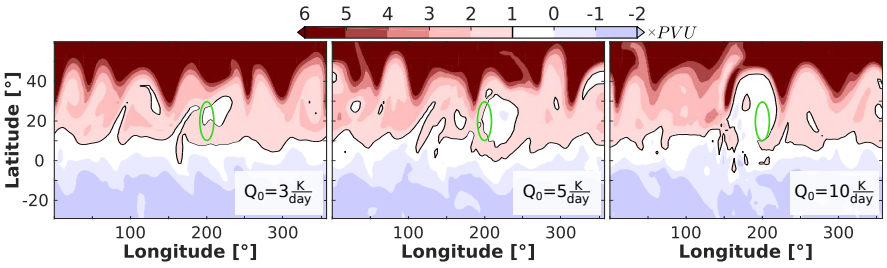

Fig. 4.11 Day 1525 PV response at $335K$ using different forcing magnitudes and a symmetric HS state with $\Delta T = 60$. Green ellipses indicate the forcing region and the $1PVU$ contour is highlighted.

For the weaker heating with $Q_0 = 3K/day$, on the other hand, the anticyclone is barely visible and could easily be misinterpreted for a feature of the basic state, i.e. a baroclinic eddy. This dependency on the response amplitude on the forcing magnitude is a persistent and usual characteristic of the flow. In all three cases the PV anomaly of the anticyclone becomes clearly visible when taking long time averages since the azonal anomalies of the background state average out and the monsoon response creates a uniquely identifiable azonal feature in or near the heating region. In re-analysis data the monsoon is pronounced and clearly visible on a day-to-day basis (see example in figure 3.10). We can therefore

[1] arising from relaxing the temperatures of the system towards the restoration profile shown in figure 4.1.

conclude that a heating of a certain magnitude is required to reproduce the short time structure of the monsoon response. The corresponding forcing scale is of course dependent on the details of the basic state.

Next we are going to document a special type of transient interaction of the PV low of the explicitly forced anticyclone and the baroclinic eddies of the background state. In order to see a clear evolution of the anticyclone we choose a forcing magnitude of $Q_0 = 10K/day$ for this experiment, although we see similar behaviour for weaker magnitudes (as later indicated in figure 4.14 for $Q_0 = 5K/day$).

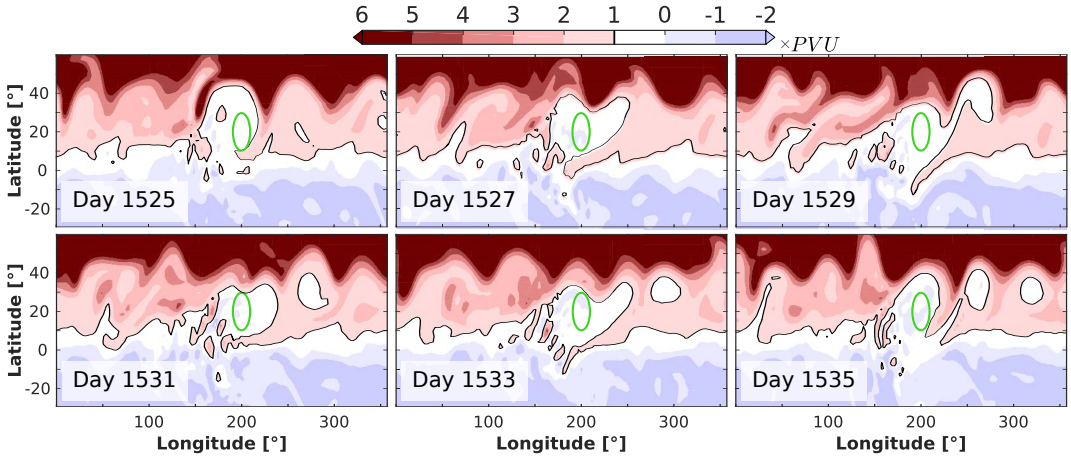

Fig. 4.12 PV response at $335K$ for various days. The forcing magnitude is $Q_0 = 10K/day$ and we used a symmetric HS state with $\Delta T = 60$. Green ellipses indicate the forcing region and the $1PVU$ contour is highlighted.

Figure 4.12 shows the evolution of PV on the 335K isentrope over the course of 10 days. Strong wave-like perturbations can be seen along the steep meridional PV gradient at about 40° latitude, representing the eastwards moving baroclinic eddies. We further can clearly see a PV minimum in the forcing region forming the monsoon anticyclone, almost elliptic in shape at day 1525. At day 1529 a filament of low PV gets pulled out of the bulk-PV region. The filament then rolls up and breaks off, forming an isolated anticyclone which gets advected eastward by the mean zonal wind of the background state. A second such event can be seen between days 1533 and 1535. This behaviour is very similar to the mechanism with which Dethof et al. [1999] explained the occurrence of observed eastward propagating features in the monsoon anticyclone (see subsection 3.1.3).

Figure 4.13 shows the time evolution of the PV field along the 330K/20° latitude line. Pronounced patches of low PV are being shed from the source region and propagate eastward for more than 100° (about 10 000km). The eddies then seem to dissipate, possibly due to the turbulent background.

The propagation of the shed eddies seems almost steady with a velocity of about $10ms$, which is very close to the difference of the intrinsic speed of westward shed eddies (estimated as $\approx 12m/s$, see figure 3.21) and the wind speed of the mean eastward background flow at 13km and 30° latitude ($\approx 20m/s$, see figure 4.7). This supports the idea of shed vortices being advected eastward by the background wind, in

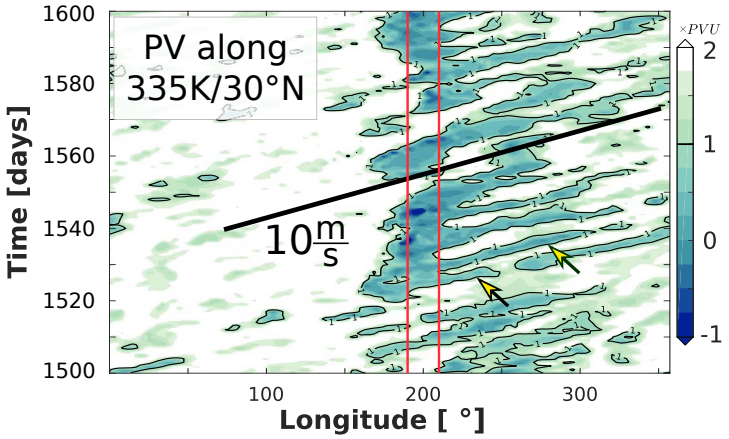

Fig. 4.13 Time evolution of PV for the case with $Q_0 = 10K/day$ and a symmetric HS state with $\Delta T = 60K$. Red vertical lines indicate the forcing region and the $1PVU$ contour is highlighted. The arrows indicate the shedding events shown in figure 4.12.

particular when considering the theoretical results for the propagation of vortices in a quasi-geostrophic single layer model derived in chapter 6. Based on the theory for the dynamics of the centre of mass of an eddy we found the propagation of circular vortices to be modified by a simple background flow with constant shear according to the wind speed at the centre of the eddy (see equations 6.30 and 6.31).

The nature of time dependence of the response changes as we gradually increase the meridional temperature gradient of the basic state. Figure 4.14 shows the time evolution along the latitude lines through the centre and at the northern edge of the forcing region for a range of values of ΔT. In the case where the basic state is at rest ($\Delta T = 0K$) we find pronounced westward shedding of vortices from the forcing region. The vortices subsequently propagate westward along the 20° latitude line, as described in subsection 3.2.3. We do not find any strong signal at 30°. In the case with strong background winds ($\Delta T = 60K$), on the other hand, almost no evidence for westward shedding can be seen, but we find clear eastward propagating features. These eastward shed eddies have pronounced PV signatures at 30°, suggesting them to also be caused be filaments being pulled out to the north-east of the forcing region by baroclinic eddies and then being advected by the background wind.

The changes in shedding behaviour seem to be caused by the increased strength of the basic state flow as ΔT increases. It requires a certain strength of both, the baroclinic eddies and the mean jet wind speed, to support the eastward shedding mechanism described earlier.

A slightly different kind of behaviour seems to be happening for a weakly baroclinic background state ($\Delta T = 10K$). As can be seen in figure 4.14 a bulk anticyclone forms at 20° latitude and between about 100° and 200° longitude. There is no pronounced time variation of preferred direction of propagation obvious and the response seems almost steady. However, to the north of the forcing region, at 30°, patches of anomaly seem to appear to the west of the forcing region and propagate eastwards towards it. In the following paragraphs we will discuss the phenomenon in more detail.

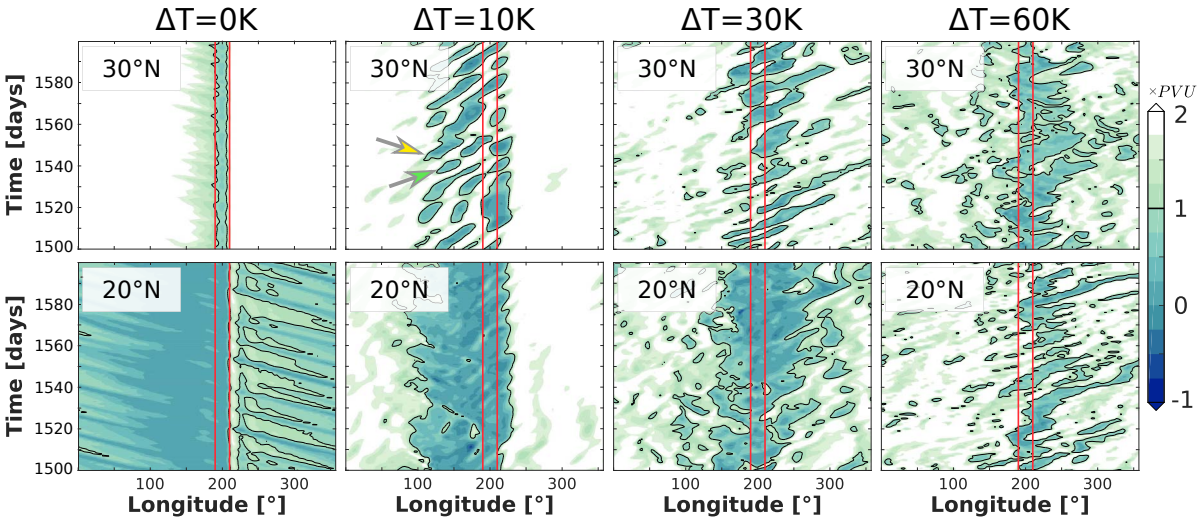

Fig. 4.14 Time evolution of PV along two latitude lines on the the $340K$ (left two panels) and $335K$ (right two panels) isentropes. The forcing magnitude is $Q_0 = 5K/day$ and the basic state uses $\tau_{asym} = 0K$ and various values of ΔT. Red vertical lines indicate the forcing region and the $1PVU$ contour is highlighted. Arrows indicate the events shown in figure 4.15.

Figure 4.15 shows how the PV field on the 340K isentropic surface evolves between days 1542 and 1550 for a background state with $\Delta T = 10K$. The arrows show the position of two pronounced baroclinic eddies forming a wave-like structure on the jet PV gradient. As the eddies move eastward, they start to interact with the PV minimum of the anticyclone. The meridional winds associated with the horizontal gradients in PV pull up low PV of the anticyclone on one side and advect heigh-value PV southward on the other. A potential dynamic interaction of the monsoon anticyclone could then further intensify this baroclinic wave structure. The process leads to the emergence at 100° longitude and subsequent eastward propagation of coherent PV anomaly structures that can be seen at 30° latitude in figure 4.14 for the $\Delta T = 10K$ case.

Amemiya and Sato [2018] observed a similar phenomenon in a steadily forced single-layer model with meridionally varying mean depth, inducing a westerly mean wind. They describe a westward shedding of eddies followed by a "circling back" of shed vortices towards the forcing region. The phenomena presented in figures 4.14 and 4.15 for $\Delta T = 10K$ is potentially the same as the described "circling back". It is not clear if the process is completely induced by internal dynamics of the anticyclone or if external wave perturbation (by the baroclinic eddies) play a role. While there appears to be a correspondence between incoming wave structures on the jet (yellow arrows in figure 4.15) and pronounced wave modulations of the northern anticyclone edge, Amemiya and Sato [2018] performed their experiments in a model without explicit time dependence. However, it is possible that the combination of strong westerlies of the mid-latitude jet and the northern part of the anticyclone form a sort of wave-guide, as pointed out by Enomoto et al. [2003], which additionally favours certain waves and hence leads to a stronger modulation of the PV field.

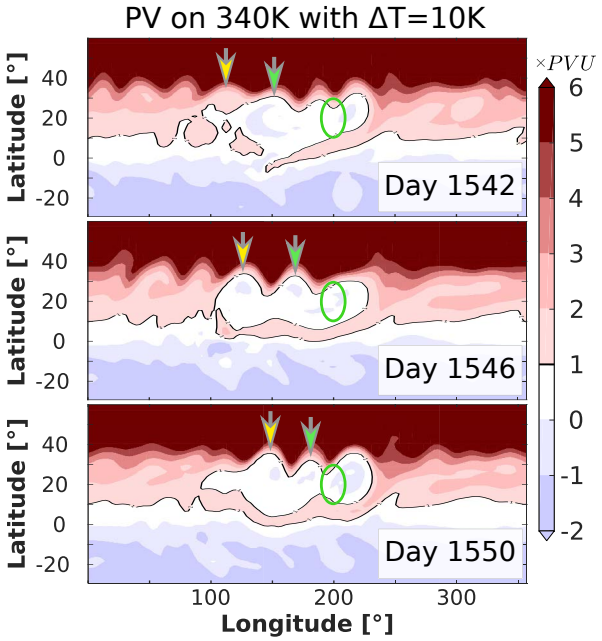

Fig. 4.15 Snapshots of PV at $340K$ for a forcing with $Q_0 = 5K/day$ and a symmetric basic state with $\Delta T = 10K$. Green ellipses indicate the forcing region and the $1PVU$ contour is emphasised. The arrows illustrate the position of different wave structures on the sharp PV gradient associated with the jet stream.

Since the phenomenon modulates the northern edge of the anticyclone it creates a north-south asymmetry of the PV minimum in the form of a wavy northern edge and an only weakly perturbed southern edge. We find similar modulations of the northern edge in PV fields of re-analysis datasets. For example the time mean PV structure in figure 3.8 or the anticyclone just before a westward shedding event on July 15th in figure 3.10.

Various authors have suggested the existence of a bi-modality with east- or westward displaced monsoon centres or the occurrence of a "split-state" of the Asian monsoon anticyclone, with two pronounced zonally separated PV maxima (e.g. Zhang et al. [2002] and Vogel et al. [2015]). Although the modulations of the PV low of the anticyclone by baroclinic eddies in figure 4.15 do produce pronounced and zonally separated PV minima on certain latitudes, it is not clear if this mechanism can explain the time and lengths scales observed during the mentioned split-phases. Nützel et al. [2016] investigate re-analysis data from multiple sources on daily to seasonal time scales and found that only one out of seven analysed re-analysis data sets (NCEP-1) shows pronounced signs of bi-modality. This could suggest that any observed bi-modality in temporally averaged or composite fields is an artefact of a phenomenon similar to what is shown in figure 4.15 or was described by Amemiya and Sato [2018].

We do also observe east- and westward shedding behaviour in experiments with an hemispherically asymmetric basic state, i.e. when choosing $\tau_{asym} = 20K$ in equation 4.1. Figure 4.16 shows the time evolution of PV along two latitude lines on the 335K isentrope. Clear evidence for both, westward

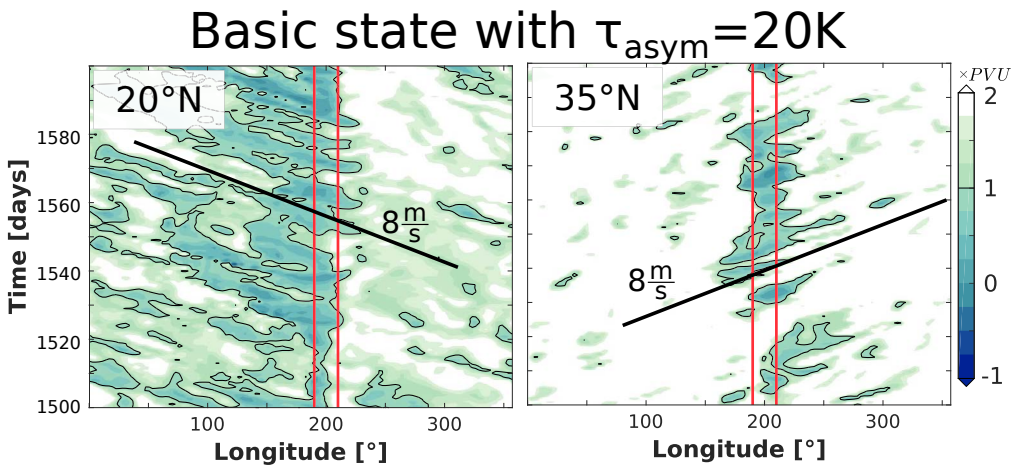

Fig. 4.16 Time evolution of PV along two latitudes on the $335K$ isentrope in an asymmetric HS setting with $\Delta T = 60K$. The forcing magnitude is $Q_0 = 5K/day$. Red vertical lines indicate the extent of the forcing, the $1PVU$ contour is highlighted.

shedding at the latitudes of the forcing region and eastward shedding north of it, is visible. The meridional shift of the two phenomena can be explained by the centre of the westerly mid-latitude jet north of the forcing region at about 40° latitude. The eastward shedding process requires the zonal winds of the jet to advect vortices eastward, while westward shedding can only occur in regions with weak eastward winds.

Westward shedding seems to occur much more frequently (than eastward shedding) in the system and the vortices travel much farther. The frequency for westward shedding seemed to have decreased slightly compared to the experiments in a resting atmosphere in section 3.2.3. Figure 4.16 would suggest a time scale of about 10-20 days per event, which is very close to the roughly bi-weekly shedding seen in observations and re-analyses (e.g. figure 3.9). The decrease in frequency can likely be explained by the effect of the mean background wind. Experiments with a single-layer model performed in chapter 6 will show a decrease in shedding frequency when introducing a eastward mean background wind. As described for the symmetric cases in figure 4.14 the westward shedding also seems to happen mostly on the latitude of the forcing, while eastward shedding has a clear signature to the north of the forcing region. Both characteristics, the north-/southward shift of east-/westward shedding and the relatively more pronounced westward events, seem to be consistent with re-analysis data observations and our general understanding of these features [Popovic and Plumb 2001; Dethof et al. 1999].

A crucial aspect of relative importance of east-/westward shedding is potentially given by the strength and position of the mid-latitude jet relative to the forcing region. As explained, figure 4.14 shows a change from west- to eastward shedding as we increase ΔT in the symmetric HS state. This induces (among other things) a strengthening of the jet and baroclinic eddies, both features essential for the eastward shedding process. Hence we find the described transition. In the asymmetric HS case we find evidence for both types of shedding, although a clear dominance of westward shedding can be

seen. Figure 4.9 indicates generally weaker and pole-ward shifted jet for $\tau_{asym} = 20K$, compared to the symmetric case. This can potentially explain the weakening of the eastward shedding process with respect to the westward shedding.

4.2 The vertical structure of the monsoon

The importance of the Asian monsoon as major transport pathway from the troposphere into the stratosphere is well known [Garny and Randel 2016; Park et al. 2007; Garny and Randel 2013; Fadnavis et al. 2013; Randel et al. 2010; Bourassa et al. 2012; Bannister et al. 2004; James et al. 2008; Ploeger et al. 2013, 2017].

The slow, but steady, large scale up-draft of the monsoon circulation can lift tropospheric air parcels while the sharp horizontal potential vorticity (PV) gradients prevent them from mixing with surrounding air. Eventually the parcels are released at the upper level of the circulation as divergent outflow. The monsoon anticyclone can therefore be regarded as source region for e.g. trace gases, aerosols and water vapour. Since the circulation can penetrate the tropical and mid-latitude tropopause the monsoon provides a way for tropical moist air to avoid extreme freeze drying effects at the cold temperatures within the tropical tropopause layer (TTL) and hence form a substantial source for water vapour within the otherwise dry stratosphere [Bannister et al. 2004; Dethof et al. 1999; Gettelman et al. 2004a; James et al. 2008].

In a combination of model output and satellite observations Randel et al. [2010] identify vertical monsoon transport of HCN produced by biomass-burning at the surface intro the stratosphere. Bourassa et al. [2012] and Yu et al. [2017] linked increased aerosol amounts in the lower stratosphere to vertical advection of the monsoon. Correspondingly, Garny and Randel [2016] performed trajectory analysis and found a large fraction of particles released within the tropospheric part of the monsoon to reach the lower stratosphere within 60 days due to vertical advection by the monsoon circulation.

Fueglistaler et al. [2009a] showed that signatures of the monsoon circulation can be found in the July mean wind and temperature fields on levels up to about 7hPa (roughly corresponding to 18km or 425K in the tropics) and hence significantly above the tropopause. We found similar evidence of a JJA-mean circulation in form of a (rescaled) PV feature above the tropopause (see figures 3.6 and 3.8) in ERA-I data. It seems therefore likely that the circulation pattern of Asian monsoon anticyclone extends above the tropopause and into the lower stratosphere.

Many previous authors have focused on the horizontal structure of the monsoon anticyclone [Hoskins and Rodwell 1995; Hsu and Plumb 2000; Dethof et al. 1999]. However, the vertical structure of the monsoon (anticyclone) potentially plays critical role in determining its circulation and transport properties. We want to explore the processes and interactions that determine the vertical structure of the monsoon anticyclone (in PV and SF) and outline possible mechanisms that allow the monsoon

circulation to extent above the tropopause. In particular we are interested in how the position and extent of the anticyclone depend on the structure of the imposed heating and characteristics of the background state, like the vertical change of static stability at the tropopause. The study will be based on a simple analytic theory and numerical experiments performed with the simple GCM described in section 2.2. As in previous sections of this chapter, the monsoon circulation will be forced by a imposed steady and localised heating with distribution shown in equation 3.4. As unperturbed basic state of the system we will choose to follow the Held and Suarez (HS) configuration described in subsection 4.1.1. The aim is then to investigate the characteristics and modifications of the response as we vary certain parameters of the basic state (e.g. ΔT) and the imposed heating (z_{top}).

4.2.1 Vertical position and extent of the anticyclone

In order to analyse the vertical structure of the circulation we will use a similar approach as described in subsection 3.1.2 by defining a rescaled PV (see equation equation 3.2). Since in our numerical simulations we do have a well defined basic state, we will define the rescaling factor in terms of the vertical potential temperature gradient $\partial_z \Theta_0$ of the zonal mean basic state at 20° latitude and an idealised hydrostatic density profile $\rho_0 = e^{-z/H}$ for an atmosphere of scale height $H = 7km$. Note that this is a different definition of rescaled PV than was used in section 3.1.2, but follows the same general idea. The rescaling factor $\chi(\Theta)$ can therefore be expressed as a function of potential temperature Θ and the rescaled PV $\hat{q}$ can then be calculated from Ertel's PV via

$$\hat{q} = PV \frac{\rho_0}{\partial_z \Theta_0} = PV \; \chi(\Theta). \tag{4.2}$$

All potential vorticity profiles shown in this section will be given as rescaled PV and anomalies with averages and rescaling performed on isentropic surfaces, before (in some cases) being transformed into height coordinates (see the discussion to figure 3.4).

At first we want to investigate the influence of an increase in meridional temperature gradient of the background on the PV response. Figure 4.17 shows the change in the time mean structure of PV at the latitude of the forcing (20°) for various values of ΔT. The most obvious change is probably a decrease of the zonal length scale and magnitude of the response as ΔT increases. As discussed in subsection 4.1.2 the interaction with mid-latitude dynamics of a baroclinically unstable background has a localising effect on the forced anticyclone. In the cases with $\Delta T = 30K$ and $\Delta T = 60K$ in figure 4.17 we further find a pronounced anticyclonic PV feature to the east of the forcing and at about 330K . This feature is a signature of the eastward shedding process observed in these experiments and clearly visible e.g. in figure 4.14.

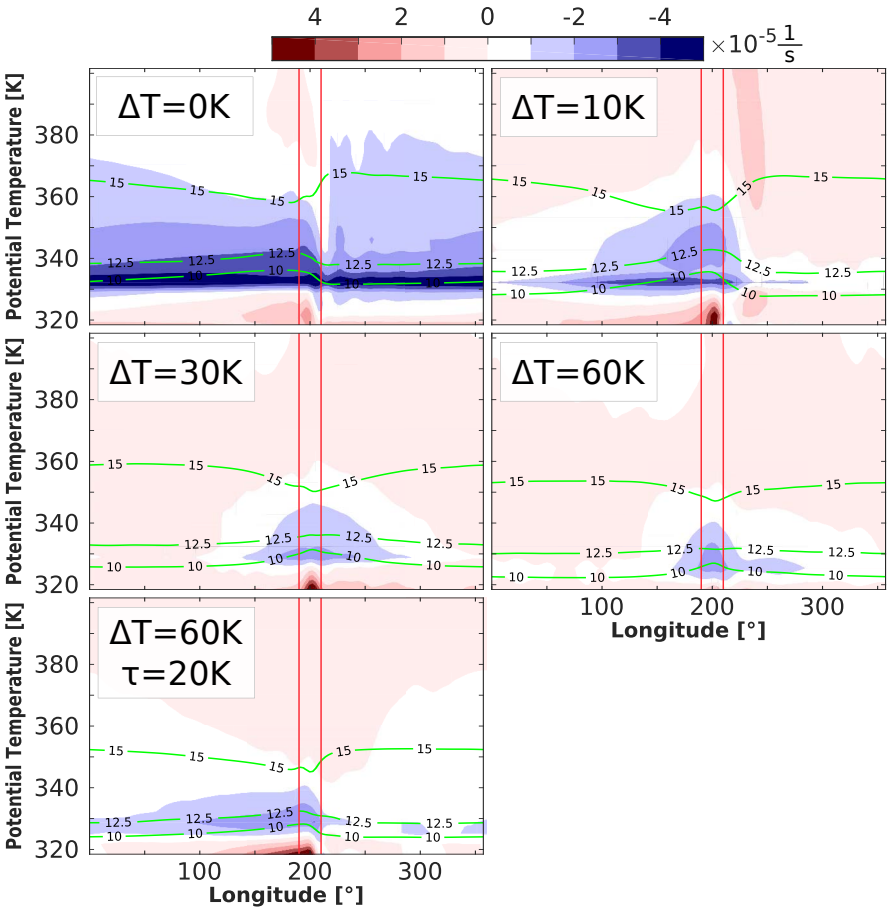

Fig. 4.17 Mean PV anomaly along 20° for a forcing with $Q_0 = 5K/day$ and various basic states. Bottom most plot uses an asymmetric HS basic state with $\tau_{asym} = 20K$, all other plots use $\tau_{asym} = 0K$. Green horizontal contours show height contours of 10,12.5 and 15km. Red vertical lines indicate the extent of the forcing region.

The green contours in figure 4.17 indicate the heights[1] of maximum heating ($z_{max} = 10km$), maximum negative vertical gradient of the heating ($z = 12.5km$) and the top of the heating ($z_{top} = 15km$). In all cases the bulk part of the response seems to be confined by the top of the heating. For small values of ΔT we find a penetration of the 15km contour by the mean PV response and hence an extension of the response above the heating. for larger values of ΔT, however, the response seems to be vertically more confined. In addition, we can observe a reduction in response magnitude as ΔT increases. Both phenomena, the reduction of vertical extent and the decrease in magnitude, can potentially be explained by the change in static stability profile of the basic state, and in particular a smoothing and raising of the tropopause (see also figure 4.3). The change in static stability as ΔT varies is illustrated in figure 4.18, while we will show how a smoothed tropopause affects the PV forcing in subsection 4.2.2 (in particular figure 4.23).

As a side note, one can observe a change in magnitude of the lower level cyclone, corresponding to a positive PV anomaly near 320K. The increase in magnitude is likely to be associated with an increase in static stability N^2 close to the surface for non-vanishing ΔT (see figure 4.18). The resulting negative gradient of N^2 can provide a positive PV forcing, as we will show later. Due to the general reduction in temperature of the basic state at low heights in the case of $\Delta T = 60K$ the cyclone drops below the 320K isentrope and is not visible in figure 4.17 (although it can be seen later in figure 4.25).

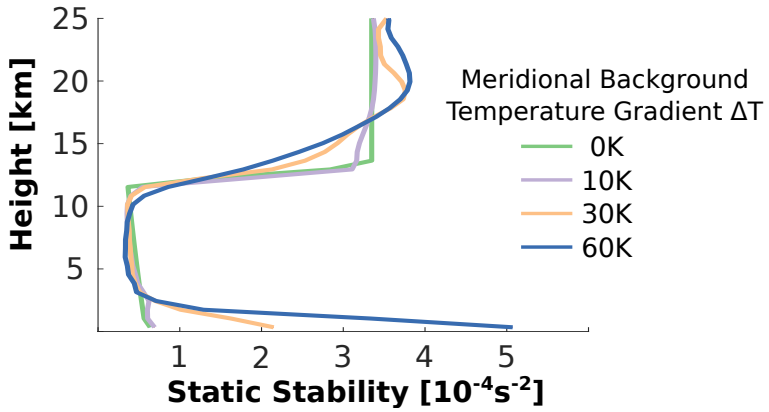

Fig. 4.18 Time and zonal mean static stability profile at 20° latitude for symmetric HS basic states with different values of meridional temperature gradient parameter ΔT.

We also find changes in the vertical structure of the streamfunction (SF) response as ΔT varies. Figure 4.19 shows the azonal part of the mean vertical SF profile in the centre of the forcing. The zonal mean was removed to exclude the effect of the anticyclone wrapping around the globe for $\Delta T = 0K$. The magnitude of the response corresponding to the $\Delta T = 0K$ state is therefore not directly comparable with the other cases. All the other SF profiles show a gradual decrease in magnitude of the anticyclone as the basic state becomes more baroclinic, similar to what is seen for the PV anomaly in figure 4.17.

[1] Recall that heights are calculated as hydrostatic log-sigma coordinates via equation 2.1.

This can potentially be explained by two points:

- As mentioned before, the changes in background static stability with ΔT can lead to a modification of the PV forcing for a specific heating heating and subsequently a decrease in the magnitude of the PV response, which can then correspond to a decrease in the SF response.
- For larger values of ΔT the basic state develops stronger baroclinic mid-latitude eddies. This can lead to an increased turbulent advection of anomaly our of the source region and hence reduce the response magnitude, in particular at the vertical levels where the baroclinic eddies are strong (roughly 10km, see figure 4.6).

The vertical position and extent of the anticyclone, however, does not change significantly. In all cases presented in figure 4.19 the circulation clearly extends above the range of the heating profile ($z_{top} = 15km$). Also note, that the SF anomaly corresponding to the low level cyclone does not show significant changes between all cases with $\Delta T > 0$.

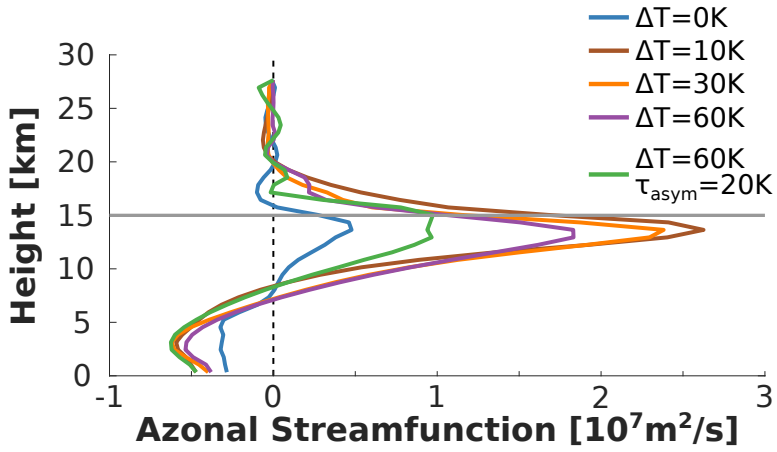

Fig. 4.19 Mean streamfunction anomaly at 20° latitude and 200° longitude and with zonal mean removed for a forcing with magnitude $Q_0 = 5K/day$ and HS basic states with various meridional temperature gradient parameters ΔT. Green curve uses an asymmetry parameter $\tau_{asym} = 20K$, all other curves use $\tau_{asym} = 0K$. Horizontal grey line indicates the top of the explicit heating at $z_{top} = 15km$.

In the next subsection we will study the influence of certain characteristics of the heating and the basic state on the PV forcing and hence try to explain the observed model response shown in figure 4.17 and 4.19. This will in particular involve the influence of the sharpness of the tropopause and its position relative to the top branch of the heating distribution.

4.2.2 The influence of the tropopause on the PV forcing

We now want to use the GCM to further investigate the vertical structure and the structural dependencies of the response to a localised heating. In general, since the monsoon circulation in our model is driven

solely by an imposed heating, different heating distributions should result in different vertical profiles of the anticyclone, including a potential change in extent and position. To test this hypothesis we performed a series of experiments using the same baroclinically unstable basic state and imposed a heating distribution with a variety of vertical profiles. In all of the experiments we kept the region of negative vertical heating gradient constant (i.e. $z_{top} - z_{max} = 5km$ in all cases) and only changed the vertical position of the region, specified by the top of the heating z_{top}.

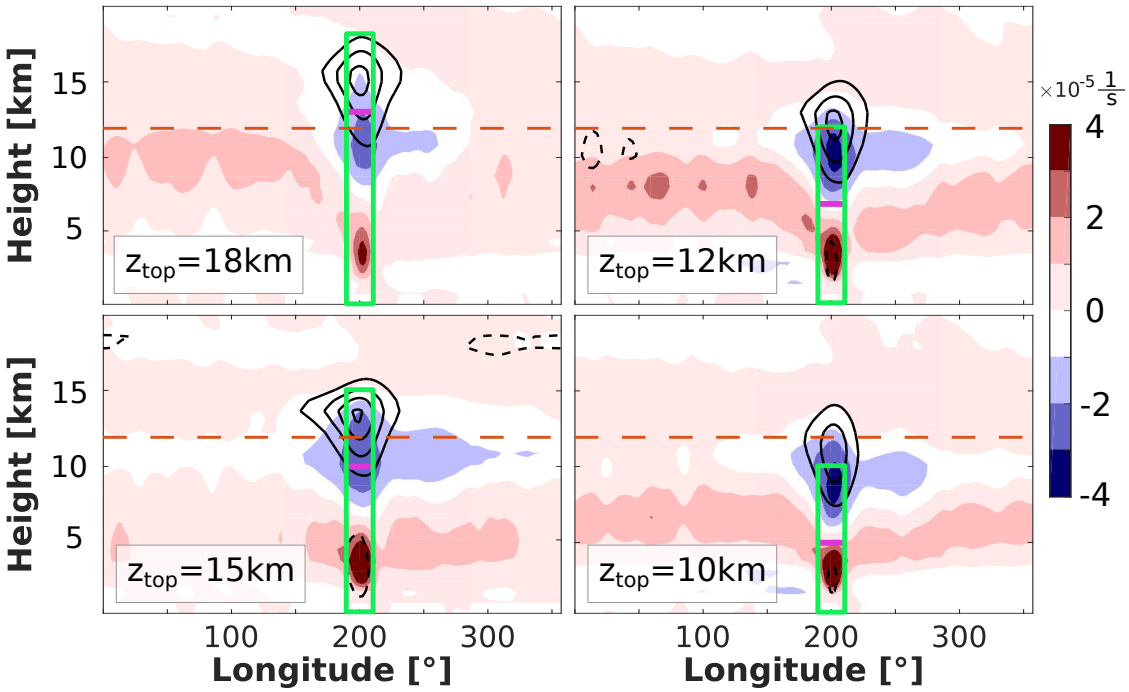

Fig. 4.20 Mean PV (shading) and SF (contour) anomaly along 20° latitude for a basic state with $\Delta T = 60K$ and a forcing with $Q_0 = 5K/day$. The forcing uses various values of maximum height z_{max} and top z_{top}, keeping the difference constant at $z_{top} - z_{max} = 5km$. Contour interval of the SF is $5 \cdot 10^6 m^2/s$, negative contours are dashed, and the zero contour is not shown. Green rectangle shows extent of the heating distribution with the pink line indicating the height of maximum heating z_{max}, i.e. the vertical heating gradient is positive below and negative above the pink line. The dashed orange line indicates a height of 12km.

Figure 4.20 shows the corresponding results in form of the temporally averaged PV and SF fields along 20° latitude. The green box represents the extent of the heating, with the height of maximum heating indicated by the horizontal pink line. As can be seen, a clear anticyclone in the form of a localised region of negative PV anomaly and positive SF anomaly is present in all cases. The strength of the response does not seem to decrease marginally for taller heating distributions. We can also identify a low PV feature at about 10km and to the east of the forcing region. As explained for figure 4.17 this feature corresponds to eastward shedding events.

The vertical position and extent of the PV and SF anomaly extrema varies relatively little (compared to the changes in z_{max} and z_{top}) with the change in vertical heating profile.

In particular the following observations can be made:

- In the case of $z_{top} = 10km$ the heating is entirely confined within the troposphere. In this case the response does significantly extend above the heating and up to a height between 13 and 15km. The height of strongest PV response is located at the top of the heating while the SF response maximises above.
- As we raise the heating to $z_{top} = 15km$ the SF and PV extrema can both be found within the upper branch of the heating. The negative PV response vanishes at the top of the heating, but does now extend below the maximum of the heating, into the region of positive vertical heating gradient.
- The trend continues as the heating is raised to $z_{top} = 18km$, showing a pronounced penetration of the response into the lower branch of the heating, i.e. below z_{max}, while the top is given by z_{top}.

We will later come back to these observations and will try to explain some of the features seen in figure 4.20 with the help of a simple theory for the PV forcing. In particular we are interested in the processes and mechanisms that allow the response to extend out of the region of negative vertical heating gradient, i.e. above the green box for $z_{top} = 10km$ and below the pink line in the case with $z_{top} = 18km$.

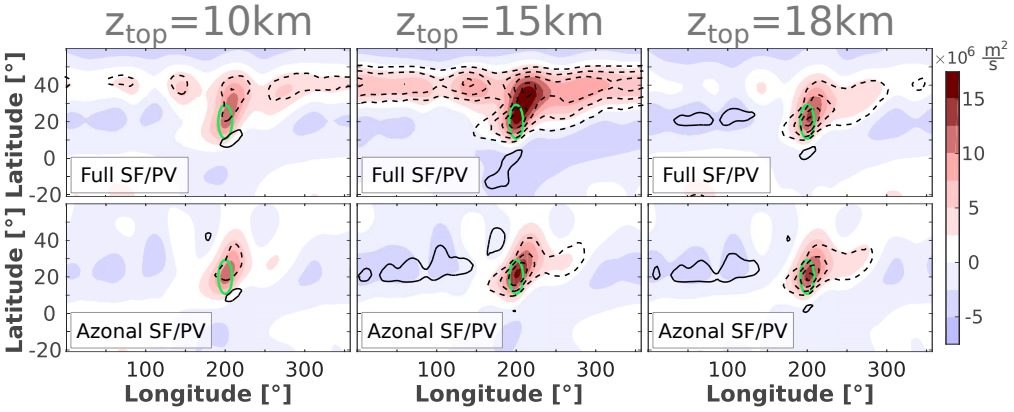

Fig. 4.21 Shading: Streamfunction (top) and deviation from zonal mean (bottom) at 12km, corresponding to the dashed line in figure 4.20. Contour: the corresponding PV field on 330K, interval is $5 \cdot 10^{-6} s^{-1}$ and the zero contour is not shown. The basic state uses $\Delta T = 60K$ and the forcing has $Q_0 = 5K/day$. The three horizontal panels correspond to forcing distributions with different values of the height of maximum heating z_{max} and heating top z_{top}. The range $z_{max} - z_{top} = 5km$ is kept constant in all three cases. Green ellipses show the heating regions. Note that the usage of shading/contours for the shown fields is opposite to that in figure 4.20.

To obtain an idea of the horizontal structure of these extending features we plotted the SF and PV response at 12km and 330K, respectively, in figure 4.21. The top panel shows the full horizontal response for three different vertical heating profiles while the bottom plot shows the azonal part only.

There are again several observations that can be made:

- The full response shows a zonally elongated structure in all three cases, mostly visible in the SF response. This structure corresponds to an annular mode response of the mid-latitude jet of

the basic state, as explained in subsection 4.1.2. The jet-response is strongest for a heating with $z_{top} = 15$, since it maximises roughly at the height of the jet at $z_{max} = 10km$ (see figure 4.2). Since the annular mode is mostly zonally symmetric it is not visible in the azonal part.

- A localised anticyclone, i.e. positive SF and negative PV anomalies, mostly confined to the forcing region (green ellipse). The general shape of the response is almost identical in all three cases. The slightly weaker magnitude of the $z_{top} = 10km$ case is due to the 12km surface being at the top of the anticyclone response (see dashed line in figure 4.20).
- We again find an indication of eastward eddy shedding in the form of a north-eastward extension of the PF and SF responses in all three cases. The northward shift is due to the the centre of the jet being located at around 40°. Correspondingly we find a slight westward extension of the response at the southern edge of the response. This is a signature of westward shedding, which preferably happens at the latitudes of the forcing or south of it, in order to avoid the strong westward winds of the jet (see figure 4.16 and subsection 5.1).

Next we are going to identify potential processes that can modify the vertical structure of the response to an imposed heating. To do so we will make use of a simple analytic model of PV forcing. We want to consider the linear dynamical evolution of the quasi-geostrophic (QG) potential vorticity q. For simplicity we will apply an f-plane approximation to the system and hence not account for modifications due to the intrinsic dynamics of the response, i.e. the "β-effect" of a spherical earth. We can expect the use of quasi-geostrophic theory on a f-plane and the linearity of the dynamics to give good approximations of the response during early times and for weak forcing magnitudes. Both requirements are in particular fulfilled during the switch-on period of the heating, when the forcing, and hence response, is still weak and time scales are short compared to β/r_0, i.e. the ratio of meridional background PV gradient and horizontal length scale of the forcing.

We can now formulate a theory for the response to a heating Q. Since we are restricting ourselves to early times and weak anomalies we can expect the Newtonian cooling part of the diabatic heating to be small, especially for large damping times δ^{-1} we find $|\delta T'| \ll Q$. Correspondingly the following numerical "early-time-experiments" will be performed without any Newtonian cooling. In an atmosphere at rest the evolution of the system can then be described by the single equation

$$\partial_t q = \frac{fR}{H\rho_0}\partial_z\left[\frac{\rho_0 Q}{N^2}\right], \tag{4.3}$$

where $\rho_0 = e^{-z/H}$ is the normalised hydrostatic density of the basic state with scale height $H = 7km$ and the static stability is described by the squared buoyancy frequency and can be calculated from the temperature profile of the basic state T_0 via

$$N^2 = \frac{R}{H}\left(\frac{RT_0}{Hc_p} + \partial_z T_0\right). \tag{4.4}$$

The symbols $R \approx 287 JKg/K$ and $c_p \approx 1004 JKg/K$ represent the specific gas constant of dry air and its specific heat capacity for constant pressure. Integrating equation 4.3 over time will then give us a prediction formula for the potential vorticity reading

$$q = \frac{fR}{H\rho_0}\partial_z\left[\frac{\rho_0 \bar{Q}}{N^2}\right], \tag{4.5}$$

where the integrated heating is given by $\bar{Q}(x,y,z,t) = \int_0^t \mathrm{d}t'\ Q(x,y,z,t'))$. As can be seen the vertical profile of the PV prediction q is fully determined by the vertical heating distribution Q and the static stability profile $N^2$of the background state. We can think of the right-hand side of equation 4.5 as consisting of two terms: one proportional to $\left(\rho_0 \partial_z \bar{Q}\right)/N^2$ and one proportional to $\bar{Q}\partial_z\left(\rho_0/N^2\right)$.

As a consequence, there are essentially two interesting cases to distinguish, for which equation 4.5 gives contributions to the PV forcing: we can either have or not have an overlap of the imposed forcing with the sharp jump in static stability at the tropopause. In the latter case the PV response at early times will be mostly determined by the term involving the derivative of the heating profile, divided by the almost constant tropospheric static stability. The term involving the derivative of N^2 will be insignificant. If the imposed heating, on the other hand, does intersect with the tropopause, the PV forcing equation receives a second contribution due to the static stability gradient term. This will possibly lead to an increase (or an additional peak) in PV forcing at the tropopause height, depending on the precise heating profile. The corresponding PV forcing profile might then explain certain features of the PV response of the system.

We can now compare the PV anomaly output of our GCM experiments (forced with different vertical heating profiles) with the predicted vertical structure of the PV response according to the quasi-geostrophic theory presented in equation 4.5. All extracted PV profiles correspond to the model response at the first day of the smooth switch on period[1], as described in subsection 3.2.2.

The left panel in figure 4.22 shows a comparison of vertical QG-PV profiles predicted by equation 4.5 and the PV anomaly output according to equation 4.2 at the centre of the heating for the first day of the corresponding GCM experiment (a comparison of the PV forcing with the time mean PV structures of figure 4.20 will be shown later). The right panel shows the vertical structure of the heating distribution and the static stability profile (calculated using equation 4.4) of the corresponding basic state. The experiments are labelled according to the height z_{top} of the top of the corresponding heating distribution.

[1]This gives a maximum of $\bar{Q} = 7.13 \cdot 10^{-3} K$ in the centre of the forcing for a heating magnitude of $5K/day$.

The size of the region of negative vertical heating gradient is kept constant at $z_{top} - zmax = 5km$, similar to the experiments shown in figure 4.20.

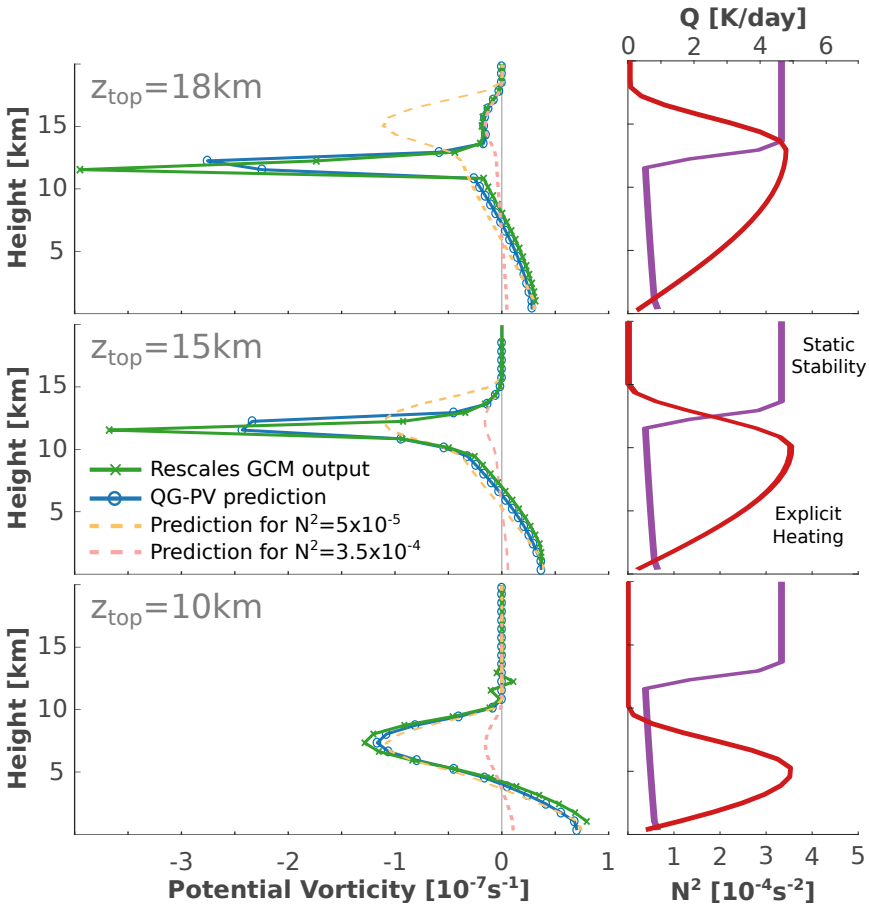

Fig. 4.22 Left: vertical profiles of PV predicted according to the PV forcing shown in equation 4.5 and PV anomaly at 20° latitude, 200° longitude as observed at day one of the switch-on period in GCM experiments with the UHS basic state. Right: basic state static stability and explicit heating profiles for three experiments with forcing magnitude $Q_0 = 5K/day$. The three rows use forcing distributions with values of z_{max}/z_{top} being $5km/10km$, $10km/15km$ and $13km/18km$, respectively. Dashed lines give predictions for constant values of static stability chosen close to the tropospheric/stratospheric values used in the simulation.

Results for three different heating distributions are illustrated in figure 4.22. The bottom panel shows a case where the explicit heating vanishes above $z_{top} = 10km$, while the tropopause is located at a height of about $12.5km$. The resulting PV anomaly is (relatively) weak and follows the vertical derivative of the heating, i.e. in particular it maximises at the height where the vertical heating gradient is largest $(0.5(z_{top} + z_{max}) = 7.5km)$. The yellow dashed line gives the predicted PV anomaly for theoretical case with constant static stability of $N^2 = 5 \cdot 10^{-5}$, which is close to the value in the troposphere of our simulations. As expected the PV response can be mostly explained by the contribution of the term involving the vertical gradient of the heating in equation 4.5. Since the PV response does not exten above the top of the imposed heating distribution the vertical structure of the time mean response to a

purely tropospheric forcing in a baroclinic background (shown in the bottom right plot in figure 4.20) is not simply set by the vertical profile of the PV forcing, but aspects of the dynamical response also seem be important. We will discuss a corresponding example of a feedback of the forced temperature anomaly on the PV forcing later and investigate its potential role in determining the vertical structure of the PV response.

The middle panel of figure 4.22 illustrates a case with a certain overlap of heating and tropopause. The corresponding response is significantly stronger than when assuming a constant value of N^2 corresponding to either the troposphere or stratosphere (dashed lines). Since in this case the vertical locations of the tropopause and maximum negative vertical heating gradient are both at about $12.5km$, this is the height where the response peaks. In the top panel one can see a third case. This time the maximum in negative vertical heating gradient is located at $15.5km$, but we find the response to be strongest at the height of the tropopause. The response magnitude is very similar to the middle case, which is due to a rough cancellation of the reduction in PV forcing due to a reduced vertical heating gradient at that height, but an increase in forcing due to the gradient in static stability multiplied by a stronger heating. We can also see a gradual decrease in strength of PV anomaly associated with the lower-level cyclone as we increase z_{max} and z_{top}, which is likely to be explained by a reduction in vertical heating gradient near the surface.

It should be noted that, although the profiles presented in figure 4.22 are shown in height coordinates, it is crucial that the corresponding PV anomaly extracted from the GCM output is calculated in isentropic coordinates, as explained in section 3.1.2 and demonstrated in figure 3.4. The result is then interpolated onto a height scale. Further, the calculation of vertical gradient in combination with the sharp gradients of the tropopause can lead to numerical problems, like the spurious oscillation that can be seen in the green curve of the bottom left plot in figure 4.22 at about 12km. In a similar fashion, one should be cautious when interpreting the magnitude of the PV extremum of the PV anomaly profiles in the left top and middle plots of figure 4.22, also caused by the sharp increase in static stability. Subtle modifications arising from the discretisation and numerical analysis can potentially alter the exact value of these peaks and hence explain the over-estimation of the PV-minimum in the two cases where the heating intersects the tropopause. However, the good agreement of both, the extracted PV distributions and corresponding QG-PV predictions, gives confidence that the practical computation of the presented profiles does not unreasonably skew the results of the analysis.

The results shown in figure 4.20 indicate that the early time PV response of the GCM to a localised heating in an atmosphere at rest can partly be explained by a simple, linear QG-PV theory. This theory predicts, among other things, a strong contribution to the PV forcing, and hence a strong signal in the PV field, at the heights of the tropopause in cases where the heating and the tropopause intersect. It also suggests rather small differences in PV forcing and response between the two cases with $z_{top} = 15km$ and $z_{top} = 18km$. The PV response of the numerical simulation will be compared to the predicted QG-PV forcing in 4.25 for different vertical heating profiles.

The process described above might therefore be an explanation for the downwards extension of the PV response below the height of maximum heating in the cases shown in the two left plots of figure 4.20. However, it does not predict an upwards extension of the response above the top of the heating, like it can be seen in the corresponding right two plots. According to the simple theory presented here, a contribution to the PV forcing by a change in static stability can only be given for a locally non-vanishing heating. Hence the process cannot explain a PV forcing in a region with $Q = 0$.

Since the sharp increase in static stability at the tropopause seem to significantly alter the structure of the PV response we want to investigate the sensitivity of the PV forcing on the smoothness of the static stability transition. This might be of particular interest since we have seen in figure 4.18 that the mid-latitude eddies of the baroclinically unstable Held and Suarez (HS) profile (see subsection 4.1.1) can smoothen the tropopause. A smoother tropopause will then lead to an altered PV forcing according to equation 4.5 and hence an altered PV response.

For simplicity we want to to perform the corresponding experiments in a baroclinically stable atmosphere. Hence we will use a horizontally symmetric basic state similar to the (horizontally) uniform Held and Suarez (UHS) profile described in subsection 3.2.2. To still obtain a smoother tropopause we will present a smoothing scheme, enabling us to define a smoothed UHS profile with a transition from troposphere to stratosphere is given by a more graduate change in static stability. This concept could correspond to the idea of a tropopause layer with finite vertical extent instead of a sharp tropopause (see e.g. Fueglistaler et al. [2009a]).

The smoothed UHS profile is defined based on an non-modified vertical UHS temperature profile $T_0(z)$ ranging from bottom at height z_b to the model top at z_t. We smooth the function around a discontinuity at z_0 between the heights $z_1 = z_0(1-s)$ and $z_2 = z_0 + s(z_t - z_0)$, where $s \in [0,1]$ is a parameter setting the smoothness of the final profile. The final smooth profile T_{smooth} is given via the piecewise definition

$$T_{smooth} = \begin{cases} T_s & \text{for } z_1 < z < z_2 T_0 \\ \text{otherwise,} \end{cases} \tag{4.6}$$

where T_s is a 3^{rd} order polynomial constructed by application of the boundary conditions (continuity and differentiability):

$$\begin{aligned} T_s(z_1) &= T_0(z_1), \\ T_s(z_2) &= T_0(z_2), \\ \partial_z T_s(z_1) &= \partial_z T_0(z_1), \\ \partial_z T_s(z_2) &= \partial_z T_0(z_2). \end{aligned} \tag{4.7}$$

We performed a range of numerical experiments with the simple GCM imposing T_{smooth} as initial vertical temperature profile (without any Newtonian cooling). Figure 4.23 shows the PV anomaly response for three experiments with different values of the smoothing parameter s and therefore different levels of tropopause smoothness. The imposed heating uses $z_{max} = 10km/z_{top} = 15km$ and a magnitude of $Q_0 = 5K/day$. Solid lines give the early-time PV response, while dashed lines show the response predicted by the QG-PV forcing theory presented in equation 4.5.

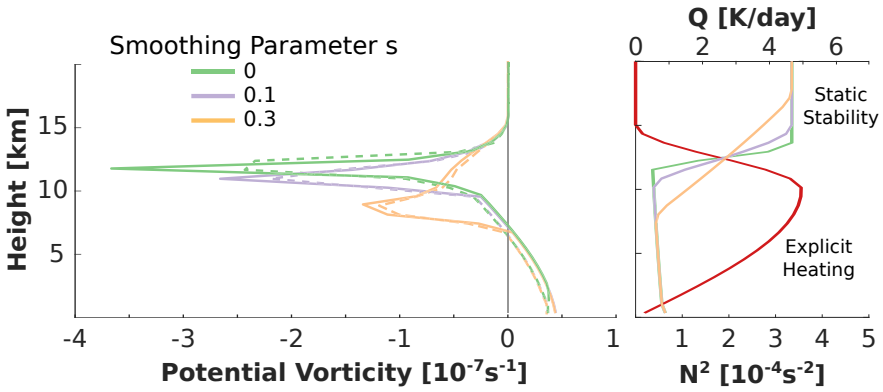

Fig. 4.23 Vertical profiles of mean PV at 20° latitude and 200° longitude (left), as well as static stability and explicit heating profiles (right), for experiments with forcing parameters $Q_0 = 5K/day$, $z_{max} = 10km$ and $z_{top} = 15km$. The PV anomalies extracted from GCM runs are based on the PV at day 1 and rescaled according to equation 4.2. The basic state uses $\Delta T = 0K$ and various smoothing parameters s. Dashed lines show PV predictions according to the quasi-geostrophic theory shown in equation 4.5.

All three cases show a very good agreement between the GCM output and the prediction according to the QG-PV forcing theory. A clear reduction in magnitude of the PV response is visible for smoother static stability profiles. The reduction in PV anomaly is likely to be accompanied by a reduction in circulation strength and hence SF, giving potential explanations for the reduction in SF and PV response with increasing ΔT shown in figures 4.17 and 4.19.

As explained, an interaction of the imposed heating with the abrupt change in static stability at the tropopause can only explain the downward extension of the PV response below the level of maximum heating for the cases with $z_{top} = 15km$ and $z_{top} = 18km$ in figure 4.20, but not the upward extension of the response above the heating distribution in the other two cases. Aspects of the dynamic response have to play a role in determining the vertical structure of the circulation. We therefore want to review another process that could potentially influence the vertical extent of the PV response. The process is based on simple quasi-geostrophic principles and results described by Haynes and Ward [1993], who investigated the deepening of vertically localised PV structures due to Newtonian relaxation. The general idea is that the non-local relationship between PV and SF leads to an anticyclonic circulation and a negative temperature anomaly extending above a given anticyclonic PV feature. If the system is subject to Newtonian cooling, the vertically extended temperature anomaly causes a heating and a PV forcing above the original PV anomaly.

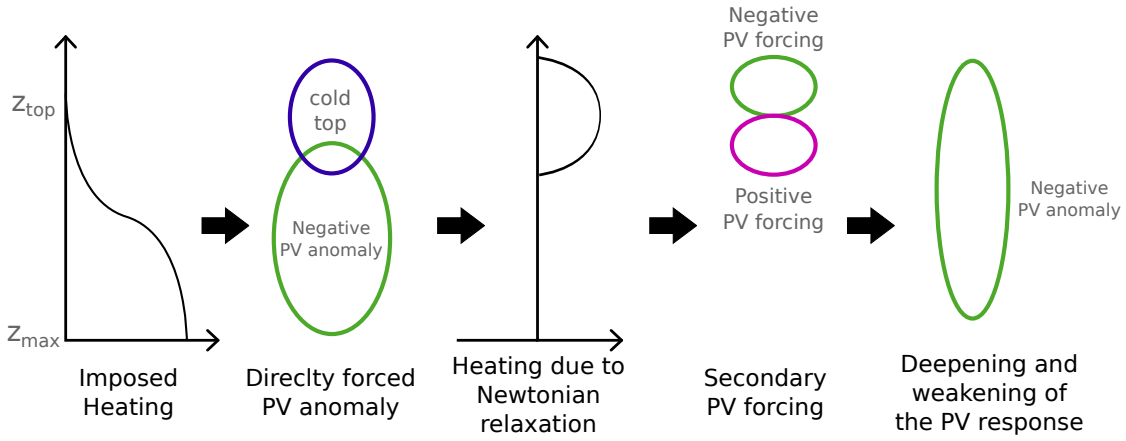

Fig. 4.24 Schematic illustration of the mechanism that can lead to a deep PV anomaly because of Newtonian cooling processes.

Figure 4.24 illustrates the process as a sequence of five steps:

- At first we impose a steady heating
- Following equation 4.3 the heating will create a PV anomaly confined to the region of negative vertical heating gradient. In addition to the PV anomaly, the heating will cause a negative temperature anomaly at its top. The cold top is a result of a re-organisation of the system in order to minimise pressure gradients and extents above the imposed heating and hence above the PV anomaly.
- Due to the Newtonian relaxation of the system the negative temperature anomaly will lead to an additional positive heating contribution at the top of the forcing.
- The Newtonian cooling will create a secondary PV forcing, with positive forcing at the bottom of the cold top, i.e. in the region of the negative PV anomaly, and negative PV forcing at the top of the cold top, and thus above the originally imposed heating.
- As a result, the negative PV anomaly will weaken in magnitude and deepen above the imposed heating.

The described mechanism might give an explanation for the upward extension of the response in the cases where the forcing uses $z_{top} = 10km$. Figure 4.25 illustrates the vertical time mean profiles at the centre of the heating of four different quantities (columns) and three heating distributions with different vertical extent (rows).

In the far lefts plot we can see the mean PV anomaly. A clear down/upward extension of the response beyond the region of negative vertical PV gradient (region between the green and purple solid lines) can be seen in all cases. The second column shows the PV forcing due to the imposed heating profile and according to equation 4.3. The third column shows the PV forcing according to equation 4.3 when

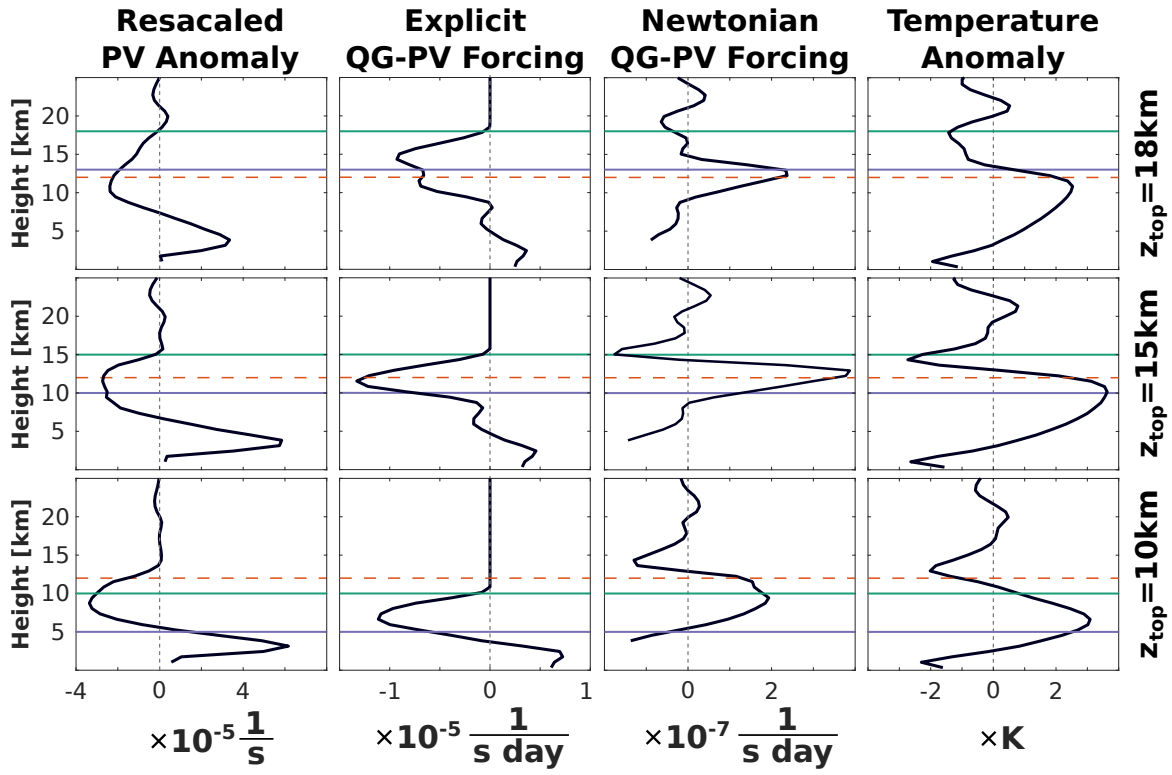

Fig. 4.25 Four different fields (columns) for imposed forcing functions according to equation 3.4 with $Q_0 = 5K/day$, different values of vertical heating extent z_{top} (rows) and a fixed extent of the region with negative vertical heating gradient $z_{top} - z_{max} = 5km$. The horizontal green and purple lines show z_{top} and z_{max}, the dashed orange line indicates 12km. Note the factor 100 magnitude difference between the second and third column.

choosing the heating as $Q = -\delta T'$, i.e. the Newtonian cooling caused by a temperature anomaly T'. And the far right plots show the mean temperature anomaly of the response. In all experiments a clear positive temperature anomaly directly caused by the imposed heating can be identified. It is centred around the height of maximum heating z_{max} (purple line). Further we find clear negative temperature anomalies (cold tops) above, with finite negative values above the top of the heating at z_{top} (green line).

For the experiments with $z_{top} = 15km$ and $z_{top} = 18km$ find a clear negative explicit PV forcing (directly caused by the imposed heating) at height below z_{max}. This negative forcing is explained by the interaction between heating and tropopause (as illustrated in figure 4.22) and explains the corresponding extension of the PV low below the region of negative vertical heating gradient.

In the case with $z_{top} = 10km$ the explicit PV forcing vanishes at the top of the heating and can hence not explain the extension of the PV response above the forcing region. We do find a clear negative temperature anomaly at about 13km (and thus above z_{top}) which, as illustrated in figure 4.24 does induce a negative PV forcing due to the corresponding Newtonian cooling. However, it seems like this secondary PV forcing can not explain the upwards extension of the PV response. This conclusion is based on two observations. First one should note that the magnitude of the Newtonian PV forcing is two orders of magnitude smaller than the explicit PV forcing, making it unlikely that the two processes cause PV anomalies of equal strength. Second the peak of the negative Newtonian PV forcing lies at about 15km, which is located clearly above the extent of the negative PV response. In fact the Newtonian PV forcing is positive between 10-12km (solid green and dashed orange lines), i.e. the region with the unexplained negative PV response. However, one should keep in mind that the Newtonian PV forcing profiles shown in figure 4.25 are based on the time mean temperature anomalies and hence do not capture transient effects that might be important.

4.3 Summary and discussion

In this chapter we introduced a comprehensive numerical model for the Asian monsoon anticyclone. The idealised model setting included a simple representation of mid-latitude dynamics and a monsoon circulation was explicitly forced by a steady, three-dimensional, confined heating. The response was then studied for a range of parameter combinations and various behaviours and characteristics have been observed. In particular we were able to reproduce a range of phenomena and scales identified in earlier chapters in relation with the monsoon anticyclone. Performing experiments with this comprehensive model we studied in particular three aspects of the circulation:

- The horizontal scale,
- the vertical structure
- and the time dependence of the response.

We have seen in subsection 4.1.2 that mid-latitude dynamics can have a localising effect on the response to a localised heating and thus reduce the zonal extent of the monsoon anticyclone. The interaction with baroclinic eddies and/or the mid-latitude jet leads to an anticyclone confined to the vicinity of the forcing region without the need of any strong mechanical friction as is the case in other models (e.g. the model presented by Matsuno [1966] and Gill [1980]).

Although it remains an open question which properties of the mid-latitude dynamics are in fact necessary to achieve the localisation and how the mid-latitude flow confines the response, the presented results give important insights into potential processes setting the zonal scales of the monsoon flow. The presented experiments could be used as a starting point for further investigations into the physical mechanisms involved. In that sense identifying the potential importance of mid-latitude dynamics for achieving a monsoon anticyclone response with realistic zonal scale could help to improve future attempts to study the monsoon circulation in idealised numerical settings.

We have further shown that a gradual change of basic state, from an atmosphere at rest to one including mid-latitude dynamics, can qualitatively alter the time dependence of the flow. The anticyclone transitions from a state exhibiting intrinsically caused westward shedding to a state dominated by eastward propagating vortices. This transition and the details of the flow depend on e.g. the position and strength of the mid-latitude jet and baroclinic eddies. As presented in section 3.1 re-analysis data shows the occurrence of both, west- and eastward shedding events, simultaneously. The results presented in this section indicate that it is indeed possible for the system to be in an intermediate state in which eddies are shed in both directions, e.g. when using a representation of mid-latitude dynamics close to the boreal summer-time configuration. The proposed model was able to transition from westward shedding to eastward shedding by only varying a single model parameter (the meridional temperature gradient of the basic state) and hence gives a convenient way to further study these phenomena and their interactions. It should also be noted that both types of temporal variability occur despite the use of only steady forcing and are generated entirely by the internal dynamics of the system. The resulting time and velocity scales are, however, generally in good agreement with observations.

Analysing the vertical structure of the model response we found that the signal of the anticyclone is much deeper than the corresponding heating, if the latter is confined to the troposphere. This is in agreement with re-analysis observations discussed earlier. As was shown, the deep anticyclone in these cases cannot be explained by steady quasi-geostrophic theory, in which the vertical extent of the response is confined to the heating region. The presented model setting, however, could be used as a starting point for further investigations into the topic and can potentially give insights into the mechanisms leading to penetration of the tropopause by the anticyclone in re-analysis data.

In experiments with a heating distribution that reaches deep into the stratosphere, on the other hand, the top of the heating sets the top of the response and no PV signal can be found above. In these cases, however, anticyclonic PV can be found below the height of maximum heating. We have shown that the corresponding PV features can potentially be explained by an interaction of the heating with the

tropopause and thus an increase in negative PV forcing in the upper troposphere. Although ERA-I data suggests the latent heating field to be confined to the troposphere (and thus make such a deep heating unlikely to be representative for the actual monsoon heating) these results give an important contribution to the general understanding of the behaviour of numerical models and additionally point out the fundamental importance of the tropopause for mid-atmospheric dynamical problems.

In conclusion we found a simple idealised model setting that shows a range of behaviours for various parameter combinations and is able to reproduce a range of characteristics observed in relation with the Asian monsoon anticyclone. Since the model therefore gives a comprehensive representation of the monsoon in a minimal setting it could in particular be used in future studies to gain even further insights into the controlling processes and mechanisms.

Chapter 5

Eddy shedding from a steady mass source in a single-layer model

The numerical experiments presented in chapter 3 showed the existence of two qualitatively different types of response in a three-dimensional numerical model[1] when forced by a steady and localised heat source with different magnitudes. While weak forcing magnitudes lead to a steady response in the form of a westward extended plume of potential vorticity (PV) anomaly and streamfunction (sometimes referred to as beta-plume), a strong heating causes a periodic creation and westward shedding of discrete eddy structures. Figure 5.1 illustrates again the two different states of the system, using the model described in section 2.2.

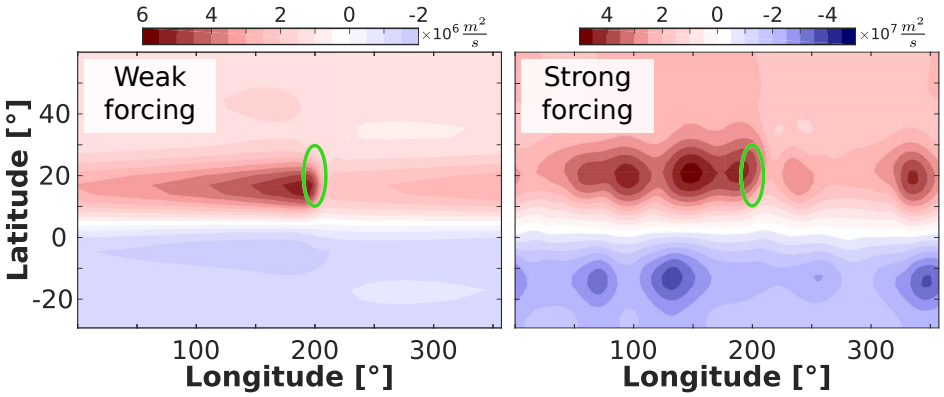

Fig. 5.1 Day 1525 streamfunction anomaly response at $13km$ for GCM experiments with the UHS basic state without stratospheric friction ($\delta_0 = 0$) and different a forcing with either a weak ($Q_0 = 0.5K/day$) or a strong ($Q_0 = 5K/day$) magnitude. The green ellipses indicate the forcing region. See section 2.2 for a description of the used model or chapter 3 for more information on the corresponding experiments.

Similar shedding phenomena have been observed in relation to the Asian monsoon anticyclone. Popovic and Plumb [2001] used re-analysis data and found a periodic occurrence of westward-propagating

[1] With resting basic state.

features originating from the monsoon region on the 370K isentrope. They also point out (less frequent) eastward moving structures. Garny and Randel [2013] also found observational evidence of westward (and eastward) shed eddies and additionally show a strong correlation between PV anomalies and chemical tracers, e.g. CO, leading to potentially significant implications for the time dependency of corresponding tracer fields and tracer transport. In a follow-up study using trajectory calculations, Garny and Randel [2016] showed how tracer particles can get caught inside the shed eddies as they propagate westward. Vogel et al. [2014] proposed a mechanism to explain enhanced tropospheric trace gases in the European lower stratosphere as a result of rapid uplift by typhoon systems near the Asian monsoon region and subsequent horizontal transport by eastwards shed eddies.

Plumb [2007] argued that divergent outflows such as the monsoon anticyclone are subject to strong dynamical constraints, limiting the potential for tracer transport of the monsoon anticyclone, especially in the meridional directions. The author suggests eddy-shedding as a mechanism to bypass these constraints and allow a far-reaching mean net-transport through transient eddy PV fluxes.

Fadnavis et al. [2018] performed a series of numerical model sensitivity experiments and showed that the transport due to monsoon eddy shedding can have a substantial effect on the chemical composition of the upper troposphere and lower stratosphere region, further inducing a change in radiative forcing due to a reduction of Ozone.

In a set of shallow-water model experiments Hsu and Plumb [2000] investigated the dynamics of a thermally forced monsoon anticyclone and showed that the response to a steady heating can exhibit spontaneous eddy shedding for certain parameter combinations. They argued that the monsoon anticyclone does indeed correspond to a parameter range for which the response shows eddy shedding behaviour and present comparison with observed shedding events of the monsoon anticyclone. In contrast to the experiments that we will perform in this chapter, Hsu and Plumb [2000] used a model with a representation of thermal damping acting on the whole layer, which can influence the temporal behaviour of the system (as we will show in chapter 6).

Davey and Killworth [1989] studied a similar system in order to explain certain oceanographic phenomena. They performed a series of numerical experiments with a steady, localised mass flux into a single-layer system and found the westward stretching response to break into discrete patches for strong forcing magnitudes. They suggest this mechanism as source for a range of observations of ocean eddies in regions with steady currents present. In a laboratory experiment Cenedese and Linden [1999] reproduced similar behaviour to what was observed numerically by Davey and Killworth [1989] when investigating the response to a continuous mass flux into a two-layer system with a sloped bottom topography. They also found a transition from a zonally symmetric response to periodic shedding when increasing the flux.

We now want to extend our studies on the spontaneously emerging time dependency of the response in chapter 3 using the quasi-geostrophic single layer model described in section 2.3. This simplified model allows us to investigate the phenomenon in a model with reduced complexity and hence develop

a more comprehensive understanding and even analytical theories of some of the features and scales of the system.

Section 5.1 will give an overview on the different types of temporal behaviour that we observe in our steadily forced experiments and give an idea about some of the characteristics of the response. As will be shown in section 5.2 the different states of the response are due to a change in the spatio-temporal stability properties of the forced system. For certain combinations of forcing parameters the response can be either stable, convectively unstable or absolutely unstable, a distinction that will be defined and discussed in more detail later in this chapter. To understand the complex behaviour of the system we will review the theoretical concept of spatial stability analyses (convective and absolute) in section 5.2.1. At last we will perform a spatio-temporal stability analysis for an idealised set of flows and use our findings to explain the temporal states of the response to a steady forcing in section 5.3.

5.1 Different types of temporal behaviour

As mentioned earlier, the horizontal structure and temporal evolution of the response to a continuous mass source in a single layer has previously been investigated by various other authors. We want to focus on the results found by Davey and Killworth [1989], who observed a state transition when increasing the forcing magnitude above a predicted (equation 5.1) for a certain, fixed length scale. They showed, that the response changes from a steady, westward extended plume of PV anomaly (as predicted by linear theory) to a state in which vortices form spontaneously and periodically inside the forcing region and are then being shed to the west.

As we will show in this chapter, we can interpret this eddy shedding as a dynamical instability of the plume, triggered by a small, random wave perturbation near the source region. The Rayleigh inflexion point theorem then provides a necessary condition for such waves to form and grow: the requirement of a reversal of the meridional PV gradient. Figure 5.2 illustrates the break-up of a steady plume of PV anomaly. The left plot shows a zonally extended, steady plume of anomaly. In some cases such a state is unstable and the large gradients at the meridional edges of the plume can act as an energy source for small wave perturbations. Hence, these waves can grow and disrupt the original plume and even break it into discrete patches.

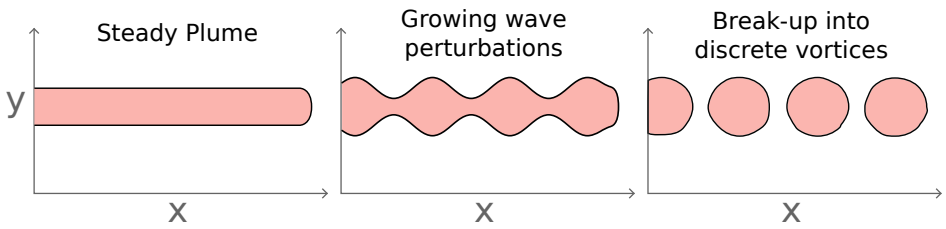

Fig. 5.2 Illustration of the break-up of a steady zonally extended plume of anomaly into a chain of vortices through a dynamical instability.

Since steady, linear theory predicts a steady, local forcing to form such a zonal plume, it seems plausible that non-linear and sufficiently unstable cases (with reversed meridional PV gradient) can lead to a continuous formation and break-up of a plume, so that the plume never actually elongates as much as schematically illustrated in figure 5.2. The corresponding response would then appear as periodic shedding of vortices from the source.

Davey and Killworth [1989] used the idea of instability and the Rayleigh inflexion point theorem to derive formula 5.1 for the occurrence of eddy shedding in a full shallow water model forced by a steady mass source. Equation 5.1 can be used to estimate the threshold value F_{th}, where forcing magnitudes satisfying $|F_0| > F_{Th}$ can cause the system to become unstable and hence shed eddies.

$$F_{Th} = \frac{\beta^2}{\max_y \left| \int_{-\infty}^{\infty} \mathrm{d}x \partial_y^3 \tilde{F} - \partial_y \tilde{F} \right|}, \tag{5.1}$$

where $\tilde{F} = F/F_0$ describes the spatial dependency of the forcing with a magnitude of unity.

An identical formula to equation 5.1 can be derived for the equivalent QG model described in section 2.3 using the same approach of PV gradient reversal. Our first aim is to investigate the applicability of formula 5.1 in a QG system with parameters closer to atmospheric values (see table 2.1). Figure 5.3 shows the model response at day 400 for forcing profile 2.4 and different sets of forcing parameters. Two different length scales r_0 for the mass source F are shown, with each three values of forcing magnitude F_0. The thresholds for non-steady behaviour are $F_{Th} = 0.048$ for $r_0 = 2$ and $F_{Th} = 0.103$ for $r_0 = 4$. For comparison: Davey and Killworth [1989] use a fixed forcing radius of $r_0 = 3$.

One can clearly see that for forcing magnitudes below the corresponding threshold the response does not reverse the meridional PV gradient and stays therefore steady (left panel in 5.3). The response in this case is, as Davey and Killworth [1989] show, well described by steady, linear theory. For $F_0 > F_{Th}$, on the other hand, we do find discrete vortices to be created from the steady mass source, just like described and predicted by Davey and Killworth [1989].

However, we do observe two qualitatively different kinds of vortex creation. For certain parameter combinations (e.g. $r_0 = 4, F_0 = 0.3$) we find the response in and close to the forcing region to be almost steady and similar to the solution predicted by steady, linear theory. The westward extending plume does then become gradually perturbed downstream and eventually breaks up into discrete patches. In other cases (e.g. $r_0 = 4, F_0 = 0.5$), the vortices form directly within the mass source region and get shed westward without a steady plume developing. These cases are characterised by a strong time dependency of the flow near the forcing region. In the following we will refer to the three different types of system behaviour as **steady**, **break-up** and **shedding** states. The three states will be defined in more detail in subsection 5.3.2.

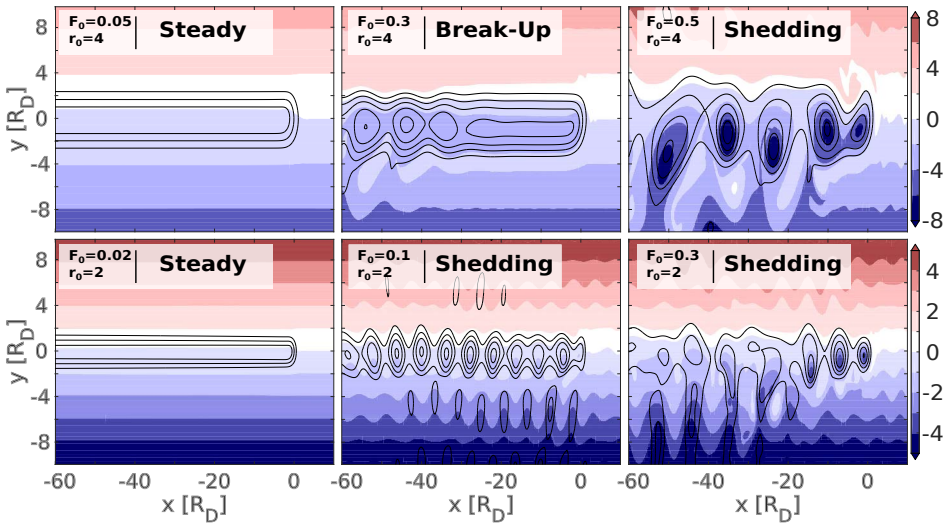

Fig. 5.3 Day 400 PV snapshots using different forcing magnitudes F_0 and length scales r_0. The system is exhibiting various states of behaviour and structure. We can distinguish steady, break-up and shedding states. The contours show the positive part of the height anomaly field, using different contour intervals for the different plots. The shedding thresholds according to formula 5.1 are $F_{Th} = 0.048$ for $r_0 = 2$ and $F_{Th} = 0.103$ for $r_0 = 4$.

In this chapter we will present a comprehensive quantitative theory describing these three states. Generally, the transition of the system from the steady into the break-up regime happens when the stretched out plume of PV anomaly develops a convective instability. This is the case when perturbations can grow while they propagate away from the source region, giving rise to a spatially amplifying, but temporally statistically steady, wave structure. Hence the plume breaks into discrete patches downstream, where the wave perturbations become comparable in magnitude to the background flow. The flow experiences the shedding state when the formed plume becomes absolutely unstable. An absolute instability leads to perturbations that do not only grow in space, but also in time at any fixed location. Disturbances can therefore grow directly within the forcing region and break the flow into vortices.

The breakup up of the westward extending plume into discrete patches leads to several changes in the flow behaviour and its characteristics. McWilliams and Flierl [1979] found that the zonal speed of discrete vortices in a quasi-geostrophic two-vertical-model can differ significantly from what linear wave theory would predict. Additionally they found a finite meridional propagation of eddies. Davey and Killworth [1984] made similar observations in a full shallow water model. They find a dependency of the zonal speed on the eddy magnitude and describe an initial meridional propagation of vortices. Both motions showed anisotropic behaviour for cyclones and anticyclones in their theory.

In a follow-up study Killworth and Davey [1987] used an idealised theoretical "ad-hoc" model to show that this meridional drift results from a mismatch of the centre of the circular height anomaly profile and the centre of the corresponding closed PV contour. This results in a net-Coriolis force on the eddy anomaly. They further showed, that the meridional drift is weaker for more pronounced vortices,

i.e. if the eddy perturbation becomes strong compared to the β-plane background. Early et al. [2011] demonstrated that the drift is a non-linear effect and argued that it results from asymmetric dispersion during the eddy evolution. This leads to changes in the zonal gradients and with it a meridional net-advection of anomaly.

We find potential hints of such a meridional drift of shed vortices in the GCM experiments of chapter 3, e.g. in figure 3.20, indicating a southward shift of the time mean response (compared to the linear response) when the system exhibits eddy shedding.

Chelton et al. [2007] showed that a similar meridional drift of large-scale ocean eddies is also visible in observational data. This tendency of meridional propagation can be seen in the mean zonal height anomaly profiles shown in figure 5.4. For the case with $F_0 = 0.5$, where we observe eddy shedding directly from the the circular forcing region. The created vortices do then propagate westward with a mean southward drift. Hence, the anomaly along the $y = 0$ line drops while we get a corresponding increase along $y = -5$. Note, that the anomaly is moving beyond the extent of the forcing region, which vanishes at $y = -4$. The meridional propagation, however, stagnates at about $x = -70$ and the eddy travels purely zonally from here on, in agreement with the theory presented by Davey and Killworth [1984]. Note that plotting anomaly profiles along specific latitude lines can suggest a zonal localisation of the response, which is simply given by the meridional propagation off the corresponding latitude. In order to capture the full eddy, most of the measures and plots will involve an average over a zonal band, i.e. an average over a finite y-region.

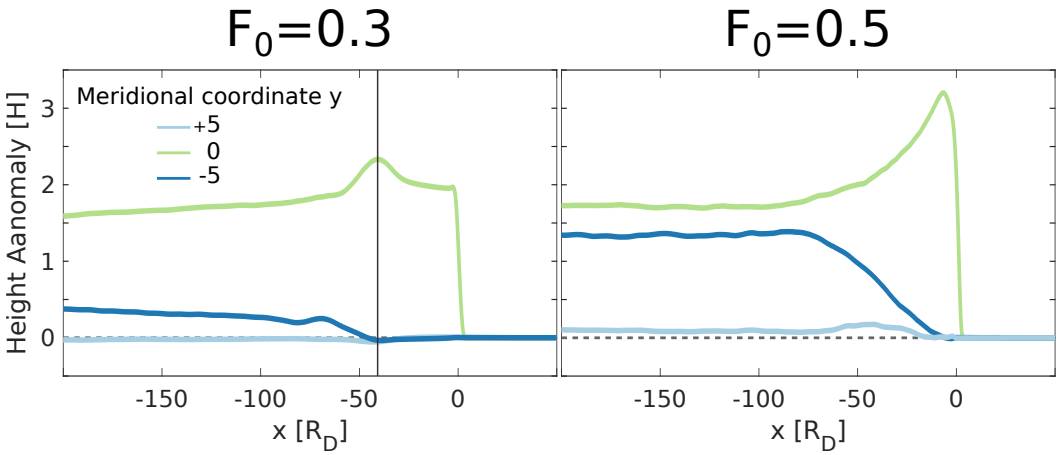

Fig. 5.4 Time mean of zonal height anomaly profiles at different meridional locations for a forcing with $r_0 = 4$. The black vertical line indicates the start of southward eddy propagation at $x = -40$.

We observe a slightly different behaviour for $F_0 = 0.3$. Since in this case we find the response to be almost zonally symmetric near the forcing region (see figure 5.3) there is no meridional propagation close to the origin. However, the gradual growth of perturbations and the corresponding break-up of the zonal plume leads to the formation of isolated patches at about $x = -40$ (vertical line in figure 5.4). The

eddy formation seems to give rise to some meridional convergence of height anomaly along $y = 0$. Once closed PV contours are formed, i.e. for $x < -40$, we again observe a southward drift of height anomaly patches. The southward velocity, as well as adjustment rate of the corresponding vortex profiles, seems to be much lower than for the $F_0 = 0.5$ case, which might be explained by less isolation of the involved vortices.

In addition to the meridional drift, the difference in zonal velocity between linear Rossby waves and discrete vortices might influence the dynamics and structure of the response. Chapter 6 discusses the zonal propagation of coherent eddies and derives a analytic theory for their zonal propagation speed. We found, that vortices in a resting domain should move with the long Rossby wave speed β.

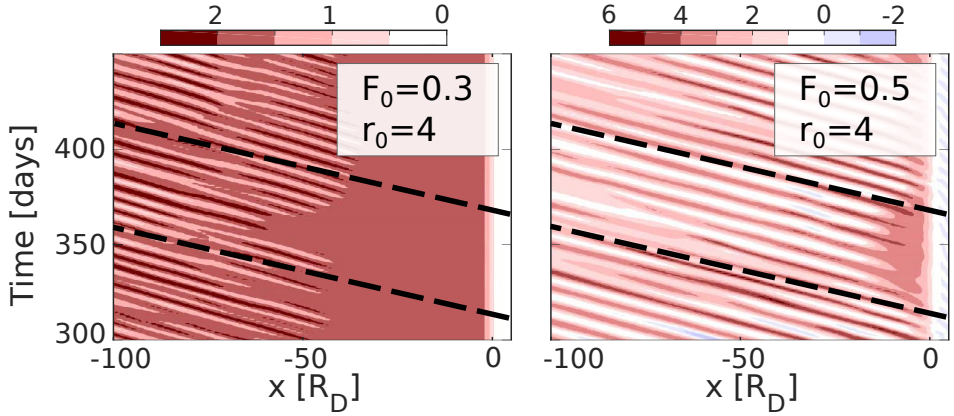

Fig. 5.5 Time evolution of height anomaly averaged between $-4 < y < 4$ for two different steadily forced experiments in the break-up (left) and shedding states (right). The slope of the dashed lines indicate the long Rossby wave speed β.

Figure 5.5 shows the time evolution of the response for two different parameter combinations. One can clearly see how in the case with weaker forcing magnitude F_0 the response is steady near the forcing and breaks into isolated patches at about $x = -50$. The response to the stronger forcing leads to eddy formation inside the forcing region. In both cases, however, the eddies are propagating westward with a constant velocity very close to the long Rossby wave speed (indicated by dashed lines).

As figure 5.5 suggests, the shedding seems to be relatively periodic with a fixed frequency and wave number (giving rise to the constant propagation speed). Figure 5.6 shows the results of a Fourier decomposition in time and the zonal direction for the height anomaly response to a forcing with $r_0 = 4$ and $F_0 = 0.5$, averaged between $-4 < y < 4$. The analysis was performed for either days 300 to 1000 or $-100 < x < 0$ and averaged over the other range, respectively. The analysis shows global maxima at frequency $\omega = 0.846$ and wave number $k = 0.441$. Note that the frequency peak (given in $rad/days$) corresponds to a time scale of 7.4 days per shedding event, which is of the same order of magnitude as the roughly bi-weekly time dependence that other authors have reported (see e.g. Popovic and Plumb [2001] or Ortega et al. [2017]). Keeping in mind the high level of idealisation and conceptualisation of our experiments the good agreement gives further confidence that the modelled shedding process is a

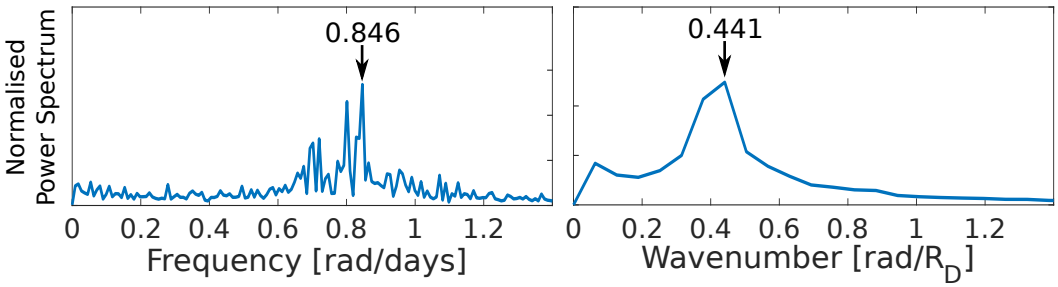

Fig. 5.6 Fourier decompositions of the height anomaly response to a forcing in the shedding state with $r_0 = 4$ and $F_0 = 0.5$. The response was averaged over $-4 < y < 4$ and either days 300 to 1000 or $-100 < x < 0$, while the analysis was performed over the respective other range. Global maxima are indicated.

good description of the observed intra-seasonal temporal variability of the monsoon anticyclone. It is also roughly representative of the shedding frequency in the GCM experiments from chapter 3 (see e.g. 3.21, suggesting about 10 days per shedding event).

Our aim is now to explain some of the presented features and characteristics through a spatio-temporal stability analysis of the system. Since these analyses can be a bit subtle to perform in practice we will first review some of the fundamental ideas and the mathematical basis of spatial stability theory.

5.2 Stability of geophysical shear flows

Many features of geophysical flows can be described in terms of (parallel) shear flows, e.g. atmospheric jets or certain ocean currents. One example can be the zonally extended plume-features of the response the steady and break-up states, as shown in figure 5.3. In certain cases small perturbations can extract energy from these shears and hence grow, eventually leading to a finite disruption of the base flow. This sort of unstable behaviour can drastically alter the properties of the geophysical feature and is therefore well worth studying.

A special branch of instability research covers the area of spatio-temporal instabilities, where perturbations can grow in time and/or space. It becomes necessary to think about the spatial structure of the unstable modes when the flow is perturbed by a spatially varying disturbance or the base flow itself has a spatial structure to it. The corresponding theory was first developed in the field of plasma physics [Briggs 1964; Bers 1973]. The value of such a theory to describe various continuous media was recognized quickly and it has been applied to a range of fluid dynamical and geophysical problems (Merkine [1977], Huerre and Monkewitz [1990] and Pierrehumbert [1986]).

The theoretical concepts of spatio-temporal instabilities and their application to geophysical flows seem to have received regular attention in recent years. Diwan [2015] revisited the conditions under which

a basis flow can support spatial instability and found a criterion similar to Rayleigh's inflexion point theorem.

Wang [2011] performed a comprehensive spatio-temporal stability analysis to explain small scale structures observed in oceanic eastern boundary currents, and Diaz and Aiyyer [2015] applied the idea of spatio-temporal instabilities to model wave patterns found within the African easterly jet. They, however, do perform any kind of analytic stability analysis of a given flow, but deduce the presence of absolute instability due to the local growth of certain energetic diagnostic quantities.

We want to revisit some of the fundamental basics of shear flow instabilities and use the corresponding analysis methods to explain the different states of the response to a steady and spatially confined forcing, as it is described in section 5.1. For the following analysis we want to distinguish between three different kinds of instability, depending on the spatial and temporal structure of the unstable mode.

- We speak of **temporal** (in)stability if a certain mode has a single, fixed wave number in the streamwise direction and the perturbation grows or decays in time.
- **Convective** instability corresponds to modes, where the disturbance grows with distance from the initial perturbation or forcing region, but stays finite for all times at any fixed location in space.
- And last we have **absolute** instability, which describes perturbations that grow in time and space, i.e. the disturbance will grow indefinitely at any fixed location, while also growing with distance from the origin region of the perturbation.

The three types of instability are not necessarily mutually exclusive and details of how to excite corresponding modes do partially depend on the nature of the perturbation and boundary conditions.

While temporal instability is most relevant for initial value problems of infinitely extended perturbations or periodic, e.g. when the system gets perturbed with a fixed wave number, convective and absolute instabilities are usually excited by spatially confined perturbation. The idea of how the different kinds of instabilities affect a flow is visualised in Figure 5.7 by looking at their effects on a confined and infinitesimal initial disturbance. If the perturbation is a delta function it will contain Fourier components of all possible wave numbers (k). If the flow is unstable, some of these Fourier components are will grow, probably at different rates and simultaneously propagate at different speeds. This will lead for the perturbation to disperse and grow in magnitude[1].

In the case of convective instability all growing Fourier components will propagate in the same direction, i.e. their group velocities $c = \partial\omega/\partial k$ all have the same sign. Here k is the wave number and ω the frequency of the corresponding wave. If, however, the unstable Fourier components include unstable modes with phase speeds of different signs, i.e. it includes a point with $\partial\omega/\partial k = 0$, the growing and spreading perturbation will always include the location of the initial perturbation and the signal will

[1] This interpretation already suggests that we require temporally unstable behaviour of the system over a band of wave numbers to obtain convectively and absolutely unstable modes. If only isolated Fourier modes are unstable these will grow independently and eventually we will be left with the fastest growing mode only.

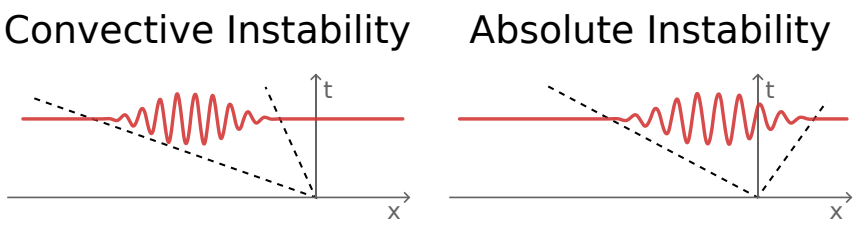

Fig. 5.7 Schematic illustrating the effects of convective and absolute instability on an infinitesimal initial wave packet perturbation at the origin (after Huerre and Monkewitz [1990]). Red curves show the zonal profile of the wave packet at a given instance in time and dashed lines indicate the evolution of the edges of the wave packet.

grow indefinitely. This also means the presence of absolute instability does strongly depend on the frame of reference. Spatially (convectively and/or absolutely) unstable modes are often excited by a confined, steady forcing. This situation can be interpreted as a superposition of repeatedly emitted delta-peak perturbations that can now give rise to oscillating modes with temporally varying or constant magnitude and spatial structure.

We now want to investigating the stability of the single-layer QG-system described in section 2.3. At first we choose to perturb a zonally symmetric basic state given by the height anomaly profile $\bar{h}(y)$ and a corresponding zonal basis flow $U(y) = -\partial_y \bar{h}$ with vanishing meridional mean. We will then assume the obtained results can be transferred to certain zonally more localised profiles and can therefore explain some of the stability characteristics of the flow created by a steady, localised forcing (see figure 5.3). The basic idea can be regarded as the forcing creating a plume of PV anomaly, which is stretching out to the west (similar to the steady, linear solution). This plume can then become unstable and convective and absolute modes can be excited by random small scale perturbations. These modes can then grow and eventually lead to a break-up of the plume into discrete patches.

We will outline the mathematical description of spatio-temporal stability analyses in 5.2.1. This will give us constructive arguments of how to calculate and identify convectively and absolutely unstable modes of a given basis state profile $\bar{h}(y)$. We then develop and discuss practical approaches and procedures for the different kinds of instabilities in sections 5.2.2 to 5.2.4 and apply them to idealised states. Section 5.3.2 will then verify our findings by comparing them to results of numerical experiments, before we eventually apply our theory to steadily forced flows in 5.3.

5.2.1 Mathematical description of spatio-temporal instabilities

The theoretical framework of convective and absolute instabilities was well discussed by Briggs [1964]. This section will revisit some of the mathematical background and arguments used to develop stability analyses for shear flows. We start with a set of QG-PV equations, expressed in terms of height anomaly $h(x,y,t)$ and PV $q(x,y,t)$. The relevant quantities and normalisation constants are listed in table 2.1.

$$\begin{aligned} q &= \partial_x^2 h + \partial_y^2 h - h + \beta y \\ \partial_t q - \partial_y h \partial_x q + \partial_x h \partial_y q &= 0. \end{aligned} \tag{5.2}$$

Combining the equations and linearising about a steady, zonally symmetric basis state $\bar{h}(y) = h - \hat{h}$ we can express this set of equations as linear partial differential operator L with

$$L\hat{h} = \left[(\partial_t - \partial_y \bar{h} \partial_x)(\partial_x^2 + \partial_y^2 - 1) + (\partial_y^3 \bar{h} - \partial_y \bar{h} + \beta)\partial_x\right] \hat{h} = 0. \tag{5.3}$$

Next we assume that our perturbation is given as a set of exponential normal modes $\hat{h}(x,t) = h'(y)e^{i(kx-\omega t)}$ where the wave number k and the frequency ω are allowed to be complex. We can then write the differential equation as eigenvalue problem with complex eigenvalue(-function) $D(k,\omega)$, where the condition $D = 0$ represents the dispersion relation of the system:

$$L\hat{h} = D(k,\omega)\hat{h}. \tag{5.4}$$

Note, that D can have multiple roots and will usually have different branches satisfying the condition. The root-branches of the dispersion relation D now links ω to values of k corresponding to the different waves that are supported by the system. We can further assume there exists a Green's function for this operator L which satisfies

$$LG(x,t) = \delta(x)\delta(t). \tag{5.5}$$

Mathematically the response $h(x,t)$ to a perturbation $F(x',t')$ can then be expressed as

$$\hat{h}(x,t) = \int_0^t \mathrm{d}t' \int_{-\infty}^{\infty} \mathrm{d}x' \; G(x-x',t-t')F(x',t'), \tag{5.6}$$

where we assumed $F(x,t<0) = 0$. Performing a Fourier transform in x and a Laplace transform in t we obtain

$$\begin{aligned}\hat{h}(k,\omega) &= \int_0^\infty \mathrm{d}t \int_{-\infty}^{\infty} \mathrm{d}x\, \hat{h}(x,t) e^{-ikx+i\omega t} \\ &= G(k,\omega)F(k,\omega).\end{aligned} \tag{5.7}$$

We have now transformed our problem involving unknown differential operator L into a problem with unknown Green's function G. Remember that the Green's function and the dispersion relation are closely related. Combining equations 5.4 to 5.7 leads to $(G(k,\omega))^{-1} = D(k,\omega)$ and $\partial D/\partial k = \partial \omega(k)/\partial k$, where $D \equiv \omega - \omega(k) = 0$. Hence we have expressed our problem in the form of an unknown dispersion relation D.

As next step we restrict the analysis to the response to a periodic point source at the origin with real frequency ω_0, i.e. $F(x,t>0) = \delta(x)e^{-i\omega_0 t}$. The corresponding transforms lead to

$$F(k,\omega) = \frac{1}{i(\omega_0 - \omega)}, \text{ if } \mathrm{Im}(\omega) > 0, \tag{5.8}$$

Note that the source has a pole at real frequency $\omega = \omega_0$. We can substitute these functions into equation 5.7 and perform the corresponding inverse transforms to obtain a formula for $\hat{h}(x,t)$, giving equation 5.9. Since it does involve a double integral, and k and ω can in principle both have finite imaginary parts, the two integration paths will generally have to be taken in the complex planes for k and ω.

Following Pierrehumbert [1986], the integration path of the inverse Laplace transform for ω is taken along the $\mathrm{Im}(\omega) = \sigma$ contour, where σ has to be sufficiently large[1]. Choosing a large value of σ ensures causality within the system, i.e. vanishing perturbation before $t = 0$ with $\hat{h}(x,t<0) = 0$, since no poles of $G(k,\omega)F(k,\omega)$ lie above the corresponding σ-path. Using Cauchy's residue theorem the contour can be closed over $\omega = +i\infty$ without giving any contribution and the value of the integral in equation 5.7 vanishes. These ω-integration paths are called Bromwich contours and the lines in wave numbers space, that correspond to these ω-paths and satisfy $D(k,\omega) = 0$, are referred to as Bromwich images.

$$\begin{aligned}\hat{h}(x,t) &= \frac{1}{4\pi^2} \int_{-\infty+i\sigma}^{\infty+i\sigma} \mathrm{d}\omega \int_{-\infty}^{\infty} \mathrm{d}k\, \frac{G(k,\omega)}{i(\omega_0-\omega)} e^{ikx-i\omega t} \\ &= \frac{1}{4\pi^2} \int_{-\infty+i\sigma}^{\infty+i\sigma} \mathrm{d}\omega \int_{-\infty}^{\infty} \mathrm{d}k\, \frac{e^{ikx-i\omega t}}{i(\omega_0-\omega)D(k,\omega)}.\end{aligned} \tag{5.9}$$

[1] As shown later σ has (initially) to be larger than the ω_i of the fastest growing temporal mode. We will later reduce the value of σ to ensure transient modes to not give any contribution to the integral.

The path for the k-integration is taken along the real k-axis and closed below. Since we are interested in the region $x < 0$ we find that the contribution of the closure path is proportional to e^{ikx} and hence vanishes for $k \to -i\infty$. Note that this means we are only taking modes into account that decay for $x < 0$, and we do not account for any spatially growing modes (yet).

Equation 5.9 shows that singularities are given by solutions of the dispersion relation and therefore we only have to keep track of wave numbers that satisfy $D(k,\omega) = 0$ for a given ω. The k integration can be performed analytically using the residue theorem, which states that the integral over a closed path in the complex plane is proportional to the sum of residues of any enclosed singularities of the integrand, i.e. of $D^{-1}(k,\omega)$. If we, for now, assume D^{-1} does only have first order poles and we use again $\partial D/\partial k = \partial\omega(k)/\partial k$ we find

$$\hat{h}(x,t) \propto \int_{-\infty+i\sigma}^{\infty+i\sigma} \mathrm{d}\omega \sum_{k_i \leq 0 D=0} \frac{e^{ikx-i\omega t}}{(\omega_0-\omega)\frac{\partial\omega}{\partial k}}. \tag{5.10}$$

Note that $\hat{h}$ is now expressed as a sum of exponentials that decay for $x < 0$, since we are only considering k-values in the lower half plane. We can therefore conclude that none of the enclosed modes does give a spatially growing contribution.

Since we are considering convectively unstable problem with $\omega_i = 0$ the next step would be to take the limit $\sigma \to 0$, as we will later do in equation 5.11. This would ensure that equation 5.10 is only describing the long time limit of temporally stable solutions [Pierrehumbert 1986]. However, we might encounter a possible problem while doing so: As we lower the Bromwich contour the corresponding Bromwich images in the k-plane will move and change. At some point parts of these Bromwich images might cross the real k-axis and hence enter or leave the integration area. But this would lead to a discontinuous jump in h due to an additional (or fewer) singularity to be counted in equation 5.9.

The solution to the problem lies in an analytic continuation and a deformation of the k integration contour to prevent this from happening. We try to deform the k contour in such a way, that no roots of D will cross it as we take the limit $\sigma \to 0$ This requires, in principle, an analytic continuation of the integrand, which we assume to be possible since the causality condition requires it to be holomorphic above all singularities in ω. The new, closed k-integration contour C has to enclose all, and only those, Bromwich images that were also included for $\sigma \gg 1$. Note that we also need to ensure ω_0 is still within the ω-integration.

Figure 5.8 shows the deformation of the k-integration path as we decrease the value of σ. The important observation is, that our integration now includes wave numbers with $k_i > 0$, i.e. modes that grow exponentially for $x < 0$. Note that, in order for a Bromwich image to cross the real k-axis, the

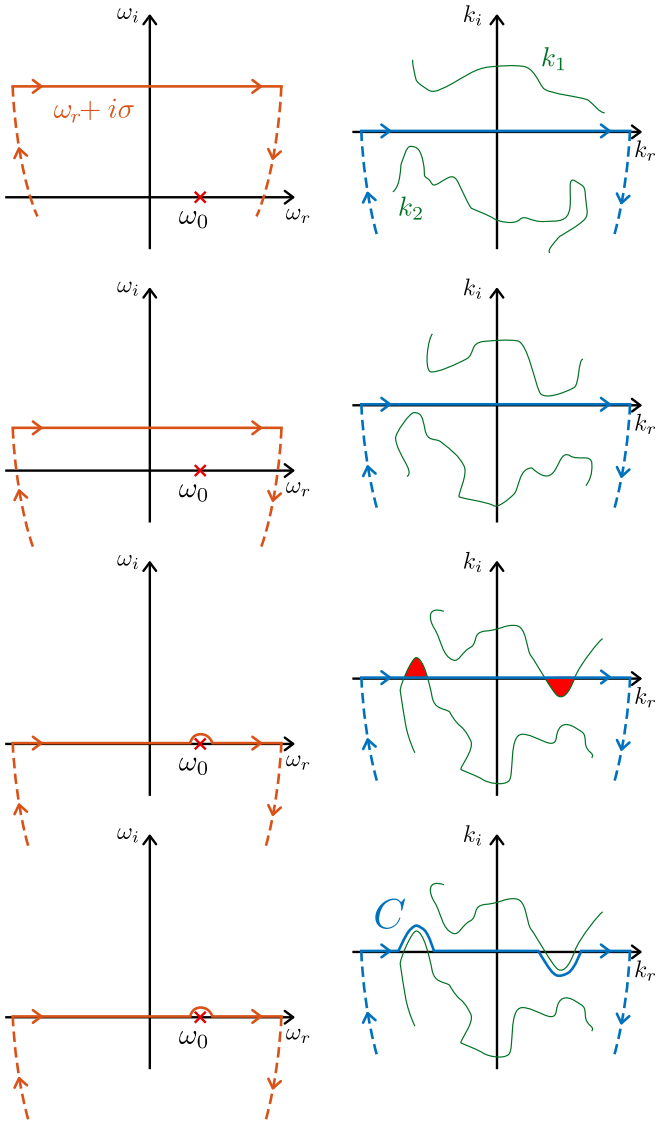

Fig. 5.8 Correlation between Bromwich contours $w_r + i\sigma$ (orange curve) and corresponding Bromwich images $k(w_r + i\sigma)$ (green curves) as $\sigma \to 0$. The bottom panel shows the deformation of the k-integration path C (blue curve) to include/exclude Bromwich paths that crossed the real k-axis as $\sigma \to 0$.

corresponding Bromwich image has to intersect with the temporal[1] branch $\omega(k_r)$ that corresponds to $D(k = k_r, \omega)$. Hence, if we choose $\sigma > \max \mathrm{Im}\,\omega(k_r)$ none of the $D = 0$ lines initially cross $k_i = 0$ and equation 5.10 holds. Although, for smaller values of σ, when we have to deform the k-integration contour C, we have to re-write equation 5.10 and estimate formula 5.9 as

$$\begin{aligned}\hat{h}(x,t) &= \frac{1}{4\pi^2} \lim_{\sigma\to 0} \int_{-\infty+i\sigma}^{\infty+i\sigma} \mathrm{d}\omega \int_C \mathrm{d}k \, \frac{e^{ikx-i\omega t}}{i(\omega_0-\omega)D_U(k,\omega)} \\ &\propto \lim_{\sigma\to 0} \int_{-\infty+i\sigma}^{\infty+i\sigma} \mathrm{d}\omega \sum_{k_i<C(k_r)D_U=0} \frac{e^{ikx-i\omega t}}{(\omega_0-\omega)\frac{\partial\omega}{\partial k}} \\ &\propto \sum_{k_i<C(k_r)D_U=0} \frac{e^{ikx-i\omega_0 t}}{\frac{\partial\omega}{\partial k}} \propto e^{-i\omega_0 t},\end{aligned} \tag{5.11}$$

where we used the fact that $(\partial\omega/\partial k)^{-1} e^{ikx-i\omega t}$ is now analytic within the sum and we therefore computed the ω integral as residue of the single pole at ω_0. The only time dependency of our height anomaly perturbation is now given by the factor $e^{-i\omega_0 t}$. Since ω_0 is real, the perturbation can grow in space[2] but does only oscillate in time without any growth.

However, we still might run into a problem, namely when it simply is not possible to deform the contour in a way that excludes/includes all roots of $D(k,\omega)$ that cross the $k_i = 0$ line for all values $\sigma \geq 0$. This is, for example, the case if two Bromwich images from opposite sides of the real k-axis merge in a point k_a. The contour C would then simply get "trapped" between the converging roots as the Bromwich contour is lowered. Such a point would correspond to a double root in $\omega(k)$ and is mathematically given as a saddle. Hence, we have $\partial\omega/\partial k = 0$, which already indicates a problem with the developed framework, e.g. given equation 5.10. The criterion of vanishing complex derivative of $\omega(k)$ will provide us with a constructive way to practically calculate absolutely unstable modes in section 5.2.4. Pierrehumbert [1986] pointed out the importance of the two modes originating from opposite sides of the real k-axis when σ is large, otherwise it would be trivial to deform C.

Figure 5.9 illustrates an example of such a trapping at a stationary point k_a. Since we cannot lower the Bromwich contour below a certain value $\sigma = \mathrm{Im}(\omega_a)$, we do once more need a different way to evaluate equation 5.9 for this case. One way is to expand the dispersion relation to leading order around the merging point k_a with corresponding ω_a. Using the condition that D has a double root at k_a this gives (all in the limit $k \to k_a$)

[1] Recall that we stated temporal instability is a necessary condition for convective and absolute instability. We will use this connection as a starting point to practically calculate convectively unstable modes in section 5.2.3.

[2] If modes with $k_i > 0$ are enclosed by the contour C.

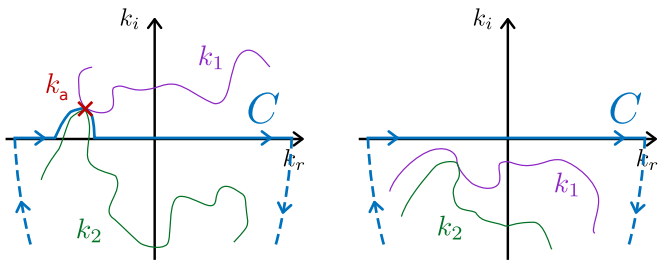

Fig. 5.9 Merging of two roots of $D_U(k, \omega_r + i\sigma)$ with modes originating from opposite sides (left) or the same side (right) of the real k-axis. Only in the left case a further reduction of σ below a value w_a is not possible without a mode crossing the C contour.

$$D(k,\omega) \approx \frac{\partial D(k_a,\omega_a)}{\partial \omega}(\omega-\omega_a) + \frac{1}{2}\frac{\partial^2 D(k_a,\omega_a)}{\partial k^2}(k-k_a)^2 \xrightarrow{k\to k_a} 0 \tag{5.12}$$
$$\implies (k-k_a)^2 = -2\frac{\partial D(k_a,\omega_a)}{\partial \omega}(\omega-\omega_a)\left[\frac{\partial^2 D(k_a,\omega_a)}{\partial k^2}\right]^{-1},$$

which can be differentiated with respect to k to give a leading order contribution of

$$\begin{aligned}\frac{\partial D(k,\omega)}{\partial k} &= \frac{\partial^2 D(k_a,\omega_a)}{\partial k^2}(k-k_a) \\ &\propto \left[\frac{\partial^2 D(k_a,\omega_a)}{\partial k^2}\frac{\partial D(k_a,\omega_a)}{\partial \omega}(\omega-\omega_a)\right]^{\frac{1}{2}} \\ &\propto \left[\frac{\partial^2 \omega(k_a)}{\partial k^2}\frac{\partial k(\omega_a)}{\partial \omega}(\omega-\omega_a)\right]^{\frac{1}{2}}.\end{aligned} \tag{5.13}$$

Using this approach we can treat the double pole as sum of two simple singularities that merge as we approach $\sigma \to \sigma_a = \mathrm{Im}(\omega_a)$. Plugging this expression into the second line of equation 5.11 we obtain

$$
\begin{aligned}
h(x,t) &\propto \lim_{\sigma\to\sigma_a} \int_{-\infty+i\sigma}^{\infty+i\sigma} \mathrm{d}\omega \sum_{k_i<C(k_r)D_U=0} \frac{e^{ikx-i\omega t}}{(\omega_0-\omega)\left[\frac{\partial^2\omega(k_a)}{\partial k^2}\frac{\partial k(\omega_a)}{\partial\omega}(\omega-\omega_a)\right]^{\frac{1}{2}}} \\
&\propto \frac{1}{\left[\frac{\partial^2\omega(k_a)}{\partial k^2}\frac{\partial k(\omega_a)}{\partial\omega}\right]^{\frac{1}{2}}} \lim_{\sigma\to\sigma_a} \int_{-\infty+i\sigma}^{\infty+i\sigma} \mathrm{d}\omega \sum_{k_i<C(k_r)D_U=0} \frac{e^{ikx-i\omega t}}{(\omega_0-\omega)(\omega-\omega_a)^{\frac{1}{2}}} \\
&\propto \frac{e^{ik_a x-i\omega_a t}}{\left[(\omega_0-\omega_a)\frac{\partial^2\omega(k_a)}{\partial k^2}\frac{\partial k(\omega_a)}{\partial\omega}t\right]^{\frac{1}{2}}}.
\end{aligned}
\tag{5.14}
$$

We can estimate the ω-integral via the method of steepest descent and Gaussian integration, since $\omega(k)$ is stationary at k_a and we are only interested in growing modes ($\omega_i > 0$) and the asymptotic behaviour for $t \to \infty$ and fixed x. As equation 5.14 states we do now have a wave which grows (or decays) in time and space, since usually k_a and ω_a are complex. Obviously we can theoretically lower the value of σ even further for all $\omega \neq \omega_a$. The corresponding integration path would look like shown in Figure 5.10.

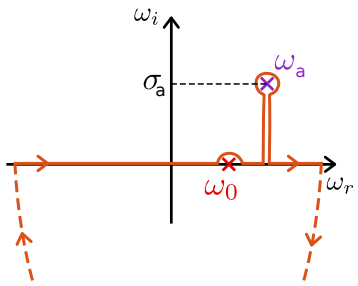

Fig. 5.10 Path for the ω-integration in the presence of a single absolutely unstable point.

In the rest of this sections we use the properties of the different types of instability described earlier to calculate the correspondingly unstable modes for a given base flow in a single layer model. We will apply the different methods for each type of instability (temporal, convective and absolute) separately and directly present the obtained results.

5.2.2 Temporal stability

The system we will be discussing in the following subsections shall (once more) be described by the linearised single-layer QG-PV equations for a given basis state $\bar{h}$ and perturbation $\hat{h}$ shown in equation 5.3.

Defining a zonal wind basis state profile $U(y) = -\partial_y \bar{h}$ and assuming the perturbation to be given by a normal mode $\hat{h} = h'(y)e^{ik(x-ct)}$ we can express the evolution of the system via its Rayleigh equation in terms of a phase speed c and wave number k:

$$c\left[(k^2+1)h' - \partial_y^2 h'\right] - U\left[k^2 h' - \partial_y^2 h'\right] + h'\left[\beta - \partial_y^2 U\right] = 0. \tag{5.15}$$

We can discretise equation 5.15 using a second order central differences scheme to obtain a generalised Eigenvalue problem of the form $Ah = cBh$ for matrices A, B and Eigenvalues c. The relation of Eigenfunction h at grid point i and neighbouring nodes then reads

$$\begin{aligned} &-\left[(k^2\Delta y^2+2)U_i - \Delta y^2(\beta - \partial_y^2 U|_{y_i})\right] h'_i + h'_{i+1}U_i + h'_{i-1}U_i \\ &= -c\left[\left((k^2+1)\Delta y^2+2\right) h'_i + h'_{i+1} + h'_{i-1}\right]. \end{aligned} \tag{5.16}$$

If we constrain the problem using boundary conditions $h_0 = h_N = 0$ we can define the tridiagonal matrix equation

$$\begin{aligned} &\begin{pmatrix} \gamma_1 & U_1 & & & & \\ U_2 & \gamma_2 & U_2 & & & \\ & & & \vdots & & \\ & & U_{N-2} & \gamma_{N-2} & U_{N-2} & \\ & & & U_{N-1} & \gamma_{N-1} & \end{pmatrix} \begin{pmatrix} h'_1 \\ h'_2 \\ \vdots \\ h'_{N-2} \\ h'_{N-1} \end{pmatrix} \\ &= c \begin{pmatrix} \delta_1 & 1 & & & & \\ 1 & \delta_2 & 1 & & & \\ & & & \vdots & & \\ & & 1 & \delta_{N-2} & -1 & \\ & & & 1 & \delta_{N-1} & \end{pmatrix} \begin{pmatrix} h'_1 \\ h'_2 \\ \vdots \\ h'_{N-2} \\ h'_{N-1} \end{pmatrix}, \end{aligned} \tag{5.17}$$

with $\gamma_i = -\left[(k_0^2\Delta y^2+2)U_i - \Delta y^2(\beta - \partial_y^2 U|_{y_i})\right]$ and $\delta_i = -(k_0^2+1)\Delta y^2 + 2$. Solving this equation using a real value for wave number k_0 we can find a matching set of (complex) values for c and hence frequencies $\omega = k_0 c$. These correspond to neutral, simply propagating waves if $\mathrm{Im}(\omega) = 0$, and exponentially growing or decaying modes for $\mathrm{Im}(\omega) > 0$ and $\mathrm{Im}(\omega) < 0$, respectively.

In general the $N \times N$ Eigenvalue problem 5.17 will return N values for ω for every k_0. Since we are interested in steady states and long time behaviour we will concentrate on the fastest growing mode only,

i.e. the mode with the most positive ω_i.

We can now specify a basis state and investigate its stability properties. At first we choose a set of idealised states with height anomaly profile described by

$$\bar{h}(y) = \begin{cases} \eta \cos^4\left(\frac{\pi y}{2\rho}\right) & \text{for } |y| < \rho \\ 0 & \text{otherwise} \end{cases} . \tag{5.18}$$

The two free parameters are the width ρ and the magnitude η of the profile. If not specified otherwise we will fix either $\rho = 6$ or $\eta = 2$. We chose the specific profile in equation 5.18 to ensure a continuous meridional PV gradient of the unperturbed system. Another approach would be to use the cos^2 profile based on the linear response to the steady forcing used in the experiments described in section 5.1. Such a profile, however, would lead to discontinuities in the PV gradient at $y = \pm\rho$ which might be complicated to handle in numerical calculations. Instead we will later use a fitting procedure to link the response of the $\cos^2$ forcing experiments to the results of this stability analysis using a cos^4 structure.

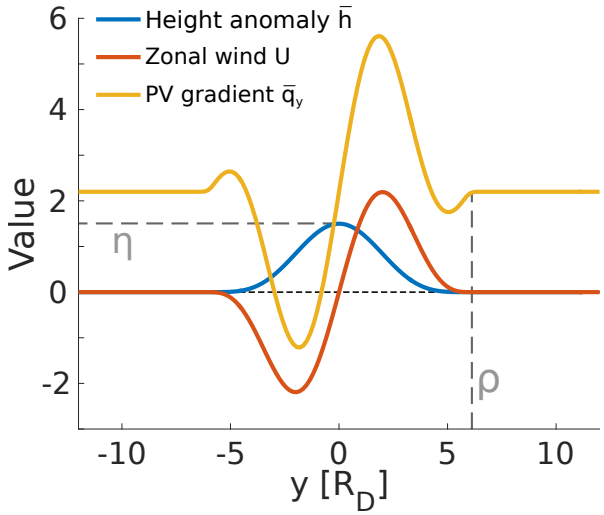

Fig. 5.11 Idealised basis state profile with $\eta = 1.5$ and $\rho = 6$.

All stability analyses are performed using a beta plane with $\beta = 0.51 f_0 R_D^{-1}$, and a grid with 256 grid points equally distributed over a meridional channel width of 40 Rossby radii R_D. All presented simulation results are not sensitive to doubling the number of grid points or the domain size. The profile and resulting meridional PV gradient of the basis state is illustrated in figure 5.11.

Performing the described temporal stability analysis for this system we find consistent modes with positive imaginary frequency for a range of real wave lengths k_0. Figure 5.12 shows the frequency ω and wave speed c for the fastest growing mode as a function of k_0 for two different basis state magnitudes η and a fixed width of $\rho = 6$.

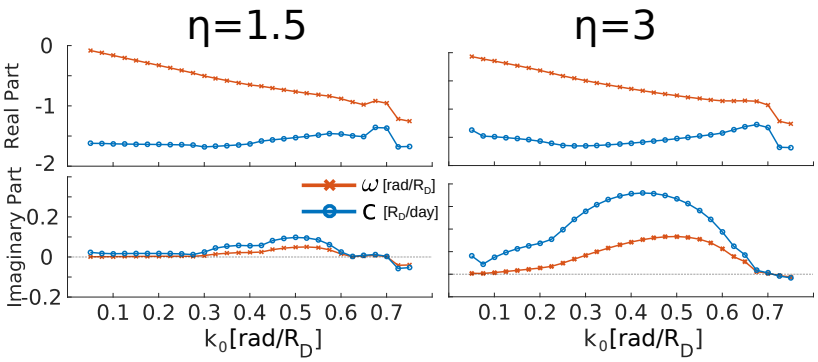

Fig. 5.12 Frequency and wave speed of the fastest growing temporal mode for idealised basis states with fixed width $\rho = 6$ and different magnitudes.

In contrast we can investigate the sensitivity to changes in ρ while keeping η constant. The results are presented in figure 5.13.

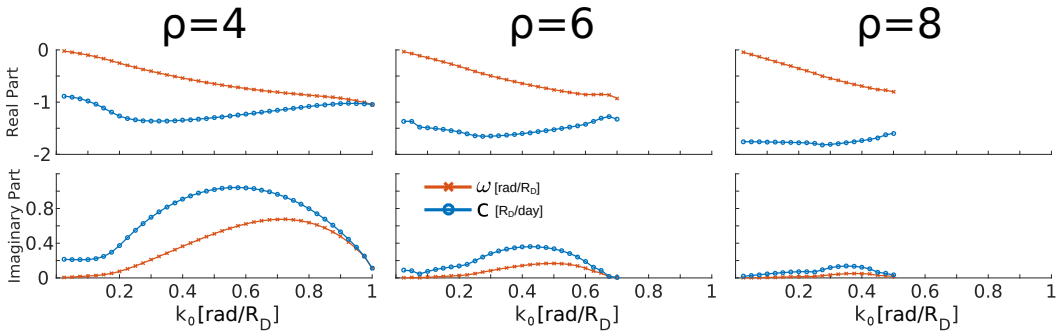

Fig. 5.13 Same as figure 5.12 but for fixed magnitude $\eta = 3$ and varying width.

A distinct, continuous dispersion relations can be identified in all cases, which we interpret as the relevant mode. The overall shape of the structure is fairly similar for the various magnitudes and widths and shows a clear maximum. However, the value of the maximum varies and seems to increase for narrower and stronger basis states, making the flow less stable in these cases. Further note that the range of k_0 with $\omega_i > 0$ seems to decrease rapidly as ρ increases.

To obtain a sense of the spatial structure of these modes figure 5.14 illustrates the real and imaginary parts of the meridional profiles $h'(y)$ for $\eta = 5$. All profiles are normalised to a square-integral of one. It can be see that the profiles are all fairly confined to the vicinity of the region with non-zero background wind, see figure 5.11.

5.2.3 Convective stability

This section explains how to perform a convective stability analysis for the system presented in equation 5.2, i.e. finding instabilities with real $\omega = \omega_0$ and complex k. Starting with the Rayleigh equation

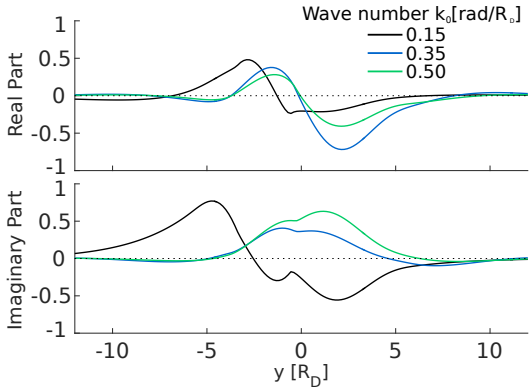

Fig. 5.14 Spatial structure of the fastest growing temporal mode for certain real wave numbers and an idealised basis state using $\eta = 3$ and $\rho = 6$.

presented in section 5.2.2 one can re-arrange equation 5.15 for the height anomaly perturbation h' and the background wind U in the following way:

$$h'_{yy} = (k^2+1)h' + \frac{\beta + U - U_{yy}}{c-U}h'. \tag{5.19}$$

We can solve the equation numerically when discretising via a central differences scheme. This way the equation can be written in form of an Eigenvalue problem for k^2 reading

$$h'_{i+1} + h'_{i-1} + \Delta y^2 \left[\frac{\beta + c - \partial_y^2 U|_{y_i}}{U_i - c} - \frac{2}{\Delta y^2} \right] h'_i = \Delta y^2 k^2 h'_i. \tag{5.20}$$

or in matrix notation

$$\begin{pmatrix} \gamma_1 & 1 & & & & \\ 1 & \gamma_2 & 1 & & & \\ & & \vdots & & & \\ & & 1 & \gamma_{N-2} & 1 & \\ & & & 1 & \gamma_{N-1} & \end{pmatrix} \begin{pmatrix} h'_1 \\ h'_2 \\ \vdots \\ h'_{N-2} \\ h'_{N-1} \end{pmatrix} = k^2 \begin{pmatrix} h'_1 \\ h'_2 \\ \vdots \\ h'_{N-2} \\ h'_{N-1} \end{pmatrix}, \tag{5.21}$$

where $\gamma_i = \Delta y^2 \frac{\beta + c - \partial_y^2 U|_{y_i}}{U_i - c} - 2$.

To obtain a convectively growing mode (in the negative x-direction) we need to find a mode with $\mathrm{Im}(\omega) \equiv \omega_i = 0$ and $\mathrm{Im}(k) \equiv k_i > 0$. Unfortunately equation 5.19 does not allow us to explicitly solve for a given value of ω, but only for a value of (complex) c. Hence it is non-trivial to find solutions with vanishing imaginary frequency.

However, since the phenomenon of convective instability is closely related to temporal instability and even requires temporally unstable modes to exist, as explained in section 5.2.1, we can use the latter as a starting point to find the former. This means we will start by finding the value of c, and hence $\omega = kc$, that corresponds to an imposed real wave number $k = k_0$. If we then assume that our dispersion relation is analytic we can vary the given c and track the changes we obtain in k and ω when solving equation 5.19.

Like for the temporal case, equation 5.21 will return a large number of values for k for any fixed c. We will label the corresponding modes according to their distance in k-space to the known solution k_0 of the temporal problem. The concept is illustrated in figure 5.15.

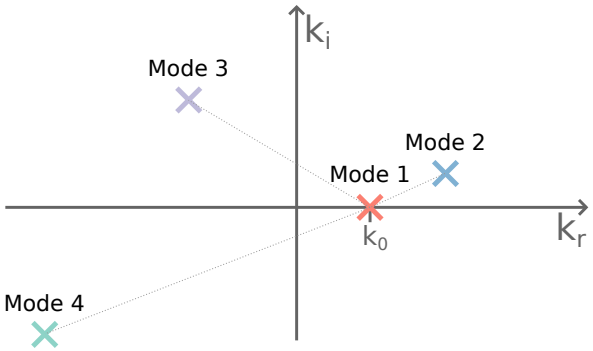

Fig. 5.15 Concept of labelling the different solutions of equation 5.21 based on their distance in k-space to the known, real solution k_0 specified in the temporal problem.

Next we slightly vary our input parameter c. This gives us a new set of complex solutions k. We then label each of the new k solutions according to the label of the closest solution of the previous c-value, as is shown in figure 5.16. This procedure can be repeated for a set of discrete values for c following an arbitrary path in complex c-space.

As discussed earlier and in section 5.2.1, we can use this **mapping approach** to track the wave number and frequency a coherent mode as we map out a certain path (or area) in c space, in particular one that starts at or intersects with the real k-axis. Doing so, we will occasionally find solutions that have a real frequency $\omega = \omega_0$. Note that this approach, as we will show, can be used to study not only absolute instability, but also convective instability. This is in contrast to approaches that simply attempt to find the saddle point of the dispersion relation (e.g. Lin and Pierrehumbert [1993]).

Figure 5.17 shows ω and k for phase speeds c with fixed imaginary part and varying real part around the solution obtained from the temporal instability problem for the real value $k_0 = 0.35$ and a basis state using $r = 6$ and $\eta = 3$. As can be seen we indeed find a zero crossing when tracking the frequency at

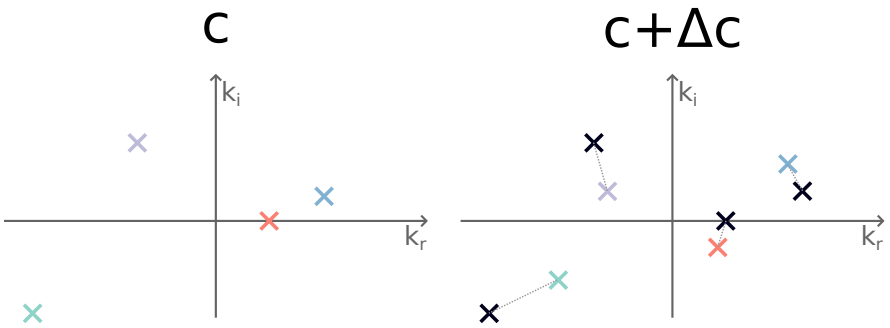

Fig. 5.16 Procedure to label the solutions of equation 5.21 for a certain $c+\Delta c$ based on their distance to the solutions of the equation for an input parameter c.

about $\omega = -0.57 + 0.12i$ with $k = k_0 = 0.35$, suggesting a purely temporally growing mode. Since the analysis returns multiple modes with different values of k we label the modes corresponding to their distance to the known temporally unstable solution in k-space. As we then gradually perturb the real part of the imposed wave speed c_r we group each newly calculated point in $k-space$ together with the correspondingly closest mode of the previous value of c_r.

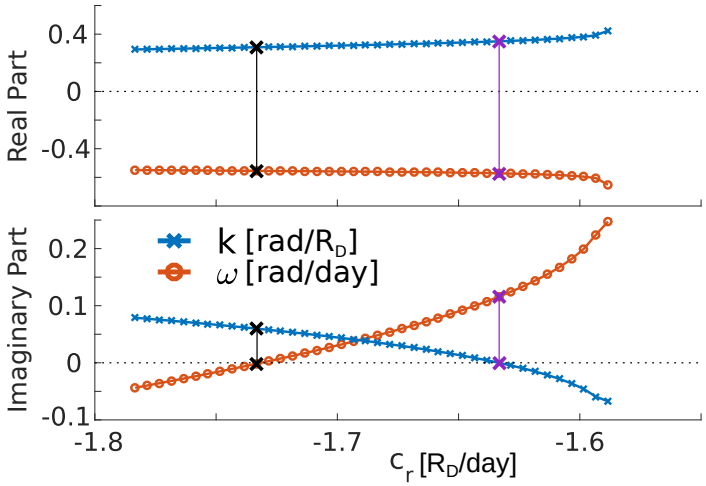

Fig. 5.17 Frequency and wave number for various values of c_r around the temporally most unstable mode with $k_0 = 0.35$ in a basic state with $\rho = 6$ and $\eta = 3$. The figure illustrates how to find a convective mode (black crosses) starting from a temporal mode (purple crosses).

As we approach $c_r = -1.73$ the frequency becomes real, while k is now fully complex with a positive imaginary part. We identify this point as solution to the convective instability problem with corresponding spatial growth rate $k_i = 0.059$, wave number $k_r = 0.31$ and frequency $\omega = -0.55$. By construction it connects to a solution of the temporal instability problem, suggesting it is indeed a physically meaningful mode. Note that the method described uses k_0 as free parameter, but, since every value of k_0 corresponds to a specific complex c, and we keep the imaginary part of the phase speed fixed while varying the real part, we can qualitatively interpret changes in k_0 as changes in c_i. Using various values of k_0 therefore

corresponds to a mapping of the dispersion relation in the complex c plane.

Running the analysis visualised in figure 5.17 for different values of k_0 we can identify convectively unstable modes for a range of wave numbers and frequencies. Figure 5.18 shows how the wave number k_r and spatial growth rate k_i change for real frequencies ω_0 for basis states using $r = 6$ and two values of η. The quantity ω_i is practically zero everywhere, verifying that the found dispersion indeed describes a convective mode for real frequency $\omega_0 = \omega_r$. The spatial growth rate k_i and the zonal wave number k_r do depend strongly on the frequency of the forcing ω_0, although a detailed analysis of the convective dispersion relation in figure 5.17 seems problematic due to the limited number of data points and the relatively small frequency-range covered.

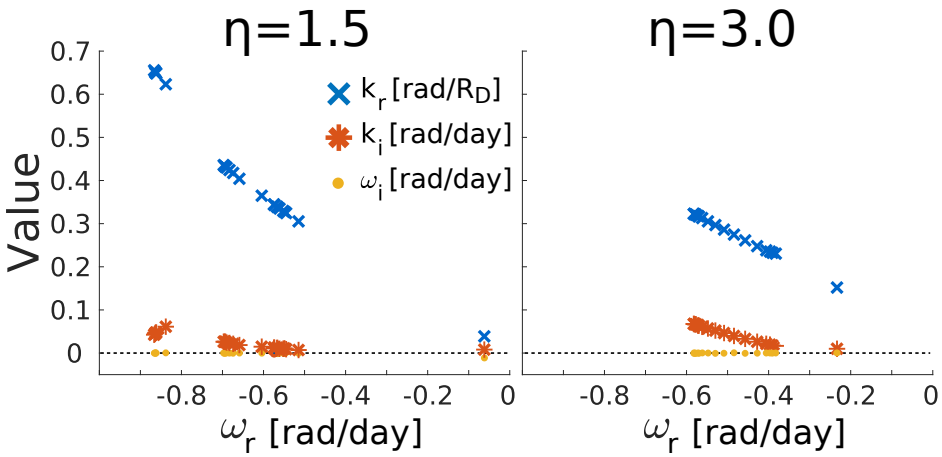

Fig. 5.18 Dispersion relation for a convectively unstable mode of two basic state profiles with $\rho = 6$ and different magnitudes η obtained using the mapping approach and input values $0.02 \leq k_0 < 0.6$.

A main reason for the limited frequency range is due to the fact that the procedure used to obtain figure 5.17 relies on mapping out a large area of the dispersion relation in order to find points with $w_i = 0$, without any prior knowledge about the dispersion relation itself. With such a "brute-force" mapping approach it can be computationally expensive to obtain the dispersion relation for a sufficiently wide range of real frequencies w_0. We therefore also implemented a more direct, iterative method based on a linear argument to obtain the convective dispersion relation. The aim of this **stepping approach** is to find the function $\omega(k)$, while we can only access the two distinct functions $\omega(c)$ and $k(c)$. Assuming the complex dispersion relation $k(c)$ is analytic we can use the unique, local, complex derivative $k'(c) \approx \Delta k/\Delta c$ to estimate the change in $\omega = kc$:

$$\begin{aligned} \Delta\omega &= c\Delta k + k\Delta c \\ &\approx (ck' + k)\Delta c. \end{aligned} \tag{5.22}$$

Next we set either $\Delta\omega_r$ or $\Delta\omega_i$ equal zero and solve for Δc to obtain

$$\begin{aligned} \Delta\omega_i = 0 &\implies \mathrm{Im}\left[\overbrace{(c\Delta k + k\Delta c)}^{=M}\Delta c\right] = 0 \implies \Delta c_i = -\frac{M_i}{M_r}\Delta c_r \\ \Delta\omega_r = 0 &\implies \mathrm{Re}\left[M\Delta c\right] = 0 \implies \Delta c_i = \frac{M_r}{M_i}\Delta c_r. \end{aligned} \tag{5.23}$$

This allows us to constructively choose a Δc for which either the real or complex part of $\Delta\omega$ vanishes. Hence, once we found a single convectively unstable point we can easily obtain the full convective dispersion relation by following a path $\omega(c)$ with constantly vanishing imaginary part. In addition we can choose to keep the real part of ω fixed and only vary ω_i, which will become useful in section 5.2.4. Figure 5.19 shows the dispersion relation found following the described iterative method for a basis state with fixed width $\rho = 6$.

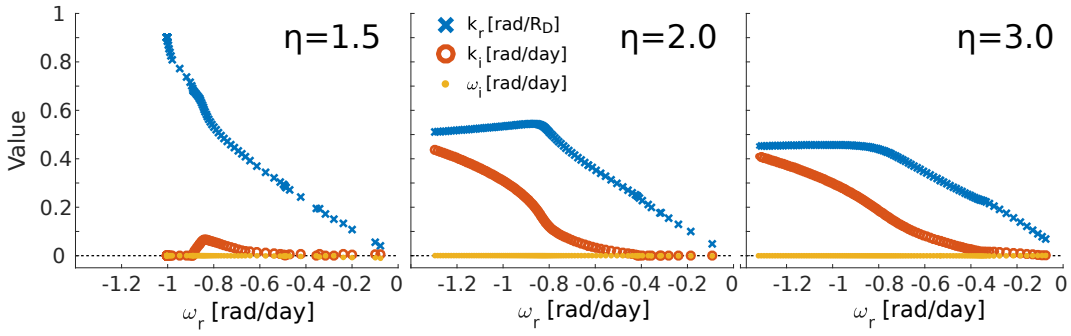

Fig. 5.19 Convective dispersion relation for flows with meridional scale $\rho = 6$ and different magnitude η calculated using the stepping approach based on equation 5.23.

Several observations can be made. At first we find the plots to show a clear qualitative difference between the case with $\eta = 1.5$ and the cases using $\eta = 2,3$. As will be discussed in more detail later this indicates the transition of the system from being absolutely stable to being absolutely unstable. Here the merging point of two modes of the dispersion relation crosses the real ω axis and our iterative stepping method starts to follow different arms of the function $k(\omega)$ for frequencies exceeding the absolute frequency, i.e. for $|\omega| > 0.87$. The concept of absolute instability is illustrated in figure 5.9. The discontinuous nature of the profiles is particularly apparent for $\eta = 2$.

Further one can see a distinct maximum spatial growth rate in the case $\eta = 1.5$ and one can therefore assume the corresponding wave number of $k_r \approx 0.6$ to be the dominant mode. For the other two cases the convective dispersion relation would only hold up to the absolute frequency, i.e. for $|\omega| < \omega_a \approx 0.87$. Beyond that the relation seems to follow a mode that does not lie within the integration contour C of equation 5.10 any longer.

The concept can be understood by looking at the left schematic of figure 5.9. At the point k_a two different modes merge and we can therefore not distinguish between them. If we start following one Bromwich image (e.g. the green curve) we can easily swap to the other one (purple curve) at the absolutely unstable point. Figure 5.19 supports this interpretation since for $\eta = 2,3$ and $\omega_r > 0.87$ the real part of k stays effectively constant, while k_i increases rapidly. This suggests a vertical movement in k-space and hence a penetration of the C integration contour in figure 5.9 and with it a swap into the other mode. Since this mode lies outside the integration area it can not be considered as physically relevant. In any case, the absolute instability of these basis states would dominate the long time behaviour and the presence of convective instability would become negligible anyway.

The qualitative and quantitative structure of the dispersion relation in figure 5.19, found using the stepping approach shown in equation 5.23, however, seems to agree well with the corresponding profiles in figure 5.18, found by a simple mapping approach illustrated in figure 5.17. This gives confidence in both methods and the results of the analysis.

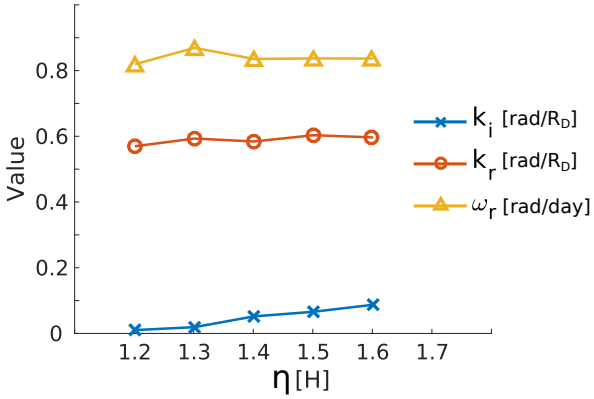

Fig. 5.20 Wave number and frequency for the fastest growing convective mode of background states with basis state width $\rho = 6$ and different basis state magnitudes η.

Figure 5.20 shows the sensitivity of the maximum growth rate and the corresponding frequency and wave number of the convective instability. As can be seen ω and k_r stay almost unchanged, while k_i seems to increase with the magnitude η of the basis state specified in section 5.2.2.

5.2.4 Absolute stability

As we perturb c_r around a temporally unstable solution with wave number k_0 we find that the functions $k(c)$ and $\omega(c)$ vary in the complex plane. Plot 5.21 illustrates the behaviour of the first two modes, defined according to the labelling procedure described in section 5.2.3. It can be seen, that, as we gradually increase k_0 (indicating where the blue paths hit the real k axis), the paths of mode 1 and 2 move closer together and each seem to transform into two distinct, almost piecewise linear, branches,

rather than a single smooth path. At $k_0 \approx 0.35$ the two modes seem to merge and subsequently swap one of their respective "branches" and move apart from each other.

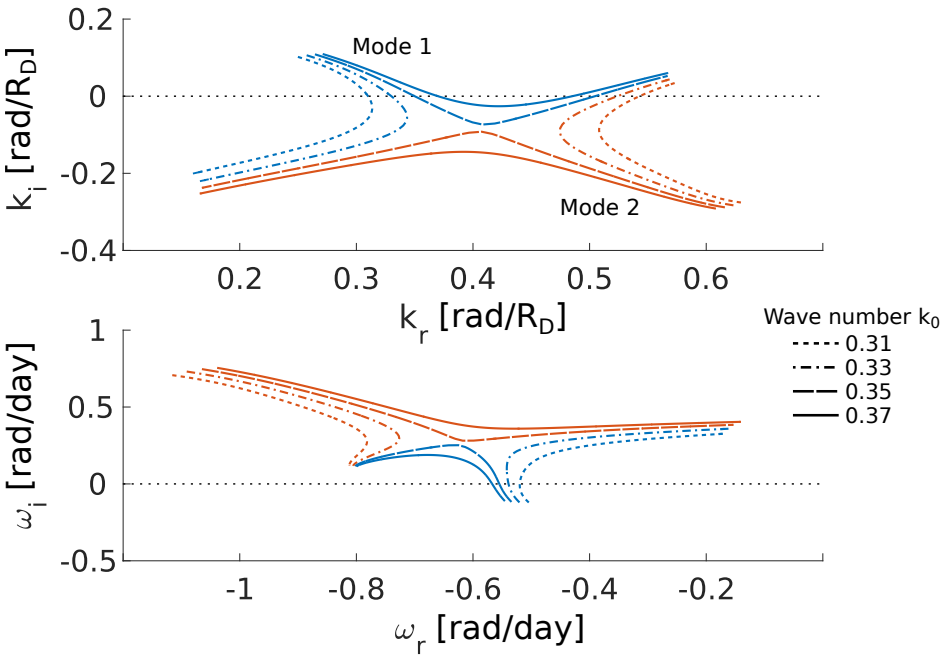

Fig. 5.21 Complex frequencies and wave numbers for imposed waves speeds with real part perturbed around the fastest growing solution of the temporal instability problem for $0.045 \leq k_0 \leq 0.082$. The modes are labelled according to their distance in k-space to the temporally unstable solution or the solution corresponding to the nearest value of perturbed wave speed, as described in section 5.2.3.

This sort of merging and interchange of branches of two different modes as we change c_r can also be observed in the meridional structure of the perturbation height anomaly h'. Figure 5.22 displays the first two modes for a values of c mapped around a temporally unstable solution with $k_0 = 0.33$. The transition between the two modal structures does occur when $k_i(\text{mode } 1) = k_i(\text{mode } 2)$.

After the merging, figure 5.23, there is no more such apparent bi-modality visible. This suggests that the different spatial structures do indeed correspond to the branches of two different modes in k-space.

The behaviour described in this section and illustrated in figure 5.21 corresponds to a saddle point in the complex dispersion relation $\omega(k)$, i.e. a point with $\mathrm{d}\omega/\mathrm{d}k = 0$. As explained in section 5.2.1, such a point suggests the existence of absolute instability (see e.g. Huerre and Monkewitz [1990],Pierrehumbert [1986]). In contrast to a convective instability, where perturbations travel downstream fast enough so they eventually decay at any fixed point in space, an absolute instability leads to perpetual growth of the anomaly at (and away from) the point where the perturbation was initially induced.

As explained in section 5.2 and illustrated in figure 5.7, the underlying idea is based on the existence of two modes with oppositely signed group velocities $\mathrm{d}\omega/\mathrm{d}k$ in cases where ω_i is sufficiently large, e.g. a system where the forcing magnitude increases rapidly. As one reduces the temporal growth rate

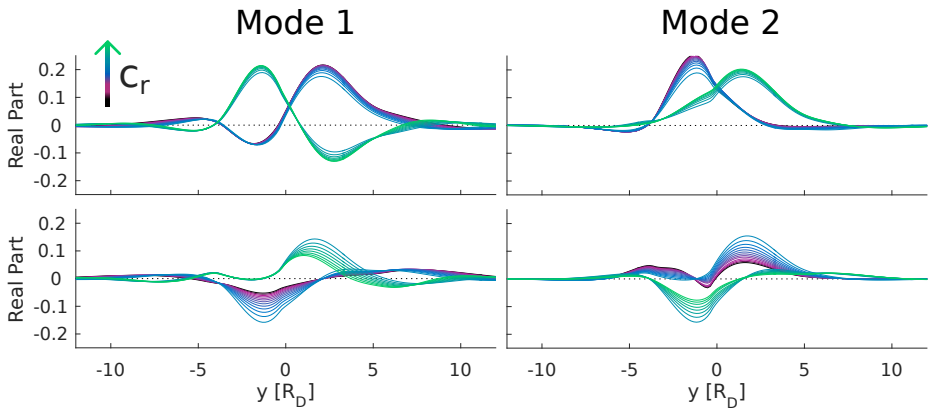

Fig. 5.22 Rapid change in mode structure for gradual change in c_r and a fixed value of c_i corresponding to the temporally most unstable mode at $k_0 = 0.33$.

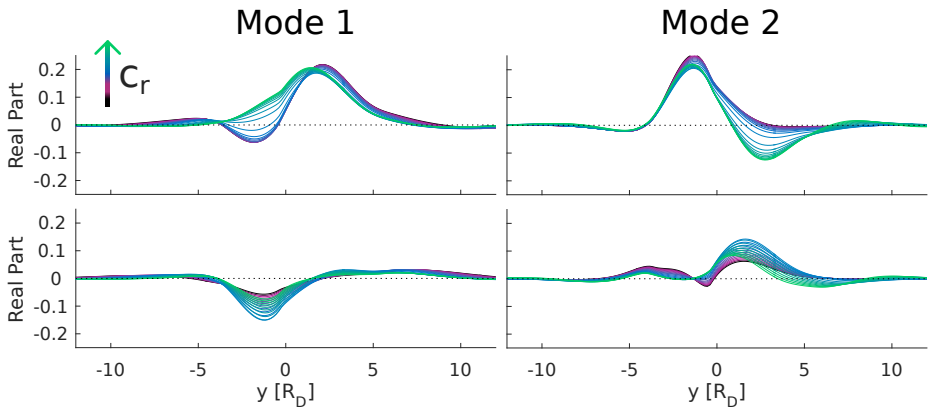

Fig. 5.23 Same as figure 5.22, but for $k_0 = 0.37$.

and approaches a steady forcing magnitude the group velocities of both modes vanish[1]. A system is considered as absolutely unstable if the two modes merge at a point in k-space with wave number k_a and corresponding frequency ω_a, where $\mathrm{Im}(\omega_a) > 0$. At this point the two modes can interfere constructively and energy can grow in place without propagating since the group velocity is zero. Hence, we have $\mathrm{d}\omega/\mathrm{d}k = 0$ and are mathematically describing a saddle point in $\omega(k)$.

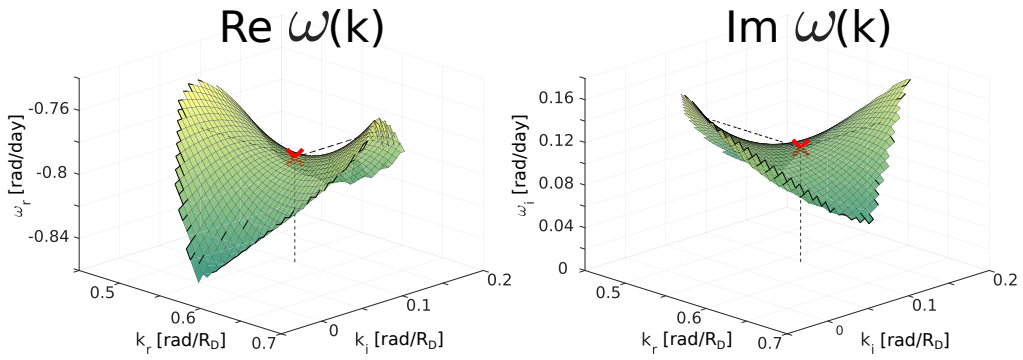

Fig. 5.24 Complex dispersion relation $\omega(k)$ showing a pronounced saddle point (red cross), i.e. a point with vanishing complex gradient.

To practically analyse the system for absolute instability we start by evaluating the frequency and wave number according to equation 5.19 for various values of c, mapped around a specified temporal solution k_0 near temporal growth rate maximum indicated in figure 5.12. Next we can map ω against k use the saddle point criterion to find points $\omega_a(k_a)$ with vanishing complex gradient. The saddle point of the dispersion relation for a basis state with $\eta = 3$ and $\rho = 3$ is displayed in figure 5.24.

For the saddle point to actually correspond to absolute instability we require the two merging modes $k(\omega)$ to approach it from opposite sites of the real k-axis as we lower the Bromwich contour and approach $\omega \to \omega_a$,see Pierrehumbert [1986] and figure 5.9. To check this is the case we plotted $k(c)$ for values mapped around a specified c and coloured them according to their value of ω_i. The results are given in figure 5.25. It can be seen how lines of fixed ω_i get bent towards the saddle point as $\omega_i \to \omega_{a,i}$. The contour lines indeed seem to originate from opposite k half-planes.

Similar to the convective instability calculation[2] the pure mapping of arbitrary values of c around a specified value can be computationally challenging, especially since we find more and more spurious numerical modes away from them temporal solution. Hence, to increase the range of output values, we again make use of the iterative stepping scheme introduced in equation 5.23. Starting at the theoretically calculated saddle point we create lines of constant ω_i around various points with $\omega_i = \omega_{a,i}$ for the two first modes. These then represent the Bromwich contours as they approach ω_a. Plotting the corresponding values of k we can track the merging roots of the dispersion relation and the deformation

[1] They have to in order to achieve a steady state in the long time limit.
[2] See figure 5.19.

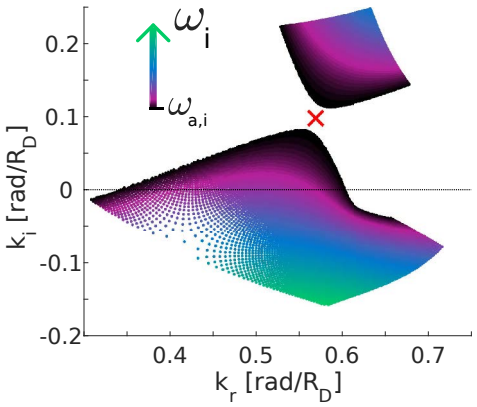

Fig. 5.25 Wave numbers $k(c)$ relating to wave speeds c mapped around a temporal solution. Colours indicate corresponding temporal growth rates $\omega_i > \omega_{a,i}$. The red cross gives the location of the calculated saddle point. The used basis states is described by $\eta = 3$ and $\rho = 6$.

of the Bromwich images as they approach the saddle point from opposite sides of the real k-axis. The results are shown in figure 5.26.

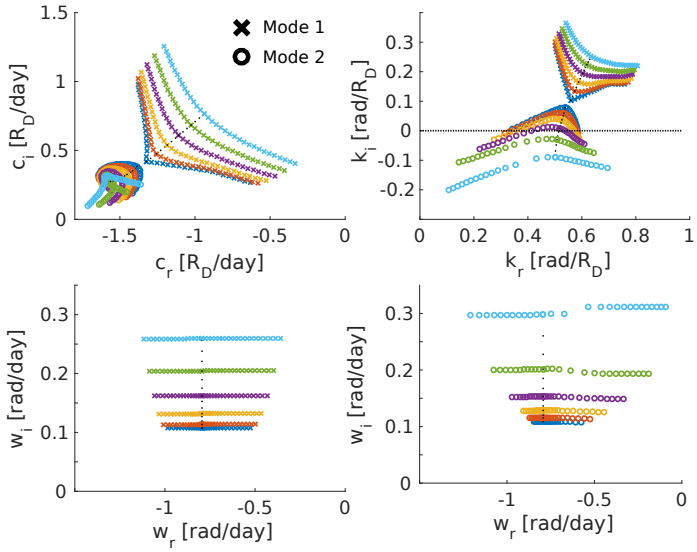

Fig. 5.26 Numerically obtained Bromwich images of the first two modes as the Bromwich contour gets lowered to $\omega_i \to \omega_{a,i}$.

After ensuring the saddle point does correspond to absolute instability we can perform the calculation for various basis states to investigate the sensitivity of the absolute instability on the specified profile. Figure 5.27 shows the absolute frequency ω_a and wave number k_a as function of basis flow magnitude η.

Two main observations can be made:

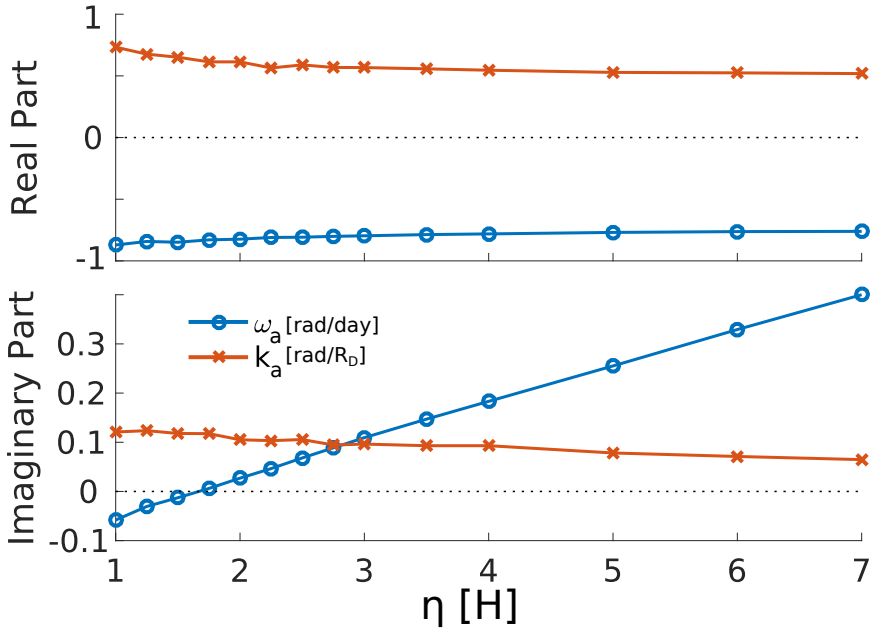

Fig. 5.27 Change in ω_a and k_a for increasing flow strength of the idealised basis state with $\rho = 6$.

- The three quantities $\omega_{a,r}$, $k_{a,r}$ and $k_{a,i}$ seem not very sensitive to changes in basis state magnitude. Their absolute values only increase slightly for weaker basis flows.
- The temporal growth rate on the other hand depends strongly on η. In particular $\omega_{a,i}$ changes sign at $\eta \approx 1.65$. Here the basis stated transitions from being absolutely stable to being absolutely unstable.

The idea of a mode being absolutely stable would correspond to a trapping of the C integration contour, like shown in figure 5.9, but for cases where we lower the Bromwich contour 5.8 into the negative imaginary ω half-plane. This is a valid procedure since any saddle point contribution with $\sigma < 0$, coming from $\sigma_a < 0$, will give vanishing long time contributions to the integral defined in equation 5.14.

We also investigated the characteristics of the absolute instability for various values of the width ρ of the basis state flow. Figure 5.28 illustrates similar qualitative behaviour as for changes in η, in the sense that the system becomes more stable for larger length scales and $\omega a, i$ does even become negative for certain parameters.

5.3 Numerical stability experiments

Section 5.2 presented results of a stability analysis for zonal shear flows of idealised profiles defined in equation 5.18. In this section we will analyse the stability of shear flows using a numerical approach. At

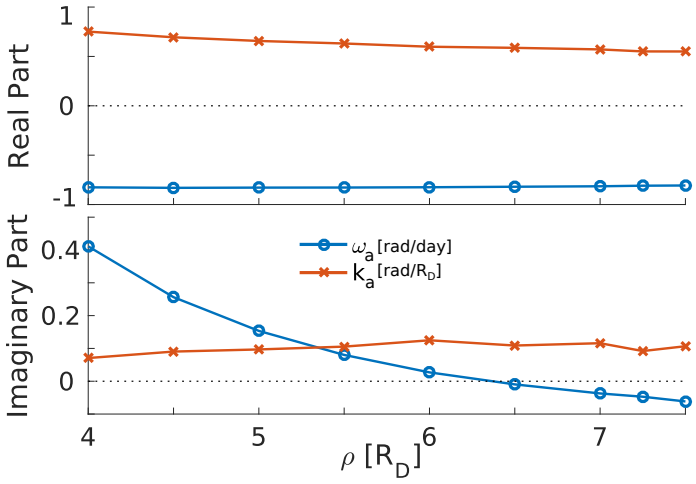

Fig. 5.28 Changes in absolute stability based on the width of the basis flow with $\eta = 3$.

first, in subsection 5.3, we are going to use the same idealised profiles and compare our results with the outcome from earlier in this chapter. We will then, in subsection 5.3.2, try to transfer our analysis methods and findings onto profiles extracted from the steadily forced experiments described in section 5.1.

5.3.1 Stability of a zonal plume

To verify the applicability of the developed stability theory we conducted a series of numerical simulations, based on a linearised version of the quasi-geostrophic single layer model described in section 2.3. The simulations are performed as perturbation experiments, with the system being linearised about the same steady and zonally symmetric basis state as described in equation 5.18 and displayed in figure 5.11, for various radii ρ and magnitudes η, and the evolution equations of the model are linearised about this state. The full model equations for the perturbations $\hat{h}$ and $\hat{q}$ of the basis state with $\bar{h}$ and $\bar{q}$ are given by

$$\begin{aligned} \hat{q} &= \partial_x^2 \hat{h} + \partial_y^2 \hat{h} - \hat{h} \\ \partial_t \hat{q} - \partial_y \bar{h} \partial_x \hat{q} + \partial_x \hat{h} \partial_y \bar{q} &= F_0 F(x,y,t). \end{aligned} \tag{5.24}$$

We perturb this basis state by applying a forcing of the form[1]

$$F = \begin{cases} F_0 \sin(\omega_0 t) \cos^4\left(\frac{\pi x}{2\rho}\right) \cos^4\left(\frac{\pi y}{2\rho}\right) & \text{for } t > 0, |x|, |y| < \rho \\ 0 & \text{otherwise} \end{cases},$$

with magnitude $F_0 = 10^{-4}$. The main free parameter for a given basis state is the real forcing frequency ω_0. The conceptual idea of the experiments is that the forcing with fixed frequency will only excite waves and unstable modes of exactly that frequency. Hence it should be possible to numerically construct a dispersion relation for the set basis state. To the far west of the forcing the system has a zonally localised sponge region damping non-zonally-symmetric perturbations, attempting to simulate an infinitely extended domain. Experiments without sponge region and larger domain sizes gave similar results.

Figure 5.29 visualises the response of two systems to a forcing with $\omega_0 = 0.8$. This frequency corresponds roughly to the maximum growth rate of the convective instability of the system (see figure 5.19). The top panel shows the response of the linear model at day 200. Both basis states exhibit a strong spatial structure in the zonal direction, indicating spatio-temporal instability. However, the perturbations of the system with $\eta = 3$ do also grow in time and are hence much more dominant after a certain time has passed. This indicates an absolute instability of the basis state. It should be noted that the temporal growth happens throughout the zonal extent of the domain, i.e. in particular at the origin and even for $x > 0$. However, the pronounced spatial structure makes it difficult to see any perturbations near $x = 0$.

The bottom panel shows the response of the same basis states but using the full QG single layer model presented in equation 5.2, not linearised about the basis state. We can observe only small differences to the linear case for $\eta = 1.5$. For the state with $\eta = 3$, however, the non-linearity of the system limits both, the temporal and the spatial growth, drastically and hence the perturbations are much smaller than when using linearised equations. Although, since the instability still occurs over the full length of the domain the initially zonally symmetric basis state now breaks into isolated vortices everywhere.

Figure 5.30 shows the response of the non-linear QG model to a localised, steady forcing with different magnitudes F_0 as described in section 5.1. For weak magnitudes the flow develops a steady plume, which stretches out to the west of the forcing. The plume then gets gradually perturbed as it travels westward and eventually breaks into isolated patches, similar to what is shown in the bottom left plot of figure 5.29.

For stronger magnitudes we observe formation and shedding of vortices within the forcing region. We conclude that the case with $F_0 = 0.3$ does produce a zonally extended plume which becomes convectively unstable and breaks up downstream. The forcing with $F_0 = 0.5$ on the other hand does,

[1] Although the precise structure of the forcing seems to have, as expected, little influence on the results shown.

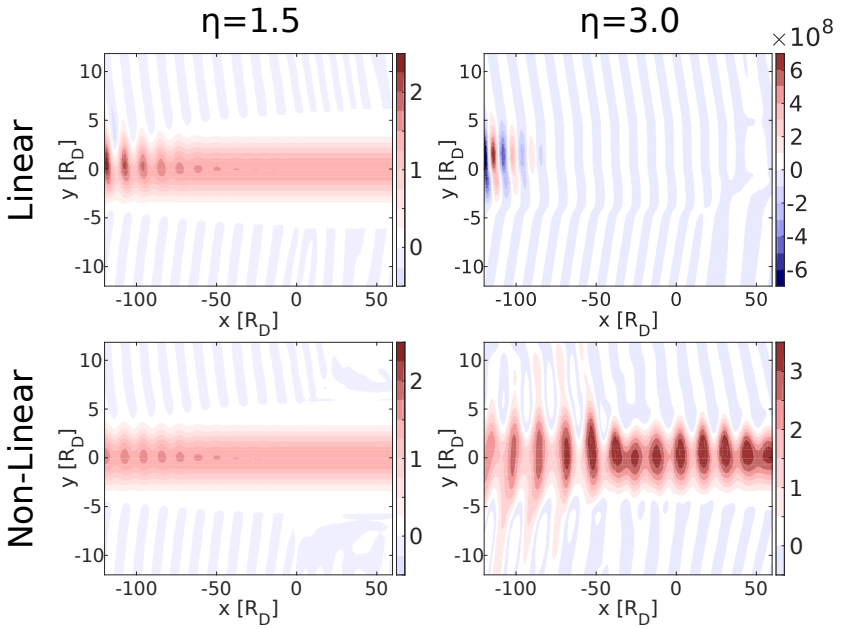

Fig. 5.29 Day 200 snapshots of the height anomaly response of zonally symmetric basic state profiles with $\rho = 6$ and different magnitudes η to a small periodic perturbation at the origin. The model uses linear (top) or non-linear (bottom) advection.

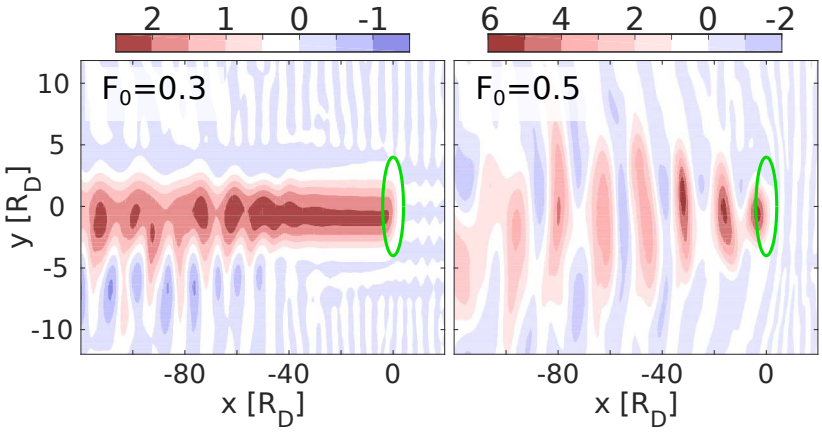

Fig. 5.30 Day 300 snapshots of the height anomaly response to a localised, steady forcing (green ellipses) with forcing magnitudes F_0 and length scale $r_0 = 4$. The model exhibits a different behaviour (break-up and shedding) qualitatively similar to the responses shown in figure 5.29 (convective and absolute instability).

conceptually, produce a plume which is absolutely unstable. Hence it quickly breaks up into isolated patches everywhere and therefore inhibits the actual formation of a steady plume. The response is therefore similar to what is shown in the bottom right plot of figure 5.29. It should be noted that we do of course not have any anomaly travelling eastward in the experiments in figure 5.30, and hence do not find any vortices developing at $x > 0$.

Figure 5.31 shows the spatial and temporal structure of the response of various basis states with $\rho = 6$. The case with $\eta = 1.5$ shows practically no instability in time but a clearly exponentially growing spatial structure. Even though present for all three displayed frequencies the spatial growth seems to be strongest for $\omega_0 = 0.8$ in the $\eta = 1.5$ case.

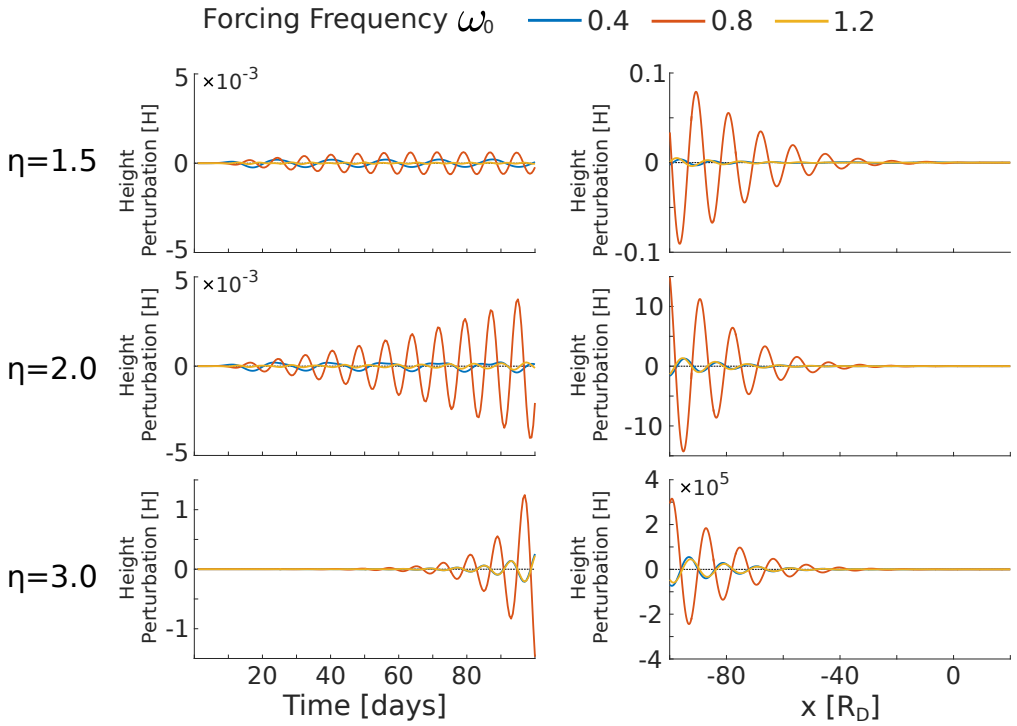

Fig. 5.31 Temporal evolution at $x = -10$ (left) and zonal structure at day 100 (right) of basis states with $\rho = 6$ and different η for locally forced perturbations with forcing frequency ω_0. All anomalies were averaged over $-5 < y < 5$ and normalised to either vanishing value at day 1 or zero zonal mean.

For $\eta = 2,3$ we find both, a temporal and a spatial growth of the signal. But also in these case the growth rates seem to peak for frequencies of $\omega \approx 0.8$. The results agree with our interpretation of figure 5.29 and suggest a convective instability in the case $\eta = 1.5$ and absolute instability for the other basis states. The maximum growth rates at $\omega_0 = 0.8$ are in agreement with the maximum spatial growth rate presented in figure 5.19 and the value of the absolute frequency $\omega_{a,r}$ shown in figure 5.28. In the case of the absolutely unstable basis states we do force with a given frequency ω_0. However, numerical imperfections and a 10-day switch on process introduce perturbations over a range of other frequencies, including $\omega_{a,r}$. Hence the absolute mode gets triggered in all cases and starts growing,

quickly dominating the system. When forced with $\omega_0 \approx \omega_{a,r}$ the corresponding mode gets triggered explicitly and much stronger, hence the response is stronger as well.

To better understand the response in terms of convective and absolute instabilities we performed Fourier decompositions of the height anomaly signal in time and space. Again, there is a clear difference between the cases with $\eta = 1.5$ and $\eta = 3$. For the first basis flow magnitude we do find sharp temporal peaks, located almost exactly at the forcing frequency. Correspondingly we observe isolated and pronounced spatial Fourier peaks for the different values of ω_0. Note that the Fourier peaks are normalised to have equal integrals over the domain range[1].

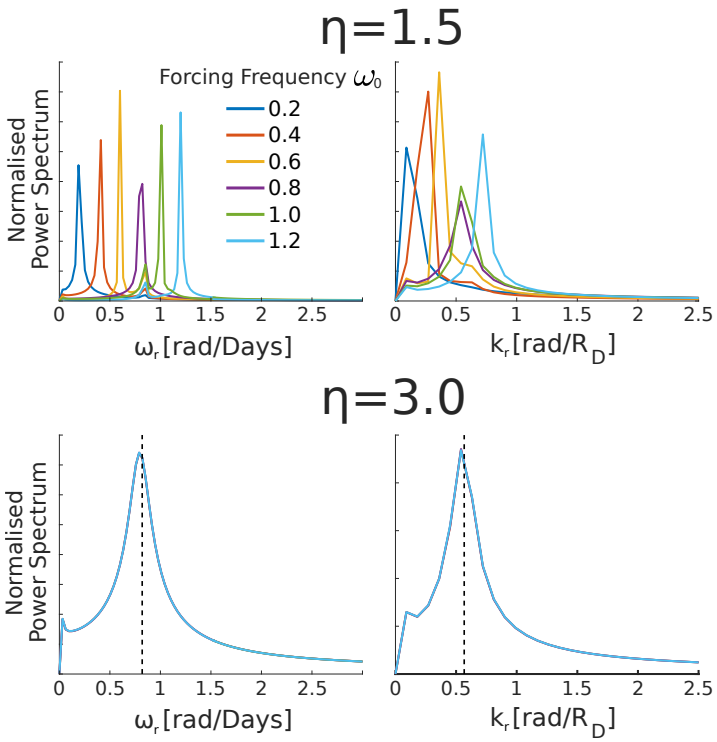

Fig. 5.32 Temporal (left) and spatial (right) Fourier decomposition of the azonal response along $y = 0$ between days 100 and 200 and $-80 < x < -10$ (averaged over the respective spatial/temporal range) for the response of different basis states with $\rho = 6$ to a periodic forcing with frequency ω_0. Dashed lines indicate theoretical prediction of absolute frequency/wavenumber according to figure 5.28. The bottom panel shows all 6 values of ω_0 but the spectra are identical.

For the case with a stronger basis flow and $\eta = 3$ we do not observe isolated temporal peaks, but both power spectra (temporal and spatial) are independent of the forcing frequency and the corresponding spectra are practically identical. This kind of excitation of a specific frequency can, again, be explained by the presence of an absolute instability. The vertical, dashed lines in the bottom panel illustrate the values of $\omega_{a,r}$ and $k_{a,r}$ according to figure 5.28.

[1] Their actual magnitude varies similar to the magnitude of the perturbation shown in figure 5.31, with a maximum near $\omega_0 = 0.8$.

Since the theoretical prediction in section 5.2.4 predicts a strong sensitivity of the temporal growth rate $\omega_{a,i}$ to changes in basis flow strength we can expect the absolute mode to only grow slowly for states with η just above the threshold value of $\eta = 1.65$. Figure 5.33 shows the temporal peaks of a Fourier decomposition over a varying time window of 30 days when using a constant forcing frequency $\omega_0 = 0.4$ and different values of basis flow strength.

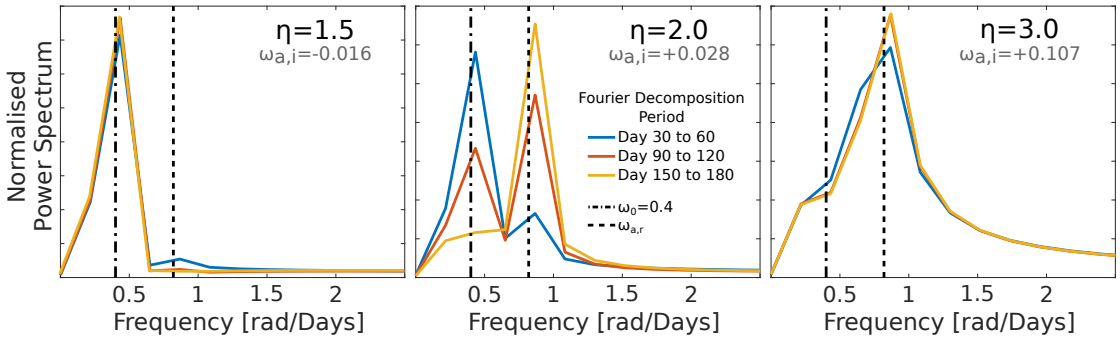

Fig. 5.33 Temporal Fourier decomposition of the azonal response along $y = 0$ averaged over $-50 < x < -10$ and different time periods for basis states with $\rho = 6$ and different magnitudes η, giving rise to different absolute growth rates $\omega_{a,i}$. The system is forced with constant frequency $\omega_0 = 0.4$.

In the case with $\eta = 1.5$ the system is absolutely stable, i.e. $\omega_{a,i} < 0$. The response shows a clear and localised peak exactly at the forcing frequency independent of the analysed time period. However, if we enter a system with $\eta = 2$, and hence weak absolute instability, we initially observe the same temporal peak at $\omega = \omega_0$ when analysing early times between days 30-60. As we move the time window to later times we see the peak at the forcing frequency becoming weaker (in a relative sense) and a second peak grows at the position of the predicted absolute frequency $\omega_{a,r}$. This behaviour illustrates the domination of the system by absolute instability for later times, where the time scale for the instability to take over is given by $\omega_{a,i}^{-1}$. Using a strong background state with $\eta = 3$ the response is dominated by the strong absolute instability right away.

We can combine the numerically obtained results shown in figure 5.32 with the theoretically derived dispersion relation presented in figure 5.28. Plotting the real positions of the spatial Fourier peaks $k_{r,exp}$ for the case $\eta = 1.5$ against the corresponding temporal ones we find very good agreement for $|\omega_r| < 0.8$. The results are illustrated in figure 5.34. As argued in section 5.2.4 it is not clear if the theoretical dispersion relation can be trusted for $|\omega_r| > \omega_{a,r}$, which can explain the disagreement in that region.

5.3.2 Application to steadily forced experiments

Our aim is to use the presented spatio-temporal instability analysis as a theory to explain and predict the different behaviours of the single-layer QG model introduced in section 2.3 when forced by a localised,

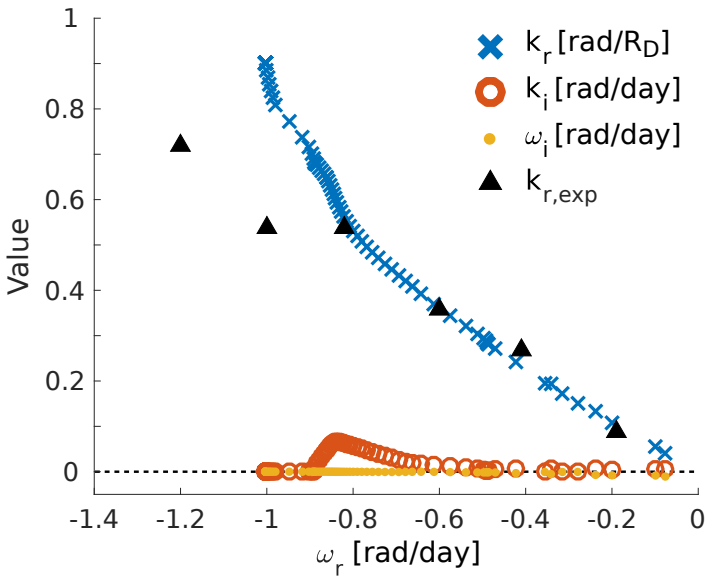

Fig. 5.34 Dispersion relation obtained from numerical experiments (figure 5.32) for the case $\eta = 1.5$ and $\rho = 6$ in comparison to the theoretical predicting presented in figure 5.19.

steady mass source. Figure 5.35 illustrates the different states we observe depending on the forcing scale r_0 and magnitude F_0. We generally observe a steady response for weak and/or large scale forcing. If the forcing is strong and/or of small scale, on the other hand, we find the response to shed vortices produced inside the forcing region. For any intermediate forcing strength/scale we observe a state which is almost steady near the forcing and breaks up into isolated patches downstream.

To classify the type of response to a certain forcing we looked at the temporal behaviour close to the forcing and the zonal structure of the surface displacement. In the **steady** cases we expect no strong variations anywhere west of the forcing at any time, meaning we should find the zonal and temporal variances to be small. We classify the system to be in the **break-up** state if the surface displacement stays steady near the forcing region but develops strong temporal (and zonal) variations further to the west. And we decided the response to be in the eddy **shedding** regime if it shows strong temporal (and zonal) variations throughout the domain, in particular near the forcing region. Figure 5.36 displays examples of the three situations in terms of zonal profiles and time series.

As can be seen the steady and break-up states do not show any temporal variability at $x = -10$, i.e. near the forcing (note that the curves for $F_0 = 0.05$ and $F_0 = 0.3$ in the middle panel of figure 5.36 lie on top of each other at a constant value of one). The shedding state exhibits temporal deviations of the order of one (meaning of the order of the corresponding time mean) near and away from the forcing. The temporal variance, however, increases with distance from the forcing region in the break-up state ($F_0 = 0.3$) and time variations are clearly non-negligible at $x = -80$.

This gives us a potential way to define the three states in a more quantitative way. Equation 5.25 shows a set of possible criteria to define the states in terms of temporal variance $\langle h^2 \rangle_t$ and mean $\langle h \rangle_t$ of the

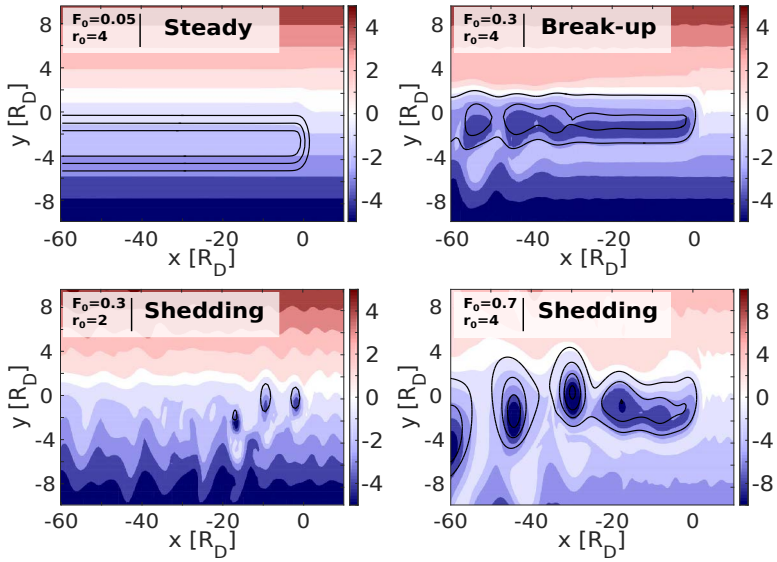

Fig. 5.35 Day 300 PV snapshots of steadily forced experiments using different forcing parameters and exhibiting various states with different behaviour and structure. A set of realistic profiles is extracted (see figure 5.37) by averaging the height anomaly response at $x = -10$ between days 300 and 1000.

height anomaly field near and away from the forcing region.

$$\begin{aligned}
\textbf{Steady:}\ & \left\langle h(x<0)^2 \right\rangle_t \approx \left\langle h(x<0) \right\rangle_t^2, \\
\textbf{Break-up:}\ & \left\langle h(x\approx -r_0)^2 \right\rangle_t \approx \left\langle h(x\approx -r_0) \right\rangle_t^2 \\
& \quad \text{and } \left\langle h(x\ll -r_0)^2 \right\rangle_t \gg \left\langle h(x\ll -r_0) \right\rangle_t^2, \\
\textbf{Shedding:}\ & \left\langle h(x<0)^2 \right\rangle_t \gg \left\langle h(x<0) \right\rangle_t^2.
\end{aligned} \tag{5.25}$$

We want to point out that equation 5.25 is only an attempt to define the three states of the system in a systematic way. The shedding (and break-up) state is intrinsically highly variable and, as shown earlier, a result of a linear instability limited by non-linear processes. The complexity of the system requires that strict criteria are used with extreme caution. The classification via equation 5.25 does therefore not involve any hard threshold values and additionally requires the (subjective) assessment of the evolution of the full height anomaly and PV fields in terms of qualitative vortex- or beta-plume-formation (see figure 5.3).

In the following we will use the idealised spatio-temporal instability theory developed in this chapter to explain the three different states we observe in our experiment. To do so we distinguish between two sets of profiles.

- **Idealised profiles**: given by equation 5.18 with defining parameters ρ and η.

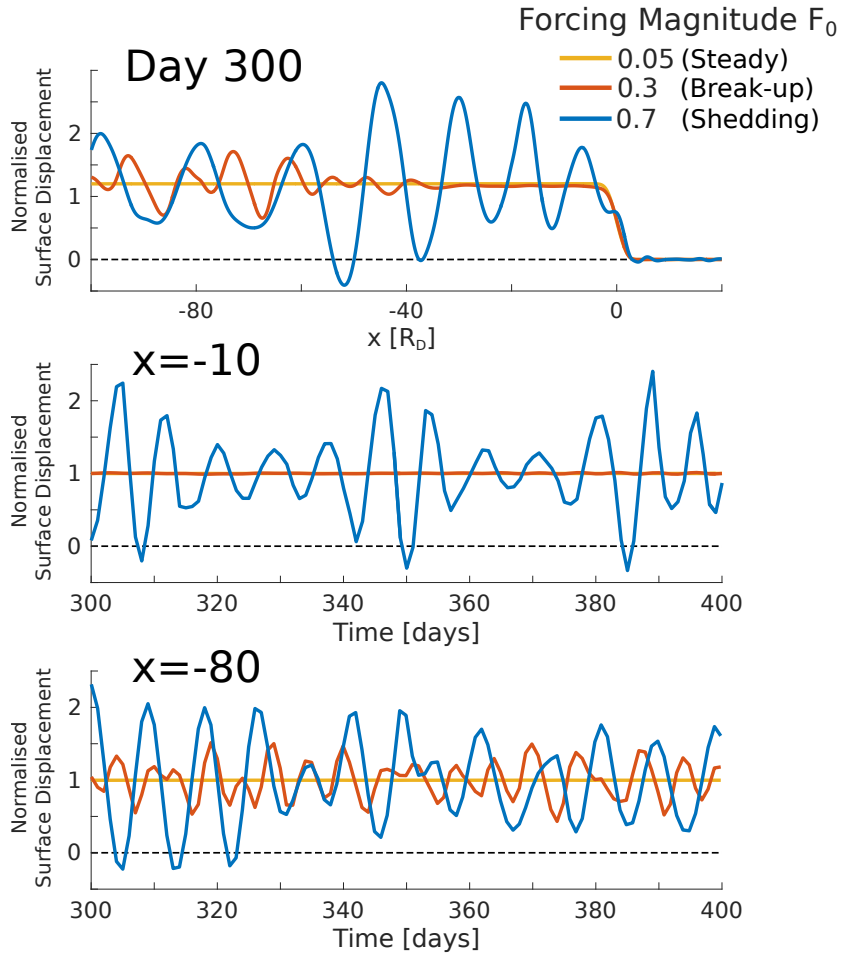

Fig. 5.36 Examples of zonal profiles at day 300 and time series near the forcing ($x = -10$) and far to its west ($x = -80$) for different forced experiments with $r_0 = 4$ used to classify the state of the flow. All profiles are averaged between $-5 < y < 5$ and normalised by their mean over the given time or longitude range.

- **Realistic profiles**: extracted from forced experiments shown in figure 5.35, with forcing profile defined in equation 2.4. The profiles are obtained by averaging along the $x = -10$ line between days 300 and 1000. These states are defined by the forcing parameters r_0 and F_0.

Figure 5.37 shows an example of an idealised and a realistic profile and their corresponding wind and PV gradient structures. The idealised fits reproduce many features of the realistic profiles, including a reversal of the PV gradient south of the origin as well as small and smooth secondary extrema of the PV gradient near $y = \pm\rho$.

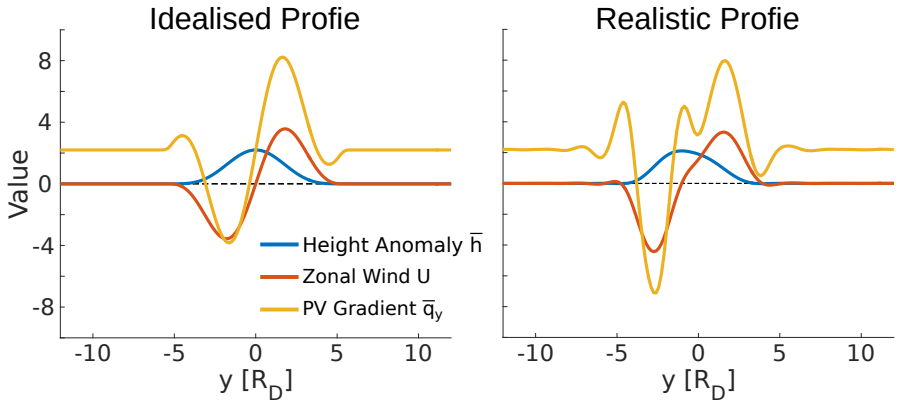

Fig. 5.37 Examples of different basis state height anomaly profiles and corresponding structures of zonal wind and meridional PV gradient: idealised profile with $\rho = 5.4$ and $\eta = 2.2$ (left) obtained as fit of realistic profile (right) with forcing $r_0 = 4, F_0 = 0.3$.

To link the set of realistic profiles to corresponding idealised states we fitted the height anomaly structures of the latter onto the former and hence obtained a set of idealised width ρ and magnitude η for each.

The idealised nature of the fit leads to slightly changed stability characteristics compared to the actual realistic profiles. Figure 5.38 shows comparisons of realistic height anomaly profiles and the corresponding idealised fits. Table 5.1 then gives an example of theoretically derived stability characteristics for different profiles.

Table 5.1 Comparison of stability analysis results for two realistic profiles and their corresponding fits (see figure 5.38).

Profile	ω_a	k_a
$r_0 = 4, F_0 = 0.5$	$-0.810 + 0.203i$	$0.471 + 0.118i$
Fit: $\rho = 5.5, \eta = 3.7$	$-0.795 + 0.257i$	$0.573 + 0.082i$
$r_0 = 4, F_0 = 0.3$	$-0.557 - 0.035i$	$0.495 + 0.071i$
Fit: $\rho = 5.4, \eta = 2.2$	$-0.821 + 0.104i$	$0.609 + 0.097i$

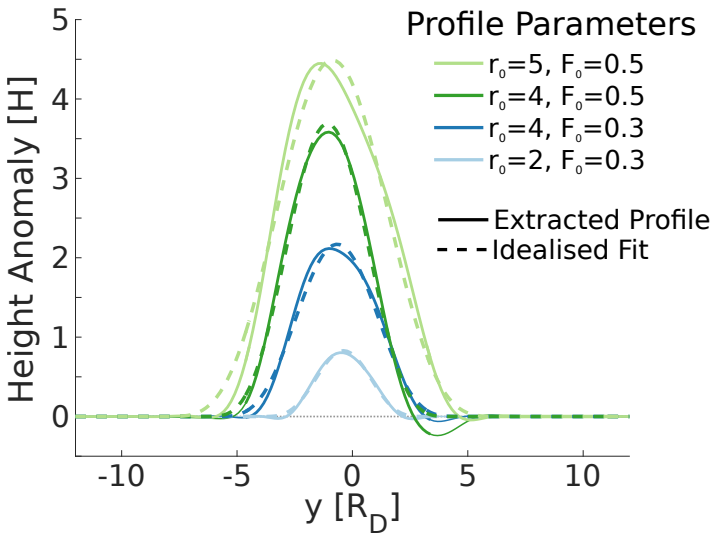

Fig. 5.38 Comparison of meridional height anomaly profiles of various realistic profiles extracted from steadily forced experiments with forcing scale r_0 and magnitude F_0 (solid lines) and corresponding idealised fits (dashed lines). Table 5.1 shows results of the absolute stability analysis (ω_a and k_a) for two of these profiles and fits.

As can be seen from table 5.1, the results of the absolute stability analysis for the realistic profile and the fit are fairly close to each other for the case with $r_0 = 4, F_0 = 0.5$. In particular both values of ω_a predict the system to be absolutely unstable. The system with $r_0 = 4, F_0 = 0.3$ on the other hand shows a significant difference in stability when compared to its idealised fit. While the realistic profile predicts the system to be absolutely stable, with $\omega_{a,i} < 0$, the fit suggests the opposite. However, we can in general assume the fitting to give reasonably good estimates of the stability, especially for very unstable or very stable systems. Also note that the predicted (both, using idealised fit and realistic profile) frequency of the absolutely unstable mode in the case with $r_0 = 4, F_0 = 0.5$ is in very good agreement with the observed value of $\omega = 0.846$ shown in figure 5.6. The good agreement gives confidence that the shedding process can indeed be interpreted as result of an absolute instability.

At last we can combine the gathered information about the experimental results and the results of our theoretical stability analysis of section 5.3 to create a phase map indicating the transitions between the three presented states as we vary the width and magnitude of the forcing. For the theoretical part we expect the behaviour of the response to change in the following way:

- For the flow to become unstable we need the meridional PV gradient to be reversed within some finite region. Generally the minimum PV gradient for the idealised cos^4 profiles will become more negative for stronger forcing. Hence we can follow the approach of Davey and Killworth [1989] and calculate for which forcing magnitude the linear response to a forcing of width ρ leads to such a PV reversal. For any forcing with a magnitude below this threshold we would expect the response to be stable and hence steady.

- Above the described line the flow can be unstable. However, results shown in figures 5.27 and 5.19 suggest that the response will develop convective instability for forcing magnitudes just above the critical threshold for PV inversion, since the flow is (still) absolutely stable. As we increase the forcing magnitude further the flow will become absolutely unstable. Hence, we can expect a transition from convectively unstable to absolutely unstable where $\omega_{a,i}$ changes sign and, on this basis, would predict a change from the break-up into the shedding regime.

Figure 5.39 illustrates the theoretical lines where the minimum PV gradient of the linear solution becomes negative and the temporal growth rate of the absolute instability becomes positive.

We then plotted diagnostics derived from the steadily forced experiments on top of the lines from the idealised theory. The position of each marker corresponding to a certain set of forcing parameters r_0 and F_0 is given by its corresponding idealised fit as illustrated in figure 5.38. The classification of the type of response for each experiment is done by analysing the flow according to figure 5.36.

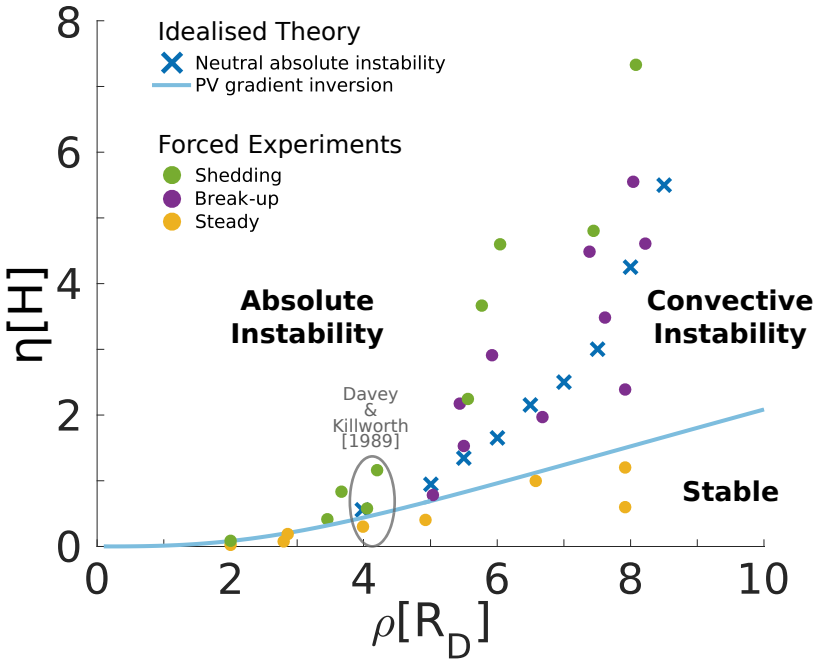

Fig. 5.39 Comparison of theoretically obtained phase map of idealised basis states with fitted realistic profiles obtained from forced experiments. Experiments using the same forcing length scale r_0 as Davey and Killworth [1989] are highlighted.

Figure 5.39 shows a good agreement between the theoretical predictions and the experimental results. Both sets of analyses show a clear division into three regions with states corresponding to the break-up state or convective instability to be unlikely to occur for small forcing magnitudes or small length scales.

Davey and Killworth [1989] discussed the response experiments using a shallow water model forced by a similar steady mass source. They restricted their analysis to a forcing with $r_0 = 3$ and observed only

steady and shedding states, but no convectively unstable break-up behaviour. This could either be due to the fact that they used a rather short periodic channel of length $L_x = 60$ or because the restriction of the forcing length scale puts their experiments in a regime where the break-up state is practically impossible to observe. Figure 5.39 indicates three of our forced experiments with $r_0 = 3$ and their position within the developed phase map. As can be seen the region with inverted PV gradient and $\omega_{a,i} < 0$ is very small here, making it unlikely to observe a corresponding state. However, it is not clear what changes in convective and absolute stability their different choice of β is causing, hence this comparison needs to be done with caution.

5.4 Summary and discussion

This chapter discussed in detail the phenomenon of spontaneous westward shedding of eddies from a steady localised mass source in a single-layer model. Motivated by the observations of three states with qualitatively different temporal and spatial dependency we developed a theory to describe eddy shedding as a result of an absolute instability of the forced flow.

In section 5.1 we summarised and reviewed existing studies on the spontaneous formation of a zonal chain of discrete vortices as response to a steady mass source in general and westward eddy shedding of the monsoon anticyclone in particular. A strong focus of many of these studies was given on the transition from a steady, almost linear beta-plume state to a shedding state with strong time dependence, e.g. when increasing the forcing magnitude at a fixed forcing length scale. One of the main conclusions of this transition was that the phenomenon of westward eddy shedding from the monsoon anticyclone does not rely on e.g. fluctuations in the strength of the forcing, but can emerge spontaneously due to the internal dynamics of the circulation.

In addition to the two known states (steady and shedding) we presented evidence for the existence of a third state that is characterised by a strong spatial dependence of the temporal variability and hence suggests the flow to be convectively unstable. Even though this convectively unstable state might be unlikely to be a good representation of the monsoon anticyclone, its observation motivated a new approach to the problem in the form of a spatio-temporal stability analysis.

We thus performed a comprehensive stability analysis for a certain idealised set of parallel shear flows. Section 5.2 outlined some of the known relevant theories about the concept of spatio-temporal instabilities and its application to two-dimensional (geophysical) shear flows. This involved revisiting the mathematical basics of linear spatio-temporal stability analyses and the corresponding framework of line integrals in the complex plane to identify physically meaningful unstable modes. We then discussed various practical procedures and the numerical implementation of algorithms to identify modes that show unstable behaviour in either a temporal, convective or absolute sense. Unlike other authors we did not restrict our analysis to absolutely unstable modes, but were able to also obtain information on the

convective stability of the system. The proposed procedure can potentially be used to investigate the spatio-temporal stability of other systems as well.

We further applied the different types of stability analysis to various sets of idealised flows aiming to represent a zonally elongated monsoon anticyclone and investigated their stability properties depending on different imposed flow parameters, i.e. the magnitude and meridional scale. Among other results, we found the studied system to develop an absolute instability for strong magnitudes and small meridional length scales, while weak magnitudes and large meridional scales typically lead to convective instabilities or stable behaviour. We were further able to numerically calculate various physical scales, e.g. the required threshold values for the state transitions and the frequency of the resulting unstable mode for a given shear flow profile. The range of found absolute frequencies is in good agreement with the roughly bi-weekly shedding frequency reported by other authors based on monsoon observations. Up to now a theoretical basis of this frequency was lacking.

Finally we applied the developed theory to a set of steadily forced experiments where the parallel shear flow is not prescribed but is directly forced by the heating. We showed that the use of spatio-temporal instability theory can potentially explain the observed transition between the different types of temporal behaviour based on the forcing parameters and allows us to predict certain characteristics of the shedding state, such as the shedding frequency.

Davey and Killworth [1989] proposed a theory to quantitatively estimate the parameter regimes for which the response exhibits eddy shedding. As we have shown, this theory is, however, not valid for large forcing length scales, where the response can enter a regime of convective instability that is not captured by Davey and Killworth [1989]. The spatio-temporal stability analysis performed in this chapter extends the Davey-Killworth theory and allows predictions for a larger range of parameters. Although the monsoon anticyclone is likely to be in a regime in which the Davey-Killworth theory is a good description of the system, our extended theory allows for a more complete conceptual understanding of the processes involved. Further, the presented theory might be of interest for a wider range of fluid-dynamical and geo-physical systems.

The good agreement of the predicted and numerically observed state transitions and shedding frequencies gives confidence that the proposed instability is indeed the cause of westward eddy shedding from the monsoon anticyclone. The description of the eddy shedding process as spatio-temporal instability does therefore not only serve as new conceptual model for the phenomenon, but is able to make quantitative predictions on scales and behaviours that have previously not been possible.

Chapter 6

Propagation of waves and vortices

The Asian monsoon anticyclone shows evidence of periodically produced vortex-structures, which are then propagated westwards away from their source [Popovic and Plumb 2001]. Garny and Randel [2016] show how such vortices shed from the monsoon can trap tracers inside and carry them along, and hence provide a mechanism for transport over large horizontal distances. Some of the numerical experiments described in chapters 3 and 5 show analogue pronounced vortex structures being created and shed from a localised, steady mass source. Figure 6.1 illustrates two of these experiments performed with the single-layer model described in section 2.3. A series of distinct eddies can be seen in both of them.

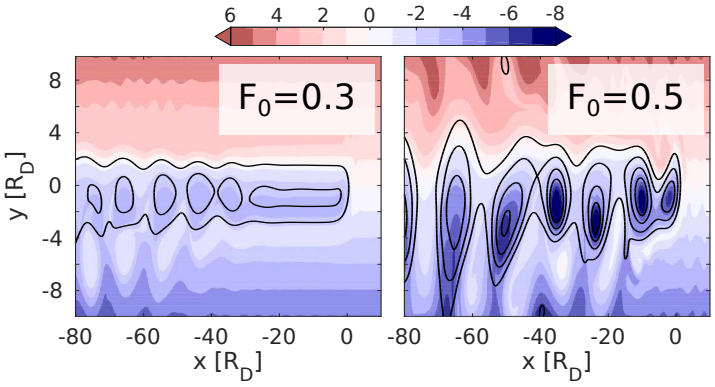

Fig. 6.1 Typical examples of day 400 PV (shading) and height anomaly (contours) response for numerical single layer experiments described in chapter 5, with steady forcing at the origin using a forcing scale $r_0 = 4$ and two different magnitudes F_0.

Many other features of geophysical flows also manifest in the form of such coherent, localised eddy-structures, like a range of eddies in open oceans, Gulf-Stream rings, tropical cyclones or Jupiter's Great Red Spot. In a number of cases these eddies are self-contained. This means they do not require any external energy input to persist over sufficiently long time scales and are therefore able to propagate within the system domain. Often, this propagation is purely caused by the internal dynamics of the feature and not simply by the advection of a background flow.

Analysing sixteen years of observational see-surface height data, Chelton et al. [2007] tracked over 35000 eddies with radii of about $100km$ and lifetimes of more than 16 weeks. They further find a considerable fraction of these eddies to travel westward distances of more than thousand kilometres.

Eddies often correspond to closed potential vorticity (PV) contours and can therefore trap the contained fluid, and with it heat and tracers, carrying it over very long distances. This gives a strong potential for dynamical teleconnections and tracer transport. Zhang et al. [2014] use observational data to show that the meridionally integrated eddy-induced zonal mass transport in oceans can be of the order of total $30Sv$.

We want to investigate the general zonal propagation of such features, with particular interest in the propagation of a zonal chain of discrete vortices. The response to a steady, localised PV forcing can take three different states, shown in figure 5.3 of chapter 5. It can either produce a **steady**, elongated plume of anomaly or form discrete eddies in the **break-up** or **shedding** states. The different states occur based on the stability properties of the system, as explained in chapter 5. Figure 6.1 illustrates the break-up (left) and shedding (right) states. Both cases show a region with discrete vortices.

If a theoretically formed steady plume is unstable, infinitesimal perturbations will grow and eventually become strong enough to perturb the basis flow. This will lead to the formation of discrete eddies, either within the forcing region or downstream. As shown in figure 5.29 (other chapter), the non-linearity of the model limits the growth of the perturbations and hence states can exist, which are statistically steady and zonally periodic over a finite length. We can conceptually separate the zonal eddy perturbations from the underlying steady plume profile and characterise our system depending on the relative strength of these two components. Figure 6.2 illustrates this idea in terms of a theoretical disturbance measure γ.

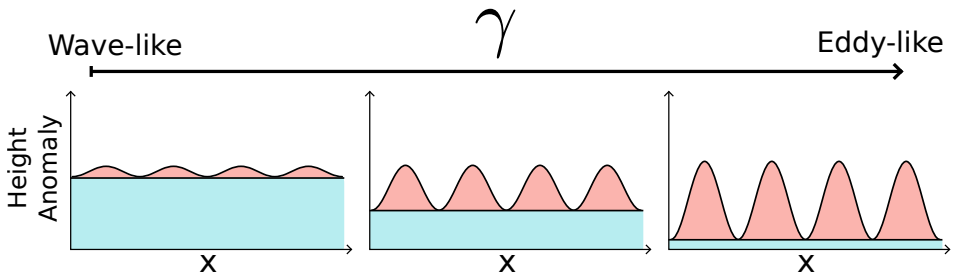

Fig. 6.2 Schematic differences in zonal height anomaly profiles for systems defined by a steady plume with weak wave-pattern perturbations (γ small) and a series of eddies connected by a weak band of anomaly (γ large).

The disturbance measure γ is meant to quantify to what extent the response is dominated by a zonally and temporally steady plume or overlaying perturbations. At first we consider the measure in a conceptual and qualitative way; a more quantitative definition will be given later in equation 6.1. The introduction of such a measure γ is potentially useful since systems with different values of γ can generally be expected to behave differently in many ways. The one extreme is given by systems that consist mainly of a zonally

symmetric plume and are only, if at all, perturbed by weak disturbances (γ small). The perturbation is not strong enough to significantly alter the PV field and produce pronounced regions with closed PV contours (eddies), hence we would expect the response to be well described by linear Rossby wave theory.

The other case is represented by a system with strong zonal variability of the height field (γ large). These strong variations will (almost certainly) lead to confined regions of strong PV anomaly and will thus modify the meridional PV gradient of the background β-plane. As a consequence the flow will produce pronounced regions of closed PV contours. The corresponding vortices are then isolated and connect to each other only by a weak band of anomaly. In this case the zonal propagation of the eddies should be well described by the centre of mass theory for coherent vortices presented later in section 6.1. Early et al. [2011] emphasised in a comparison of linear and non-linear numerical models how different the evolution of eddies is depending on whether they behave like linear waves or non-linear structures. In particular, they found non-linearity to reduce the amount of dispersion and hence showed that localised height anomaly structures stay coherent for much longer than a superposition of linear waves.

It should be noted, that figure 6.1 indicates a good agreement between the height anomaly and PV fields, in particular in terms of the closed contours corresponding to formed vortices in the shedding state. For the weakly perturbed plumes we still find the height anomaly to describe the corresponding waves reasonably well. We will therefore use both fields, height anomaly and PV (anomaly), to define, describe and track the eddies and waves.

The γ measure introduced earlier is mainly a conceptual tool to simplify the discussion of different flow behaviours. Equation 6.1 is a possible way of defining γ for the steadily forced experiments of section 2.3.1. Following this definition, γ can be calculate from the zonal variance and the zonal mean between $-150 < x < -50$. It is further divided by F_0 and averaged over days 300 to 500. The normalisation by the forcing magnitude F_0 is supposed to eliminate the corresponding dependency due to the linear scaling $h \sim F_0 r_0/\beta$ that follows from the model equations (see section 2.3).

$$\gamma = \frac{1}{F_0}\left\langle \frac{\langle h^2\rangle_x}{\langle h\rangle_x} - \langle h\rangle_x \right\rangle_t , \tag{6.1}$$

where $\langle\cdot\rangle$ denotes averages over the indicated dimension. Figure 6.3 shows how the γ measure increases in numerical experiments with fixed forcing radius and increasing magnitude and hence shows how the system changes from being dominated by an almost steady beta-plume to consisting of a series of pronounced vortices connected only by a weak band of anomaly.

We find responses covering a range of γ values when forced with different magnitudes. Figure 6.4 shows normalised zonal height anomaly profiles at day 400 for experiments with different forcing magnitudes. It is clearly visible how the zonal variability increases with F_0, meaning γ is expected to increase, similar to what is schematically illustrated in figure 6.2.

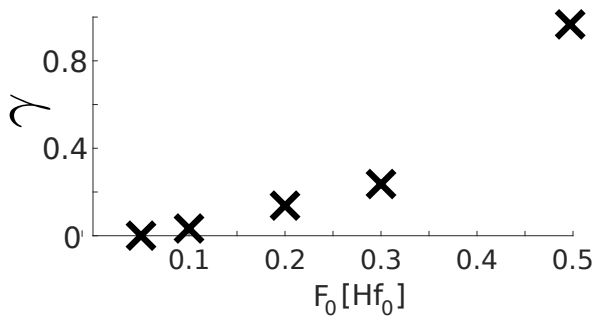

Fig. 6.3 Disturbance measure γ (defined by equation 6.1) for steadily forced experiments with forcing radius $r_0 = 4$ and different forcing magnitude F_0.

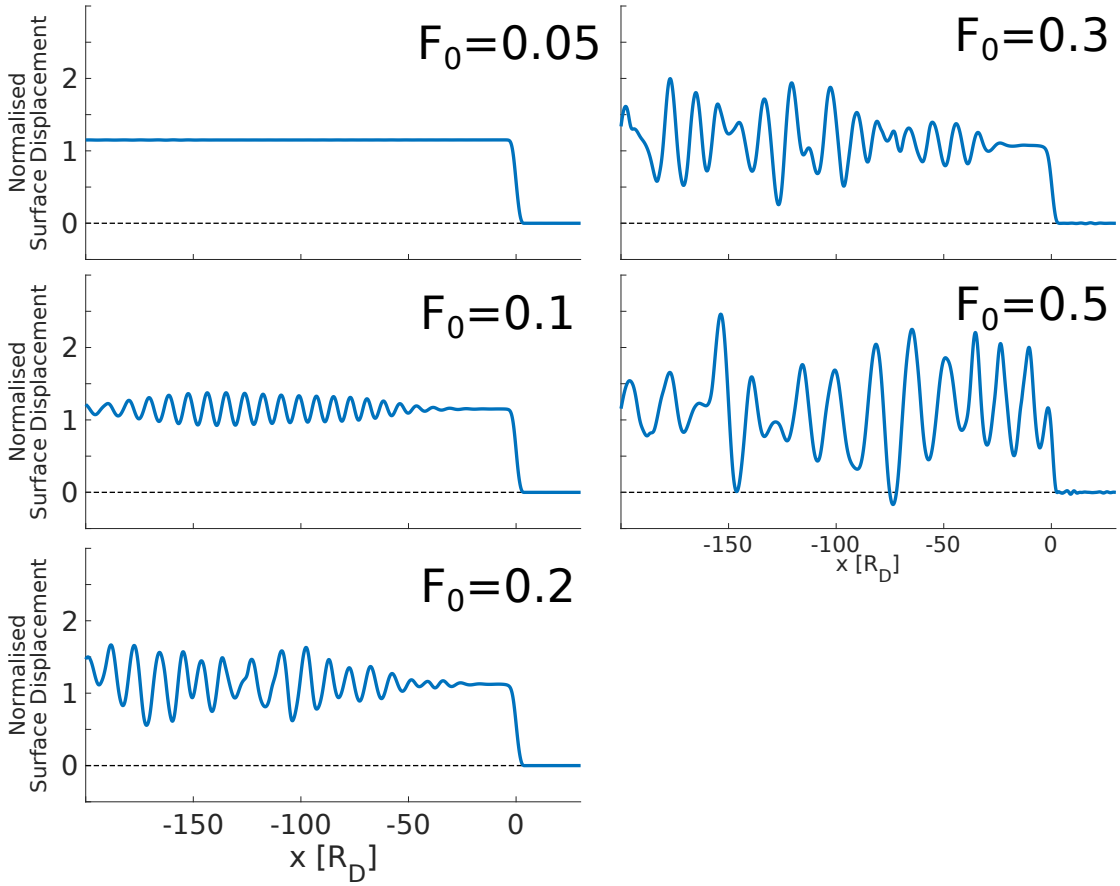

Fig. 6.4 Day 400 height anomaly profiles along $y = 0$ and normalised to a mean of one for steadily forced experiments with $r_0 = 4$ and different forcing magnitudes F_0.

We want to investigate the zonal propagation speed of coherent eddies in a single-layer, β-plane model. The problem of intrinsically propagating eddies is not new and has been the subject of research in various geophysical settings. Flierl [1977] used a linear, quasi-geostrophic model to analytically estimate velocities of Gulf-Stream rings, based on their pressure extreme. McWilliams and Flierl [1979] showed in a quasi-geostrophic single-layer simulation, that the non-linearity can slow down the decay of the vortex due to Rossby wave radiation and found a meridional drift, as well as an increased westward propagation, for finite amplitudes.

Another group of authors used an analytical centre-of-mass approach, first formulated by Ball [1963], to derive equations for the propagation of isolated vortices. Davey and Killworth [1984] found the eddy propagation in a shallow water model to be predominantly westward, with the eddy speed depending on the magnitude of the corresponding height anomaly. They showed analytically and in numerical simulations that anticyclones travel faster and cyclones slower than the long Rossby wave speed. Cushman-Roisin et al. [1990] slightly extended the calculation and used quasi-geostrophic approximations to derive a closed form expression for the zonal eddy velocity. Toorn and Zimmerman [2010] presented a more complex formulation in terms of angular momentum integrals to derive a formula for the propagation velocity for a vortex on a rotating sphere. The corresponding equation for the centre-of-mass propagation on a β-plane is given as asymptotic solution for slow drift speeds.

Leeuwen [2007] extended the centre-of-mass velocity calculation of Cushman-Roisin et al. [1990] by including a geostrophic background wind (but no bottom topography). They find, in agreement with our results in section 6.1, that a basic state in form of a background surface displacement does not change the eddy speed. This is due to cancelling effects of the corresponding background winds and a change in background PV gradient through a layer depth gradient. A similar f-plane calculation was performed by Nof [1983] studying the motion of eddies moving on a sloped ocean-floor without any background wind. The author finds the bottom topography gradient to induce a zonal velocity that can advect the eddy.

Early et al. [2011] modelled the short and long term evolution of isolated ocean eddies as a numerical quasi-geostrophic initial value problem. They found the zonal velocity to be strongly sensitive to the magnitude of the height anomaly for weak eddies and approaching the long Rossby wave speed in the large amplitude limit. A possible explanation of these findings is given in subsection 6.2.1.

The theory that will be presented in section 6.1 is based on the approach used by Cushman-Roisin et al. [1990] for the zonal centre-of-mass speed of isolated vortices, but additionally includes both, a zonal background wind and a bottom topography, into the calculation. Further, we are reviewing the corresponding extension of the concept of an eddy-chain by Davey and Killworth [1989] in section 6.1.2. Our results, however, are in disagreement with those found by Davey and Killworth [1989] in the sense that we do not find evidence for a change in centre-of-mass propagation speed depending on whether an eddy is well isolated or part of a periodic chain. A clear example of such an eddy-chain can be seen in the left plot of figure 6.1.

In section 6.2 we will investigate the applicability of the centre-of-mass theory to the steadily forced experiments described in chapter 5 and compare the theoretical predictions for simple basis flows with the numerical results. Finally, in subsection 6.2.3, we will use our estimates for the eddy speed to explain the effects of a zonal background jet and thermal damping on the zonal time mean profiles and other features of the flow.

6.1 Zonal propagation of coherent vortices

This section is designated to explaining some of the integral mechanisms and theories which do describe the zonal propagation of eddy features. The numerical experiments shown in figure 6.1 suggest that the created vortices can have considerable lifetimes and can therefore travel a long distance before they decay. This can potentially provide a mechanism for non-local dynamical interactions and tracer transport [Zhang et al. 2014]. Since we can assume the eddies to be shape preserving the centre of mass is an adequate definition of the eddy position and a good way to describe its motion. We will adapt an approach used previously by several authors to study similar problems [Ball 1963; Davey and Killworth 1984; Cushman-Roisin et al. 1990]. Our calculation generalises the calculation to include a zonal background wind and the idea of a periodic eddy chain, instead of a single, isolated vortex.

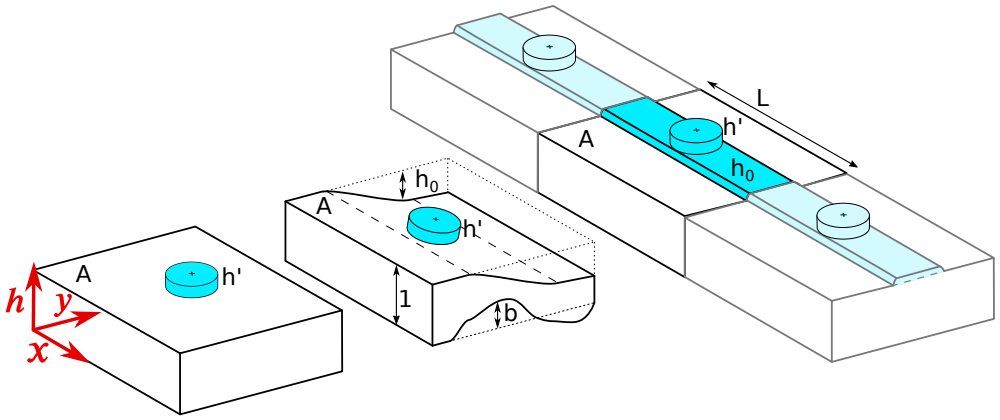

Fig. 6.5 Different set-ups of a single layer system: A confined patch of height anomaly h', well isolated in a large, resting domain (left), on top of a zonally symmetric zonal background flow created by a basis state h_0 and/or a bottom topography b (middle) and as part of a periodic chain of eddies connected by a band of anomaly (right).

Figure 6.5 illustrates the different potentially interesting system set-ups and displays their corresponding basis states. The far left set-up describes an isolated patch of height anomaly h' in an infinitely extended domain A. This case was studied by Davey and Killworth [1984]. The second setting generalises the problem to include meridionally varying bottom topography b and basic state profiles h_0. This allows us to impose a zonally symmetric basic state wind and study its effect on the eddy propagation. We will consider this case in subsection 6.1.1.

The third state includes a finite domain size and periodic boundaries in the zonal direction. This way we can represent a periodic series of vortices. Since it also means the height anomaly does not necessarily have to vanish at the zonal boundaries, we can investigate the modifications to the propagation if neighbouring eddies are not isolated, but connected by a band of height anomaly. This case is studied in subsection 6.1.2. In disagreement with the findings of Davey and Killworth [1989], we do not obtain a "chain-effect" in the form of a modification of the propagation speed when changing the system to a series of connected eddies.

We will perform the calculation using two different models. In sections 6.1.1 and 6.1.2 we are investigating the propagation of eddy structures in the shallow water (SW) model used by Davey and Killworth [1989] and will transfer our findings onto the quasi-geostrophic (QG) model in subsection 6.1.3.

6.1.1 Confined eddy in a shallow water system

In this section we will study the behaviour of a single, isolated eddy in a single layer model. The model is described in detail in section 2.3. To simplify the calculation we will assume the winds to be in geostrophic balance with the height field and only let the surface displacement evolve in time. The corresponding set of unforced equations then reads

$$\begin{aligned} v = \frac{1}{f}\partial_x h,\ u = -\frac{1}{f}\partial_y h, \\ \partial_t h = -\nabla\cdot\left[\boldsymbol{u}(1+h-b)\right], \end{aligned} \tag{6.2}$$

where we specify the unperturbed layer depth as 1 and describe the surface displacement as $h(x,y,t) = h'(x,y,t) + h_0(y)$. Here h' describes the localised eddy and h_0 is the zonally symmetric basic state profile. As boundary conditions we require the eddy anomaly h', but not h_0, and its derivative to vanish at the x and y boundaries. We further introduce a bottom topography $b(y)$, which can be used in combination with h_0 to impose a zonal background wind. The total fluid layer depth is then given by $1+h-b$. The Coriolis frequency f is a function of y, normalised to its value at the reference latitude $y=0$, and describes the vertical component of the Earth's angular momentum. We will at a later stage apply the β-plane approximation $f = 1+\beta y$, but want to keep the theory as general as possible for now.

The presented calculation is an extension of that performed by Cushman-Roisin et al. [1990]. If we choose a static, square domain $A = [0,L]\times[0,L]$, which is sufficiently large to enclose the localised vortex perturbation at all times, h and all derivative vanish at the domain boundaries. Davey and Killworth [1989] showed that the propagation of almost circular eddies is predominantly westwards, hence we will focus on the zonal propagation and start by defining the zonal centre of mass position X as

$$MX = \int_A \mathrm{d}S\, x(h-h_0), \qquad (6.3)$$
$$M = \int_A \mathrm{d}S\, (h-h_0),$$

with constant perturbation mass M and $\mathrm{d}S = \mathrm{d}x\mathrm{d}y$ describing an infinitesimal surface element. Taking the time derivative of this expression and using the shallow water continuity equation $\partial_t h = -\nabla \cdot [\boldsymbol{u}(1+h-b)]$ leads to a formula for the zonal centre of mass propagation velocity of the eddy:

$$\begin{aligned} MX_t &= \int_A \mathrm{d}S\, x h_t(x,y,t) = -\int_A \mathrm{d}S\, x\nabla\cdot[\boldsymbol{u}(1+h-b)] \qquad (6.4)\\ &= \int_A \mathrm{d}S\, \left[u(1+h-b) - \partial_x\left[(xu(1+h-b)\right]\right] \\ &= \int_A \mathrm{d}S\, \left[u(1+h-b) - u_0(1+h_0-b)\right], \end{aligned}$$

where the third and fourth equality signs make use of the product rule of differentiation, the zonal symmetry of the basic state and the boundary conditions for the eddy anomaly h'. Next we insert the expressions for the geostrophic zonal wind, i.e. $u = -f^{-1}\partial_y h$, to obtain a simplified version of the formula in terms of the height anomaly only:

$$\begin{aligned} MX_t &= -\int_A \mathrm{d}S\, \left[f^{-1}(1+h-b)\partial_y h - f^{-1}(1+h_0-b)\partial_y h_0\right] \qquad (6.5)\\ &= -\int_A \mathrm{d}S\, \left[(1-b)f^{-1}\partial_y(h-h_0) + \frac{1}{2}f^{-1}\partial_y(h^2-h_0^2)\right] \\ &= \int_A \mathrm{d}S\, \left[(h-h_0)(1+h_0-b)\partial_y f^{-1} - (h-h_0)f^{-1}\partial_y b + \frac{1}{2}(h-h_0)^2\partial_y f^{-1}\right]. \end{aligned}$$

Here we used for the second equality sign that $h\partial_y h = 0.5\partial_y h^2$ and partial integration to derive the last line. Rearranging the different terms leads to

$$X_t = \frac{1}{M}\int_A \mathrm{d}S\, \left[h'(1+h_0-b)\partial_y f^{-1} - h' f^{-1}\partial_y b + \frac{1}{2}(h')^2\partial_y f^{-1}\right]. \qquad (6.6)$$

The formula for X_t consists of three terms:

- The first term describes the propagation of associated PV anomalies due to meridional variations in f and is additionally involving a factor $h_0 - b + 1$, similar to the way the linear Rossby wave

speed depends on the layer depth. In case of a β-approximation ($f = 1+\beta y$) this term corresponds to the standard β-effect.

- The second term describes the effective change in the meridional background PV gradient due to a changed layer thickness induced by the bottom topography. This change in PV gradient can influence the wave propagation. In principle a similar change is coming from variations in h_0, but these simultaneously induce a zonal wind and the two effects cancel each other exactly [Leeuwen 2007].
- The last term is a higher order correction to the centre of mass velocity. It does not change sign with the dominant sign of h', i.e. for cyclonic ($h' < 0$) or anticyclonic ($h' > 0$) eddies. However, keep in mind that $M \propto h'$, and hence this term can speed up anticyclones and slow down cyclonic anomalies. Those findings are in agreement with the results of Davey and Killworth [1984].

If we apply the β-plane assumption $f = 1+\beta y$, with f being normalised to its value at $y = 0$, and approximate equation 6.6 to first order in β we find a simplified formula for the zonal eddy propagation speed:

$$X_t = -\beta - \frac{1}{M}\int_A \mathrm{d}S \left[\beta h'(h_0 - b) - h'(1 - y\beta)\partial_y b + \frac{\beta}{2}h'^2\right]. \tag{6.7}$$

Formula 6.7 is consistent with the expression Cushman-Roisin et al. [1990] found for an atmosphere at rest ($h_0 \equiv b \equiv 0$).

6.1.2 Effects of a vortex chain

We now investigate how the propagation speed of the system is altered when there is a single, isolated vortex, rather than a chain of eddies. To model the characteristics and effects of such an eddy chain we choose our domain of length L to have periodic boundaries in the zonal direction, i.e. the total height anomaly satisfies $h(x,y,t) = h(x+L,y,t)$. Unlike we did in subsection 6.1.1, this time we do not require the eddy height anomaly to vanish at the zonal boundaries[1], meaning that $h|_{\partial_x A} \neq 0$. This gives the chance to introduce a band of height anomaly connecting neighbouring vortices and with it include vortex-vortex interactions in our calculation. To simplify the calculation we will, however, not include any bottom topography or explicit basic state profile.

A similar approach was taken by Davey and Killworth [1989], although their concluding results differ from the ones presented here. This mainly seems to be due to a subtle misinterpretation of the derived equations, as explained at the end of this subsection. Further, they do not make it clear how their system is set-up exactly. As is demonstrated below, a poor choice of reference frame, and therefore integration

[1] We still require h and its derivatives to vanish at the meridional boundaries. This implies all winds to vanish at the y-boundaries.

domain, can lead to conceptual problems and should be avoided. To show this, we will first perform the calculation in a frame where the surrounding fluid is resting, and then repeat the equivalent derivation for an observer moving with the eddy.

Resting frame of reference

At first we present an approach using a static, rectangular domain $A = [0,L]\times]-\infty,\infty[$. For simplicity, the system is assumed not include any bottom topography or background wind. If we define the eddy profile as $h(x,y,t)$, the total layer depth is given by $1+h$ and the zonal centre of mass position X is defined by

$$\begin{aligned} MX &= \int_0^L \mathrm{d}x \int \mathrm{d}y\, xh(x,y,t), \\ M &= \int_A \mathrm{d}S\, h, \end{aligned} \tag{6.8}$$

where the total mass M is independent of time and any translation of h. If we assume a statistical steady state and therefore our eddy chain to move as a whole with constant drift velocity c we find $h(x,y,t) = h(x-ct,y,0)$. A change into the reference frame of the vortex then gives

$$\begin{aligned} MX &= \int_0^L \mathrm{d}x \int \mathrm{d}y\, xh(x-ct,y,0) \\ &= \int_{-ct}^{L-ct} \mathrm{d}x \int \mathrm{d}y\, (x+ct)h(x,y,0). \end{aligned} \tag{6.9}$$

The zonal centre of mass velocity is calculated as the time derivative of this expression, where, according to the Leibniz integral rule, we have to be careful to include terms coming from the time dependent integration boundaries.

$$\begin{aligned} MX_t &= -cL \int \mathrm{d}y\, h(-ct,y,0) + c \int_{-ct}^{L-ct} \mathrm{d}x \int \mathrm{d}y\, h(x,y,0) \\ &= -cL \int \mathrm{d}y\, h(-ct,y,0) + c \int_0^L \mathrm{d}x \int \mathrm{d}y\, h(x,y,t). \end{aligned} \tag{6.10}$$

If we now integrate this expression over the time of one periodic cycle L/c we obtain

$$\begin{aligned} M\int_0^{\frac{L}{c}} \mathrm{d}t\, X_t &= -cL\int \mathrm{d}y \int_0^{\frac{L}{c}} \mathrm{d}t\, h(-ct,y,0) + c\int_0^{L} \mathrm{d}x \int \mathrm{d}y \int_0^{\frac{L}{c}} \mathrm{d}t\, h(x-ct,y,0) \\ &= -L\int \mathrm{d}y \int_0^{L} \mathrm{d}p\, h(p,y,0) + \int_0^{L} \mathrm{d}x \int \mathrm{d}y \int_0^{L} \mathrm{d}q\, h(q,y,0) \\ &= 0, \end{aligned} \tag{6.11}$$

Here we substituted $p = -ct$ and $q = x - ct$ for a fixed x and used the periodicity of the boundary conditions to shift the q and p integration boundaries.

Hence the average centre of mass velocity vanishes for a static domain, which is a conceptual problem. The reason for this is a conflict arising from the centre of mass definition and the interactions with the boundaries. For a periodic system with a constant drift the centre of mass has to oscillate around a mean position and hence its average velocity has to vanish. This issue is illustrated in figure 6.6.

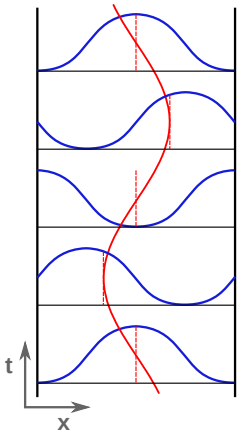

Fig. 6.6 Schematic time evolution of the zonal position of the centre of mass (dashed red lines) of a steadily propagating height anomaly profile (blue curves) in a static and periodic domain.

Steadily moving frame

To bypass the conceptual problems described above we will perform the centre of mass calculation in a frame moving with the eddy. The boundary conditions stay the same, in particular that means periodic in x. Once again, we start by defining the zonal centre of mass position for our system:

$$MX = \int_A \mathrm{d}S\ (x - ct)h(x,y,t), \tag{6.12}$$

where the integral is taken over the moving domain $A = [ct, ct+L]\times]-\infty,\infty[$. The velocity c is chosen so the eddy is stationary in our frame of reference, and hence

$$h(x,y,t) = h(x-ct,y,0). \tag{6.13}$$

The assumption of a steady drift is valid since we are only interested in shape-preserving eddies in statistical steady states. By construction the zonal centre of mass is stationary. Substituting $p = x - ct$ therefore gives

$$\begin{aligned} MX &= \int_{ct}^{L+ct} \mathrm{d}x \int \mathrm{d}y\ (x-ct)h(x-ct,y,0) \\ &= \underbrace{\int_0^L \mathrm{d}p \int \mathrm{d}y\ ph(p,y,0)}_{\text{independent of } t}. \end{aligned} \tag{6.14}$$

Comparing equations 6.14 and 6.8 shows that the formulation using a moving, periodic domain is conceptually equivalent to a static frame of reference keeping the anomaly profile fixed in time. It also represents the idea that, if c is constant and completely determined by the instantaneous h profile, we can calculate the drift velocity at any arbitrary, single point in time. This subtle difference avoids the problem of an oscillating centre of mass position and hence a vanishing drift speed.

Since MX is independent of t, its time derivative has to vanish. Again we need to be careful to include the terms coming from the time dependent integration boundaries. We then find

$$\begin{aligned} 0 &= \partial_t \int_A \mathrm{d}S\ (x-ct)h(x,y,t) \\ &= cL \int \mathrm{d}y\ \bar{h} + \int_A \mathrm{d}S\ [x\partial_t h - c\partial_t(th)] \\ &= cL \int \mathrm{d}y\ \bar{h} + \int_A \mathrm{d}S\ (x-ct)\partial_t h - c\underbrace{\int_A \mathrm{d}S\ h}_{=M}, \end{aligned} \tag{6.15}$$

where we defined the boundary profile $\bar{h}(y) = h(ct, y, t)$. We can now introduce a reduced mass $M' = M - L\int \mathrm{d}y\ \bar{h} = \int_A \mathrm{d}S\ (h - \bar{h})$, which represents the bulk anomaly part without any zonal boundary contribution. If we further use the continuity equation $\partial_t h = -\nabla \cdot [\boldsymbol{u}(h+1)]$ we obtain

$$\begin{aligned} M'c &= \int_A \mathrm{d}S\ (x - ct)\partial_t h \\ &= \int_A \mathrm{d}S\ x\partial_t h - ct \overbrace{\int_A \mathrm{d}S\ \partial_t h}^{=0} \\ &= -\int_A \mathrm{d}S\ x\partial_x\left[u(h+1)\right] \\ &= -L\int \mathrm{d}y\ \bar{u}(\bar{h}+1) + \int_A \mathrm{d}S\ u(h+1), \end{aligned} \tag{6.16}$$

The last line is derived following similar steps to the case of an isolated eddy in a static frame. Rearranging the terms gives us an equation for the drift velocity c reading

$$M'c = -L\int \mathrm{d}y\ \bar{u}(\bar{h}+1) + \int_A \mathrm{d}S\ u(h+1). \tag{6.17}$$

The formula only differs to equation B10 presented by Davey and Killworth [1989] in the sense that none of the terms are explicitly time-dependent. This is by construction, the usage of a moving domain and arguments similar to the ones shown in equation 6.14. Hence, any time integration is equivalent to a simple multiplication and keeps the equation unchanged.

Davey and Killworth [1989] interpret the first term in equation 6.17 as correction of the zonal velocity of an isolated vortex due to the inclusion of an eddy chain. However, this interpretation would only be valid if the second term in the equation were actually the velocity of an isolated eddy. Note, that the second term does involve the total perturbation profile h, which includes contributions of the boundary values $\bar{h}$. As we will show below, these contributions cancel with the first term, which was wrongly identified as eddy chain correction term.

If the winds are in geostrophic balance we can again use the relation $u = -f^{-1}\partial_y h$ to simplify the equation to

$$M'c = L\int \mathrm{d}y\ f^{-1}(\bar{h}+1)\partial_y\bar{h} - \int_A \mathrm{d}S\ f^{-1}(h+1)\partial_y h. \tag{6.18}$$

Next we decompose the height field via

$$h = \hat{h} + \bar{h}. \tag{6.19}$$

This corresponds to a representation of the anomaly in terms of a boundary profile $\bar{h}$ and a bulk contribution $\hat{h}$. Note that this decomposition implies $\partial_x \bar{h} = 0$ and $\hat{h}(ct) = 0$. This approach is conceptually similar to the decomposition into a zonally symmetric and a wave part when defining the disturbance measure γ in figure 6.2. We then find

$$\begin{aligned} M'c &= L \int \mathrm{d}y\, f^{-1}(\bar{h}+1)\partial_y \bar{h} - \int_A \mathrm{d}S\, f^{-1}(\hat{h}+\bar{h}+1)\partial_y(\hat{h}+\bar{h}) \\ &= -\int_A \mathrm{d}S\, f^{-1}\hat{h}\partial_y \bar{h} - \int_A \mathrm{d}S\, f^{-1}(\hat{h}+\bar{h}+1)\partial_y \hat{h} \\ &= \int_A \mathrm{d}S\, \left[\bar{h}\partial_y(f^{-1}\hat{h}) - f^{-1}\bar{h}\partial_y \hat{h}\right] - \int_A \mathrm{d}S\, f^{-1}\partial_y \hat{h} - \frac{1}{2}\int_A \mathrm{d}S\, f^{-1}\partial_y \hat{h}^2 \\ &= \int_A \mathrm{d}S\, \hat{h}\bar{h}\partial_y f^{-1} + \int_A \mathrm{d}S\, \hat{h}\partial_y f^{-1} + \frac{1}{2}\int_A \mathrm{d}S\, \hat{h}^2 \partial_y f^{-1}. \end{aligned} \tag{6.20}$$

Rearranging the different terms gives

$$c = \frac{1}{M'}\int_A \mathrm{d}S\, \left[\hat{h}(1+\bar{h})\partial_y f^{-1} + \frac{1}{2}\hat{h}^2 \partial_y f^{-1}\right]. \tag{6.21}$$

The resulting expression is equivalent to equation 6.6, where we investigated the case of a single isolated vortex in a sufficiently large, non-periodic domain with a zonally symmetric background flow, when putting $h_0 \equiv \bar{h}$ and $b \equiv 0$, i.e. no bottom topography. Hence the inclusion of a chain connecting neighbouring vortices is equivalent to imposing a corresponding basic state, but does not modify the resulting eddy propagation beyond this simple change in basic state. Applying the β-plane approximation by choosing $f = 1 + \beta y$ we can simplify the expression to

$$c = -\beta\left(1 + \frac{1}{M'}\int_A \mathrm{d}S\, \left[\hat{h}\bar{h} + \frac{1}{2}\hat{h}^2\right]\right). \tag{6.22}$$

The boundary profile $\bar{h}$ does only enter the equation 6.22 as part of the first term correction term. There are three observations we want to make regarding this term:

- The purpose of the boundary profile in this term is to account for the change in layer depth and the corresponding change in long Rossby wave speed.

- If we assume the chain profile to be of similar shape and magnitude as the eddy anomaly, i.e. $\bar{h} \approx \hat{h}$, we find the correction term to be of second order and hence of minor importance. Note, that the term in equation B12 in Davey and Killworth [1989] is not a higher order term, despite the square involved, since it is proportional to $(\bar{h}+1)^2 - 1 = \bar{h}^2 + 2\bar{h}$, which scales linearly for $|\bar{h}| \ll 1$.
- The sign of our correction term is set by the dominating sign of $\bar{h}$. For anticyclonic anomalies ($\hat{h} > 0$), and if we assume the chain profile $\bar{h}$ to be of the same dominating sign as the eddy, we find our correction term to accelerate the eddy. The term found by Davey and Killworth [1989], on the other hand, is found to slow them down.

We therefore conclude, that there is no significant interaction of the different eddies with the connecting chain or with each other. This conclusion is in disagreement with the findings of Davey and Killworth [1989].

6.1.3 Quasi-geostrophic formulation

Next we want to perform an analogous calculation for the QG-PV model introduced in section 2.3. We will adapt the derivation for the shallow water model[1] of the previous subsections and apply it to the QG system. While the model used in the previous subsections is more general, the results for a fully quasi-geostrophic model can potentially be easier to interpret and are hence worth studying. The corresponding model equations are

$$\begin{aligned} \partial_t q &= -(\boldsymbol{u}\cdot\nabla)q - \beta y, \\ q &= \nabla^2 h - h + b, \\ u &= -\partial_y h,\ v = \partial_x h. \end{aligned} \tag{6.23}$$

As shown earlier, it is sufficient to investigate an isolated vortex in an infinite, static domain A. For the QG approach we will define our vortex in terms of PV anomaly, rather than via the height field. Since we are investigating shape-preserving vortices, the corresponding centres of mass will move on equivalent paths. We define the eddy anomaly $q' = q - q_0$ as PV perturbations to the basis state $q_0(y)$ and correspondingly decompose the other flow quantities into eddy and basic state parts. In addition, we choose to include a bottom topography profile $b(y)$. As before, the background state and bottom topography profiles can be used to change the layer depth and impose background winds.

[1] Note that we re-defined the quasi-geostrophic PV q as anomaly from the β-plane background in order to simplify the definition of coherent eddies. The model evolution is not affected by this change.

The zonal centre X of the PV anomaly and the total anomaly Q are then defined as

$$\begin{aligned} QX &= \int_A \mathrm{d}S\, x(q-q_0), \\ Q &= \int_A \mathrm{d}S\, (q-q_0) \\ &= \int_A \mathrm{d}S\, \left[\nabla^2(h-h_0) - (h-h_0)\right] \\ &= -\int_A \mathrm{d}S\, (h-h_0), \end{aligned} \tag{6.24}$$

were we used equation 6.23 to show the equivalence of the total PV and mass anomalies. As for the SW model, we take the time derivative and use the evolution equation of the model to obtain the zonal eddy speed:

$$\begin{aligned} QX_t &= \int_A \mathrm{d}S\, xq_t \\ &= -\int_A \mathrm{d}S\, x\left[\nabla\cdot(\boldsymbol{u}q) + \beta v\right] \\ &= -\int_A \mathrm{d}S\, \left[u_0 q_0 - uq - x\beta v\right], \end{aligned} \tag{6.25}$$

where we used $\nabla\cdot\boldsymbol{u} = 0$ for geostrophic winds. Substituting the expressions for q and u in equation 6.23 and similar transformations as in subsection 6.1.1, we obtain

$$\begin{aligned} X_t &= \frac{1}{Q}\int_A \mathrm{d}S\, \left[(\partial_y h_0)(\nabla^2 h_0 - h_0 + b) - (\partial_y h)(\nabla^2 h - h + b) + \beta(h-h_0)\right] \\ &= \frac{1}{Q}\int_A \mathrm{d}S\, \left[\frac{1}{2}\partial_y(h^2 - h_0^2) - (h-h_0)\partial_y b + \beta(h-h_0)\right] \\ &= -\beta + \frac{1}{Q}\int_A \mathrm{d}S\, (h-h_0)\partial_y b. \end{aligned} \tag{6.26}$$

To obtain the second line we applied the rigid boundary conditions, which state that the derivatives of h and h_0 vanish at all domain edges. Note that we can obtain this result asymptotically from equation 6.7 by assuming small length scales and weak perturbations to the layer depth, i.e. $|h|, |h_0|, |b|, |\beta y| \ll 1$. As one can see, all anomalies travel with the non-dimensionalised long Rossby wave speed β if the system has no bottom topography. The second order terms in the equivalent shallow water model equation are not present in the QG version.

Next we assume a constant layer depth for the unperturbed background state. This is defined via $b \equiv h_0$ and enables us to introduce a background wind $u_0 = -\partial_y h_0$ without a corresponding change in Rossby wave speed. Linear profiles of $h_0 \equiv b$ in particular do not alter the PV structure of the basic state, and hence to not alter the wave propagation in the tropics. This approach was used by multiple other authors before to investigate the sensitivity of a single-layer model response to basic state winds in tropical regions [Kraucunas and Hartmann 2007; Bao and Hartmann 2014]. We then obtain a final, constructive formula for the centre-of-mass velocity of an isolated vortex:

$$\begin{aligned} X_t &= -\beta + \frac{1}{Q}\int_A \mathrm{d}S\, h' \partial_y b \\ &= -\beta + \frac{\int_A \mathrm{d}S\, h' u_0}{\int_A \mathrm{d}S\, h'}. \end{aligned} \tag{6.27}$$

Equation 6.27 shows that a background wind changes the propagation speed according to simple Doppler shift by the weighted average velocity. In particular, for constant basis wind profiles we find $X_t = -\beta + u_0$ and the correction vanishes for linear shear winds without mean value.

6.2 Application to steadily forced experiments

The theory presented in section 6.1 describes the zonal velocity of coherent eddies in the form of closed PV contours in a single layer-model. This section is dedicated to investigate the applicability of the theory for the zonal propagation of eddies to the vortex structures observed in the numerical simulations described in chapter 5 (also illustrated in figure 6.1).

The numerical model used is a time-dependent, non-linear QG-PV model forced by a localised, steady mass source. The aim is to apply the developed theory to these experiments and explain the propagation behaviour of the observed eddy-features, as well their interaction with simple background flows.

6.2.1 Transition from wave to vortex systems

The analytic theory derived in section 6.1 can be used to calculate the zonal velocity of discrete vortices, either isolated, or in an eddy-chain. A main aspect of equation 6.27 is, that eddies travel with the long Rossby wave speed in a quasi-geostrophic system without any background winds. In numerical simulations of vortex evolution, however, Early et al. [2011] found the zonal vortex speed to be consistently lower and only approaching the long Rossby wave speed in the limit of large eddy anomaly magnitudes. A possible explanation can be, that the small-amplitude eddies, i.e. small perturbations of the background, behave more like linear Rossby waves, rather than isolated vortices, and hence travel with a velocity slower than the long Rossby wave speed.

A similar idea of a change in propagation speed for differently strong eddy perturbations was emphasised at the beginning of this chapter. Following these thoughts, we can expect flow perturbations in an eddy-chain to behave differently depending on the strength of the eddies with respect to the connecting band of anomaly (as an adequate measure of the background). Figure 6.4 defined the γ measure as a way to quantifies how much the vortex chain is dominated by the eddies. The figure also suggests that experiments with a localised steady forcing of stronger magnitude F_0 generally leads to a response with a larger value of γ.

The theory derived in section 6.1 was derived for sufficiently pronounced vortices. We would therefore expect perturbations in experiments with weak forcing magnitudes (γ small) to propagate with a speed close to the zonal Rossby wave phase speed, given by

$$c_{p,x} = -\frac{\beta}{k^2 + l^2 + 1}, \tag{6.28}$$

where k and l are the zonal and meridional wave numbers. In contrast, the eddies formed in experiments with large magnitude forcing, i.e. a system in the shedding state[1], should propagate with velocity

$$X_t = -\beta, \tag{6.29}$$

as predicted by equation 6.27 for a fluid at rest ($u_0 \equiv 0$). Note that $|c_{p,x}| \leq \beta$ is always smaller than the long Rossby wave speed and only approaches it in the long wave limit $k, l \to \infty$. We should therefore see a clear transition in the zonal propagation speed when increasing the forcing magnitude, and with it γ.

In order to calculate $c_{p,x}$ from equation 6.28 we need to estimate k and l for an experiment with sufficiently weak flow perturbations, i.e. F_0. At first we can assume $k \approx l$, due to the rotational nature of the vortices. An intuitive to estimate the wave numbers would then be to use the scale of the forcing and estimate for $r_0 = 4$ the wave numbers as $k, l = \pi / r_0 \approx 0.79$. A Fourier analysis in the zonal direction of the response to a forcing with magnitude $F_0 = 0.1$ and scale $r_0 = 4$ (figure 6.7) shows a pronounced peak at $k = 0.80$ and suggests that this is indeed a reasonable approach. Note that the response to a weaker forcing magnitudes is steady and does not develop any pronounced eddy-features.

Further, a clear transition is obvious in 6.7 from a dominant wave number $k \approx 0.8$ to a value of around 0.4 as the forcing magnitude increases. The spatial stability analysis in chapter 5 suggests that the flow enters the shedding state due to the development of an absolute instability with wave number $k \approx 0.47$ for a source with radius $r_0 = 4$ and magnitude $F_0 = 0.5$ (see table 5.1). Hence, the system transitions

[1] See section 5.1 for the definition of the different states.

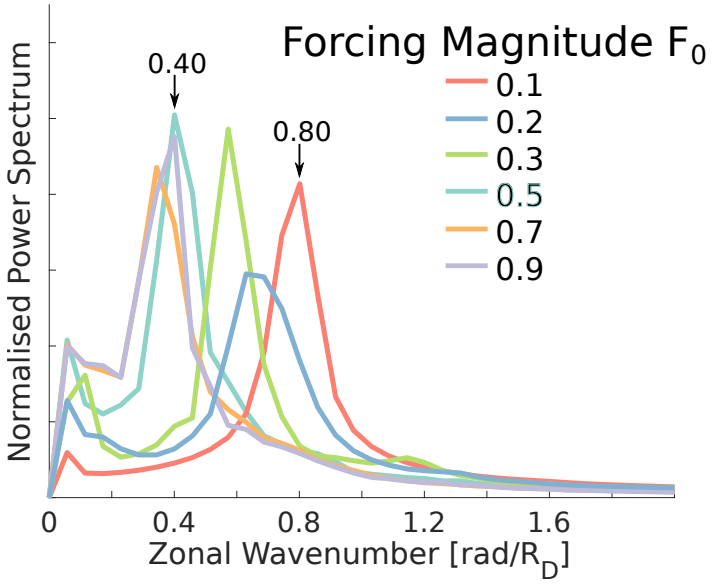

Fig. 6.7 Fourier analysis of the height anomaly response to a forcing with radius $r_0 = 4$ and various magnitudes. Analyses have been performed for the range $-100 < x < -10$ and shown spectra were averaged over $-2 < y < 2$ and days 100 to 500. Arrows mark the position of two peaks of interest.

from a weakly perturbed state to a state dominated by pronounced eddies. As explained, this transition means the system changes from a state in which the propagation of perturbations is determined by the linear Rossby wave phase speed (equation 6.29) to a state governed by propagation following the centre-off-mass theory (equation 6.29).

The top panel of figure 6.8 presents the height anomaly evolution along $y = 0$ for two steadily forced experiments with different forcing magnitudes. In both cases a clear periodic creation of discrete patches of anomaly and a following steady, westward propagation of these can be seen. The slope of the corresponding lines represents the propagation velocity of the formed eddies. We superimposed lines indicating the Rossby wave speed calculated from equation 6.28 for a wave with $k, l = \pi/r_0$. (yellow) and the theoretical propagation speed of isolated vortices as derived in equation 6.29 (red). In agreement with the arguments made earlier in this subsection, the perturbations in the weakly forced case ($F_0 = 0.1$) seem indeed to propagate with the corresponding Rossby wave phase speed, and the response can mostly be interpreted as a simple linear wave. In the case with the stronger forcing ($F_0 = 0.5$) the well pronounced vortices travel with the predicted long Rossby wave speed β.

Figure 6.8 illustrates the transition in propagation behaviour as we increase the forcing magnitude for a fixed forcing radius $r_0 = 4$. This simultaneously corresponds to an increase in γ (defined in figure 6.4) and hence a change of the response from being dominated by a steady plume to being dominated by isolated vortices. The qualitative difference of the horizontal structure of the response can be seen in the bottom panel, showing the height anomaly field at day 400.

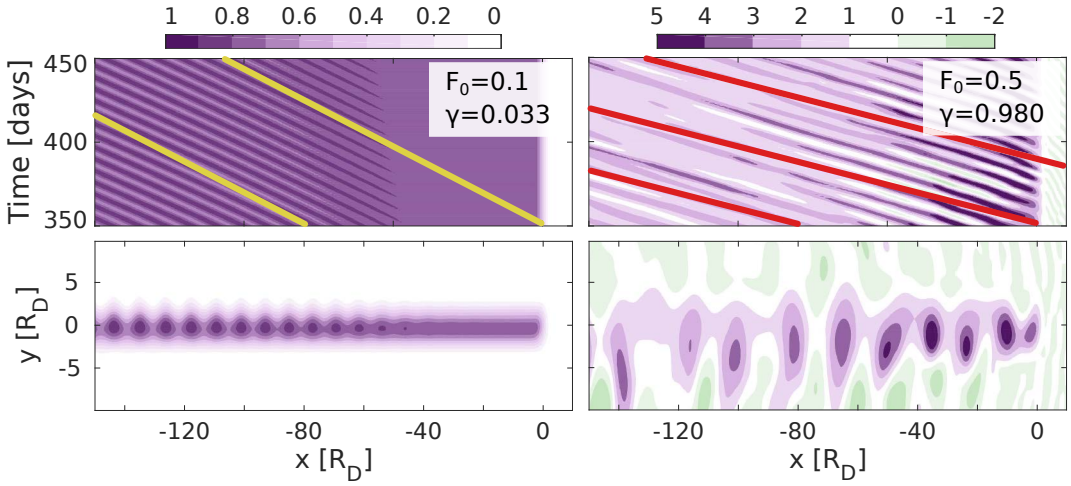

Fig. 6.8 Time evolution along $y = 0$ (top) and day 400 snapshot (bottom) of height anomaly for forcing radius $r_0 = 4$ and different magnitudes and corresponding calculated value of γ. The slope of the red lines correspond to the long Rossby wave speed β, the slope of the yellow lines indicate to the Rossby wave phase speed corresponding to $k, l = \pi / r_0$.

Two points should be noted. First, figure 6.7 and the bottom panel of figure 6.8 indicate an increase in size of the eddies when increasing F_0, even though the forcing scale r_0 is kept fixed. This would also lead to an acceleration of the vortices and a change of their velocities towards β. This change incorporated in linear theory, however, still seems to underestimate the eddy velocity. Using a value of $k = l = 0.4$, as suggested by figure 6.7 for $F_0 = 0.5$, equation 6.28 leads to a value of $c_{p,x} \approx 0.39$, compared to a long Rossby wave speed of 0.51.

Second it should be pointed out that the velocity drop with decrease of γ could hint towards a "chain effect", as proposed in subsection 6.1.2. As Davey and Killworth [1989] state, the centre-of-mass approach does not fully account for the interaction of the vortex with the surrounding fluid and might hence not capture such an effect.

6.2.2 Interaction with simple background flows

The structure and evolution of the flow produced from a localised forcing can be altered by introducing a background flow. In order to obtain a sense of the system's response and validate the eddy-propagation theory of section 6.1.2, we will investigate the modifications of a flow in the shedding state due to a constant and homogeneous background flow, as well as a flow with linear meridional shear.

Changes in the zonal centre-of-mass velocity of an isolated vortex by non-vanishing background winds are given as an overlap surface integral of the height anomaly profile of the eddy and the induced background winds, as shown in equation 6.27. Homogeneous mean flows with $u_0 = U = const$ lead to a simple Doppler-shifted propagation, as one would expect:

$$X_t = -\beta - \frac{1}{Q}\int_A \mathrm{d}S\, h'U \qquad (6.30)$$
$$= -\beta + U.$$

Figure 6.9 shows the time evolution of the height anomaly field between $-4 < y < 4$ for a steadily forced experiment with forcing scale $r_0 = 4$ and magnitude $F_0 = 0.5$ and constant background wind with speed U. The field shows clear indication of eddies being formed within the forcing region (origin) and being shed westwards. Their velocities are in good agreement with the analytical estimates from equation 6.30, which are indicated by the slopes of the superimposed lines.

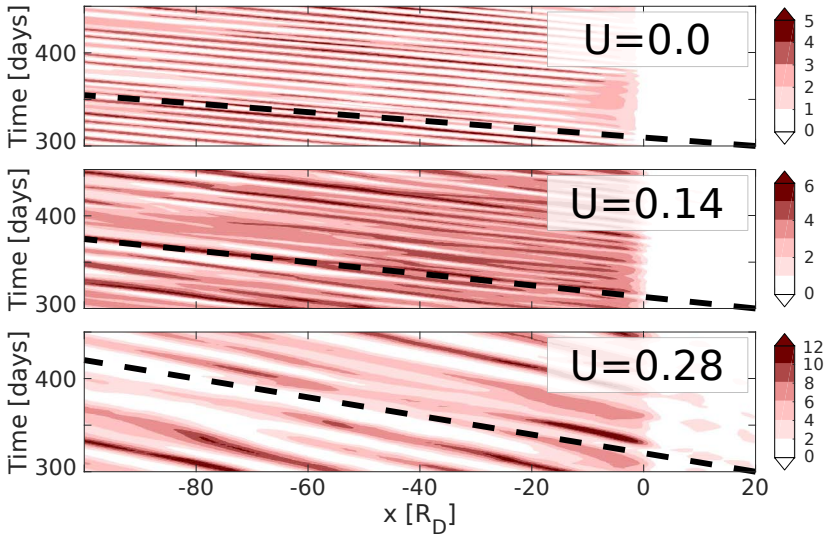

Fig. 6.9 Time evolution of height anomaly response to a steady forcing with $r_0 = 4$ and $F_0 = 0.5$ and different homogeneous background wind with strength U. The field is averaged over $-4 < y < 4$. Dashed lines indicate the theoretical zonal vortex speed according to equation 6.30, with $\beta = 0.51$.

Hence, the introduction of a homogeneous background wind is equivalent to a change of reference frame in terms of response propagation speed. However, figure 6.9 also shows a reduction of shedding frequency with increase in background wind speed. Figure 6.10 shows temporal and spatial Fourier decompositions of the corresponding flows for a for a zonal range of $-100 < x < 0$ and time period of days 300 to 1000, averaged over the respective other range and the linear trend was removed. The arrows and numbers indicate the global maximum location of each graph.

One can clearly see that the frequency ω decreases monotonically as the background wind speed is increases. This is a direct measure of the decrease in shedding frequency, since the vortices travel with an almost constant zonal velocity (see figure 6.9). The maximum zonal wave number k of the response, i.e. the eddy size, does not change significantly and not systematically. Interpreting the response as

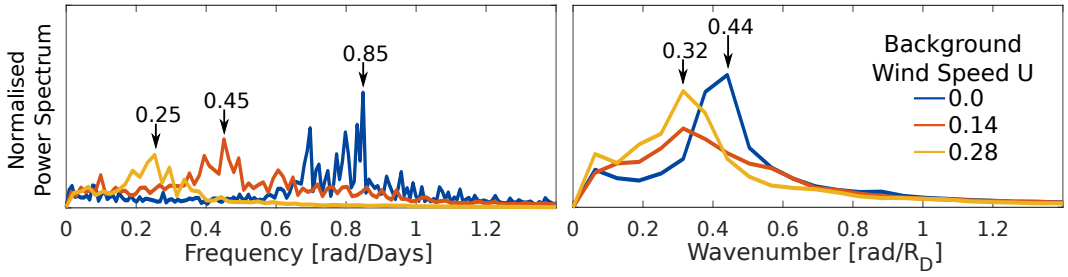

Fig. 6.10 Fourier decomposition of the azonal response to a forcing with $r_0 = 4$ and $F_0 = 0.5$ and various homogeneous background wind speeds U, calculated over a zonal range of $-100 < x < 0$ or time period of days 300 to 1000 and averaged over the respective other range and $-4 < y < 4$. The frequency and wave number of the global maximum of each graph is indicated.

a wave-structure with propagation velocity $c_p = \omega/k$ we can estimate the speed of the disturbances in a quantitative way, using the global maxima of the different spectra to estimate the propagation velocity.

The results are shown in table 6.1, compared to the theoretical predictions of equation 6.30. A clear drop in velocity is obvious in both and, generally, the experimental results and the theory seem in reasonable agreement. Davey and Killworth [1989] argued, that the scaling for the propagation speed if given by ωr_0, where r_0 is the zonal length scale of the forcing. This idea would suggest that the wave number k is set by the inverse of the forcing scale, and not by its meridional structure, which would be the case in the instability picture described in chapter 5. Our results suggest $k \approx 0.4 > 1/4$ for a forcing with $r_0 = 4$. However, the analysis is not detailed enough to give a definitive answer on this matter.

Table 6.1 Propagation speed of anomalies experimentally quantified as phase speed $c = \omega/k$ based on frequency ω and wave number k decompositions for different homogeneous background wind speeds U, as well as theoretically derived values based on equation 6.31 for $\beta = 0.51$.

U	Experiment c_p	Theory $\beta - U$
0	0.45	0.51
0.14	0.33	0.37
0.28	0.18	0.23

It should also be noted that the experimental estimate seems to be consistently below the corresponding theoretical predictions. This could be due to a chain effect, which is not captured by the centre-of-mass approach, or due to linear dispersion slowing down the eddies, as stated by Early et al. [2011]. However, the deviation from theory is not obvious in figure 6.9 and one has to be careful with over-interpreting figures in table 6.1, keeping in mind the noisy nature of the Fourier spectra and the simple approach used, which only considers the maximum frequency/wave number.

Next we want to change the background zonal wind to a linear shear to centred at $y = 0$, i.e. $u_0 = sy$. According to equation 6.31, based on the theory presented in subsection 6.1.2, a simple linear shear

should only affect the vortex speed via the local wind speed at the centre in the forcing if we assume the vortices to be meridionally symmetric about their centre, i.e. $h'(x,y) = h'(x,-y)$.

$$\begin{aligned} X_t &= -\beta - \frac{1}{Q}\int_A \mathrm{d}S\, h' s y \\ &= -\beta - \frac{s}{Q}\left(\int_{A>y} \mathrm{d}S\, h' y + \int_{A<y} \mathrm{d}S\, h' y\right) \\ &= -\beta - \left(\frac{s}{Q}\int_{A>y} \mathrm{d}S\, h' y - \frac{1}{Q}\int_{A>y} \mathrm{d}S\, h' y\right) \\ &= -\beta. \end{aligned} \tag{6.31}$$

Any linear shear component of the background flow should have no effect on the centre of mass velocity. Figure 6.11 shows that the vortex propagation velocity indeed does not change as we increase the linear shear strength s and their velocity matches the theoretically predicted long Rossby wave speed very well.

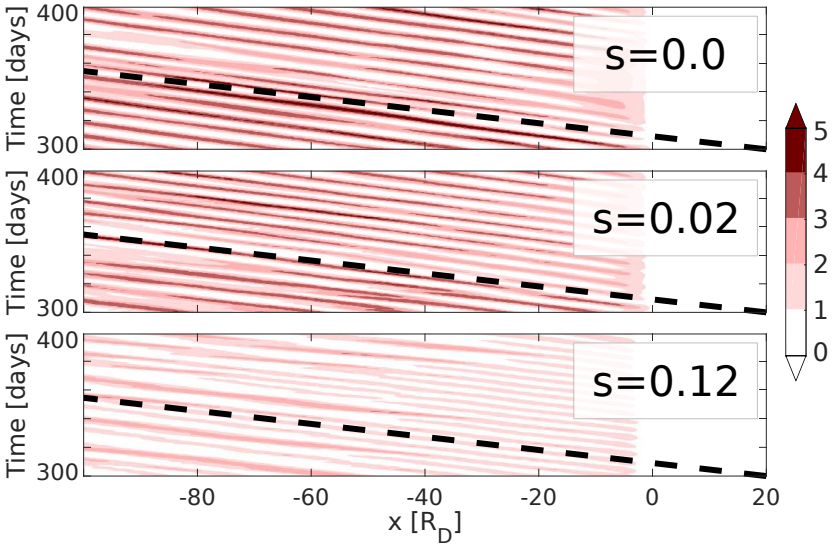

Fig. 6.11 Height anomaly evolution of the response to a forcing with $r_0 = 4$ and $F_0 = 0.5$ and a linear background shear s with vanishing wind at $y = 0$. The field is averaged over $-4 < y < 4$. Dashed lines indicate the long Rossby wave speed β.

However, other features of the response seem to be altered by the shear. Figure 6.12 indicates a change in shedding frequency and potentially eddy length scale. A similar Fourier decomposition as in the homogeneous background wind case indicates indeed a drop of shedding frequency. This change is accompanied by a decrease in zonal wave number, i.e. shed eddies generally become larger.

The changes in frequency and wave number, however, seem to happen in a way that keeps the propagation speed constant. Again using the peak positions to estimate a phase speed $c_p = \omega/k$, we find the eddy

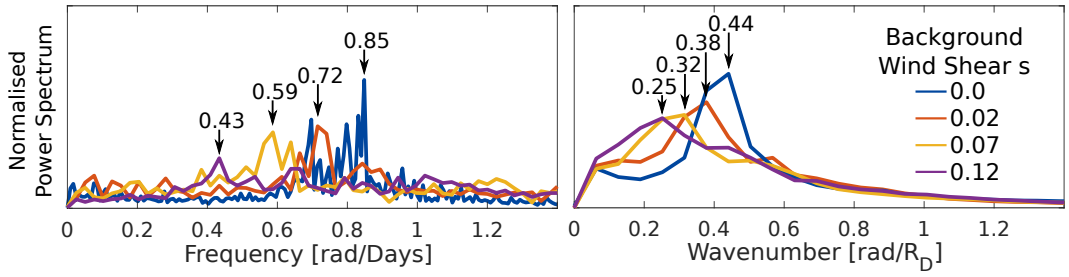

Fig. 6.12 Fourier decomposition of the azonal response to a forcing with $r_0 = 4$ and $F_0 = 0.5$ and various background winds with shear strength s, calculated over a zonal range of $-100 < x < 0$ or time period of days 300 to 1000 and averaged over the respective other range and $-4 < y < 4$. The frequency and wave number of the global maximum of each graph is indicated.

velocities to stay almost unchanged and close to the predicted value of $\beta = 0.51$. The experimentally estimated velocities, again, seem to be systematically below the predictions, as stated and explained earlier.

Table 6.2 As in table 6.1, but for background winds with shear strength s.

s	Experiment c_p	Theory β
0	0.45	0.51
0.02	0.44	0.51
0.07	0.43	0.51
0.12	0.40	0.51

Even though figure 6.12 shows a decrease in shedding frequency and increase in eddy scale with increasing s, a close look at the bottom plot in figure 6.11 hints towards a slightly different and more complicated idea. The frequency and zonal scale of the flow seems to depend on x, with the flow near the forcing region corresponding to larger ω and smaller k. A power spectrum analysis for the respective sub-domains $-100 < x < -50$ and $-50 < x < 0$ was inconclusive due to the high level of noise. The phenomenon, however, can be explained by vortex-merging.

Figure 6.13 shows the height anomaly field at different points in time. Clear vortices are visible, generally moving westward. While all vortices are well separated at day 170, two of them move close to each other at day 173 and merge at day 176. They then form a larger, single eddy, which is even more separated from adjacent ones.

This merging is likely to be caused by small perturbations in meridional positions of vortices and hence a small difference in zonal propagation speed of two neighbouring eddies. This allows eddies to come closer to each other and eventually exchange fluid parcels. The merging of similar vortices has been extensively studied by various authors in different numerical and laboratory settings [Christiansen 1973; Griffiths and Hopfinger 1987; Cerretelli and Williamson 2003], and a strong dependency on the vortex separation was found in some cases. Marcus [1990] investigated the behaviour of vortices in a shear

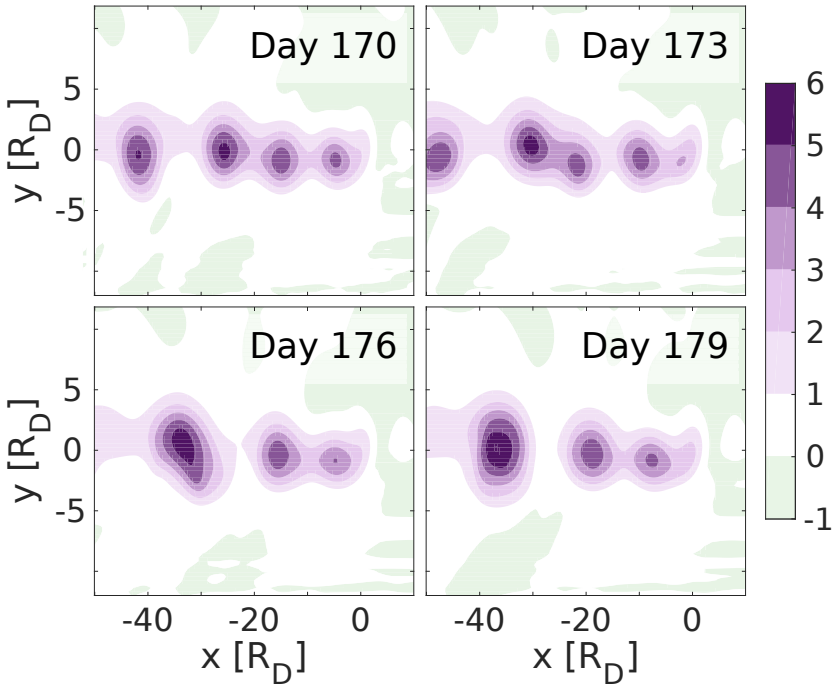

Fig. 6.13 Height anomaly snapshots for a forcing with $r_0 = 4$ and $F_0 = 0.5$ in a system with a background wind shear of strength $s = 0.12$. The figure shows the formation and downstream merging of vortices.

flow and found that, if the vorticity of the shear is of the same sign as the vorticity of the vortex, merging is likely to happen at separations of the scale of the eddy size. Despite the merging phenomenon, which seems to be a regular behaviour of the response in a shear flow, the vortices stay mostly coherent circular structures for a range of tested values of s.

6.2.3 Effects of a zonal jet and thermal damping

Section 6.2 investigated the time evolution of the response to a localised forcing, with particular focus on the propagation speed of eddies without the influence of external physical processes and with simple background flows, like a homogeneous zonal wind or a zonal shear wind. We now want to see how the characteristics of the response change as we introduce a more complex basic state wind and thermal damping, i.e. choosing $\varepsilon > 0$ in equation 2.3. The damping is supposed to represent radiative forcing of the surrounding fluid and the corresponding mass flux in and out of the modelled layer. Just like in the previous sections of this chapter, we want to focus on strongly forced systems in the shedding state, where the response takes the form of isolated, westwards travelling vortices.

As the theory presented in section 6.1.1 suggests, the eddies shed from the forcing region travel westward. Without any dissipation and a constant forcing magnitude the mean mass flux west of the source region will therefore be constant. Since the vortices' motion is steady this will lead to a zonally constant

mean height anomaly profile. If we introduce a forcing of e-folding time scale ε^{-1} the eddies will be damped as they propagate and the mean mass flux and mean height anomaly profile will decay with westward distance from the forcing. This behaviour is illustrated in figure 6.14, showing zonal mean height anomaly profiles for different damping rates.

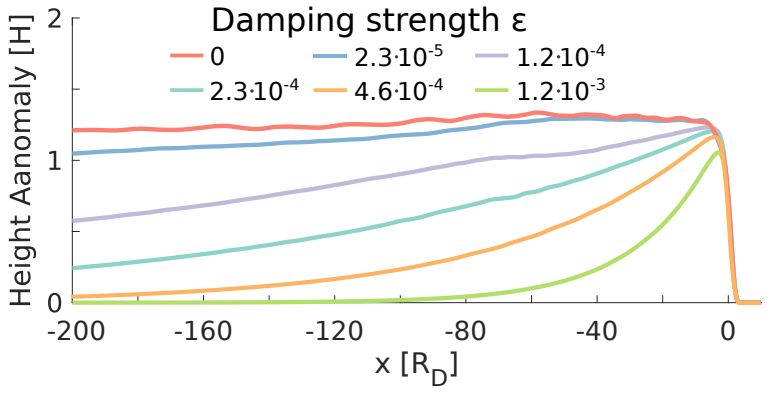

Fig. 6.14 Mean height anomaly profile between $-6 < y < 6$ for a forcing with scale $r_0 = 4$ and magnitude $F_0 = 0.5$ and different values of thermal damping rate ε.

The zonal height anomaly profiles decay exponentially for $x < 0$. Equation 6.29 predicts the shed vortices to travel steadily with the long Rossby wave speed, given by $\beta = 0.51$ in rescaled units (see 2.1 in section 2.3). We might therefore expect the e-folding length scale of the profiles to scale like the ratio of the propagation speed and the damping rate. Figure 6.15 shows the zonal mean height anomaly profiles for systems with different damping strengths on a logarithmic scale. Superimposed are straight lines with slope $18\varepsilon/\beta$. The factor 18 indicates that some (dynamical) process is enhancing the damping and therefore effectively increasing the damping rate. The effect of this process, however, also seems to scale with the damping rate ε.

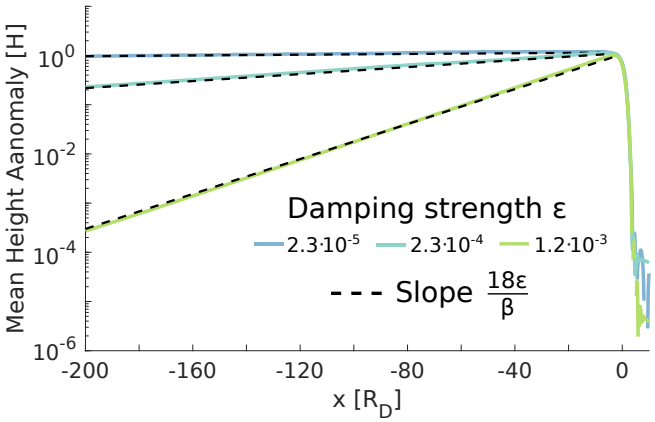

Fig. 6.15 Three of the profiles shown in figure 6.14 displayed as semi-logarithmic plot (solid lines) superimposed with corresponding exponential scaling predictions with slope length $\beta/(18\varepsilon)$ (dashed lines).

Despite reducing the zonal extent of the response, thermal damping can also affect its temporal dependency. Without dissipation the system is in the shedding state, using the characterisations explained in chapter 5. The top panel of figure 6.16 shows the time evolution of the azonal component of the height anomaly response along a zonal band for systems with different damping rates ε. The bottom panel shows the two-point correlation defined by

$$C(\chi,\tau) = \langle h(x_0,y_0,t)h(x_0+\chi,y_0,t+\tau)\rangle_t, \tag{6.32}$$

where $\langle\cdot\rangle_t$ describes temporal average and we chose a base point $x_0 = -4, y_0 = 0$ and different spatial offsets χ and temporal lags τ.

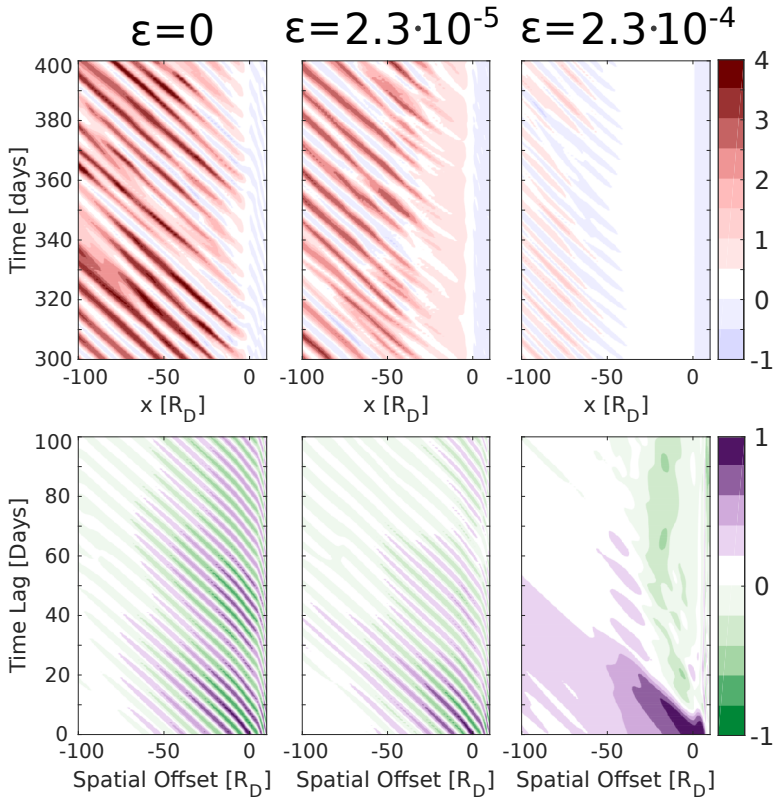

Fig. 6.16 Analysis for three experiments using a steady, localised forcing with $r_0 = 4$ and $F_0 = 0.5$ and different thermal damping parameters ε Top: height anomaly response, averaged between $-4 < y < 4$. Bottom: mean correlation C, calculated using equation 6.32 for a base point $x_0 = -4, y_0 = 0$.

In both, the time evolution and the correlation plots of figure 6.16, a clear periodic formation of discrete patches of anomaly in the forcing region is visible for the case without damping, even if the correlation decays with increasing offset and lag due to the turbulent nature of the system. As we increase ε, however, the behaviour of the system changes. For the case with strong damping, i.e. $\varepsilon = 2.3 \cdot 10^{-4}$,

we do not see any height anomaly perturbation near the forcing region. All wave-petters develop downstream at $x < -50$. Note that their corresponding propagation speed seems to be the same as in the other cases. The correlation plot does also not show the existence of a systematic wave pattern of significant strength, but simply shows the westward propagation of random perturbations created inside the source region.

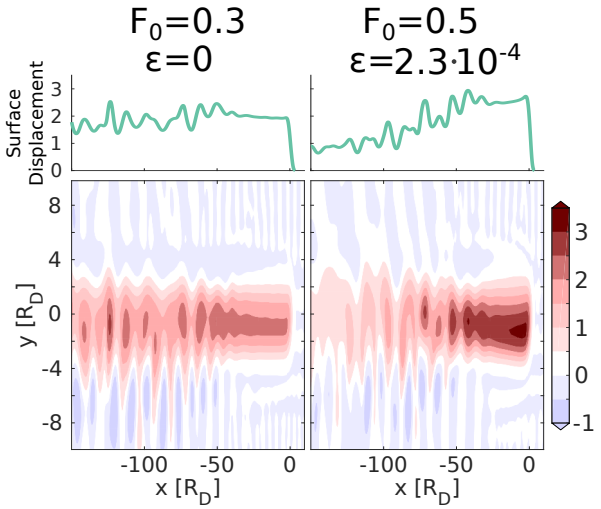

Fig. 6.17 Day 300 height anomaly response for steadily forced experiments with scale $r_0 = 4$ and different magnitudes F_0 and thermal damping rates ε. Bottom panel shows the 2D fields, top graphs show the profile along $y = 0$.

Figure 6.16 indicates a state-change of the system from shedding state to break-up state as we increase the thermal damping rate. As explained in chapter 5 this corresponds to a change from an absolute to a spatial instability of the system. Figure 6.17 compares height anomaly snapshots and zonal profiles along $y = 0$ at day 300 for two spatially unstable systems. The left panel corresponds to a case with weaker forcing magnitude ($F_0 = 0.3$) but without damping. It can be seen how the response is almost unperturbed near the origin and perturbances develop downstream. The right panel shows a case with a stronger forcing ($F_0 = 0.5$) and thermal damping. The general structure is similar to the other case, but in addition the height anomaly field does show a systematic spatial decay away from the forcing.

A second aspect of basis state change we will investigate in this section is the sensitivity of the system to a steady and zonal background flow. We are in particular interested in the changes induces by a zonal-jet-like basis wind. Figure 6.14 illustrates the meridional profile of the mass source with scale r_0 and magnitude F_0 (see equation) and the zonal wind of the basis state in form of a zonal jet. The jet is supposed to follow the profile $u_0 = U_0 \cos^2(\pi(y - y_J)/(2r_J))$, with wind magnitude U_0, width r_J and centre latitude y_J.

Following equation 6.27 the propagation speed of shed vortices will be modified proportional to the meridional integral of the zonal background wind weighted by the height anomaly of the eddy. We will

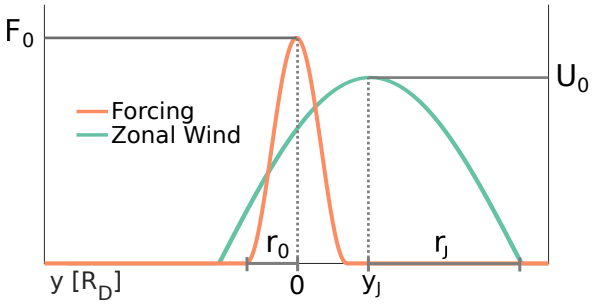

Fig. 6.18 Meridional profile of the forcing along $x = 0$ (see section 2.3.1) and meridional profile of the imposed background jet. The jet is centred at y_J and has a full width of $2r_J$.

assume the eddies to preserve the meridional shape of the mass source, and use equation 6.27 to predict their velocity, modified by the imposed background jet.

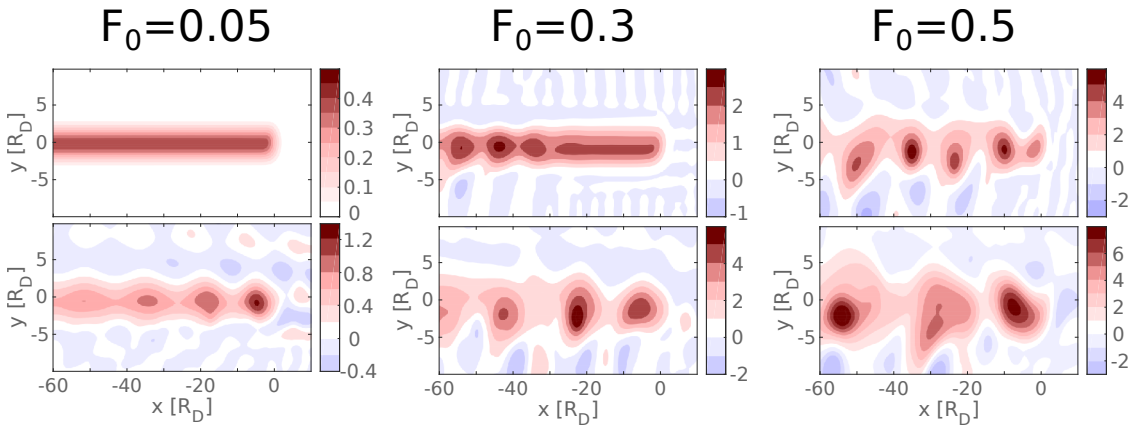

Fig. 6.19 Day 400 height anomaly snapshots for basis states without a jet (top) and with a jet of magnitude $U_0 = 14$, width $r_J = 12$ and centre position $y_J = 4$ (bottom) for three different forcing magnitudes and fixed scale $r_0 = 4$.

Figure 6.20 shows height anomaly correlation maps for systems with a forcing of scale $r_0 = 4$ and magnitude $F_0 = 0.5$ and background jets with different parameters. The correlations are defined by equation 6.32 for time lags τ and spatial offsets χ and are calculated using the base point $x_0 = -4, y_0 = 0$. The solid black lines correspond to the predicted eddy speed (see equation 6.27). The alignment with the lines of constant correlation for various sets of jet parameters indicates a good agreement between experiment and theory. As expected, the general trend of a basic state westerly jet is to slow down the propagation of westwards shed eddies. For completeness: if the (weighted) jet velocity exceeds the long Rossby wave speed the anomaly will start to be advected eastward (not shown).

The reduction in eddy velocity leads to an increase in the mean height anomaly west of the forcing for systems without damping. This has to be the case, since we can assume most of the anomaly to move predominantly westwards (see section 6.1.1) and the mass flux into/out of the system is completely

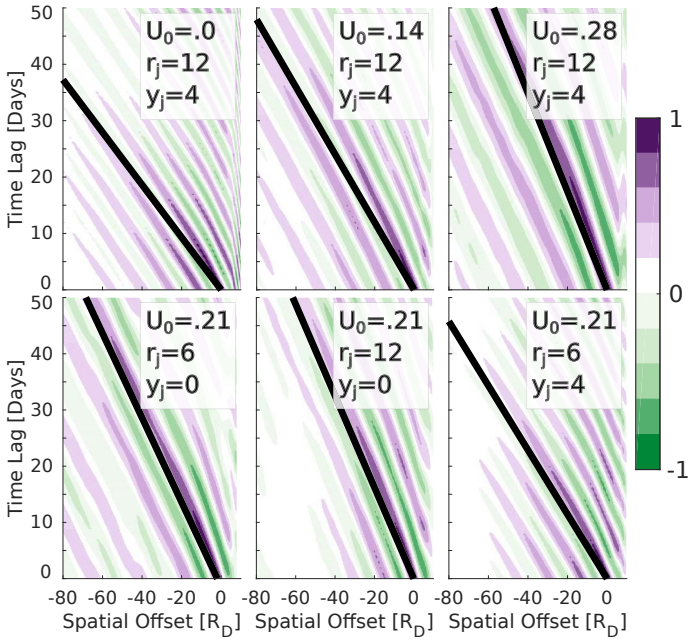

Fig. 6.20 Correlation maps according to equation 6.32 for a forcing of scale $r_0 = 4$ and magnitude $F_0 = 0.5$ and background jets with different magnitudes U_0, widths r_J and centre positions y_J. Slope of the solid lines indicate the predicted eddy speed according to equation 6.27.

given by the steady forcing. The top plot in figure 6.21 shows the temporally averaged zonal height anomaly profile for a fixed forcing of scale $r_0 = 4$ and $F_0 = 0.5$, as well as a jet of centre position $y_J = 4$, width $r_J = 12$ and different magnitudes U_0. As expected the mean height anomaly increases within the forcing region and stays constant as the response propagates westwards.

The reduction of propagation speed does not have an effect on the zonal length scale of the response. However, in combination with thermal damping the height anomaly response shows a clear localisation, as can be seen in the bottom plot of figure 6.21. As explained earlier in this section, the eddies shed from the mass source decay at a rate proportional to the thermal damping rate ε as they travel westwards. If the vortex speed is reduced due to the presence of a background jet[1] the corresponding decay length will be reduced as well. This is indicated by the dotted lines and black crosses, representing the maxima and e-folding lengths of the profiles. The slow-down of the response speed by a jet can cause a strong localisation for otherwise weak thermal damping rates.

Amemiya and Sato [2018] also analyse the response to a steady localised mass source in a single-layer model with a meridionally varying mean depth and weak thermal damping. Such a meridional depth dependence induces a zonal mean wind. They find a change in zonal extent and observe a localised mean state, in accordance with the results shown in figure 6.21, but potentially even more localised (i.e. forming sharper zonal gradients at the western edge). In addition, they describe a change in temporal

[1] Note that the thermal damping is only acting on the deviation of the height anomaly on the basic state.

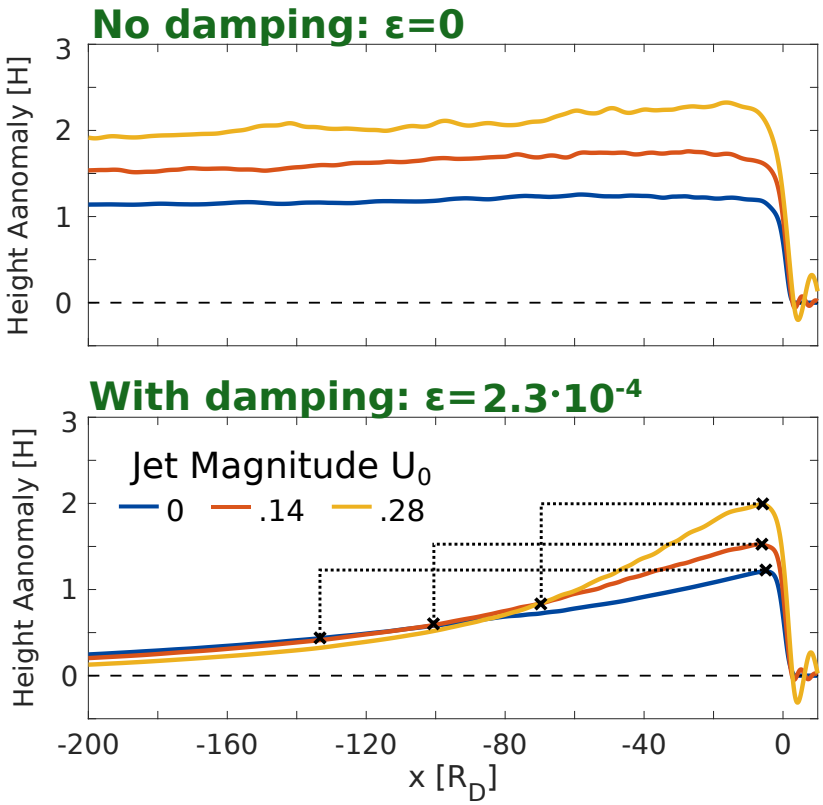

Fig. 6.21 Mean height anomaly profile between $-6 < y < 6$ for a forcing with scale $r_0 = 4$ and magnitude $F_0 = 0.5$ on top of zonal jets with width $r_J = 12$, centre position $y_J = 4$ and different magnitudes U_0. The forcing profile and background flow are illustrated in figure 6.19. The top plot illustrates the elongated response in a system without damping, the bottom plot shows zonal localisation when damping is active. Black crosses and dotted lines indicate maxima and e-folding lengths of the response profiles.

behaviour and interpret it as possible changes in the stability properties of the response (similar to what is shown in figure 6.16).

It should be noted, that the meridional change in mean depth does not only induce a zonal wind, but also alters the meridional PV gradient of the basic state. The corresponding re-distribution of PV could lead to an additional localising effect. It is, however, questionable if the cases with a stronger mean depth gradient presented by Amemiya and Sato [2018] are useful representations of the sub-tropic UTLS, since the corresponding basic state seems to develop a reversed PV gradient. As discussed in chapter 5 a reversal of the PV gradient can have a strong influence on the stability properties of a system. The problem is similar to what was described by e.g. Kraucunas and Hartmann [2007], who argue that sub- and extratropical basic state flows should not be introduced through a layer depth gradient to avoid unrealistic behaviour of the system.

At last we want to investigate how the response behaves in the presence of a very strong background wind, i.e. in particular an eastward jet with a wind speed greater than the long Rossby wave speed of $\beta = 0.51$. With such a basic wind any shed vortices (or emitted Rossby waves) should not be able to propagate westward any longer, but should be advected eastward instead. Figure 6.22 shows the time mean response (solid lines) to a localised steady forcing with a background jet according to figure 6.18 and a thermal damping parameter of $\varepsilon = 2.3 \cdot 10^{-4}$. Note that the jet speed by which the response is affected will generally be smaller than the jet magnitude due to the northward displacement of the jet and the finite extent of the anticyclone.

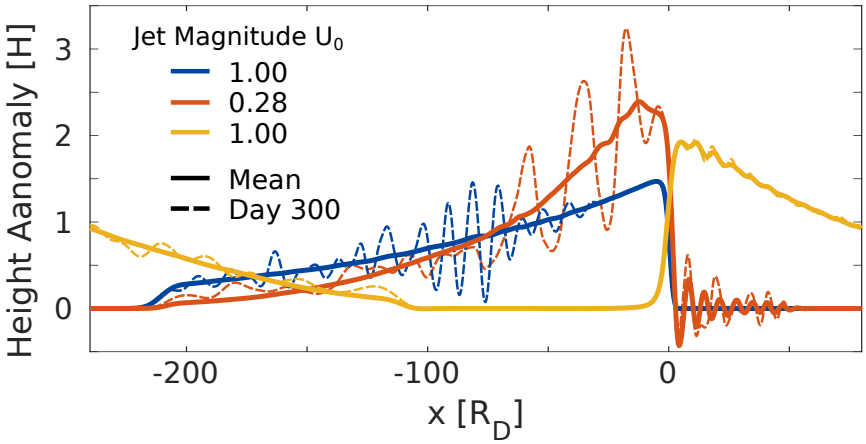

Fig. 6.22 Height anomaly profiles between $-5 < y < 5$ for a forcing with scale $r_0 = 4$ and magnitude $F_0 = 0.5$ on top of zonal jets with width $r_J = 12$, centre position $y_J = 4$ and different magnitudes U_0. Solid lines show the time mean and dashed lines the profile at day 300.

It can be seen how increasing the jet magnitude from $U_0 = 0$ to $U_0 = 0.28$ localises the response, similar to what is shown in figure 6.21. When choosing $U_0 = 1$, which ensures the wind speed around $y = 0$

to exceed the Rossby wave speed, the response clearly stretches to the east, rather than the west[1]. The push-back of the response to the east with increasing jet speed can potentially explain certain aspects of the transition from westward to eastward shedding for increasing strength of mid-latitude dynamics seen in chapter 4.

It is hereby important to remember that the eastward shedding process also involves the presence of baroclinic eddies and thus a system with steady background wind will be unlikely to fully reproduce this behaviour. This is reflected in the fact that we do not only observe a general change of propagation direction of the response, but also a qualitative change in variability. The dashed lines in figure 6.22 show the height anomaly profile at day 300 for different strengths of the background wind. It can be seen that for small values of U_0, that allow the response to propagate westwards, the system exhibits strong temporal variability. For large values of U_0, which lead to an eastward advection of the response, the system seems almost steady. Consequently we do not observe eddy shedding in cases with eastward advection of the anticyclone. This potentially suggests that the interaction with baroclinic eddies is indeed necessary to obtain the eastward eddy shedding observed in relation with the monsoon anticyclone in re-analysis data (chapter 3) and numerical experiments (chapter 4).

6.3 Summary and discussion

In this chapter we investigated the propagation of discrete vortices (e.g. representing eddies shed from a steady local mass source) in a single-layer model and how the corresponding response to a steady localised forcing is modified by certain physical processes, like thermal damping or the interaction with a background flow. The main aim of this study is to gain insights into the far-field response to a localised forcing. In addition this chapter aimed to support some of the results, features and behaviours presented in chapters 3 to 5. In particular in relation to the question of zonal localisation of the monsoon anticyclone and details of the behaviour of shed vortices.

Following these incentives we were able to gain insights into the evolution of coherent vortex structures similar to the ones observed in various geophysical flows, including the eddies which are periodically being shed from the Asian monsoon anticyclone. The problem of eddy propagation is potentially relevant to a variety of fluid-dynamical systems and thus we kept the theoretical formulation of this chapter as general as possible, although an application to the monsoon system was the main motivation.

We started by adapting a simple quantitative theory for the velocity of eddies based on their centre of mass. Section 6.1 used this centre-of-mass approach to analytically estimate the zonal velocity of coherent vortex structures in various systems. Special focus was given to how a zonal background wind can influence the eddy propagation and the question whether the zonal velocity is modified if the vortex is not well isolated but part of a zonally periodic chain of weakly connected eddies.

[1] Note that the experiments with $U_0 = 0, 0.28$ include a sponge region active for $x < -200$, while the sponge region in the case with $U_0 = 1$ is active between $-120 < X < -40$, explaining the rapid decay of the response within these regions.

We found that background winds which vary linearly with latitude alter the zonal speed of circular eddies only through the wind speed at the eddy centre. Shed vortices are slowed down and, for sufficiently strong background winds, the response changes from extending to the west to extending eastwards. This behaviour can potentially explain aspects of the qualitative transition from a state of westward shed vortices to a state dominated by eastward shedding when increasing the strength of mid-latitude dynamics in chapter 4. Further we showed that, in contrast to the conclusion of existing studies, the eddy propagation is not sensitive to the eddy being well isolated or being part of a zonal chain of vortices. Our findings suggest that the vortices, although potentially connected, can be treated as almost separated and propagate with the velocity of long Rossby waves, rather than a corresponding short-wave speed.

In addition we showed that when including a westward background wind the response can enter the shedding regime even for smaller forcing magnitudes that would otherwise lead to a steady response, increasing the potential importance of the shedding state when describing the time dependence of the Asian monsoon anticyclone. In contrast, the inclusion of (thermal) damping can increase the stability of the system and therefore suppress temporal variability. It is thus even more important to consider carefully the strength of dissipative processes included when modelling the monsoon anticyclone, as they can not only affect the zonal scale, but also the temporal behaviour of the response (see section 3.2). These findings further suggest that it might be worthwhile to extend the spatio-temporal stability analysis from chapter 5 by including damping and background winds in order to study their effect on the monsoon flow.

These results have potential implications for transport behaviour of the Asian monsoon anticyclone, although the transport itself was not investigated in this thesis. As mentioned in earlier chapters, the shed eddies can trap e.g. trace gases and transport them horizontally across the tropopause. Changes in the stability of the response, and thus e.g. a suppression of vortex formation, or the eddy velocity (and with it the zonal structure) can thus potentially have direct influence on the transport behaviour.

Chapter 7

Discussion of our findings

The focus of this dissertation has been a study on the structure and evolution of the Asian monsoon anticyclone. The aim was to improve our understanding of the dynamical and physical processes that are relevant in determining the state of the monsoon circulation and gain insights on how the the behaviour of the flow depends on certain physical scales and properties of the system.

7.1 Summary of this thesis

Chapter 1 outlined various aspects of the general circulation in the tropical and extratropical middle atmosphere, with special focus on the Asian monsoon circulation. We discussed characteristics of relevant atmospheric features, like the tropopause, the mid-latitude jets and baroclinic eddies, and defined a range of quantities that we will use to describe the dynamics of the monsoon, like potential vorticity.

In chapter 2 we introduced a set of models and data sources that we used for the analyses and studies within this dissertation. This included a detailed description of the re-analysis project ERA-Interim and the three- and two-dimensional numerical models used in chapters 3 to 6, as well as a discussion of their specific implementation.

Chapter 3 summarised, described and analysed a set of potentially relevant characteristics and behaviours of the monsoon circulation. The monsoon anticyclone was studied using a combination of re-analysis data and idealised numerical experiments in a simple general circulation model (GCM), forced by an imposed, localised, steady heating. In simulations with a resting atmosphere we observed a transition from a steady, almost linear response to a periodic westward shedding of vortices from the heating region when increasing the forcing magnitude, similar to behaviour described by other authors. In both cases the response is zonally not confined unless a finite mechanical friction is applied throughout the atmosphere.

In chapter 4 we found the system to form a zonally localised anticyclone when including a simple representation of mid-latitude dynamics, driven by a thermal relaxation towards a baroclinically unstable basic state, without the requirement for a strong mechanical damping in the upper troposphere and lower stratosphere. The temporal variability of the flow and its dependency on certain parameters of the imposed heating or the background state were investigated. As was shown, the modelled anticyclone changes between different states that exhibit east- and/or westward eddy depending on the structure of the meridional temperature gradient of the basic state and therefore the position, strength and structure of the mid-latitude jets. We also investigated the vertical structure of the monsoon, with special emphasis on the vertical extent of the circulation. It was shown that the vertical structure of the response is not simply set by the specifics of the heating distribution and that the corresponding PV anomaly associated with the monsoon anticyclone can extend significantly above the top of the heating. Following these results we discussed various mechanisms that can lead to a change in PV forcing for a given heating and evaluated their relevance for the presented system.

Chapter 5 discussed in detail the phenomenon of spontaneous westward shedding from a steady localised mass source in a single-layer beta-plane model. We observed three states with qualitatively different temporal and spatial variability depending on the forcing magnitude and length scale. In addition to the previously observed steady and eddy shedding states we found the model response to be steady near the forcing region and breaking-up into discrete patches downstream for certain parameter combinations. This behaviour motivated us to perform a comprehensive spatio-temporal stability analysis of certain idealised parallel shear flows representing a zonally elongated monsoon anticyclone in order to describe the westward eddy shedding process as a result of an absolute instability of the system.

The analysis involved the development and application of various practical procedures and (numerical) algorithms to identify modes which show unstable behaviour in either a temporal, convective or absolute sense. We investigated the properties of these unstable modes and their dependence on the magnitude and meridional scale of the base flow. Among other results, we found the studied system to develop an absolute instability for strong magnitudes and small meridional length scales and were able to numerically calculate e.g. the required threshold values and the frequency of the resulting unstable mode for a given flow profile. Finally we transferred the developed theory to the steadily forced numerical experiments and used it to explain the observed transition between the different types of temporal behaviour based on the forcing parameters.

Chapter 6 investigated the propagation of discrete vortices in a single-layer beta-plane model and the dependency of the response to a steady localised mass source on thermal damping or the strength and structure of a basic state wind. The aim was to gain insights into the evolution of coherent eddies observed in various geophysical flows, e.g. the vortices periodically being shed westwards from the Asian monsoon anticyclone. Based on a centre-of-mass approach we re-visited and adapted a theory on the intrinsic zonal propagation of coherent eddies on a beta-plane. Among other things found that the eddy propagation is not modified when the system is given by a zonally periodic chain of weakly

connected eddies compared to a single isolated vortex, in contradiction to results found by other authors. We validated some of the analytic predictions by comparing them to the response to a localised steady mass source in the shedding regime and found good agreement for a range of parameters. We further discussed how the spatio-temporal structure and the propagation characteristics of perturbations depend on the strength and structure of an imposed background flow or thermal damping. In particular, we showed that a significant localisation of the time mean structure of the response to a localised steady mass source can be achieved when combining the effects of westerly background wind and thermal damping.

7.2 Open questions and further research

In the following we want to point out a number of questions and aspects that we were not able to fully address within the scope of this dissertation.

Regarding the GCM experiments of chapters 3 and 4 it would be interesting to investigate the sensitivity of the response to changes in various other parameters of the imposed heating and the basic state. This could include a change of the horizontal scale and centre location of the forcing. The results presented in subsection 4.1.3 potentially suggest a strong dependence of the east- and westward eddy shedding behaviour on the position of the mid-latitude jets relative to the forcing region.

Figure 3.5 indicates that the PV minimum associated with the monsoon anticyclone roughly covers a region between 20-40° latitude, and hence is confined to the northern half of the corresponding latent heat distribution. The results of the numerical experiments of Hahn and Manabe [1975] of Boos and Kuang [2010] suggest that the influence of the Tibetan plateau can lead to a northward shift of the forced anticyclone. It would therefore be interesting to see how orography modifies the structure of the response and if a similar northern confinement of the anticyclone can be achieved.

In terms of single-layer model experiments one could run a set of steadily forced runs using a mass source with meridional structure following a $\cos^4$ profile. The results could then be compared with the findings of the spatial stability analysis discussed in chapter 5. The underlying idea is that the results of the presented stability analysis would then describe the linear steady solution of the forced experiments. One would therefore not require any fitting of the idealised basis profiles in the stability analysis onto the profiles extracted from the numerical experiments, but could potentially use the stability analysis outcome as predictive tool to determine the parameter regimes that lead to the three described shedding states.

It would further be interesting to investigate the relation between the single-layer experiments with a steady background flow (see subsection 6.2.3) and the results of Amemiya and Sato [2018], who performed steadily forced experiments in a basic state with varying layer depth and observed a localised response with non-trivial time dependence. This could include a reproduction of the zonally confined,

periodic state described by Amemiya and Sato [2018] and a gradual introduction of a bottom topography to reduce the mean layer depth gradient. One could then investigate if the zonal confinement of the forced anticyclone persists even without the questionable PV reversal of the basic state mentioned in subsection 6.2.3.

Finally one could try to design a set of single-layer experiments to mimic the effects of baroclinic eddies on the response to a steady localised mass source. These experiments could potentially give further insights into if and how the baroclinic eddies in the three-dimensional model experiments of chapter 3, caused by the thermal relaxation towards a baroclinically unstable basic state, can have a localising effect on the monsoon anticyclone. Such experiments could, for example, be realised by applying a random perturbation field to the height anomaly field at ever time step and hence imposing a random advective stirring effect to the system. The randomness could be achieved by using a perturbation field with fixed wave number and a phase evolving according to a random Ornstein-Uhlenbeck process with imposed temporal de-correlation time. Hence one could study the influence of baroclinic eddy perturbations with different length scales on the monsoon anticyclone response.

References

Amemiya, A. and Sato, K. (2018). *A two-dimensional dynamical model for the subseasonal variability of the Asian monsoon anticyclone*. Journal of the Atmospheric Sciences.

Andrews, D. G. (2000). *An Introduction to Atmospheric Physics*. Cambridge University Press.

Baldwin, M. P., Stephenson, D. B., Thompson, D. W., et al. (2003). *Stratospheric memory and skill of extended-range weather forecasts*. Science **301**, 636–640.

Ball, F. (1963). *Some general theorems concerning the finite motion of a shallow rotating liquid lying on a paraboloid*. Journal of Fluid Mechanics **17**, 240–256.

Bannister, R., O'neill, A., Gregory, A., and Nissen, K. (2004). *The role of the south-east Asian monsoon and other seasonal features in creating the 'tape-recorder' signal in the Unified Model*. Quarterly Journal of the Royal Meteorological Society **130**, 1531–1554.

Bao, M. and Hartmann, D. L. (2014). *The response to MJO-like forcing in a nonlinear shallow-water model*. Geophysical Research Letters **41**, 1322–1328.

Bao, X. and Zhang, F. (2013). *Evaluation of NCEP–CFSR, NCEP–NCAR, ERA-Interim, and ERA-40 reanalysis datasets against independent sounding observations over the Tibetan Plateau*. Journal of Climate **26**, 206–214.

Battisti, D. S., Sarachik, E., and Hirst, A. (1999). *A Consistent Model for the Large-Scale Steady Surface Atmospheric Circulation in the Tropics**. Journal of climate **12**, 2956–2964.

Bers, A. (1973). "Theory of absolute and convective instabilities". *International Congress on Waves and Instabilities in Plasma*.

Boos, W. R. and Kuang, Z. (2010). *Dominant control of the South Asian monsoon by orographic insulation versus plateau heating*. Nature **463**, 218–222.

Bordoni, S. and Schneider, T. (2008). *Monsoons as eddy-mediated regime transitions of the tropical overturning circulation*. Nature Geoscience **1**, 515.

Bourassa, A. E., Robock, A., Randel, W. J., et al. (2012). *Large volcanic aerosol load in the stratosphere linked to Asian monsoon transport*. Science **337**, 78–81.

Boville, B. A. (1984). *The influence of the polar night jet on the tropospheric circulation in a GCM*. Journal of the atmospheric sciences **41**, 1132–1142.

Brewer, A. (1949). *Evidence for a world circulation provided by the measurements of helium and water vapour distribution in the stratosphere*. Quarterly Journal of the Royal Meteorological Society **75**, 351–363.

Briggs, R. J. (1964). *Electron-stream interaction with plasmas*. MIT.

Butler, A. H., Thompson, D. W., and Heikes, R. (2010). *The steady-state atmospheric circulation response to climate change–like thermal forcings in a simple general circulation model*. Journal of Climate **23**, 3474–3496.

Cenedese, C. and Linden, P. (1999). *Cyclone and anticyclone formation in a rotating stratified fluid over a sloping bottom*. Journal of Fluid Mechanics **381**, 199–223.

Cerretelli, C. and Williamson, C. (2003). *The physical mechanism for vortex merging*. Journal of Fluid Mechanics **475**, 41–77.

Chang, C. P. and Krishnamurti, T. N. (1987). *Monsoon Meteorology*. Oxford University Press.

Chang, C.-P. (2004). *East Asian Monsoon*. Vol. 2. World Scientific.

Charney, J. G. (1947). *The dynamics of long waves in a baroclinic westerly current*. Journal of Meteorology **4**, 136–162.

Chelton, D. B., Schlax, M. G., Samelson, R. M., and Szoeke, R. A. de (2007). *Global observations of large oceanic eddies*. Geophysical Research Letters **34**.

Chen, G. and Plumb, R. A. (2014). *Effective isentropic diffusivity of tropospheric transport*. Journal of the Atmospheric Sciences **71**, 3499–3520.

Chen, P., Hoerling, M. P., and Dole, R. M. (2001). *The origin of the subtropical anticyclones*. Journal of the atmospheric sciences **58**, 1827–1835.

Christiansen, I. (1973). *Numerical simulation of hydrodynamics by the method of point vortices*. Journal of Computational Physics **13**, 363–379.

Cushman-Roisin, B., Tang, B., and Chassignet, E. P. (1990). *Westward motion of mesoscale eddies*. Journal of Physical Oceanography **20**, 758–768.

Davey, M. K. and Killworth, P. D. (1984). *Isolated Waves and Eddies in a Shallow Water Model*. Journal of Physical Oceanogrophy **14**, 1047–1064.

– (1989). *Flows produced by discrete sources of buoyancy*. Journal of Physical Oceanography **19**, 1279–1290.

Dee, D. P., Uppala, S. M., Simmons, A., et al. (2011). *The ERA-Interim reanalysis: Configuration and performance of the data assimilation system*. Quarterly Journal of the royal meteorological society **137**, 553–597.

DeMaria, M. (1985). *Linear response of a stratified tropical atmosphere to convective forcing*. Journal of the Atmospheric Sciences **42**, 1944–1959.

Dethof, A., O'neill, A., Slingo, J., and Smit, H. (1999). *A mechanism for moistening the lower stratosphere involving the Asian summer monsoon*. Quarterly Journal of the Royal Meteorological Society **125**, 1079–1106.

Diaz, M. and Aiyyer, A. (2015). *Absolute and convective instability of the African easterly jet*. Journal of the Atmospheric Sciences **72**, 1805–1826.

Diwan, S. S. (2015). *Necessary conditions for spatial inviscid instability*. Proceedings of the Royal Society of London A: Mathematical, Physical and Engineering Sciences **471**.

Dobson, G. M. B. (1956). *Origin and distribution of the polyatomic molecules in the atmosphere*. Proc. R. Soc. Lond. A **236**, 187–193.

Dunkerton, T. J. and Delisi, D. P. (1986). *Evolution of potential vorticity in the winter stratosphere of January-February 1979*. Journal of Geophysical Research: Atmospheres **91**, 1199–1208.

Eady, E. T. (1949). *Long waves and cyclone waves*. Tellus A **1**.

Early, J. J., Samelson, R., and Chelton, D. B. (2011). *The evolution and propagation of quasigeostrophic ocean eddies*. Journal of Physical Oceanography **41**, 1535–1555.

Enomoto, T. (2004). *Interannual variability of the Bonin high associated with the propagation of Rossby waves along the Asian jet*. Journal of the Meteorological Society of Japan. Ser. II **82**, 1019–1034.

Enomoto, T., Hoskins, B. J., and Matsuda, Y. (2003). *The formation mechanism of the Bonin high in August*. Quarterly Journal of the Royal Meteorological Society **129**, 157–178.

Ertel, H. (1942). *Ein neuer hydrodynamischer Wirbelsatz*. Met. Z. **59**, 277–281.

Fadnavis, S., Roy, C., Chattopadhyay, R., et al. (2018). *Transport of trace gases via eddy shedding from the Asian summer monsoon anticyclone and associated impacts on ozone heating rates*. Atmospheric Chemistry and Physics **18**, 11493–11506.

Fadnavis, S., Semeniuk, K., Pozzoli, L., et al. (2013). *Transport of aerosols into the UTLS and their impact on the Asian monsoon region as seen in a global model simulation*. Atmospheric Chemistry and Physics **13**, 8771–8786.

Flierl, G. R. (1977). *The application of linear quasigeostrophic dynamics to Gulf Stream rings*. Journal of Physical Oceanography **7**, 365–379.

Fueglistaler, S., Dessler, A., Dunkerton, T., et al. (2009a). *Tropical tropopause layer*. Reviews of Geophysics **47**.

Fueglistaler, S., Legras, B., Beljaars, A., et al. (2009b). *The diabatic heat budget of the upper troposphere and lower/mid stratosphere in ECMWF reanalyses*. Quarterly Journal of the Royal Meteorological Society **135**, 21–37.

Garny, H. and Randel, W. J. (2013). *Dynamic variability of the Asian monsoon anticyclone observed in potential vorticity and correlations with tracer distributions*. Journal of Geophysical Research: Atmospheres **118**, 13–421.

– (2016). *Transport pathways from the Asian monsoon anticyclone to the stratosphere*. Atmospheric Chemistry and Physics **16**, 2703–2718.

Gettelman, A., Kinnison, D. E., Dunkerton, T. J., and Brasseur, G. P. (2004a). *Impact of monsoon circulations on the upper troposphere and lower stratosphere*. Journal of Geophysical Research: Atmospheres (1984–2012) **109**.

– (2004b). *Impact of monsoon circulations on the upper troposphere and lower stratosphere*. Journal of Geophysical Research: Atmospheres **109**.

Gill, A. (1980). *Some simple solutions for heat-induced tropical circulation*. Quarterly Journal of the Royal Meteorological Society **106**, 447–462.

Gill, A. and Phlips, P. (1986). *Nonlinear effects on heat-induced circulation of the tropical atmosphere*. Quarterly Journal of the Royal Meteorological Society **112**, 69–91.

Griffiths, R. and Hopfinger, E. (1987). *Coalescing of geostrophic vortices*. Journal of Fluid Mechanics **178**, 73–97.

Grise, K. M., Thompson, D. W., and Birner, T. (2010). *A global survey of static stability in the stratosphere and upper troposphere*. Journal of Climate **23**, 2275–2292.

Hahn, D. G. and Manabe, S. (1975). *The role of mountains in the south Asian monsoon circulation*. Journal of the Atmospheric Sciences **32**, 1515–1541.

Haqq-Misra, J., Lee, S., and Frierson, D. M. (2011). *Tropopause structure and the role of eddies*. Journal of the Atmospheric Sciences **68**, 2930–2944.

Haynes, P. and Ward, W. (1993). *The effect of realistic radiative transfer on potential vorticity structures, including the influence of background shear and strain*. Journal of the atmospheric sciences **50**, 3431–3453.

Heckley, W. and Gill, A. (1984). *Some simple analytical solutions to the problem of forced equatorial long waves*. Quarterly Journal of the Royal Meteorological Society **110**, 203–217.

Held, I. M. and Suarez, M. J. (1994). *A proposal for the intercomparison of the dynamical cores of atmospheric general circulation models*. Bulletin of the American Meteorological Society **75**, 1825–1830.

Hendon, H. H. (1986). *The time-mean flow and variability in a nonlinear model of the atmosphere with tropical diabatic forcing*. Journal of the atmospheric sciences **43**, 72–89.

Holton, J. R. and Colton, D. E. (1972). *A diagnostic study of the vorticity balance at 200 mb in the tropics during the northern summer*. Journal of the Atmospheric Sciences **29**, 1124–1128.

Hoskins, B. J. and Simmons, A. J. (1975). *A multi-layer spectral model and the semi-implicit method*. Quarterly Journal of the Royal Meteorological Society **101**, 637–655.

Hoskins, B. J. (1991). *Towards a PV-θ view of the general circulation*. Tellus A **43**, 27–35.

Hoskins, B. J. and Jin, F.-F. (1991). *The initial value problem for tropical perturbations to a baroclinic atmosphere*. Quarterly Journal of the Royal Meteorological Society **117**, 299–317.

Hoskins, B. J., McIntyre, M., and Robertson, A. W. (1985). *On the use and significance of isentropic potential vorticity maps*. Quarterly Journal of the Royal Meteorological Society **111**, 877–946.

Hoskins, B. J. and Rodwell, M. J. (1995). *A model of the Asian summer monsoon. Part I: The global scale*. Journal of the atmospheric sciences **52**, 1329–1340.

Hsu, C. J. and Plumb, R. A. (2000). *Nonaxisymmetric thermally driven circulations and upper-tropospheric monsoon dynamics*. Journal of the atmospheric sciences **57**, 1255–1276.

Huerre, P. and Monkewitz, P. A. (1990). *Local and global instabilities in spatially developing flows*. Annual Review of Fluid Mechanics **22**, 473–537.

James, R., Bonazzola, M., Legras, B., et al. (2008). *Water vapor transport and dehydration above convective outflow during Asian monsoon*. Geophysical Research Letters **35**.

Jin, F. and Hoskins, B. J. (1995). *The direct response to tropical heating in a baroclinic atmosphere*. Journal of the atmospheric sciences **52**, 307–319.

Kidston, J., Vallis, G., Dean, S., and Renwick, J. (2011). *Can the increase in the eddy length scale under global warming cause the poleward shift of the jet streams?* Journal of Climate **24**, 3764–3780.

Killworth, P. D. and Davey, M. K. (1987). *Paramater regimes for studying isolated eddies*. Geophysical & Astrophysical Fluid Dynamics **38**, 225–264.

Kim, J. and Son, S.-W. (2015). *Formation and maintenance of the tropical cold-point tropopause in a dry dynamic-core GCM*. Journal of the Atmospheric Sciences **72**, 3097–3115.

Kodera, K., Yamazaki, K., Chiba, M., and Shibata, K. (1990). *Downward propagation of upper stratospheric mean zonal wind perturbation to the troposphere*. Geophysical Research Letters **17**, 1263–1266.

Kraucunas, I. and Hartmann, D. L. (2007). *Tropical stationary waves in a nonlinear shallow-water model with realistic basic states*. Journal of the atmospheric sciences **64**, 2540–2557.

Lam, J. S.-L. and Dritschel, D. G. (2001). *On the beta-drift of an initially circular vortex patch*. Journal of fluid mechanics **436**, 107–129.

Lee, S.-K., Wang, C., and Mapes, B. E. (2009). *A simple atmospheric model of the local and teleconnection responses to tropical heating anomalies*. Journal of Climate **22**, 272–284.

Leeuwen, P. J. van (2007). *The propagation mechanism of a vortex on the β plane*. Journal of Physical Oceanography **37**, 2316–2330.

Lin, J.-L., Mapes, B. E., and Han, W. (2008). *What are the sources of mechanical damping in Matsuno-Gill-type models?* Journal of Climate **21**, 165–179.

Lin, S. and Pierrehumbert, R. (1993). *Is the midlatitude zonal flow absolutely unstable?* Journal of the atmospheric sciences **50**, 505–517.

Liu, Y., Hoskins, B., and Blackburn, M. (2007). *Impact of Tibetan orography and heating on the summer flow over Asia*. Journal of the Meteorological Society of Japan **85**, 1–19.

Luo, J., Song, J., Tian, H., et al. (2017). *A Case Study of Mass Transport during the East-west Oscillation of the Asian Summer Monsoon Anticyclone*. Advances in Meteorology **2017**.

Marcus, P. S. (1990). *Vortex dynamics in a shearing zonal flow*. Journal of Fluid Mechanics **215**, 393–430.

Matsuno, T. (1966). *Quasi-geostrophic motions in the equatorial area*. J. Meteor. Soc. Japan **44**, 25–43.

McGraw, M. C. and Barnes, E. A. (2016). *Seasonal sensitivity of the eddy-driven jet to tropospheric heating in an idealized AGCM*. Journal of Climate **29**, 5223–5240.

McWilliams, J. C. and Flierl, G. R. (1979). *On the evolution of isolated, nonlinear vortices*. Journal of Physical Oceanography **9**, 1155–1182.

Merkine, L.-O. (1977). *Convective and absolute instability of baroclinic eddies*. Geophysical & Astrophysical Fluid Dynamics **9**, 129–157.

Newman, P. A. and Rosenfield, J. E. (1997). *Stratospheric thermal damping times*. Geophysical research letters **24**, 433–436.

Nof, D. (1983). *The translation of isolated cold eddies on a sloping bottom*. Deep-Sea Res **30**, 171–182.

Nützel, M., Dameris, M., and Garny, H. (2016). *Movement, drivers and bimodality of the South Asian High*. Atmospheric Chemistry and Physics **16**, 14755–14774.

Ortega, S., Webster, P. J., Toma, V., and Chang, H.-R. (2017). *Quasi-biweekly oscillations of the South Asian monsoon and its co-evolution in the upper and lower troposphere*. Climate Dynamics **49**, 3159–3174.

Park, M., Randel, W. J., Emmons, L. K., et al. (2008). *Chemical isolation in the Asian monsoon anticyclone observed in Atmospheric Chemistry Experiment (ACE-FTS) data*. Atmospheric Chemistry and Physics **8**, 757–764.

Park, M., Randel, W. J., Gettelman, A., et al. (2007). *Transport above the Asian summer monsoon anticyclone inferred from Aura Microwave Limb Sounder tracers*. Journal of Geophysical Research: Atmospheres **112**, 1984–2012.

Pierrehumbert, R. (1986). *Spatially amplifying modes of the Charney baroclinic-instability problem*. Journal of Fluid Mechanics **170**, 293–317.

Ploeger, F., Gottschling, C., Griessbach, S., et al. (2015). *A potential vorticity-based determination of the transport barrier in the Asian summer monsoon anticyclone*. Atmospheric chemistry and physics **15**, 13145–13159.

Ploeger, F., Günther, G., Konopka, P., et al. (2013). *Horizontal water vapor transport in the lower stratosphere from subtropics to high latitudes during boreal summer*. Journal of Geophysical Research: Atmospheres **118**, 8111–8127.

Ploeger, F., Konopka, P., Walker, K., and Riese, M. (2017). *Quantifying pollution transport from the Asian monsoon anticyclone into the lower stratosphere*. Atmospheric Chemistry and Physics **17**, 7055–7066.

Plumb, R. A. (2007). *Dynamical constraints on monsoon circulations*. The Global Circulation of the Atmosphere **25**.

Polvani, L. M. and Kushner, P. J. (2002). *Tropospheric response to stratospheric perturbations in a relatively simple general circulation model*. Geophysical Research Letters **29**, 18–1.

Popovic, J. M. and Plumb, R. A. (2001). *Eddy shedding from the upper-tropospheric Asian monsoon anticyclone*. Journal of the atmospheric sciences **58**, 93–104.

Randel, W. J., Park, M., Emmons, L., et al. (2010). *Asian monsoon transport of pollution to the stratosphere*. Science **328**, 611–613.

Ren, X., Yang, D., and Yang, X.-Q. (2015). *Characteristics and mechanisms of the subseasonal eastward extension of the South Asian High*. Journal of Climate **28**, 6799–6822.

Ring, M. J. and Plumb, R. A. (2007). *Forced annular mode patterns in a simple atmospheric general circulation model*. Journal of the Atmospheric Sciences **64**, 3611–3626.

Rodwell, M. J. and Hoskins, B. J. (1995). *A model of the Asian summer monsoon. Part II: Cross-equatorial flow and PV behavior*. Journal of the Atmospheric Sciences **52**, 1341–1356.

Romps, D. M. (2014). *Rayleigh damping in the free troposphere*. Journal of the Atmospheric Sciences **71**, 553–565.

Sardeshmukh, P. D. and Held, I. M. (1984). *The vorticity balance in the tropical upper troposphere of a general circulation model*. Journal of the atmospheric sciences **41**, 768–778.

Sardeshmukh, P. D. and Hoskins, B. J. (1985). *Vorticity balances in the tropics during the 1982-83 El Niñio-Southern oscillation event*. Quarterly Journal of the Royal Meteorological Society **111**, 261–278.

Schneider, T. and Bordoni, S. (2008). *Eddy-mediated regime transitions in the seasonal cycle of a Hadley circulation and implications for monsoon dynamics*. Journal of the Atmospheric Sciences **65**, 915–934.

Simmons, A. (2006). *ERA-Interim: New ECMWF reanalysis products from 1989 onwards*. ECMWF newsletter **110**, 25–36.

Thompson, D. W. and Wallace, J. M. (2000). *Annular modes in the extratropical circulation. Part I: Month-to-month variability*. Journal of climate **13**, 1000–1016.

Ting, M. and Yu, L. (1998). *Steady response to tropical heating in wavy linear and nonlinear baroclinic models*. Journal of the atmospheric sciences **55**, 3565–3582.

Toorn, R. van der and Zimmerman, J. T. (2010). *Angular momentum dynamics and the intrinsic drift of monopolar vortices on a rotating sphere*. Journal of Mathematical Physics **51**, 083102.

Vogel, B., Günther, G., Müller, R., et al. (2014). *Fast transport from Southeast Asia boundary layer sources to northern Europe: rapid uplift in typhoons and eastward eddy shedding of the Asian monsoon anticyclone*. Atmospheric Chemistry and Physics **14**, 12745–12762.

Vogel, B., Günther, G., Müller, R., et al. (2015). *Impact of different Asian source regions on the composition of the Asian monsoon anticyclone and of the extratropical lowermost stratosphere*. Atmospheric chemistry and physics **15**, 13699–13716.

Wang, B. (2002). *Rainy season of the Asian–Pacific summer monsoon*. Journal of Climate **15**, 386–398.

Wang, B., Wu, R., and Lau, K. (2001). *Interannual variability of the Asian summer monsoon: Contrasts between the Indian and the western North Pacific–East Asian monsoons*. Journal of climate **14**, 4073–4090.

Wang, J. (2011). "Instabilities of an eastern boundary current with and without large-scale flow influence". PhD thesis. Massachusetts Institute of Technology and Woods Hole Oceanographic Institution.

Wu, G., Liu, Y., He, B., et al. (2012). *Thermal controls on the Asian summer monsoon*. Scientific reports **2**.

Wu, Z., Sarachik, E., and Battisti, D. (2000a). *Vertical Structure of Convective Heating and the Three-Dimensional Structure of the Forced Circulation on an Equatorial Beta Plane*. Journal of the atmospheric sciences **57**, 2169–2187.

Wu, Z., Battisti, D. S., and Sarachik, E. (2000b). *Rayleigh friction, Newtonian cooling, and the linear response to steady tropical heating*. Journal of the atmospheric sciences **57**, 1937–1957.

Yang, J., Liu, Q., Xie, S.-P., et al. (2007). *Impact of the Indian Ocean SST basin mode on the Asian summer monsoon*. Geophysical Research Letters **34**.

Yihui, D. and Chan, J. C. (2005). *The East Asian summer monsoon: an overview*. Meteorology and Atmospheric Physics **89**, 117–142.

Yu, P., Rosenlof, K. H., Liu, S., et al. (2017). *Efficient transport of tropospheric aerosol into the stratosphere via the Asian summer monsoon anticyclone*. Proceedings of the National Academy of Sciences **114**, 6972–6977.

Zhang, G. J. and McFarlane, N. A. (1995). *Role of convective scale momentum transport in climate simulation*. Journal of Geophysical Research: Atmospheres (1984–2012) **100**, 1417–1426.

Zhang, Q., Wu, G., and Qian, Y. (2002). *The bimodality of the 100 hPa South Asia High and its relationship to the climate anomaly over East Asia in summer*. Journal of the Meteorological Society of Japan. Ser. II **80**, 733–744.

Zhang, Z., Wang, W., and Qiu, B. (2014). *Oceanic mass transport by mesoscale eddies*. Science, 1252418.

Zurita-Gotor, P. (2008). *The sensitivity of the isentropic slope in a primitive equation dry model*. Journal of the Atmospheric Sciences **65**, 43–65.